WORKSHOP ON INNOVATIVE NANOSCALE DEVICES AND SYSTEMS

ROYAL SONESTA KAUA'I RESORT, LIHUE, HI (ISLAND OF KAUA'I)

BOOK OF ABSTRACTS

EDITORS:

JAROSLAV FABIAN
JOSEF WEINBUB
BEREND JONKER
MATTHEW GILBERT
STUART PARKIN
AKIRA OIWA
STEPHEN GOODNICK
JOHN CONLEY

The 2022 Workshop on Innovative Nanoscale Devices and Systems (WINDS) is held December 4 – 9, 2022, at the Royal Sonesta Kaua'i Hotel, Lihue, Hawaii, USA.

WINDS is a week-long, international, and interactive workshop designed to explore the fundamental properties of nanoscale devices and applications thereof. In particular, WINDS provides a forum for material, device, and characterization as well as experimental and modeling researchers to interact.

The program consists of invited talks, regular talks, and poster presentations. All contributions have been peer-reviewed by the program committee.

This workshop is composed of morning and evening sessions, with afternoons free for ad hoc meetings to encourage extended interaction and discussion among participants. It is the successor of the original WINDS and the International Symposium on Advanced Nanodevices and Nanotechnology (ISANN), which were held on alternate years. WINDS itself began as an outgrowth of the successful Advanced Heterostructures Workshop, which has a long history dating from the 1980s.

WINDS 2022 is an AVS Sponsored Topical Conference, with financial support from American Elements. The conference committee greatly appreciates their support.

i

CONFERENCE CHAIRS

General chair:	Jaroslav Fabian, University of Regensburg, Germany
Europe Co-Chair:	Stuart Parkin, Max-Planck Institute of Microstructure Physics, Germany
Japan Co-Chair:	Akira Oiwa, Osaka University, Japan
US Co-Chair:	John Conley, Oregon State University, USA
Communications Chair:	Josef Weinbub, TU Wien, Austria
Local arrangements Chair:	Stephen Goodnick, University of Arizona, USA

PROGRAM COMMITTEE

Alexander Balandin, University of California, Riverside, USA

David K. Ferry, Arizona State University, USA

Eric E. Fullerton, University of California, San Diego, USA

Matthew Gilbert, University of Illinois Urbana-Champaign, USA

Koji Ishibashi, RIKEN, Japan

Satoshi Iwamoto, University of Tokyo, Japan

David Janes, Purdue University, USA

Deep Jariwala, University of Pennsylvania, USA

Berend (Berry) Jonker, Naval Research Lab, USA

Victor Klimov, Los Alamos National Laboratory, USA

Valeria Lauter, Oak Ridge National Laboratory, USA

Tomoki Machida, University of Tokyo, Japan

Kazuhiko Matsumoto, Osaka University, Japan

Wolfgang Porod, University of Notre Dame, USA

Ian Sellers, University of Oklahoma, USA

Viktor Sverdlov, TU Wien, Austria

Igor Zutic, University at Buffalo, USA

Monday, December 5

08:45-09:00   **Opening remarks**

Jaroslav Fabian and Stephen Goodnick

AM1: 2D Materials and vdW heterostructures I

Session chair: Alexander Balandin (UC Riverside, USA)

09:00-09:30   Andrea Ferrari, *Cambridge University, UK*

"Layered Materials for Optoelectronics and Quantum Technologies" (invited)   1

09:30-09:45   Fateme Mahdikhanaysarvejahany, *University of Arizona, USA*

"Origin of Narrow Interlayer Exciton Photoluminescence in 2D Semiconductor Heterostructures"   3

09:45-10:00   Hui Zhao, *University of Kansas, USA*

"Mixed-dimensional van der Waals Heterostructures for Generation of Long-lived and Mobile Photocarriers in Graphene"   5

10:00-10:30   Mikito Koshino, *Osaka University, Japan*

"Moiré Quasicrystals in Twisted 2D Systems" (invited)

10:30-10:45   Jaroslav Fabian, *University of Regensburg, Germany*

"Proximity Effects in vdW Heterostructures Tuned by the Twist Angle"   7

10:45-11:00   Zachariah Hennighausen, Jisoo Moon, Kathleen M. McCreary, Connie H. Li, Olaf M.J. van 't Erve, and Berend T. Jonker, *Naval Research Laboratory, USA*

"Interlayer Exciton–Phonon Bound State in Bi_2Se_3 / monolayer WS_2 van der Waals Heterostructures"   8

11:00-11:15   **Coffee break**

AM2: Superconductivity I: Superconducting diode effect

Session chair: Eric Fullerton (UC San Diego, USA)

11:15-11:45   C. Baumgartner, L. Fuchs, A. Costa, S. Reinhardt, P. E. F. Junior, D. Kochan, J. Fabian, N. Paradiso, and C. Strunk, *University of Regensburg, Germany*, and S. Gronin, G.C. Gardner, T. Lindemann, and M.J. Manfra, *Purdue University, USA*

"Nonreciprocal Transport in Ballistic Al/InAs Josephson Junctions" (invited)   10

11:45-12:00   Igor Žutić, David Monroe, *SUNY Buffalo, USA*, and Mohammad Alidoust, *Norwegian University of Science and Technology, Norway*

"Tunable Planar Josephson Junctions Driven by Time-Dependent Spin-Orbit Coupling"   11

12:00-12:15   Stuart Parkin, *MPI Halle, Germany*

"Chiral Spin Textures and Josephson Diodes"   13

12:15-12:30   Ananthesh Sundaresh, Jukka Ilmari Vayrynen, Yuli Lyanda-Geller, Leonid P. Rokhinson, *Purdue University, USA*

"Supercurrent Non-reciprocity and Vortex Formation in Superconductor Heterostructures"   15

12:30-12:45   John Chiles, Ethan Arnault, Chun-Chia Chen, Lingfei Zhao, Trevyn Larson, and Gleb Finkelstein, *Duke University, USA*, and Takashi Taniguchi, Kenji Watanabe, NIMS Tsukuba, Japan, and François Amet, *Appalachian State University, USA*

"Graphene-based Josephson triode"   17

12:45-13:00   Denis Kochan, SAS, Slovakia

"Anisotropic Vortex Squeezing and Supercurrent Diode Effect in Non-centrosymmetric Rashba Superconductors"   19

13:00-13:15   E. Arnault, *MIT, USA*, and J. Chiles, G. Finkelstein, *Duke University, USA*, and F. Amet, *Appalachian State University, USA*, and I. V. Borzenets, *University of Texas A&M, USA*

"RF Mediated Vortex Glass to Vortex Liquid Transition in Metallic Josephson Junctions"   21

13:15-19:00   **Ad hoc session**

PM: Quantum transport

Session chair: Akira Oiwa (Osaka U, Japan)

Tuesday, December 6

AM1: Spintronics

Session chair: Valeria Lauter (Oak Ridge NL, USA)

08:30-09:00   Andrew Kent, *New York University, USA*

"Spintronics with Ferrimagnetic and Antiferromagnetic Insulators" (invited)   35

09:00-09:15   <u>Deepak K. Singh</u>, Pousali Ghosh, Jiasen Guo, and Tom Heitmann, *University of Missouri, USA*, and Feng Ye, *Oak Ridge National Laboratory*, *USA,*

"NiSi: New Research Venue for Antiferromagnetic Spintronics"   36

09:15-09:30   <u>Kenji Hayashida</u> and H. Akera, *Hokkaido University, Japan*

"Theory of Exchange Spin-Orbit Coupling"   38

09:30-10:00   Sadamichi Maekawa, *Riken, Japan*

"Nonreciprocity in Spin Transport" (invited)   40

10:00-10:15   Alexey Kovalev, University of Nebraska, USA

"Superfluid Spin Transistor"   42

10:15-10:30   S. Fiorentini, M. Bendra, J. Ender, <u>V. Sverdlov</u>, and S. Selberherr, *TU Wien, Austria*, and W. Goes, *Silvaco Europe Ltd., Cambridge, UK*

"Evaluating Spin Transfer Torques in multilayered magnetic tunnel junctions and spin valves"   44

11:30-11:00   Matthew Beard, *National Renewable Laboratory, USA*

"Chiral Metal-Halide Organic/Inorganic Hybrid Semiconductors" (invited)

11:00-11:15   **Coffee break**

AM2: Topology I

Session chair: Jaroslav Fabian (U Regensburg, USA)

11:15-11:45   Takehito Suzuki, *Toho University, Japan*

"Singular Angular Magnetoresistance in a Nodal Semimetal" (invited)   46

11:45-12:00   Mathew Gilbert, *University of Illinois, USA*

"Pseudogravity in Topological Condensed Matter"

12:00-12:15   V. Sverdlov, A. El-Sayed, H. Seiler, and H. Kosina, *TU Wien, Austria*

"Edge State Band Gap Dependencies on the Width of Transition Metal Dichalcogenide Nanoribbons in the 1T′ Topological Phase"   48

12:30-19:00   **Ad hoc session**

PM: Oxides and Multiferroics

Session chair: John Conley (Oregon State U, USA), David Henry (Sandia NL, USA)

19:00-19:30   Thirumalai Venkatesan, *University of Oklahoma, USA*

"Robust Resistive and Mem-devices for Neuromorphic Circuits" (invited)   50

19:30-19:45   J. Lee, D. Eom, W. Lee, J. Oh, C. Park, and H. Kim, *Sungkyunkwan University, Korea*

"Interface Characteristics of Ferroelectric $Hf_{1-x}Zr_xO_2$ on Si with an Al_2O_3 Interface Layer"

51

19:45-20:00   M. David Henry, Giovanni Esteves, Travis Young, Steve Wolfley, *Sandia National Laboratories, USA*, and Shelby Fields, Samantha Jaszewski, and Jon Ihlefeld, *University of Virginia, USA*

"Ferroelectric Microelectronic Devices Utilizing NbN and Nb Electrodes with Thin Film Ferroelectric $(Hf,Zr)O_2$"   53

20:00-20:15   J. Peterson and J. F. Conley, Jr., *Oregon State University, USA,* T. Mimura, Jon Ihlefeld, *University of Virginia, USA*

"Internal Photoemission (IPE) Spectroscopy Measurement of Electrode Energy Barriers in Pristine, Woken, and Poled Ferroelectric HZO Devices"   55

20:15-20:30   A. A. Demkov, A. B. Posadas and M. Reynaud, *University of Texas at Austin, USA*

"Si-integrated Ferroelectric Thin Films for Optical Computing"   57

20:30-20:45   H. Lee, H. Kim, K. Kim, G. Y. Yeom, and H. Kim, *Sungkyunkwan University, Korea*, and K. Jeong, *Dongguk University, Korea*

"BCl_3 Plasma Treatment of MoS2 for Atomic-layer-deposition of High-k Dielectrics"   59

viii

Wednesday, December 7

AM1: 2D Materials and vdW heterostructures II

Session chair: Deep Jariwala (U Pennsylvania, USA)

08:30-09:00   Deji Akinwande, *University of Texas at Austin, USA*

"Skintronics and Beyond Based on 2D Materials" (invited)   60

09:00-09:15   S. Liang and <u>C. Gong</u>, *University of Maryland, USA*

"Effective Voltage Control of Two-dimensional Magnetic Insulator"   62

09:15-09:30   <u>Hanan Dery</u> and Dinh Van Tuan, *University of Rochester, USA*

"Hexcitons and Oxcitons in Monolayer WSe$_2$"   64

09:30-10:00   Hyeon Suk Shin, *Ulsan National Inst of S&T, Korea*

"Growth of Single-Crystal Hexagonal Boron Nitride by Chemical Vapor Deposition" (invited)   66

10:00-10:15   Vasili Perebeinos, *SUNY Buffalo, USA*

"Phonon Limited Mobility and Phonon Drag in h-BN Encapsulated Monolayer and AB-stacked Bilayer Graphene"   68

10:15-10:30   <u>S</u>. Rumyantsev, A. Rehman, J. A. D. Notario, G. Cywiński, W. Knap, *CENTERA Labs, Poland*, and J. S. Sanchez, Y. M. Meziani, *Universidad de Salamanca, Salamanca, Spain, and* A. A. Balandin, *University of California Riverside, USA*

"Mobility-fluctuations Mechanism of 1/f Noise in Graphene"   70

10:30-11:00   <u>Noah Mendelson</u>, *University of Chicago, USA*, and I. Aharonovich, *University of Technology Sydney, Australia*

"Quantum Emitters in Hexagonal Boron Nitride" (invited)   72

11:00-11:15   **Coffee break**

AM2: 2D Devices & Quantum and spintronics information

Session chairs: Berry Jonker (NRL, USA), Vasili Perebeinos (SUNY Buffalo, USA)

11:15-11:30   M. Taheri, J. Brown, F. Kargar, <u>A. A. Balandin,</u> *Unversity of California Riverside, USA*, and A. Rehman, S. Rumyantsev, *CENTERA Laboratories, Poland*, and N. R. Sesing, T. T. Salguero, *University of Georgia, USA*

"Electrical Gating of the Charge-Density-Waves in Two-Dimensional 1T-TaS2 Devices – Prospects of Memory Applications"   74

11:30-11:45   Deep Jariwala, *University of Pennsylvania, USA*

"Emerging Memory Devices from AlScN Ferroelectric"   76

11:45-12:00   <u>C. Hayashi</u>, C. Aguilar, L. Hsu, C. Torres Jr, and R. Ordonez, *Naval Information Warfare Center Pacific, USA*, and, T. Schranghamer, A. Dodda, S. Das, *Pennsylvania State University, USA*

"An Exploration of Liquid Electrolytes to Enable Graphene Electrical Switches with High On-Off Ratios"   77

12:00-12:15   Kazuhiko Matsumoto, *Osaka University, Japan*

"Detection of SARS-CoV-2 Virus by Antigen Modified Integrated Graphene FET Array with Automated Washing System"

12:15-12:30   Xinyu Zhao, Yan Xia, *Fuzhou University, China*, and <u>Xuedong Hu</u>, *SUNY Buffalo, USA*

"Adiabatic Resonance for Fast and Robust Quantum Control"   79

12:30-12:45   Yasuhiro Tokura, *University of Tsukuba, Japan*

"Rabi Frequency and Fidelity of Strongly Driven Electric Dipole Spin resonance"   81

12:45-13:00   <u>Sahel Ashhab</u>, Fumiki Yoshihara, Tomoko Fuse, and Kouichi Semba, *National Institute of Information and Communications Technology, Japan*, and Naoki Yamamoto, *Keio University, Japan*, and Adrian Lupascu, *University of Waterloo, Canada*

"Speed Limits for Two-qubit Gates with Weakly Anharmonic Qubits"   82

13:00-13:15   <u>Sangita Regmi</u>, Sanjaya Lohani and Thomas A. Searles, *University of Illionis, USA*, and Joseph M. Lukens, *Oak Ridge National Laboratories, USA*, and Ryan T. Glasser, Brian T. Kirby, *Tulane University, USA*

84

x

Thursday, December 8

AM1: Superconductivity II and 2D Materials III

Session chair: Igor Zutic (SUNY Buffalo, USA)

AM2: Light-matter interactions

Session chair: David Ferry (Arizona State University, USA)

PM: Posters and Topology II

Session chair: Victor Sverdlov (TU Vienna, Austria) and Matthew Gilbert (U Illinois, USA)

Friday, December 9

AM1: Wide gap materials and Devices

Session chair: Denis Kochan (U Regensburg, Germany)

08:30-08:45   E. Guzman, F. Kargar, F. Angeles, R. B. Wilson, and A. A. Balandin, University of California Riverside, USA, and R. V. Meidanshahi, S. M. Goodnick, *Arizona State University, USA,* and T. A. Grotjohn, *Michigan State University, USA,* and A. Hardy, M. Muehle, *Fraunhofer USA Center Midwest, USA*

"Modification of Bulk and Surface Phonons in Single-Crystal Diamond via Substitutional Boron Doping"   132

08:45-09:00   Avani Patel, Saurabh Vishwakarma, Jesse Brown, David J. Smith and Robert J. Nemanich, *Arizona State University, USA*

"Epitaxial Growth of c-BN on Diamond and Strategies for Power and RF Applications"   134

09:00-09:15   S. Marcinkevičius, R. Yapparov, *KTH Royal Institute of Technology, Sweden*, Y. C. Chow, F. Wu, S. Nakamura, and J. S. Speck, *University of California Santa Barbara, USA*

"V-Defects in Ingan Quantum Wells: Influence on Carrier Dynamics"   136

09:15-09:30   W. Miyazaki, H. Tanaka, and N. Mori, *Osaka University, Japan*

"Tight-Binding and Full-Band Monte Carlo Analysis of the Strain Effects in wurtzite GaN"   138

09:30-09:45   A. Litvinenko, B.Dieny, A.N. Slavin, and U. Ebels, *Oakland University, USA*, S. Louis, V.S. Tyberkevych, *CNRS Grenoble, France*

"Ultrafast Microwave Spectrum Analysis Using Sweep-Tuned Spin-Torque Nano-Oscillators"   140

09:45-10:00   Yevhenii Vaskivskyii, Anže Mraz, Andrej Kranjec, Igor Vaskivskyi[1], and Dragan Mihailovic, *Jozef Stefan Institute, Slovenia*, and Peter Karpov, *Brookhaven National Laboratory, USA*

"Manipulation of Fractional Charge on the Nanoscale in Charge Configuration Memory Devices Using Multi-Tip Scanning Tunneling Microscopy"   142

AM2: Quantum nanostructures

Session chair: Leonid Rokhinson (Purdue U, USA)

Layered Materials for Optoelectronics and Quantum Technologies

Andrea C. Ferrari

Cambridge Graphene Centre, University of Cambridge, Cambridge CB3 0FA, UK

Graphene and layered materials (LMs) have great potential in photonics and optoelectronics, where the combination of their optical and electronic properties can be fully exploited, and the absence of a bandgap in graphene can be beneficial. The linear dispersion of the Dirac electrons in graphene enables ultra-wide-band tunability as well as gate controllable third-harmonic enhancement over an ultra-broad bandwidth, paving the way for electrically tunable broadband frequency converters for optical communications and signal processing. Saturable absorption is observed as a consequence of Pauli blocking and can be exploited for mode-locking of a variety of ultrafast and broadband lasers. Graphene integrated photonics is a platform for wafer scale manufacturing of modulators, detectors and switches for next generation datacom and telecom. Heterostructures based on LMs have properties different from those of their individual constituents and of their three dimensional counterparts. These can be exploited in novel light emitting devices, such as single photon emitters, and tunable light emitting diodes. LMs have potential for quantum technologies, as scalable sources of single photon emitters (SPEs). Quantum emitters in LMs hold potential in terms of scalability, miniaturization, integration. Generation of quantum emission from the recombination of indirect excitons in heterostructures made of different LMs is a path with enormous potential. I will overview production, characterization and application of graphene and LMs, focusing on optical and quantum applications.
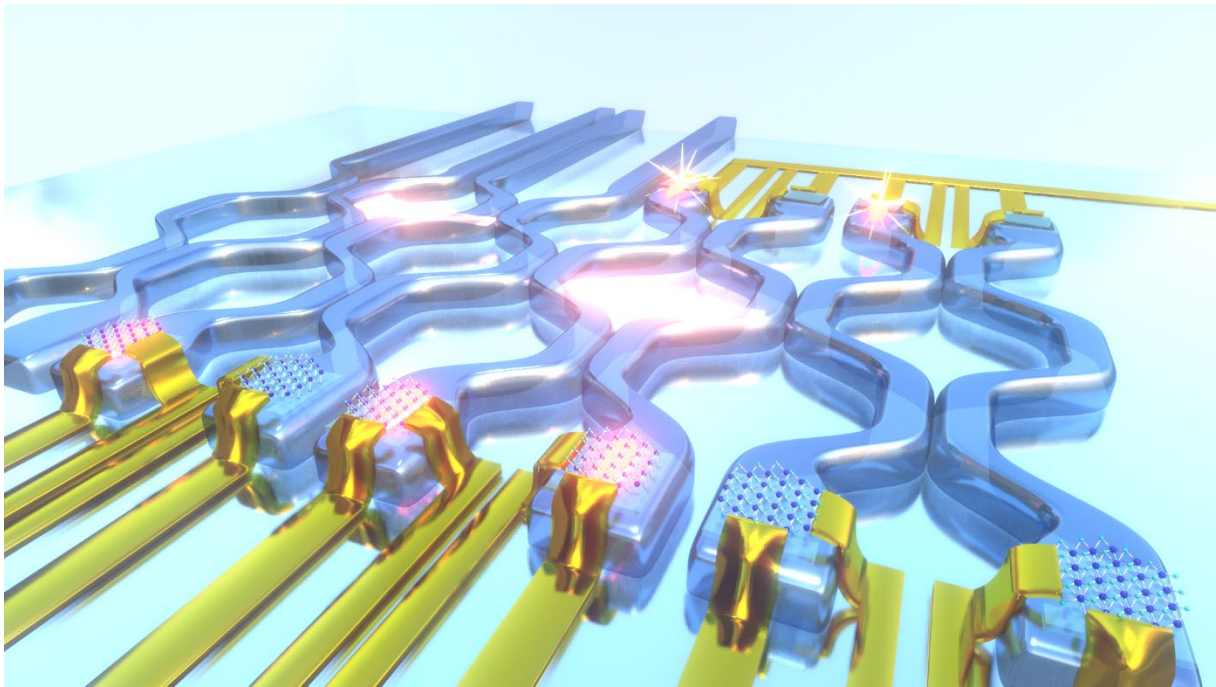
On-chip photonic circuit for quantum computation. It consists of waveguides (semi-transparent blue bent "pipes"), layered materials as photon sources on top of the waveguides (spheres with the bonds connecting each other) which are electrically contacted (Au leads). The emitted photons (bright red shades) travel through the waveguides until they reach the single-photon detectors made of layered materials, also electrically contacted.

Origin of Narrow Interlayer Exciton Photoluminescence in 2D Semiconductor Heterostructures

Fateme Mahdikhanysarvejahany

Department of Physics, University of Arizona, Tucson, Arizona 85721, USA

fmahdikhany@arizona.edu

Indirect interlayer excitons (IXs) in $MoSe_2$/WSe_2 heterostructures are composed of an electron in $MoSe_2$ and a hole in WSe_2. The long lifetime of indirect IXs and the possibility of being trapped by the moiré potential between the TMD layers make them a promising candidate for use as single quantum emitters. Previous reports on this system reported narrow (<1 meV) photoluminescence (PL) lines and attributed them to be the signature of moiré trapped IXs. To explore the effect of the moiré potential on IX trapping, we separated the two monolayer TMDs partially by two monolayers of hBN which suppresses the magnitude of the moiré potential. We show that the localization potential resulting in the narrow PL lines is independent of the moiré potential, and instead likely due to extrinsic effects such as nanobubbles or defects. Furthermore, the doping, electric field, and temperature dependence of the narrow IX lines is similar for both regions, and their excitonic g-factors have opposite signs, indicating that the IXs in the directly contacted region are trapped by both moiré and extrinsic localization potentials.
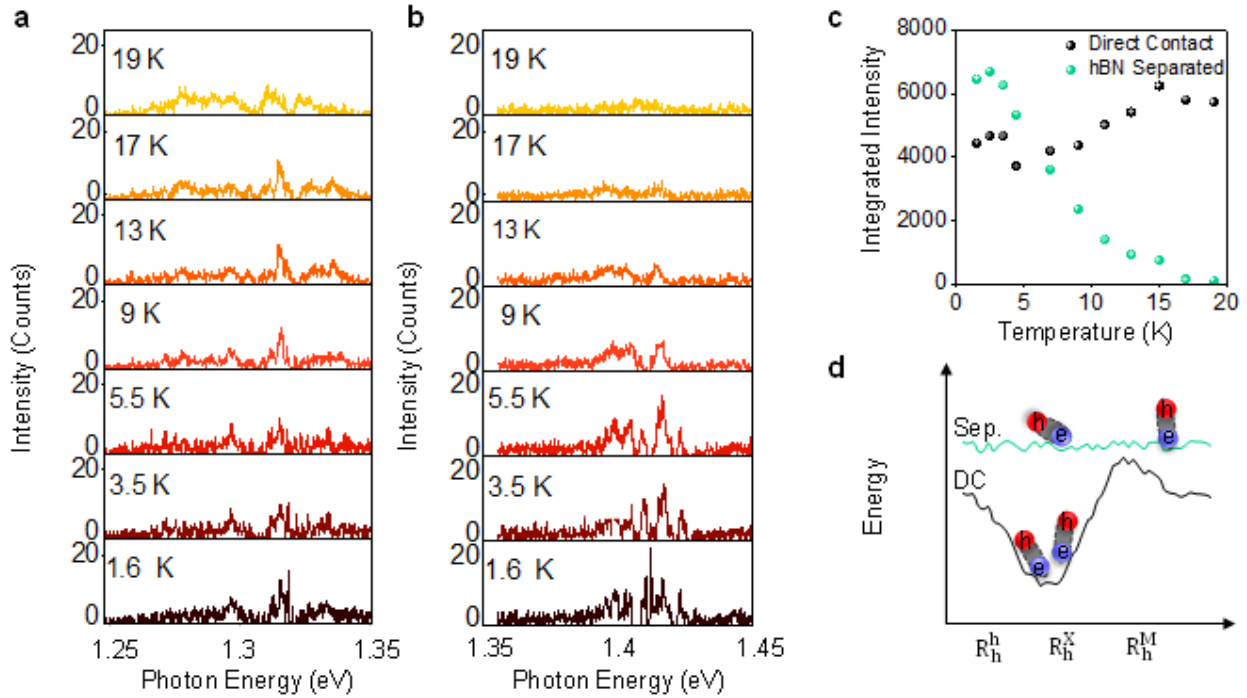
Fig. a, PL of the narrow IX lines in the DC region as a function of temperature shows the width of individual lines are increasing by 9 K and disappear completely by 17 K. The signal in the DC region includes narrow emission on top of a wider PL plateau. The wider emission persists to higher temperature (see Supplementary Fig.6) that is consistent with previous temperature dependent measurements on R-type heterostructures. b, Temperature dependent PL from the hBN separated region shows the narrow lines are widening by 9 K which is in good agreement with the DC region's temperature dependent PL. The hBN separated IX signal disappears fully by 13 K and does not have a wider PL plateau. c, Spectrally integrated PL shows IX emission in the hBN separated region disappears completely by 19 K whereas the signal from the DC region is approximately constant. d, Depiction of the IX energy as a function of position in the moiré, for DC region (black) and hBN separated (Sep.) region (green). Both regions exhibit a weak extrinsic trapping potential denoted by the fluctuations. The DC region has both moiré trapping and extrinsic fluctuations.

4

Mixed-dimensional van der Waals Heterostructures for Generation of Long-lived and Mobile Photocarriers in Graphene

H. Zhao

Department of Physics and Astronomy, University of Kansas, Lawrence, Kansas, USA

huizhao@ku.edu

Since its discovery, graphene has been regarded as a promising material for optoelectronic applications. [1,2] However, the development of graphene-based optoelectronic devices has been hindered by the difficulty of generating free and long-lived photocarriers in graphene with high efficiency. Although light can excite electrons and holes in graphene by interband absorption, they form tightly-bond excitons, [3] which prevent charge separation and cause rapid loss of energy to the lattice. In this experimental study, we show that mixed-dimensional and multilayer van der Waals heterostructures with suitable band alignments can produce long-lived and highly mobile photocarriers in graphene. The heterostructure samples are fabricated by combing a graphene monolayer with a transition metal dichalcogenide (such as MoS_2 and WS_2) few-layer (n = 1, 2, 3, and 4) and an organic semiconductor monolayer of F_8ZnPc. Photoluminescence spectroscopy measurements are performed to probe the sample quality and photocarrier property. Spatiotemporally resolved transient absorption measurements reveal that in heterostructures of F_8ZnPc/few-layer-MoS_2/graphene, electrons excited in F_8ZnPc can transfer to graphene and thus are separated from the holes. By increasing MoS_2 thickness to 4 layers, the electrons transferred to graphene acquire long recombination lifetimes of over 100 ps, a diffusion coefficient of 36 cm^2/s and a mobility of 2800 cm^2/Vs. Graphene doping with mobile holes is also achieved with another set of heterostructure samples of F_8ZnPc/few-layer-WS_2/graphene. Such artificial materials can be used in optoelectronic devices with enhanced performance. Moreover, the strategy demonstrated can be generally applied to design van der Waals heterostructures with finely controlled charge carrier properties at atomic length scales.

[1] A. K. Geim and K. S. Novoselov, Nat. Mater. **6**, 183 (2007).

[2] R. R. Nair *et al*., Science **320**, 1308 (2008).

[3] L. Yang *et al.*, Phys. Rev. Lett. **103**, 186802 (2009).
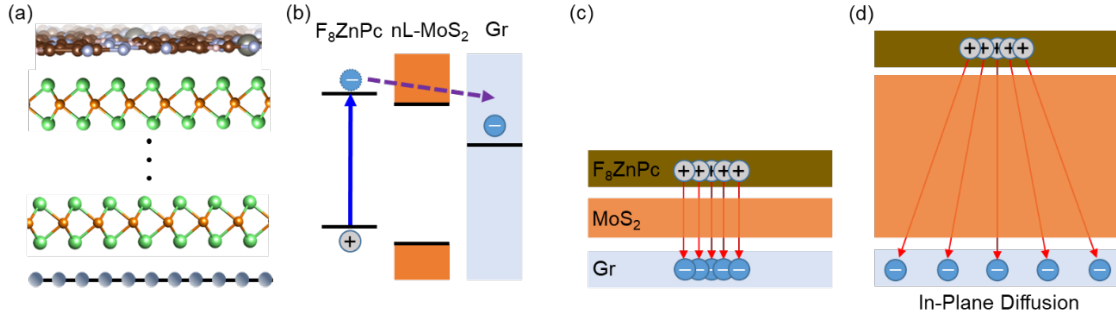
Fig.1: (a) Schematics of heterostructures formed by an F_8ZnPc monolayer, a transition metal dichalcogenide (TMD) few layer, and a graphene monolayer. (b) Band alignment of the heterostructure. The upper and lower horizontal lines on the left represent the LUMO and HOMO levels of F_8ZnPc. The orange and gray boxes represent the conduction and valence bands of TMD and graphene. Photoexcited electrons (-) are expected to transfer to graphene, while holes (+) reside in F_8ZnPc. (c) Schematics of in-plane carrier distributions in strong binding regimes. (d) Significant spread of electrons in graphene in weak binding regimes with thicker MoS_2 layer.
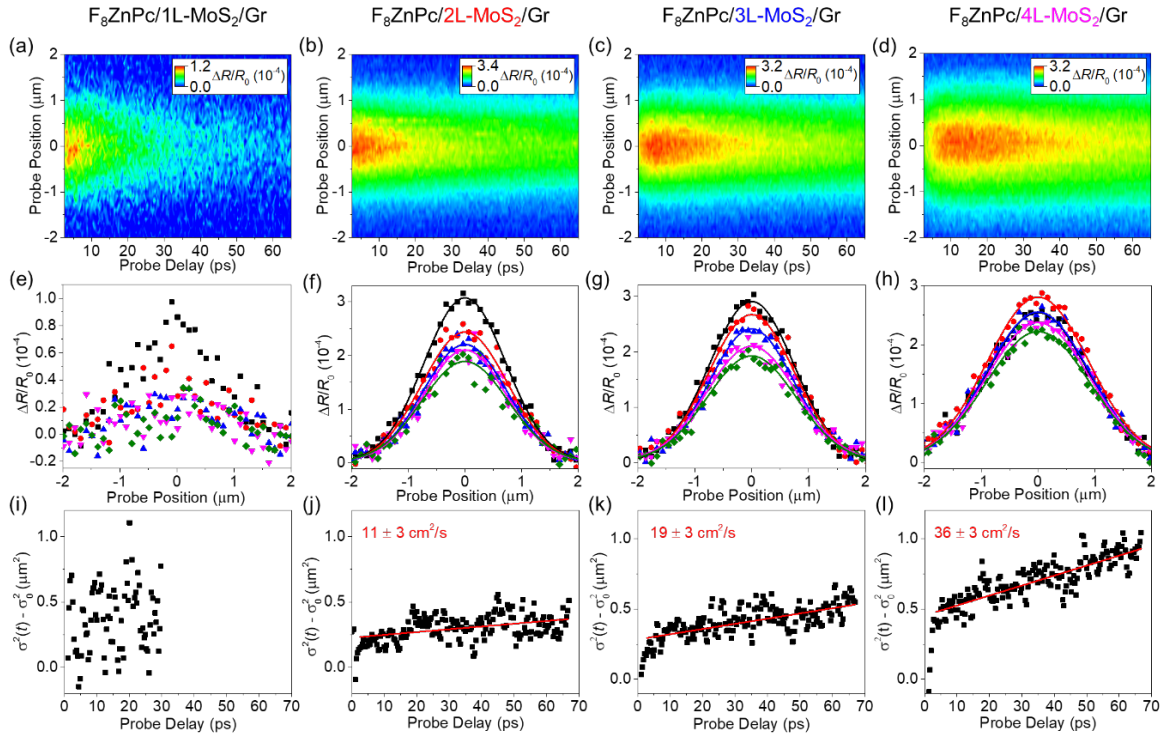
Fig. 2: (a)-(d) Spatiotemporally resolved differential reflectance measured from F_8ZnPc/nL-MoS_2/graphene heterostructure samples with n = 1, 2, 3, and 4, respectively. (e)-(h) Selected spatial profiles of differential reflectance from the 4 samples with probe delays of 5.5 (black), 20.4 (red), 35.3 (blue), 50.2 (pink), and 65.0 ps (green). The solid curves are Gaussian fits. (i)-(l) Change of the variance of the spatial distributions as a function of probe delay. Lines are linear fits.

Proximity effects in vdW Heterostructures Tuned by the Twist Angle

J. Fabian

Department of Physics, University of Regensburg, Universitätstrasse 40, 93040 Regensburg,
Regensburg, Germany
jaroslav.fabian@ur.de

Graphene has weak spin-orbit coupling and no magnetism. But when placed in proximity to a strong spin-orbit coupling material, such as a semiconducting transition-metal dichalcogenide (TMDC) (WSe_2, MoS_2, etc), graphene acquires significant (order of meV) spin-orbit coupling while preserving the Dirac band structures. The induced proximity spin-orbit coupling has the valley Zeeman functional form, leading to giant spin relaxation anisotropy and gate-tunable spin precession. Similarly, in heterostructures of graphene and magnetic semiconductors, such as $Cr_2Ge_2Te_5$, graphene picks up a magnetic moment and its Dirac electrons become spin polarized. This talk is devoted to theoretical studies of the influence of the twist angle on the spin proximity effects in graphene. First, I discuss how the spin-orbit coupling depends on the twist angle in Graphene/TMDC. I show that at 30 degrees the valley Zeeman spin-orbit coupling disappears and that the proximity Rashba coupling has a radial component. Next, I will discuss our surprising prediction that in twisted Graphene/$Cr_2Ge_2Te_5$, the induced exchange coupling in graphene changes from ferromagnetic up (0 degree) to ferromagnetic down (30 degrees). In between, at around 20 degrees, the coupling becomes even antiferromagnetic! Support from EU Graphene Flagship and DFG SPP1244, SFB 1277 is acknowledged.

[1] T. Naimer et al, Phys. Rev. B 104, 195156 (2021)
[2] K. Zollner and J. Fabian, Phys. Rev. Lett. 128, 106401 (2022)

Interlayer Exciton–Phonon Bound State in Bi₂Se₃ / monolayer WS₂ van der Waals Heterostructures

Zachariah Hennighausen[1], Jisoo Moon[1], Kathleen M. McCreary[2], Connie H. Li,[2] Olaf M.J. van 't Erve[2], and <u>Berend T. Jonker</u>[2*]

[1] *NRC Postdoc in the Materials Science and Technology Division, Naval Research Laboratory, Washington, D.C. 20375, USA*

[2] *Materials Science and Technology Division, Naval Research Laboratory, Washington, D.C. 20375, USA*

**berry.jonker@nrl.navy.mil*

The ability to assemble layers of 2D materials to form unique van der Waals heterostructures provides unprecedented opportunities in materials design and synthesis. Interlayer interactions provide a path to new properties and functionality, and understanding such interactions is essential to that end. Here we report formation of interlayer exciton-phonon bound states in Bi_2Se_3/WS_2 heterostructures, where the Bi_2Se_3 $A_1^{(3)}$ surface phonon, a mode particularly susceptible to electron-phonon coupling, is imprinted onto the excitonic emission of the WS_2. The exciton-phonon bound state (or exciton-phonon quasiparticle) presents itself as evenly separated peaks superposed on the WS_2 excitonic photoluminescence spectrum (Figure 1), whose periodic spacing corresponds to the $A_1^{(3)}$ surface phonon energy. Low-temperature polarized Raman spectroscopy of Bi_2Se_3 reveals intense surface phonons and local symmetry breaking that allows the $A_1^{(3)}$ surface phonon to manifest in otherwise forbidden scattering geometries. Previous work found significant interlayer hybridization in Bi_2Se_3/WS_2 heterostructures, facilitating electron transfer and modifying the bonding [1], conditions which encourage the formation of interlayer quasiparticles. Our work advances efforts to understand the interlayer coupling, and combine the distinctive transport and optical properties from separate materials into one device for possible spintronics, valleytronics, and quantum computing applications.

[1] Hennighausen, Z.; Wickramaratne, D.; McCreary, K. M.; Hudak, B. M.; Brintlinger, T.; Chuang, H.-J.; Noyan, M. A.; Jonker, B. T.; Stroud, R. M.; van 't Erve, O. M. Laser-Patterned Submicrometer Bi2Se3–WS2 Pixels with Tunable Circular Polarization at Room Temperature. *ACS Appl. Mater. Interfaces* **2022**. https://doi.org/10.1021/acsami.1c24205.
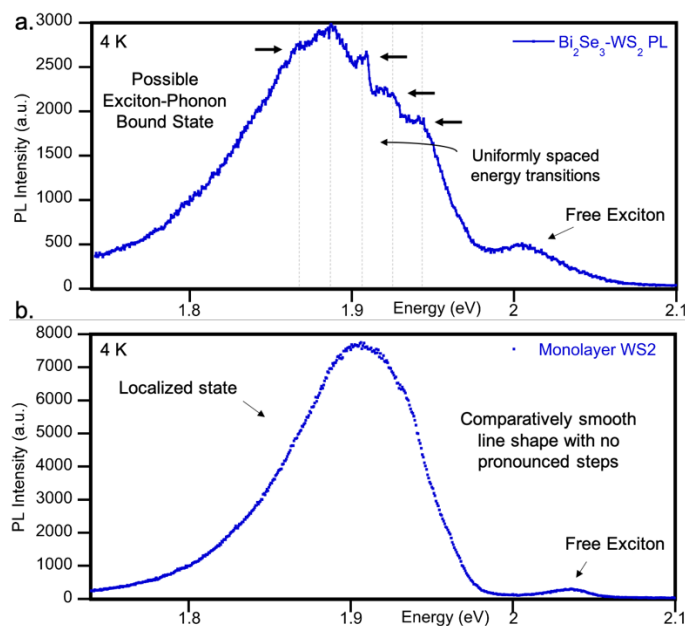
Fig. 1: **Manifestation of interlayer exciton-phonon bound state.** (a) 4-6QL Bi$_2$Se$_3$ + 1L WS$_2$ 2D heterostructure PL at 4 K showing the free exciton and localized state. Evenly spaced "steps" are observed, whose energy spacing (19.3meV) corresponds well to the 160cm^{-1} A$_1^{(3)}$ surface phonon. Previous work identified the A$_1^{(3)}$ mode as particularly susceptible to electron-phonon coupling. (b) 1L WS$_2$ PL at 4 K, where a comparatively smooth localized state is observed.

Nonreciprocal Transport in ballistic Al/InAs Josephson Junctions

C. Baumgartner,[1] L. Fuchs,[1] A. Costa,[2] S. Reinhardt,[1] S. Gronin,[3,4] G.C. Gardner,[3,4] T. Linde-mann,[4] M.J. Manfra,[3,4,5,6,7] P.E.F Junior,[2] D. Kochan,[2] J. Fabian,[2] N. Paradiso,[1] <u>C. Strunk</u>[1]

[1]Univ. Regensburg, Inst. f. Experimental & Applied Physics, Regensburg, Germany
[2]Univ. Regensburg, Inst. f. Theoretical Physics, Regensburg, Germany
[3]Purdue Univ., Microsoft Quantum Purdue, W Lafayette, IN, USA
[4]Purdue Univ., Birck Nanotechnology Ctr., W Lafayette, IN, USA
[5]Purdue Univ., Dept. Physics & Astronomy, W Lafayette, IN, USA
[6]Purdue Univ., Sch. Mat. Engn., W Lafayette, IN, USA
[7]Purdue Univ., Sch. Elect. & Comp. Engn., W Lafayette, IN, USA
(christoph.strunk@ur.de)

Non-reciprocal transport becomes possible, if inversion and time-reversal symmetries are broken simultaneously, for example, by an interplay of spin–orbit coupling (SOC) and magnetic field. We report on non-reciprocal supercurrents in highly transparent Josephson junctions fabricated on InAs quantum wells. We demonstrate supercurrent rectification also far below the transition temperature and far from the critical current. By measuring Josephson inductance, we can link the non-reciprocal supercurrent to an asymmetry of the current–phase relation, and directly derive the supercurrent magnetochiral anisotropy coefficient γ_L [1]. Orientation of the devices along different lattice directions allows for the differentiation between the contributions of Rashba and Dresselhaus SOC [2]. At low in-plane magnetic field B_{ip} the non-reciprocal inductance is linear in B_{ip}. At higher fields near the closing of the minigap by the dispersion of Andreev states, γ_L becomes strongly non-linear and features a sign change of the non-reciprocal inductance is observed that can be traced back to a zero/pi-crossover in the current phase relation. The specific form of $\gamma_L(B_{\mathrm{ip}})$ rules out other sources of non-reciprocity, such as finite momentum pairing [3].

[1] C. Baumgartner *et al*., *Nature Nanotechnology* **17**, 39 (2022).
[2] C. Baumgartner *et al*., J. Phys.: Condens. Matter., **34**, 154005 (2022).
[3] N.F.Q. Yuan and L. Fu, PNAS **119**, e2119548119 (2022).

Tunable Planar Josephson Junctions Driven by Time-Dependent Spin-Orbit Coupling

Igor *Žutić*[1,*], David Monroe[1], and Mohammad Alidoust[2]

[1]*Department of Physics, University at Buffalo, State University of New York, USA*

[2]*Department of Physics, Norwegian University of Science and Technology, N-7491 Trondheim, Norway*

**zigor@buffalo.edu*

The integration of conventional superconductors with common III–V semiconductors provides a versatile platform to implement tunable Josephson junctions (JJs) and their applications. We propose that with gate-controlled time-dependent spin-orbit coupling (SOC), it is possible to strongly modify the current-phase relations and Josephson energy and provide a mechanism to drive the JJ dynamics, even in the absence of any bias current [1]. Our generalized pendulum model of the JJ offers a guidance in understanding the interplay between the applied magnetic field and changing SOC, which can lead to novel phenomena, including the time-dependent superconducting diode effect. We show that the transition between stable phases is realized with a simple linear change in the SOC, while the transition rate can exceed the gate-induced electric field gigahertz changes by an order of magnitude. The feasibility of these predictions is supported by using the measured parameters from Al/InAs planar JJs, where the static control gate control was shown to enable the topological superconductivity and the superconducting diode effect [2]. The resulting interplay between the constant effective magnetic field and changing SOC has direct implications for superconducting spintronics, the control of Majorana bound states [3], and emerging qubits. We argue that topological superconductivity, sought for fault-tolerant quantum computing, offers simpler applications in superconducting electronics and spintronics.

[1] D. Monroe, A. Alidoust, and I. Žutić, arXiv:2208.07512 (2022), Phys. Rev. Applied (letter) in press.

[2] M. Dartiailh, W. Mayer, J. Yuan, K. Wickramasinghe, A. Matos-Abiague, I. Žutić, and J. Shabani, Phys. Rev. Lett. **126**, 036802 (2021); arXiv:1906.0117.

[3] T. Zhou, M. C. Dartiailh, K. Sardashti, J. E. Han, A. Matos-Abiague, J. Shabani, and I. Žutić, Nat. Commun. **13**, 1738 (2022).
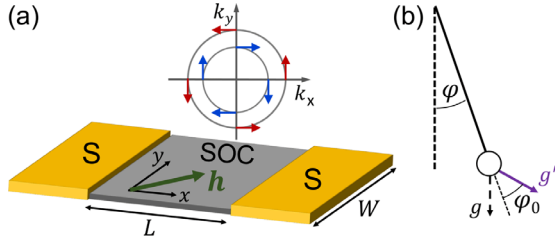
Fig.1: A schematic of the Josephson junction (JJ). Two s-wave superconductors (S) are separated by the middle region, which hosts the Rashba spin-orbit coupling (SOC), with the depicted **k**-space spin-orbit fields and an effective Zeeman field **h**. (b) A mechanical pendulum model of the JJ. The displacement angle φ is analogous to the superconducting phase difference and g is the gravitational acceleration for vanishing SOC and **h**. The pendulum is driven by changing the effective **g'**, an interplay between **h** and time-dependent SOC. This yields a tunable current-phase relation and an anomalous phase, φ_0, equivalent to the equilibrium of the displaced pendulum. Taken from Ref. [1].
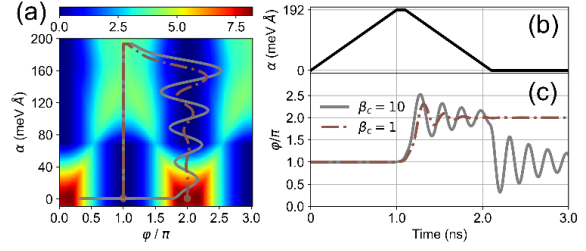
Fig.3: The JJ energy evolution with φ and the strengths of the Rashba SOC, α, at chemical potential $\mu = 10\Delta$, $h_x = (2/3)\Delta$, where Δ is the superconducting gap. The gray (brown) curve shows the energy variation for under (critical) damping starting at $\varphi = \pi$ and $\alpha = 0$ for changing α given in (d). (e) The corresponding time-dependent φ confirms the decay to different final phase states. Taken from Ref. [1].
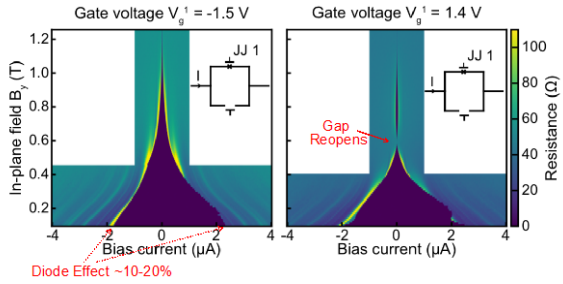
Fig. 2: A pair of individually-gated Al/InAs-based planar JJs (JJ1, JJ2) in SQUID geometry. Measurement of the differential resistance of JJ1 as function of an applied in in-plane field along the y axis at two different gate voltage: $V_g^1 = -1.5\,V$ (left) and $V_g^1 = 1.4\,V$ (right). In both cases, JJ2 is depleted ($V_g^2 = -7\,V$) and does not participate in the transport. At low-gate voltage (left) the asymmetry of the critical JJ1 current confirms the superconducting diode effect. At high gate voltage (right), a minimum of the critical current is observed around 600 mT for JJ1, consistent with the onset of topological superconductivity. Taken from Ref. [2].
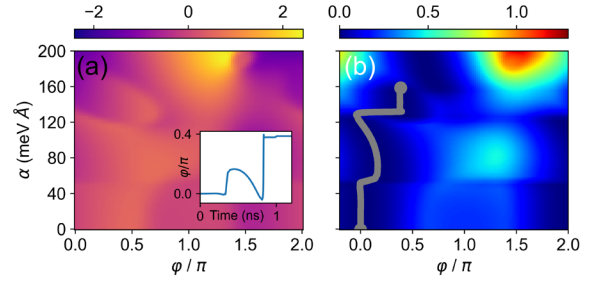
Fig. 4: The evolution of (a) JJ current-phase relation and (b) JJ energy with φ and α, for $\mu = \Delta$ and $h_y = (2/3)\Delta$, rotated by $\pi/2$ from the results in Fig. 3. An anharmonic current-phase relation breaks the $I(-\varphi) = -I(\varphi)$ symmetry in (a) and the corresponding anomalous phase, φ_0, increases with α in (b). Inset (a): $\varphi(t)$ for $\omega_p = 1000\,GHz$ and the damping parameter, $\beta_c = 1$ (consistent with the measurements from Ref. [2]) with a linearly increasing α from 0 to 160 meVÅ over 1ns, then held at maximum with its JJ energy path in (b). Taken from Ref. [1].

Chiral Spin Textures and Josephson Diodes

Stuart S.P. Parkin

Max Planck Institute of Microstructure Physics, Halle (Saale), Germany

stuart.parkin@mpi-halle.mpg.de

Chiral domain walls are just one member of an ever-expanding family of chiral spin textures that are of great interest from both a fundamental as well as a technological perspective [1]. Recently a zoology of complex spin textures stabilized by volume or interface Dzyaloshinskii-Moriya interactions have been discovered including, in our work, anti-skyrmions [2], elliptical Bloch skyrmions [3], two-dimensional Néel skyrmions [4] and fractional antiskyrmions [5]. Such nano-objects are potential candidates as magnetic storage bits on the racetrack [6]. Recently we have observed Néel skyrmions in two distinct but closely related 2D van der Waal's ferromagnetic compounds that should not allow for such structures. We show that the crystal structures are substantially modified by self-intercalation, lowering their symmetry and thereby allowing for chiral spin textures that require acentric structures [7, 8]. We also discuss the unusual properties of chiral Kagome antiferromagnets and how their magnetic structure can be manipulated by a previously unobserved seeded spin orbit torque mechanism [9]. Finally, we demonstrate the observation of long range triplet supercurrents in thin layers of a chiral antiferromagnet [10] and we discuss our recent finding of a nonreciprocal Josephson Diode Effect in 2D van der Waals layers [11] as well as in proximitized platinum [12].

[1] S.-H. Yang, R. Naaman, Y. Paltiel, and S. S. P. Parkin, "Chiral spintronics," *Nat. Rev. Phys.,* vol. 3, pp. 328–343 2021/04/08 2021, doi: 10.1038/s42254-021-00302-9.

[2] A. K. Nayak *et al.*, "Magnetic antiskyrmions above room temperature in tetragonal Heusler materials," *Nature,* Letter vol. 548, no. 7669, pp. 561-566, 08/31/print 2017, doi: 10.1038/nature23466.

[3] J. Jena *et al.*, "Elliptical Bloch skyrmion chiral twins in an antiskyrmion system," *Nat. Commun.,* vol. 11, p. 1115, 2020.

[4] A. K. Srivastava *et al.*, "Observation of Robust Néel Skyrmions in Metallic PtMnGa," *Adv. Mater.,* vol. 32, p. 1904327, 2020.

[5] J. Jena *et al.*, "Observation of fractional spin textures in a Heusler material," *Nat. Commun.,* vol. 13, p. 2348, 2022.

[6] S. S. P. Parkin and S.-H. Yang, "Memory on the Racetrack," *Nat. Nanotechnol.,* vol. 10, pp. 195-198, 2015.

[7] A. Chakraborty *et al.*, "Magnetic skyrmions in a thickness tunable 2D ferromagnet from a defect driven Dzyaloshinskii-Moriya interaction," *Adv. Mater.,* vol. 34, p. 2108637, 2022.

[8] R. Saha *et al.*, "Observation of Néel-type skyrmions in acentric self-intercalated $Cr_{1+\delta}Te_2$," *Nat. Commun.,* vol. 13, p. 3965, 2022.

[9] B. Pal *et al.*, "Setting of the magnetic structure of chiral kagome antiferromagnets by a seeded spin-orbit torque," *Sci. Adv.,* vol. 8, p. eabo5930, 2022.

[10] K.-R. Jeon *et al.*, "Long-range supercurrents through a chiral non-collinear antiferromagnet in lateral Josephson junctions," *Nat. Mater.,* vol. 20, pp. 1358-1363, 2021/08/05 2021, doi: 10.1038/s41563-021-01061-9.

[11] B. Pal *et al.*, "Josephson diode effect from Cooper pair momentum in a topological semimetal," *Nat. Phys.,* vol. online, 2022.

[12] K.-R. Jeon *et al.*, "Zero-field polarity-reversible Josephson supercurrent diodes enabled by a proximity-magnetized Pt barrier," *Nat. Mater.,* vol. online, 2022.

Supercurrent Non-reciprocity and Vortex Formation in Superconductor Heterostructures

Ananthesh Sundaresh, Jukka Ilmari Vayrynen, Yuli Lyanda-Geller, Leonid P. Rokhinson

Depertmernt of Physics and Astronomy, Purdue University, West Lafayette, Indiana, USA

leonid@purdue.edu

Recent excitement in observation of non-reciprocal supercurrent (NRS) is motivated by a suggestion that ``superconducting diode effect'' may be an intrinsic property of non-centrosymmetric superconductors with strong spin-orbit interactions. Theoretically it has been understood that linear-in-momentum energy terms, such as Rashba spin-orbit interaction or, more generally, any symmetry-allowed Lifshitz invariants, do not contribute to the supercurrent, yet the role of higher-order terms remains unclear. In this work we study non-reciprocity of critical current in nanowires fabricated from InAs/Al heterostructures. We show experimentally that the sign of NRS does not depend on the crystallographic axis, thus ruling out intrinsic NRS due to cubic-in-momentum terms. The overall shape of NRS and its multiple sign changes as a function of magnetic field are similar to NRS in superconducting loops, and point to the formation of circular currents. We present a model which shows that NRS is a generic property of two coupled dissimilar superconductors, and NRS sign change can be attributed to the formation of vortices. This extrinsic mechanism qualitatively explains ours and provides a compelling explanation to some previously published results.

[1] Ananthesh Sundaresh, Jukka Ilmari Vayrynen, Yuli Lyanda-Geller, Leonid P. Rokhinson, "Supercurrent non-reciprocity and vortex formation in superconductor heterostructures" arXiv:2207.03633
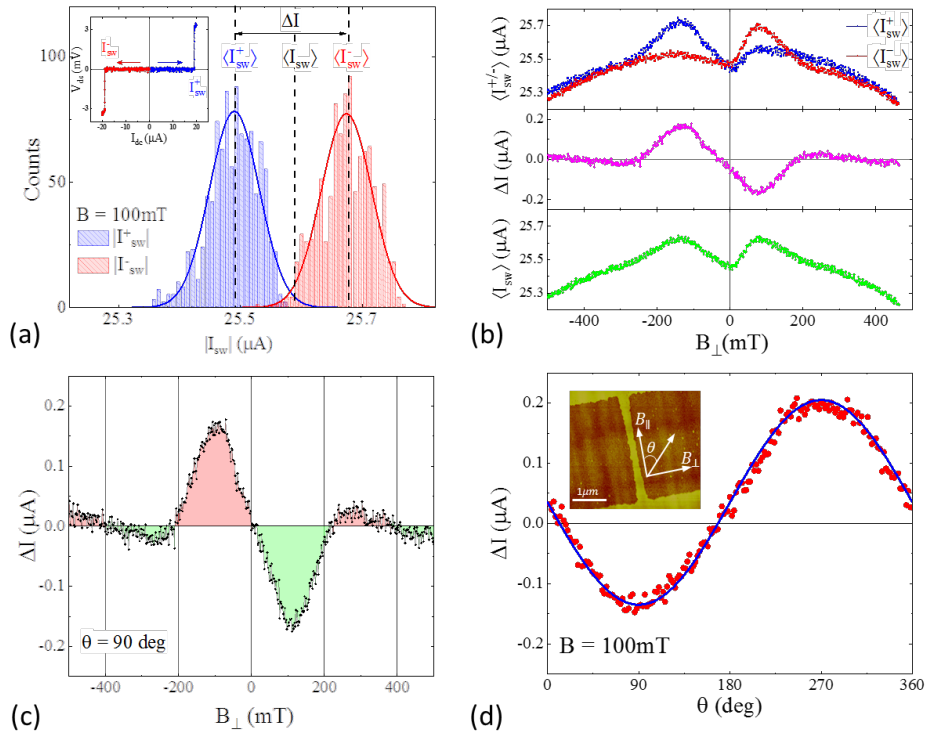
Fig. 1. **Non-reciprocal critical current in Al/InAs nanowires.** (a) Histograms of switching currents for 10,000 positive I_{sw}^+ and negative I_{sw}^- current sweeps performed at $T = 30$ mK and $B_\perp = 100$ mT. Inset shows a typical current-voltage characteristic. (b) Average switching current for positive $\langle I_{\{sw\}}^+ \rangle$ and negative $\langle I_{\{sw\}}^- \rangle$ sweeps, non-reciprocal difference $\Delta I = \langle I_{\{sw\}}^+ \rangle + \langle I_{\{sw\}}^- \rangle$ and an average of all sweeps $\langle I_{sw} \rangle$ is plotted as a function of in-plane magnetic field $B_\perp$. In (c) enlarged ΔI data is colored to signify non-monotonic field dependence and multiple sign changes. (d) Dependence of ΔI on in-plane field orientation is measured at a constant $B = 100$ mT. Blue line is a fit with a sine function. Insert shows an AFM image of a 3 μm-long wire connected to wide contacts, yellow areas are Al, in darker areas Al is removed and InAs is exposed.
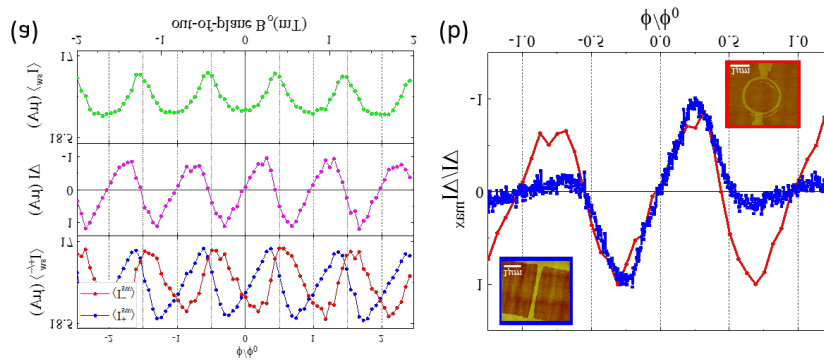
Fig. 2 **NRS in an asymmetric superconducting loop**. (a) An average switching current for positive and negative sweeps $\langle I_{\{sw\}}^{+/-} \rangle$, non-reciprocal difference ΔI and an average of all sweeps $\langle I_{sw} \rangle$ is plotted as a function of out-of-plane magnetic field B_o for a loop shown in the insert in (b). Note that \isw\ is maximum while $\Delta I = 0$ when the flux $\phi = n\phi_0$. In (b) ΔI for the nanowire and the loop are plotted together as a function of a reduced flux ϕ/ϕ_0.

Graphene-based Josephson Triode

John Chiles[1], Ethan Arnault[1], Chun-Chia Chen[1], Lingfei Zhao[1], Trevyn Larson[1],
Takashi Taniguchi[2], Kenji Watanabe[2], François Amet[3], & <u>Gleb Finkelstein</u>[1]
[1]Department of Physics, Duke University, Durham, NC 27708, U.S.A.
[2]Advanced Materials Laboratory, NIMS, Tsukuba 305-0044, Japan
[3]Department of Physics, Appalachian State University, Boone, NC 28607, U.S.A.
e-mail:gleb@duke.edu

There has been a growing interest to the materials with broken time-reversal and inversion symmetry, which can support non-reciprocal superconducting currents [1]. This search for an intrinsic superconducting diode has so far resulted in devices that typically show a few percent difference between the magnitudes of the supercurrent flowing in the positive and negative directions. We show that required time-reversal symmetry breaking can be achieved in multiterminal Josephson junctions [2], resulting in supercurrent rectification approaching 100%.

In our samples, several superconducting leads (left, right, and bottom: L, R, and B) are coupled via gate-tunable graphene Josephson junctions. The state of one of the junctions, e.g. between the left and bottom contacts (LB) can be controlled by the non-dissipative current flowing in the right contact, I_R. The phase difference induced by the control current creates the required time-reversal symmetry breaking. At zero control current, the controlled junction demonstrates a symmetric I-V curve, which becomes progressively asymmetric as the control current is tuned (Figure 1). At $I_R = -100$ nA, the supercurrent exists for the positive direction of I_L and is equal to zero for the negative direction; the rectification is complete.

The observed asymmetry of the supercurrent can be used to rectify a square wave applied to the junction, in a way a conventional diode rectifies AC current. Figure 2 demonstrates the voltage across the LB junction, upon application of a square wave current I_L. Setting the control current $I_R = \pm 50$ nA, either the positive or the negative part of the waveform yields zero V_{LB}, while the part of the waveform with the opposite I_L results in finite voltage. For comparison, at zero control current, the LB junction remains superconducting throughout the same range of I_L.

We speculate that the three-terminal junctions considered here, to which we refer as "Josephson triodes", may potentially find application in cryogenic microwave engineering, such as superconducting quantum information processing.

[1] F. Ando *et al.*, Nature **584,** 373 (2020). https://doi.org/10.1038/s41586-020-2590-4.
[2] A.W. Draelos *et al.*, Nano Lett. **19,** 1039 (2019). https://doi.org/10.1021/acs.nanolett.8b04330.
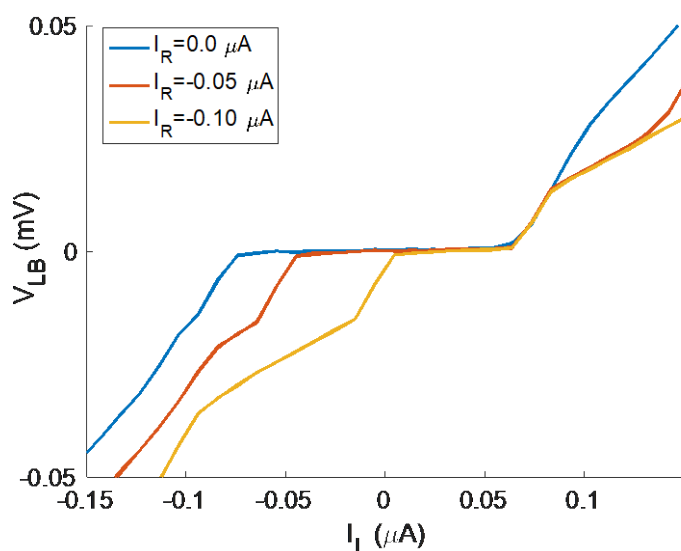
Fig.1: I-V curves of the left-bottom junction as a function of the control supercurrent flowing in the right contact. .
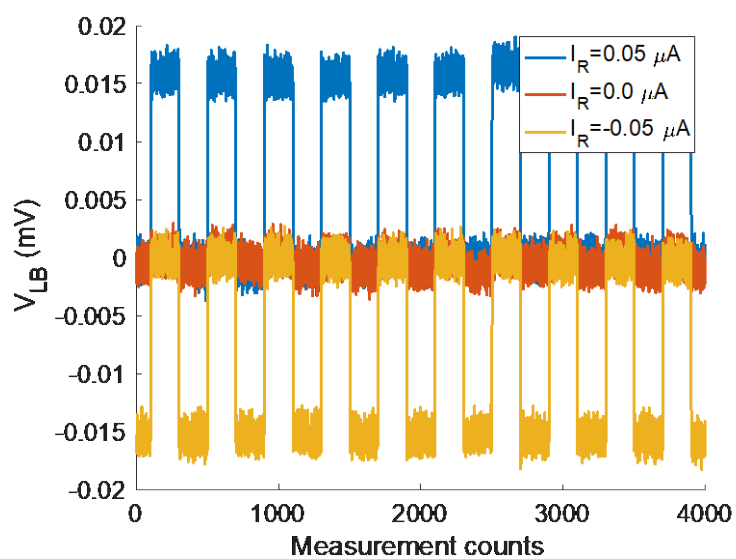
Fig.2: Voltage in the left-bottom junction as a function of time, while a square wave current is applied to the same junction. Depending on the current in the right (control) junction, the voltage across the controlled junction is zero (corresponding to the supercurrent) either for the positive (yellow), or negative (blue), or both directions (red) of the square wave. .

Anisotropic Vortex Squeezing and Supercurrent Diode Effect in Non-Centrosymmetric Rashba Superconductors

D. Kochan[1,2]

[1] *Institute for Theoretical Physics, University of Regensburg, 93040 Regensburg, Germany*
[2] *Institute of Physics, Slovak Academy of Sciences, 84511 Bratislava, Slovakia*
denis.kochan@ur.de

Most of 2D superconductors are of type II, i.e., they are penetrated by quantized vortices when exposed to out-of-plane magnetic fields. In a presence of a supercurrent, a Lorentz-like force acts on the vortices, leading to drift and dissipation. The current-induced vortex motion is impeded by pinning at defects. Usually, the pinning strength decreases upon any type of pair-breaking interaction perturbs a system.

In the talk I will discuss surprising experimental evidences showing an unexpected enhancement of pinning in synthetic Rashba 2D superconductors when applying an in-plane magnetic field. When rotating the in-plane component of the field with respect to the driving current, the vortex inductance turns out to be highly anisotropic. We explain this phenomenon as a direct manifestation of Lifshitz invariant that is allowed in the Ginzburg-Landau free energy when space-inversion and time-reversal symmetries are broken. As demonstrated in our experiment [1], elliptic squeezing of vortices---an inherent property of the non-centrosymmetric superconducting condensate---provides an access to fundamentally new property of Rashba superconductors, and offers an entirely novel approach to vortex manipulation.

Another interesting feature of the non-centrosymmetric superconductors in the applied magnetic field is the supercurrent diode effect---the critical current in one direction exceeds its counterpart in the opposite one---what stems from the Cooper pairs with finite centre of mass momentum. In the pioneering experiment [2] we demonstrated the emergence of the supercurrent diode effect in the Josephson junctions based on synthetic Rashba superconductors made of Al-InAs quantum wells. In the talk, I will discuss novel experimental method--- measurements of the Josephson inductance---and the semiquantitative microscopic model capturing all the essential features as observed in experiment.

[1] L. Fuchs, D. Kochan, C. Baumgartner, S. Reinhardt, S. Gronin, G. Gardner, T. Lindemann,
M. Manfra, C. Strunk, N. Paradiso, Phys. Rev. X 12, 041020 (2022).
[2] C. Baumgartner, L. Fuchs, A. Costa, S. Reinhardt, S. Gronin, G. Gardner, T. Lindemann,
M. Manfra, P. Faria Junior, D. Kochan, J. Fabian, N. Paradiso, C. Strunk,
Nature Nanotechnology 17 (1), 39 (2022).
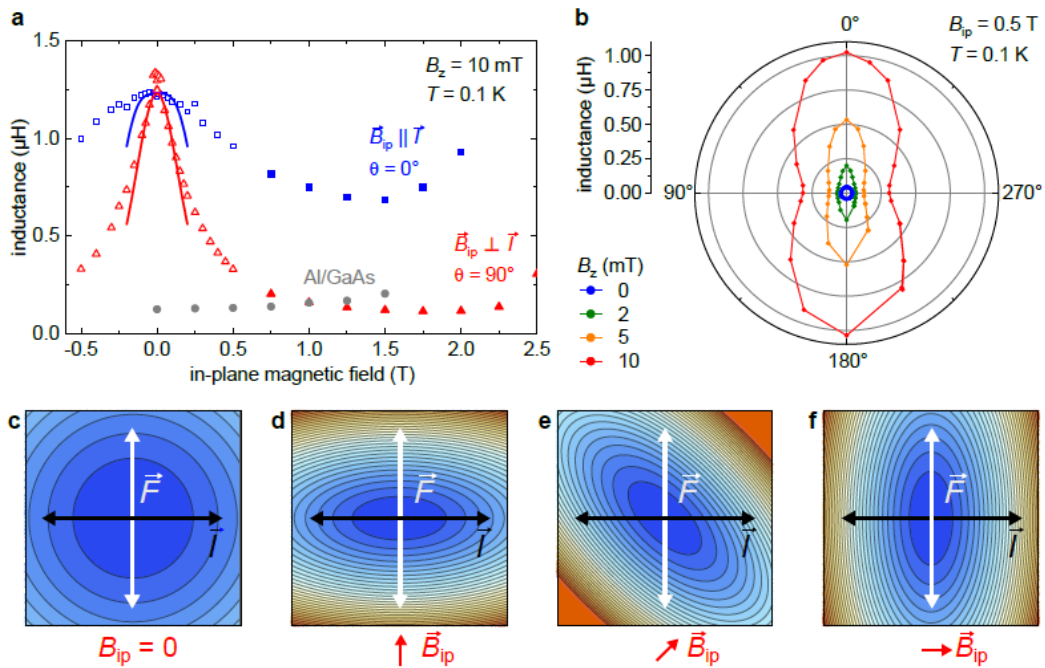
Fig.1: a, Sample inductance of Rashba superconductor as a function of in-plane magnetic field for different orientations of the driving current (red and blue symbols). The controlled measurement (grey symbols) corresponds to a centrosymmetric (i.e. non-Rashba) superconductor. b, Polar plot showing the angle dependence of the vortex inductance for selected values of out-of-plane magnetic field. c, The color plot schematically represents the modulus of the order parameter, $|\psi (x,y)|^2$, near the core of a pinned vortex, in the absence of in-plane field. The horizontal black arrow represents the direction of a current bias, while the white arrow indicates the direction at which a Lorentz force acts on a pinned vortex. The measured vortex inductance is rotation symmetric and inversely proportional to the curvature of $|\psi (x,y)|^2$ along the force direction. d-f, When a finite in-plane field is applied the vortex core is squeezed as a consequence of the Rashba spin-orbit interaction, reflecting the measured change in vortex inductance. The curvature is always probed along the white axis, rotating the in-plane magnetic field the vortex rotates keeping its small elliptic axis parallel with the direction of in-plane field. This allows one to extract from the vortex inductance the spatial profile –order parameter tomography--of $|\psi (x,y)|^2$.

RF Mediated Vortex Glass to Vortex Liquid Transition in Metallic Josephson Junctions

E. Arnault[1], J. Chiles[2], F. Amet[3], G. Finkelstein[2], and I. V. Borzenets[4,5]

[1]The Research Laboratory of Electronics, MIT, Cambridge, MA, USA
[2]Department of Physics, Duke University, NC, USA
[3]Department of Physics and Astronomy, Appalachian State University, NC, USA
[4]Department of Physics and Astronomy, Texas A&M University, TX, USA
[5]Department of Physics, City University of Hong Kong, Hong Kong
borzenets@tamu.edu

We study the transport properties of Molybdenum-Rhenium alloy superconducting constrictions at high magnetic fields: H>8T. The I-V curves exhibit a trend consistent with the flux-creep model (vortex glass). That is, voltage increases exponentially with bias current, and the curves always have a positive curvature. However, when an RF signal (300 MHz) is applied to the junction in addition to bias current, above a threshold RF power, a "kink" appears in the I-V curve. This "kinked" region has a negative curvature, and fits well to the predicted trend for a vortex liquid transport model. That is, under sufficient RF power, and above a threshold bias current we are able to dislodge (or essentially) melt the flux vortexes in the system and force a glass to liquid transition. This glass to vortex liquid transition has been previously observed in high Tc superconductors[1]. However, in conventional lower Tc superconductors, the boundaries of the vortex liquid phase lies close to the normal transition. Our scheme of applying an RF field allows for the vortices to 'feel' an elevated effective temperature, without reducing the superconducting gap, allowing access to the liquid phase in a controllable and tunable method.

[1] R. H. Koch *et al.* Phys. Rev. Lett. **63**, 1511 (1989).
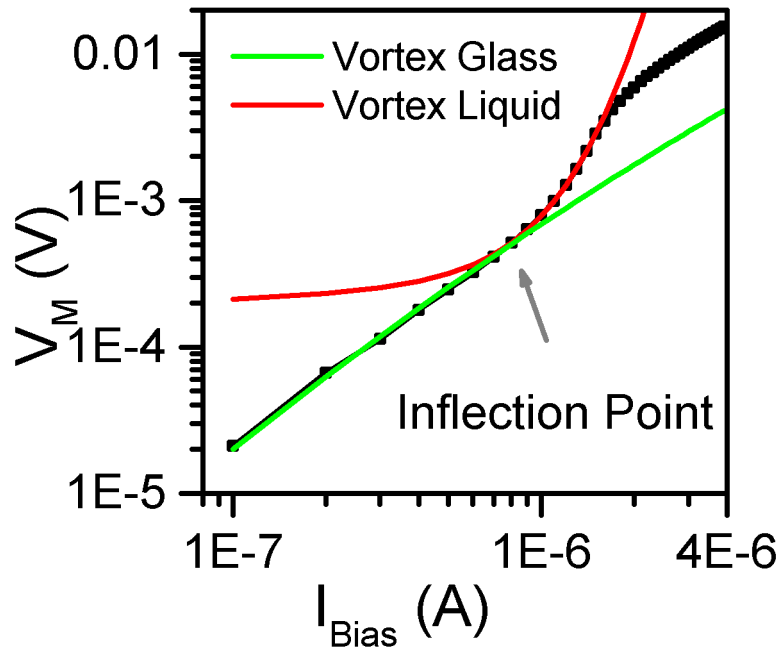
Fig.1: Voltage versus bias current characteristic of the MoRe Josephson junction at an applied magnetic field of 9.5 Tesla. Shown is the region of the bias current around the superconductor to normal metal transition. A 19dbm RF signal (300MHz) is applied to the junction together with the DC bias current. For currents below the inflection point, the I-V curve fits well to the vortex glass model. However, above the inflection point, (but below the transition to the normal metal state), the curvature changes, and follows the trend predicted by the vortex liquid model.
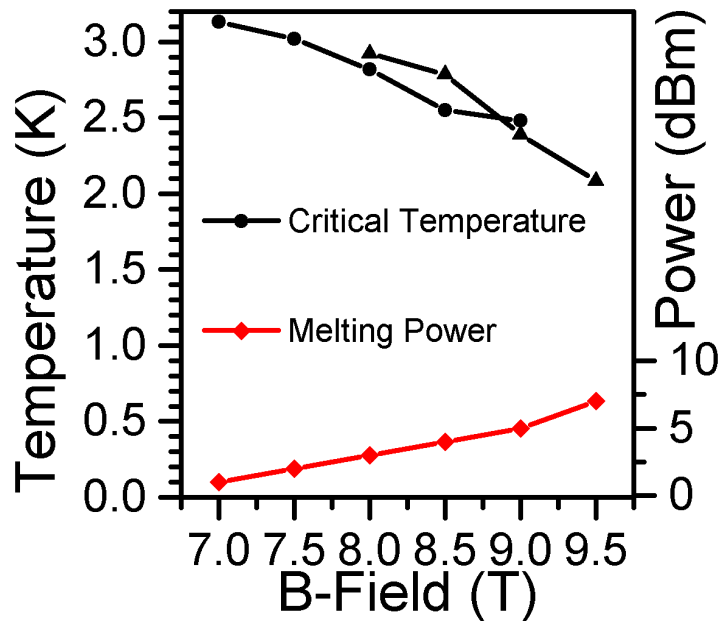
Fig.2: Critical Temperature, and threshold power versus applied magnetic field. The critical temperature is measured when no RF is applied to the junction, and scales predictably with applied field. The threshold power, is the minimum applied RF power required in order to observe vortex glass to liquid transition. The required applied power increases with magnetic field, as the vortices are expected to be pinned more strongly at higher fields.

Switching Based on a One-Dimensional Electron Gas in A Y-Shaped Device

<u>V. Mitin</u>[1], T. McDonough[1], M. Yakimov[2], V. Tokranov[2], and S. Oktyabrsky[2]

[1]EE Department, University at Buffalo, SUNY, Buffalo, NY, USA
[2]Faculty SUNY Polytechnic Institute, Albany, NY, USA
vmitin@buffalo.edu

With the goal to develop and evaluate quantum switching in Y-shaped 1D ballistic waveguides, we simulated and fabricated InGaAs/InGaAs/InP quantum well structures with e-beam lithography-patterned electron waveguides (Fig.1). Such a device concept - Y-branch switch (YBS) based on electron propagation in ballistic semiconductor heterostructures was first proposed back in 1992 [1,2]. The 1D ballistic YBS allows reducing operation current, as well as the switching energy and voltage compared to FET type of devices that are predominantly used nowadays. The simulation utilized Silvaco codes with a 3D Schrodinger-Poisson electrostatic solver and a non-equilibrium Green's function (NEGF) mode space approach for the calculation of quantum transport. A typical structure is shown in Fig. 2 with a calculated electron concentration map. To test if Silvaco was properly simulating quantum conductance, the split-waveguide structure of Fig.2 was simulated at a temperature of 10 K for different doping concentrations (Fig. 3) and revealed the characteristic quantum conductance steps. The calculation was done for low and high concentrations when single and multiple subbands are filled. An example of switching at 77 K is shown in Fig. 4. It should be noted that the switching efficiency is approximately inversely proportional to the gate length of the structure [1]. It was found, that if just the first subband is filled in the stem, electrons may directly transition to the second subband in the branches thus reducing quantum reflection [3]. The YBS structures with widths ranging from 40 to 200 nm were fabricated (Fig. 5a). A nonlinear induced stem voltage showed that these devices operated ballistically (Fig. 5b,c) at 77K [4] but showed scattering at room temperature. We have also observed the theoretically predicted change of ballistic characteristics with Fermi energy, which was controlled in this case by gate bias. The switching characteristics of a 50nm wide YBS device with ridge gates in a ballistic regime are shown in Fig. 6, where quite a low steering gate efficiency η_G =0.6 V^{-1} is likely due to the wide WG-to-gate separation. We developed sidewall MOS gates fabrication using an angled gate metal deposition from one side, a separation dielectric from the top down, and another angled gate metal deposition from the other side (Fig. 7). This design is expected to improve the gating efficiency to demonstrate quantum steering. [1] T. Palm and L. Thylén, Appl. Phys. Lett., 60, 237 (1992). [2] T. Palm, L. Thylén, O. Nilsson, and C. Svensson, J. Appl. Phys., 74, 687-694 (1993). [3] T. McDonough, V. Mitin, V. Tokranov, M. Yakimov, S. Oktyabrsky, NanoWorld J., 7. 40-45 (2021). [4] H. Q. Xu, *Appl. Phys. Lett.*,78,2064–66 (2001).
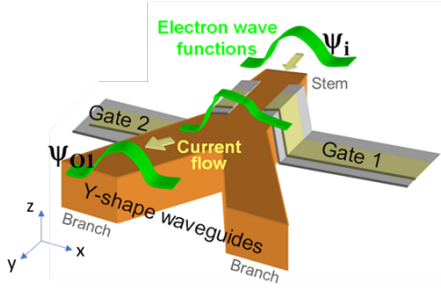
Fig. 1. A general concept of a quantum Y-branch electron wave structure (YBS). Symmetrical gates control the electron wave function in the branching region steering the current into one of the branches. Modulation of the wave function results in preferable propagation of the incoming wave into one of the two branches proportional to the matrix element of incoming and outgoing waves with applied potential.
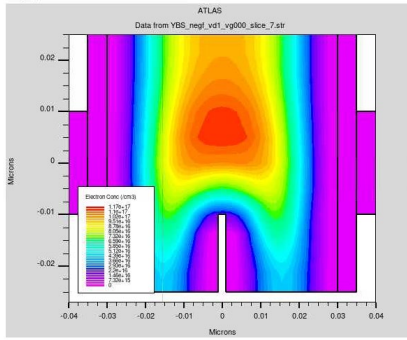

Fig. 2. Color map of electron concentration in a 60 nm wide and 10 nm thick InGaAs waveguide with split region and side 20 nm long sidewall gates.
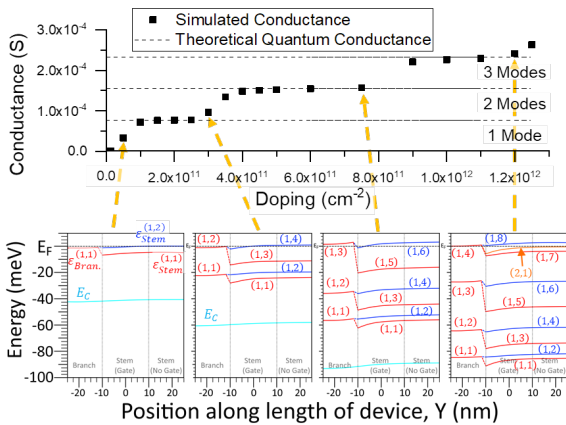
Fig. 3. Quantum transport simulation in Silvaco Atlas using the NEGF solver. The conductance equals the number of energy subbands populated in the branches times the unit of quantum conductance. Quantum bound states (bottoms of the 1D subbands) are presented along the waveguides showing occupation of bands. Fermi level position is set to zero energy in the graphs.
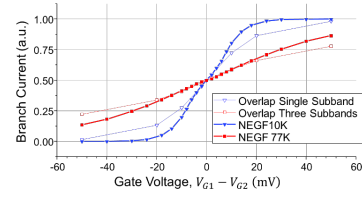
Fig.4. Comparison of switching predicted by calculating overlap integrals of the wave functions under bias compared (as in Fig. 4 below) and calculated by Silvaco Atlas NEGF simulations in a structure modulation doped to 10^{17} cm^{-3} into 5 nm thick layers.
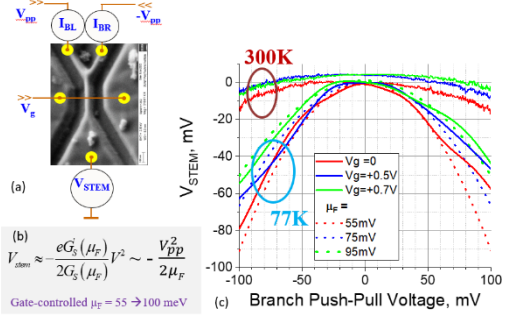
Fig.5 Ballistic junction performance of the YBS defined by electron beam lithography and dry etch with 50 nm wide waveguide and 150 nm branching region. (a) SEM top view of YBS with measurement schematics; (b) The predicted dependence of the stem potential for reflection of ballistic electrons as a function of Fermi energy in the stem [4]. (c) Nonlinearity of the induced stem potential due to ballistic injection at 77K.
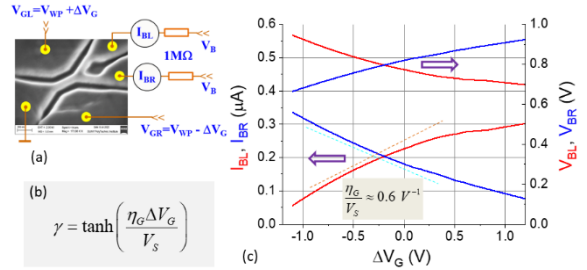
Fig.6. Ridge gate YBS characteristics at 77K: (a) SEM view of a 50 nm wide WG structure with measurement schematics; (b) Transmission amplitude control by the gate potential with gate efficiency γ; (c) Example of switching characteristics in the push-pull regime.
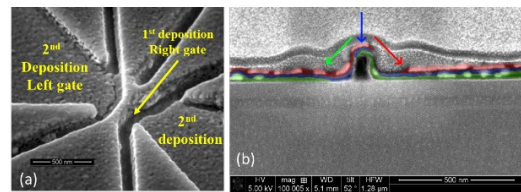
Fig.7. (a) SEM view and (b) Cross section of dielectric-separated glancing angle deposited gate metals. Though the III-V etch was insufficiently deep, the Si_3N_4 hard mask mimics the WG. The metal layers were successfully isolated from each other. The first angled metal is highlighted in green, the separation dielectric in blue, and the second angled metal deposition in red.

EMC *and* NEGF

David K. Ferry

School of Electrical, Computer, and Energy Engineering, Arizona State University, Tempe, AZ 85287 USA

Over the past several decades, the use of ensemble Monte Carlo (EMC) methods for the simulation of transport in semiconductor devices has become quite important. This method allows for the simulation utilizing particles and addressing the full physics within the device, leaving the computational difficulties to the computer. In the past decade or so, interest has shifted to the study of quantum mechanical effects within the devices, effects which also strongly affect the carrier transport itself. While particles have continued to be useful in quantum simulations using Wigner functions, interest in analytical solutions based upon the non-equilibrium Green's functions (NEGF) have become of greater interest in device simulation, despite intrinsic problems with NEGF [1], not the least being computational difficulties. Nevertheless, NEGF have been adopted by many commercial semiconductor simulation organizations. Yet, the use of particles in simulation provides a much better method of addressing the details of the physics within the device, and remains a much preferred approach to numerical simulations. Here, a particle approach to NEGF is discussed, and preliminary results presented illustrating the computational efficiency that remains with the use of particles. This approach adopts the natural basis functions for use in a high electric field and the preliminary results are obtained for quantum transport in Si at 300 K. The velocity-field characteristics are presented in Figure 1. Each data point requires less than 2 s for 10^5 particles. This approach appears to offer significant advantages for the use of NEGF.

[1] D. K. Ferry, J. Weinbub, M. Nedjalkov, and S. Selberherr, Semicond. Sci. Technol. 37, 043001 (2022).
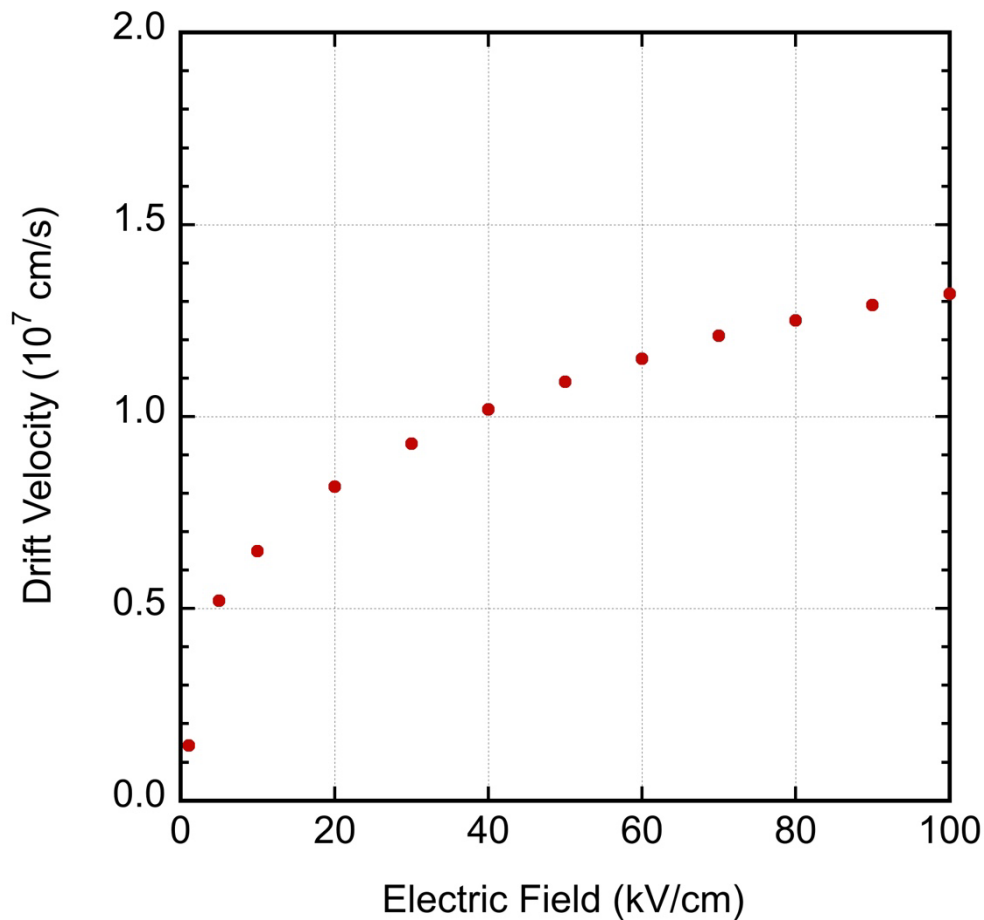
Fig. 1. The velocity-field curve for Si electrons at 300 K. The simulation was obtained for quantum transport using NEGF with 10^5 particles in a particle-based approach.

Modeling of Band-to-band Tunneling in Ultra-thin GaSb and InAs Gate-all-around Nanowire Tunnel FETs

J. Okada[1], J. Hattori[2], K. Fukuda[2], T. Ikegami[2], and N. Mori[1]

[1]Graduate School of Engineering, Osaka University, Suita, Osaka 565-0871, Japan

[2]National Institute of Advanced Industrial Science and Technology (AIST),

Tsukuba, Ibaraki 305-8568, Japan

okada@si.eei.eng.osaka-u.ac.jp

Since Kane proposed his band-to-band tunneling (BTBT) theory in his seminal paper in 1959 [1], several BTBT models for device simulations have been developed and applied to a variety of device structures including the tunnel FETs (TFETs) [2, 3]. For such models, the bulk semiconductor is assumed and a BTBT generation rate is evaluated by integrating over the transverse modes. However, only a single transverse mode contributes to the current for ultra-thin nanowires (NWs) because the transverse mode is quantized into a subband. In the present study, we have derived a formula of the BTBT generation rate for such ultra-thin NWs and performed drift-diffusion (DD) device simulation using Impulse TCAD [4] with the derived formula. We then compared the DD results with the results calculated by the non-equilibrium Green function (NEGF) method combined with the tight-binding approximation (TBA).

We have derived a formula for the BTBT generation rate in ultra-thin NWs, G_{1D}, by the WKB method. The derived G_{1D} is a physical quantity with dimensions per unit time and unit length, which must be divided by an appropriate area and converted to a physical quantity per unit time and unit volume in order to be introduced into the device simulation.

We consider GaSb and InAs p-i-n gate-all-around TFETs whose cross section is $\ell \times \ell$ square and oxide thickness is 1 nm (see Fig. 1). The tunnel mass is extracted from the TBA band structure (see Fig. 2) to be consistent with the Kane's two-band model [1]. The generation rate as a function of the uniform electric field is plotted in Figs. 3 and 4, in which G_{1D} is simply divided by the geometrical area (ℓ^2), as compared with the formula for the tunnel rate in three dimensions, $G_{3D} = \left(e^2 F^2 \sqrt{m_r} / 2\pi^3 \hbar^2 \sqrt{E_G} \right) \exp\left(-\pi \sqrt{m_r} E_G^{3/2} / 2\hbar eF \right)$ [1, 2]. Figures 5 and 6 show the *IV* characteristics; the red and blue lines represent the DD results with G_{1D}/ℓ^2 and G_{3D}, respectively. The *IV* characteristics calculated with the NEGF method using the electrostatic potential determined by Impulse TCAD are plotted as black solid line. We see that the results with G_{1D} are closer to the NEGF results. The cross-sectional area over which the tunnel current flows is considered to be smaller than the geometric area (ℓ^2), so incorporating that effect may narrow the gap between G_{1D} and NEGF results.

[1] E.O. Kane, J. Phys. Chem. Solids **12**, 181 (1959). [2] D. Esseni *et al*, Semicond. Sci. Technol. **32**, 83005 (2017).

[3] K. Fukuda *et al*, J. Appl. Phys., **114**, 144512 (2013). [4] T. Ikegami *et al*, J. Compt. Electron. **18**, 534 (2019).
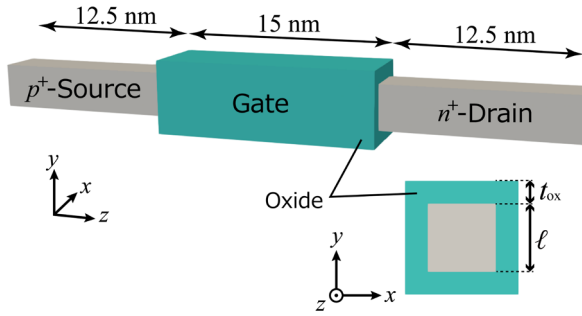
Fig.1: A shematic diagram of p-i-n gate-all-around nanowire TFET. The acceptor and donor concentration in the source and drain region are 2×10^{20} cm^{-3} and 1×10^{20} cm^{-3}, respectively.
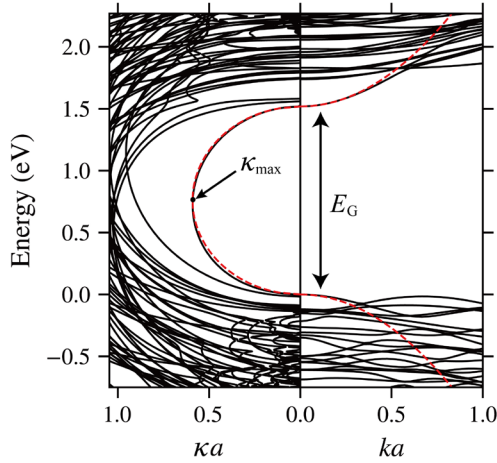
Fig.2: The band structure of GaSb nanowire ($\ell = 3$ nm) calculated with TBM (black solid line). Red dashed line shows the Kane's two band dispersion for $m_r = \hbar^2 \kappa_{max}^2 / E_G$.
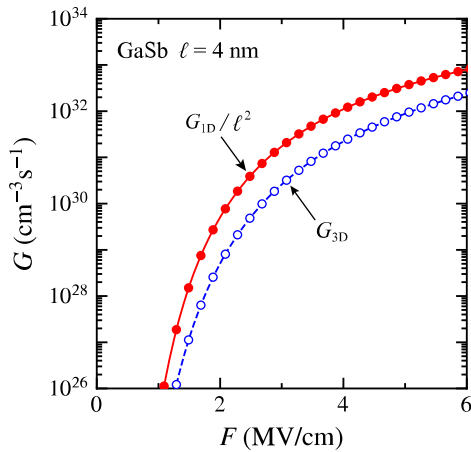
Fig.3: Generation rates of GaSb nanowires as a function of the uniform electric field F.
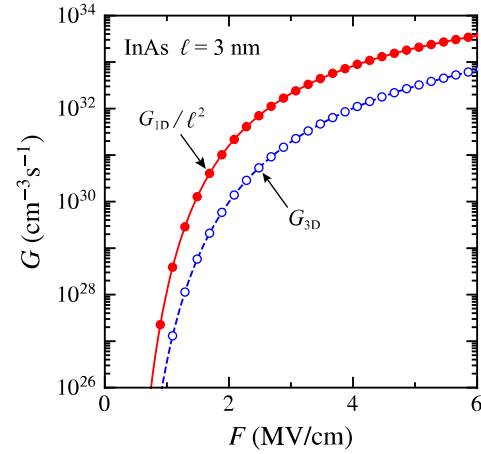
Fig.4: The same as Fig. 3 but for InAs nanowires.
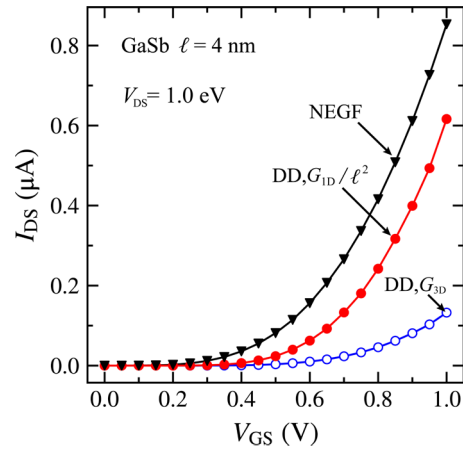
Fig.5: IV characteristics of GaSb TFET simulated with Impulse TCAD; red and blue lines represent the results of G_{1D}/ℓ^2 and G_{3D}, respectively. The black line represents the NEGF results.
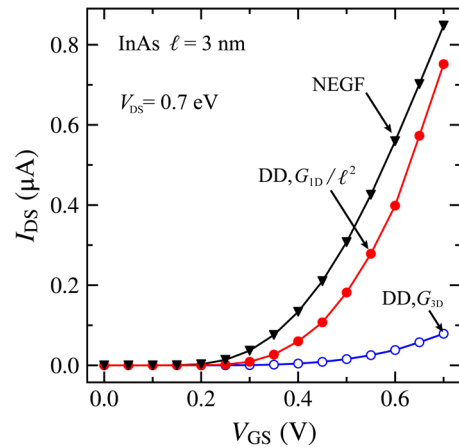
Fig.6 The same as Fig. 5 but for InAs TFET.

28

Revealing the Quantum Effects of Imperfections on the Tunneling Rate in Δ-Layer Junctions

J.P. Mendez[1], and D. Mamaluy[1]

[1]*Cognitive & Emerging Computing, Sandia National Laboratories, Albuquerque, USA*

jpmende@sandia.gov

Atomic precision advanced manufacturing (APAM) has been used to fabricate defect-based qubits for quantum computing [1], as well as to explore the next-generation of advanced nanoelectronics [2]. A recurring elementary structure common to many of these devices is δ-layer tunnel junctions (TJ), which consist of two highly-conductive δ-layers and an intrinsic gap (see Fig.1 a). For instance, H.G. House *et al.* used a δ-layer TJ for detecting electrons in quantum dots; Donnelly *et al.* presented the first δ-layer TFET reported to date. In general, these devices require a precise control on the tunneling rates in their operation.

Despite the geometry precision provided by APAM, which promises an exquisite control on the tunneling rate, APAM also involves tradeoffs between a numbers of defect mechanisms, which could affect the tunneling rate. For instance, there is an intrinsic stochasticity from the underlying chemistry resulting in a dopant placement uncertainty of around 0.3nm. After dopant incorporation, δ-layers must be capped at moderate temperature with Si to protect them, but adatom-mediated diffusion can lead to a loss of out-of-plane sharpness (of the order of 1 nm). In contrast, the low-temperature capping growth also leads to charged defects (around 1 defect per $10 \times 10 \times 10$ nm^3). A processing tradeoff would exist, where defect density can be reduced by increasing various processing temperatures, at the expense of a worse dopant placement uncertainty from activating dopant diffusion. Determining which of these disorder mechanisms is most likely to create large variations in tunneling rates will help us to inform how to navigate these tradeoffs.

In this work we will employ an efficient, charge self-consistent [3], quantum transport implementation of the NEGF formalism [4], to assess the effect of diverse imperfections on the tunneling rate in Si: P δ-layer TJ (see Fig. 1 b and c). We have revealed that while most of the imperfections moderately affect the tunneling rate, a single charged impurity in the tunnel gap can alter the tunneling rate by more than an order of magnitude due to the strong quantized conduction band of the δ-layers (see Figs. 2, 3 and 5). Moreover, we have also revealed that the tunneling rate strongly depends on the electrical charge sign of the impurity (see Fig. 6).

[1] H. G. House *et al.*, Appl. Phys. Lett. **104**, 113111 (2014).

[2] M. B. Donnelly *et al.*, Nano. Lett. **21**, 10092 (2021).

[3] D. Mamaluy *et al.*, Phys. Rev. B **71**, 245321 (2005).

[4] D. Mamaluy *et al.*, Commun. Phys. **4**, 1 (2021).
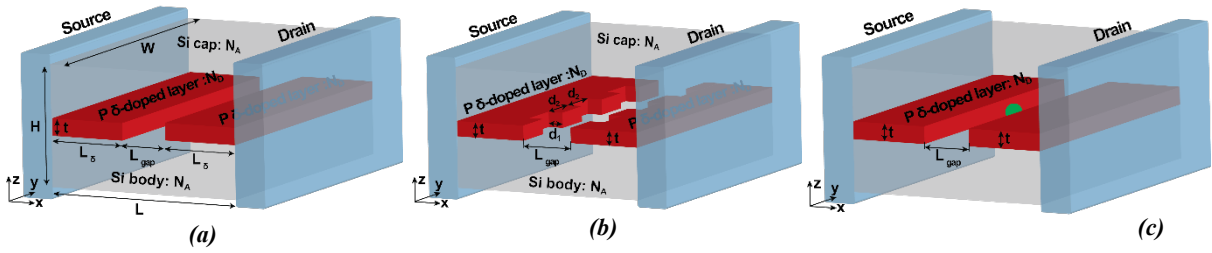
Fig.1: *Si:P δ-layer tunnel junction (TJ) devices. (a) Ideal device, which consists of a semi-infinite source and drain, in contact with the channel. The channel is composed of a lightly doped Si body and Si cap and a very thin, highly P doped-layer with an intrinsic gap of length L_{gap}. (b) Device with roughness in δ-layer edges; The edge roughness is modeled as periodic protrusions of size $d_1 \times d_2 \times t$ with a periodicity of $2 \times d_2$. (c) Device with presence of a charged impurity, either p-type or n-type, in the center of the intrinsic tunnel gap; The charged impurity is represented as a green sphere in the figure.*
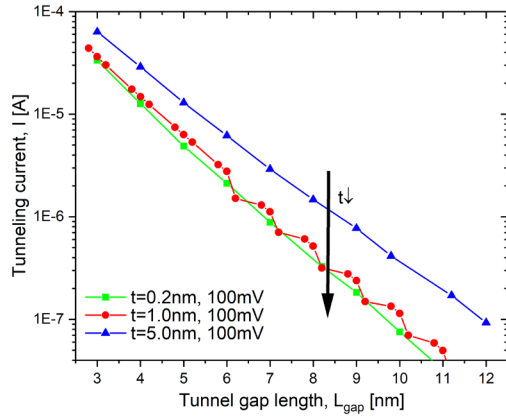
Fig.2: Characteristic tunneling current curves. Total tunneling current I vs. tunnel gap length L_{gap} for different values of δ-layer thickness t and applied voltages of 100mV. $N_D=1.0\times10^{14}cm^{-2}$ and $N_A=5.0\times10^{17}cm^{-3}$.
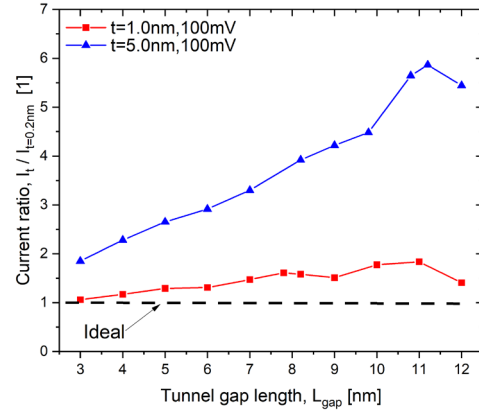
Fig.3 Effect of δ-layer thickness variation. Current ratio, $I_t/I_{t=0.2}nm$, vs. tunnel gap length for different deviations of the δ-layer thickness from the "ideal" mono-atomic layer (0.2nm).
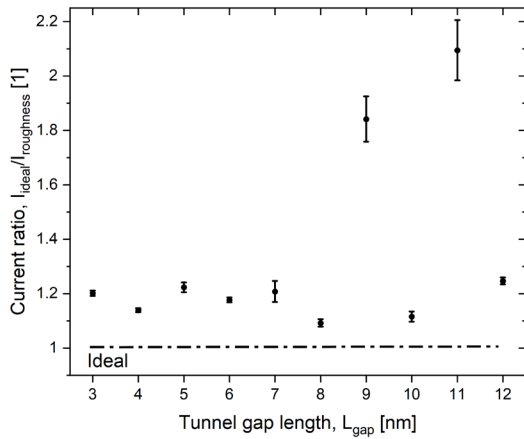
Fig.4: Effect of interface roughness. Current ratio, $I_{ideal}/I_{roughness}$, vs. tunnel gap length, L_{gap}, for an applied bias of 1.0 mV. For each tunnel gap length, different roughness sizes have been considered, ranging d_1=0.8-2.0nm and d_2=0.6-3.4nm (see Fig.1b). The dots represent the average and the bars represent the dispersion of the values. t=1.0nm, $N_D=1.0\times10^{14}cm^{-2}$ and $N_A=5.0\times10^{17}cm^{-3}$.
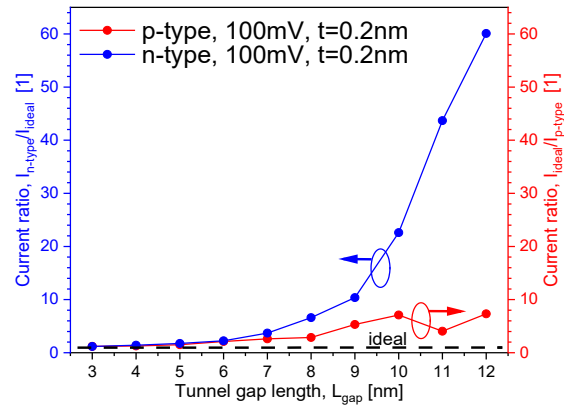
Fig.5: Effect of charged impurities. Current ratio, $I_{non-ideal}/I_{ideal}$, vs. tunnel gap length, L_{gap}, for tunnel junctions with a single n-type and p-type impurities in the intrinsic gap. $N_D=1.0\times10^{14}cm^{-2}$ and $N_A=5.0\times10^{17}cm^{-3}$.

NEMO5, a Multiscale, Multiphysics Nanoelectronics Modeling Tool used for Ultra-Scaled CMOS, 2D Transistor, Topological Materials, and Quantum Computing Devices

<u>Gerhard Klimeck</u>, Tillmann Kubis, Michael Povolotskyi, James E. Fonseca, Bozidar Novakovic, Rajib Rahman, Tarek Ameen, James Charles, Junzhe Geng, Kaspar Haume, Yu He, Ganesh Hegde, Yuling Hsueh, Hesam Ilatikhameneh, Zhengping Jiang, SungGeun Kim, Daniel Lemus, Daniel Mejia, Kai Miao, Samik Mukherjee, Seung Hyun Park, Ahmed Reza, Mehdi Salmani, Parijat Sengupta, Saima Sharmin, Yaohua Tan, Archana Tankasala, Daniel Valencia, Evan Wilson

Network for Computational Nanotechnology, Purdue University, USA

gekco0@gmail.com

The downscaling of electronic devices has reached the range where the number of atoms in critical dimensions is countable, geometries are formed in three dimensions and new materials are being introduced. Under these conditions one can argue that the overall geometry constitutes a new material that cannot be found as such in nature. The interactions of electronic, photons, and lattice vibrations are now governed by these new material properties and longer-range interaction mechanisms such as strain and gate fields. The Nanoelectronic Modeling tool suite NEMO5 is aimed to comprehend the critical multi-scale, multi-physics phenomena and deliver results to engineers, scientists, and students through efficient computational approaches. NEMO5's general software framework easily includes any kind of atomistic model and is, insofar, able to compute atomistic strain, electronics band structures, charge density, current and potential, Schrödinger eigenvalues and wave-functions, phonon spectra, and non-equilibrium Green functions (NEGF) transport for a large variety of semiconductor materials and the software is entirely parallelized. We believe that such modeling capability is not available in any other modeling tool at this time.

The NEMO modeling framework has been used to understand a variety of different device and materials concepts that will be critically important in the sub 10nm device regime. Some examples are bandstructure in Si nanowires as a function of crystal direction and strain. Interface roughness and alloy disorder scattering are modeled in the framework through an explicit atomistic representation. Gate tunneling can be modeled explicitly through quantum mechanical transport and designs can be obtained in which a good Si-based transistor is possible at 5nm gate lengths. Current developments include the explicit modeling of the metal-semiconductor interfaces, the series resistance loss and the thermal transport in nano-scale devices. Some recent examples are explorations for band-to-band tunneling transistors (BTBT) in realistic geometries in III-V, in III-N, and new 2D materials.
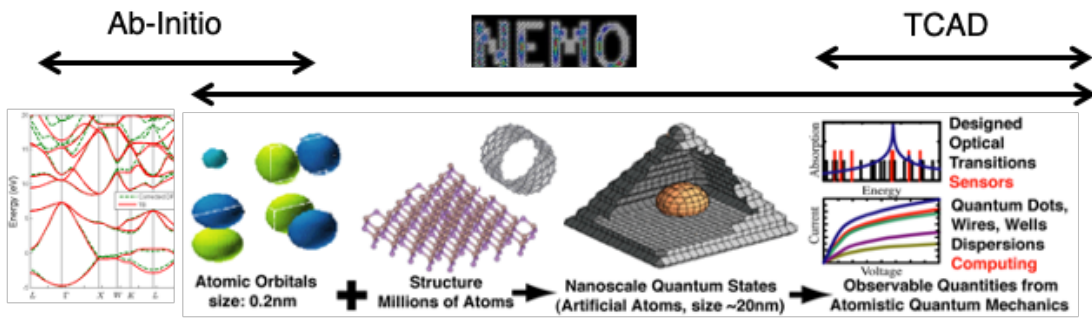
Fig. 1. NEMO modeling agenda bridging ab-initio methods to large scale TCAD simulations. Ab-initio material representations can be mapped explicitly into the device Hamiltonian via a Wannier function approach or through an approximate tight-binding mapping into a local orbital basis. The local basis representation enables an efficient numerical representation of nano-scaled devices including local disorders such as interface roughness and alloy disorder. NEGF-based boundary conditions enable linking a central quantum device to extended realistic contacts.
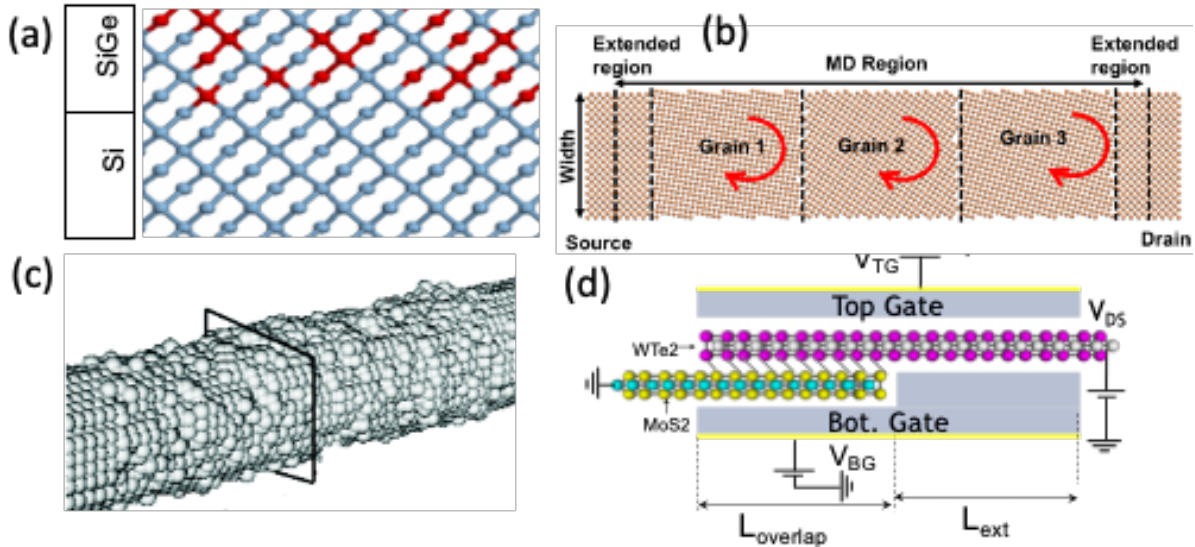
Fig. 2. Examples of NEMO5 simulation geometries. (a) Atomistic SiGe/Ge interfaces strongly influencing valley splitting for quantum computing. (b) Grain boundary scattering in nano-scale copper wires and slabs. Molecular dynamics predicts structure and NEMO5 computes conductance (c) Explicit representation of interface roughness in nanowires resulting in significant scattering. (d) Example geometry for a dual layer TMD Tunnel FET.

Theoretical Analysis of Tunneling Effect in
4H-SiC Schottky Barrier Diodes Based on Complex Band Structure

Y. Murakami, S. Nagamizo, H. Tanaka, and N. Mori

Graduate School of Engineering, Osaka University

2-1 Yamada-oka, Suita, Osaka 565-0871, Japan

murakami@si.eei.eng.osaka-u.ac.jp

4H-SiC is attracting as a power device material. However, there are still unresolved issues in the properties of 4H-SiC. In a previous study [1], to reproduce the experimental tunneling current in Schottky barrier diodes (SBDs) by calculation, the value of the effective mass must be smaller than the experimental value. In this study, we use the complex band structure of 4H-SiC to consider tunneling effect more accurately and analyze tunneling current in SBDs.

We calculate the complex band structure [2] of 4H-SiC by the empirical pseudopotential method (EPM). From the complex band structure, the damping factor κ_{EPM} is obtained. For comparison, the damping factor by the parabolic band approximation (PBA) κ_{PBA} is also considered. Then, tunneling current is calculated based on the WKB approximation [3].

Figures 1(a) and (b) show the real and the complex band structure of 4H-SiC, respectively. κ_{EPM} increases more slowly than κ_{PBA} in the forbidden band, which indicates the EPM complex bands are non-parabolic. Figure 2 shows the calculated tunneling currents by EPM and PBA. When the experimental value of effective mass is used in calculation, calculated tunneling current by PBA significantly underestimates the experimental tunneling current. Conversely, that by EPM is somewhat larger. In the above calculation, κ is assumed to be independent of the wave vector $k_\perp$ perpendicular to the transport direction. However, κ is actually dependent on $k_\perp$. Therefore, we calculate κ at each $k_\perp$ by EPM, and the corresponding tunneling result is shown in Fig. 3(a). By considering κ dependent on $k_\perp$, the calculated result is closer to the experimental result. Taking account of this effect phenomenologically, as a model to reproduce the experimental result without changing the value of the effective mass, we introduce $\kappa^* = \{\alpha \cdot \kappa_{\text{EPM}}^2 + (1 - \alpha) \cdot \kappa_{\text{PBA}}^2\}^{1/2}$. Here, κ_{EPM} and κ_{PBA} are the damping factors in Fig. 1(b) and α is a fitting parameter. Figure 3(b) shows the calculated tunneling current using κ^* with $\alpha = 0.67$. The experimental result is well reproduced by the calculation.

In summary, by considering the non-parabolicity of the complex band and κ dependent on $k_\perp$, calculated tunneling current is reasonably close to the experimental result. Also, by adjusting the non-parabolicity, the calculated result well reproduces the experimental result.

[1] M. Hara *et al.*, Appl. Phys. Lett. **120**, 172103 (2022). [2] Y. C. Chang and J. N. Schulman, Phys. Rev. B **25**, 3975 (1982). [3] W. A. Harrison, Phys. Rev. **123**, 85 (1961).
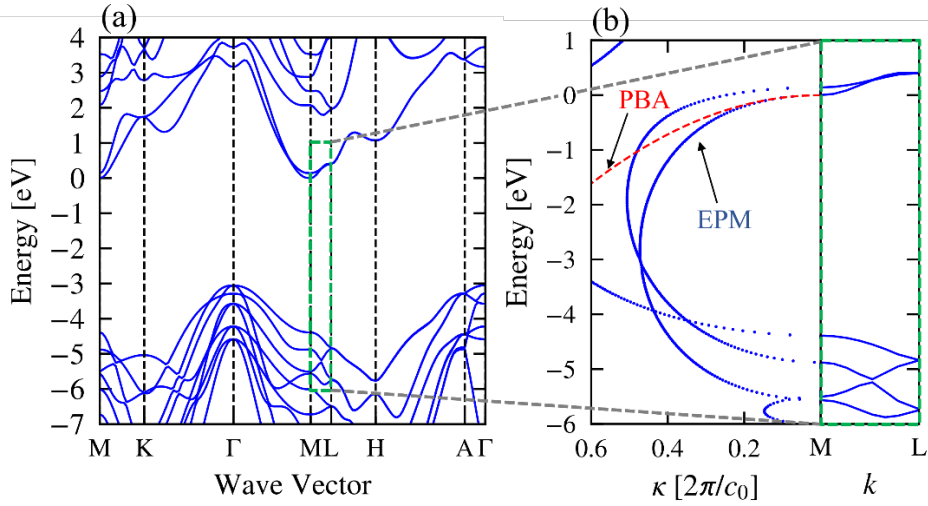
Fig.1: (a) Real and (b) complex band structure of 4H-SiC calculated by EPM. κ_{PBA} is also plotted for comparison in (b).
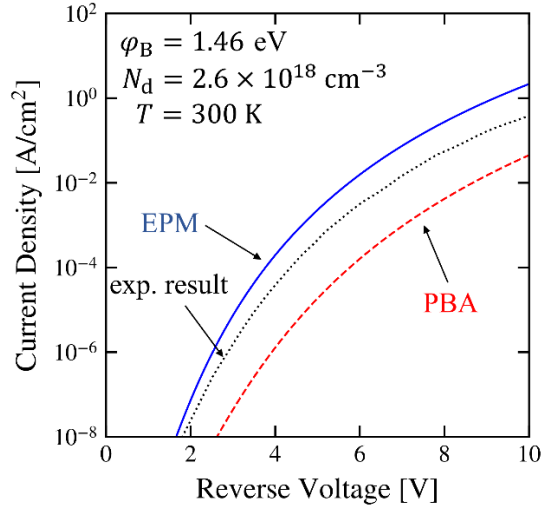
Fig.2: Reverse voltage dependence of the calculated tunneling currents by EPM and PBA. The experimental result in [1] is also shown for comparison. T is the temperature and N_d is the donor density. The value of barrier height φ_B experimentally obtained in [1] is used.
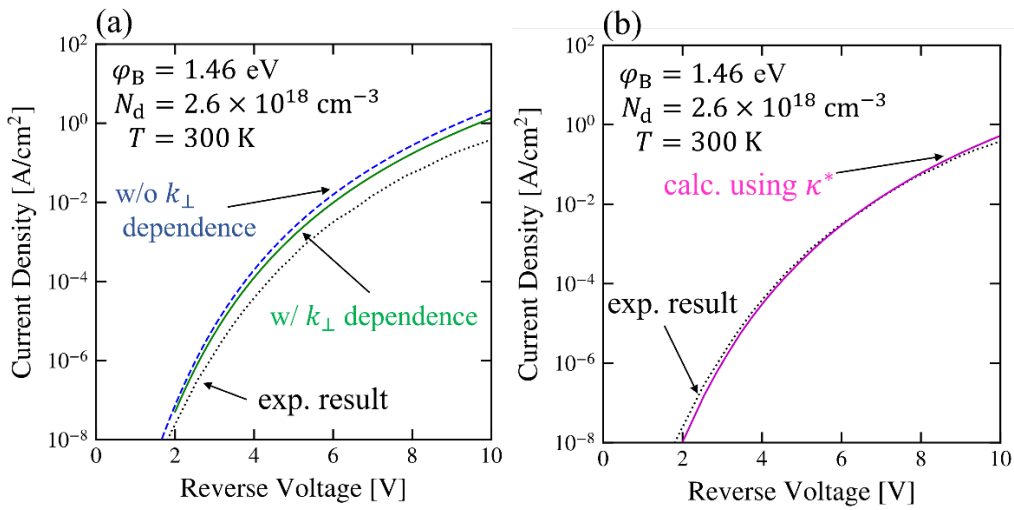
Fig.3: Reverse voltage dependence of calculated tunneling current by EPM (a) when wave vector $k_\perp$ dependence is considered and (b) the non-parabolicity of the complex band is phenomenologically adjusted by using κ^*.

Spintronics with Ferrimagnetic and Antiferromagnetic Insulators

Andrew D. Kent[1]

[1]*Center for Quantum Phenomena, New York University*
andy.kent@nyu.edu

The magnetization of a magnetic material can be excited and reversed by electric currents that transport spin angular momentum [1]. This was predicted in magnetic tunnel junctions — two metallic ferromagnetic layers separated by a thin insulating barrier — by Slonczewski in 1989 and demonstrated experimentally about a decade later. This discovery has had an enormous impact on magnetism research and technology [2], as prior to this the primary means to reorient and excite the magnetization of a magnet was by applying magnetic fields (dating to 1819 and Oersted). Remarkably, spin currents are also able to change the magnetic order of antiferromagnetic layers and excite persistent spin dynamics, known as auto-oscillations, in magnetic insulators. In this talk I will highlight my group's experimental x-ray imaging studies of current-induced reorientation of the Néel vector in hematite, α-Fe_2O_3, using the spin-Hall effect in Pt as the spin current source [3]. I will also discuss harmonic Hall effect measurements that make it possible to determine the form and magnitude of the spin-torques that act on the Néel vector [4]. Further, I will present a hybrid spin Hall nanooscillator based on ferromagnetic metal (permalloy)/ferrimagnetic insulator (epitaxial lithium aluminum ferrite) heterostructures [5]. The low damping of the ferrimagnetic insulator is shown to lead to greatly improved oscillator characteristics — *e.g.*, lower threshold currents, higher quality factors and output powers — associated with the nature of the coupled spin-wave modes excited and an increase in the excited volume.

[1] A. Brataas, A. D. Kent and H. Ohno, "Current-Induced Torques in Magnetic Materials," Nature Materials **11**, 372 (2012)
[2] A. D. Kent and D. C. Worledge, "A new spin on magnetic memories," Nature Nanotechnology **10**, 187 (2015)
[3] E. Cogulu, N. N. Statuto, Y. Cheng, F. Yang, R. V. Chopdekar, H. Ohldag, and A. D. Kent, "Direct Imaging of Electrical Switching of Antiferromagnetic Néel Order in α-Fe_2O_3 Epitaxial Films," Physical Review B **103**, L100405 (2021)
[4] E. Cogulu, H. Zhang, N. N. Statuto, Y. Cheng, F. Yang, R. Cheng, and A. D. Kent, "Quantifying Spin-Orbit Torques in Antiferromagnet/Heavy Metal Heterostructures" Physical Review Letters **128**, 247204 (2022)
[5] H. Ren, X. Y. Zheng, S, Channa, G. Wu, D. A. O'Mahoney, Y. Suzuki2, and A. D. Kent, "Hybrid spin Hall nano-oscillators based on ferromagnetic metal/ferrimagnetic insulator heterostructures" arXiv:2208.04539

NiSi: New research Venue for Antiferromagnetic Spintronics

Deepak K. Singh[1], Pousali Ghosh[1], Jiasen Guo[1], Feng Ye[2] and Tom Heitmann[3]

[1]Department of Physics and Astronomy, University of Missouri, Columbia, MO, USA
[2]Oak Ridge National Laboratory, Oak Ridge, TN, USA
[3]University of Missouri Research Reactor, Columbia, MO, USA
singhdk@missouri.edu

Antiferromagnetic system is argued to provide a superior platform for the spintronic application than ferromagnetic compound.[1] The quantum mechanical nature of strong exchange coupling in an antiferromagnet enhances the internal effective fields and the characteristic frequency for spin dynamics, thus making it faster and more robust against the external magnetic field perturbation than a ferromagnet. However, finding a suitable AFM compound for spintronic applications,[2] preferably in stoichiometric configuration, with high enough Neel temperature, for practical operability above room temperature, and strong metallic characteristic, for the generation of spin polarized current, is a challenge.[1] More recently, we discovered AFM order in single crystal nickel monosilicide (NiSi) for the first time with an onset temperature of T ~ 520 K.[3] Nickel silicides are important electronic materials that have been used as contacts for field effect transistors, as interconnects and in nanoelectronic devices. But magnetism was never detected in any of the nickel silicides.[4] The magnetic characteristics of NiSi are investigated using elastic neutron scattering measurements on CORELLI and TRIAX spectrometers at ORNL and MURR, respectively. Numerical modeling of experimental data reveals antiferromagnetically aligned Ni spins with ordered moment of ~ $0.9\mu_B$ in a-b plane, rotated with respect to c-axis, see Fig. 1. The system exhibits a remarkable one-step switching transition for magnetic field application along the [001] direction at H ~ 900 Oe in magnetic hysteresis measurements. The one-step switching is prevalent at high temperature (see Fig. 2), which makes it an attractive candidate for the spintronic application. Further insight into the electronic nature of magnetic transition is obtained by performing MR measurements in Hall configuration. As shown in Fig. 3, NiSi manifests significant hysteresis in the Rxy data, which is indicative of strong AMR for magnetic field application along the [001] direction. Cumulatively, NiSi exhibits many functionalities that can be exploited to develop new AFM spintronics platform. [1] S. Fukami et al., Antiferromagnetic spintronics, *J. Appl. Phys.* **128**, 070401 (2020); [2] T. Jungwirth, X. Marti, P. Wadley and J. Wunderlich, Antiferromagnetic Spintronics, *Nat. Nano.* **11**, 231 (2016); [3] P. Ghosh, J. Guo, G. Yumnam, T. Heitmann, F. Ye, A. Ernst, V. Dugaev and D. K. Singh, NiSi: New venue for antiferromagnetic

spintronics (in preparation); [4] A. Dahal, J. Gunasekera, L. Harriger, D. K. Singh and D. J. Singh, Metallic nickel silicides: Experiments and theory for NiSi and first principles calculations for other phases *J. Alloy Comp.* **672**, 110 (2016)
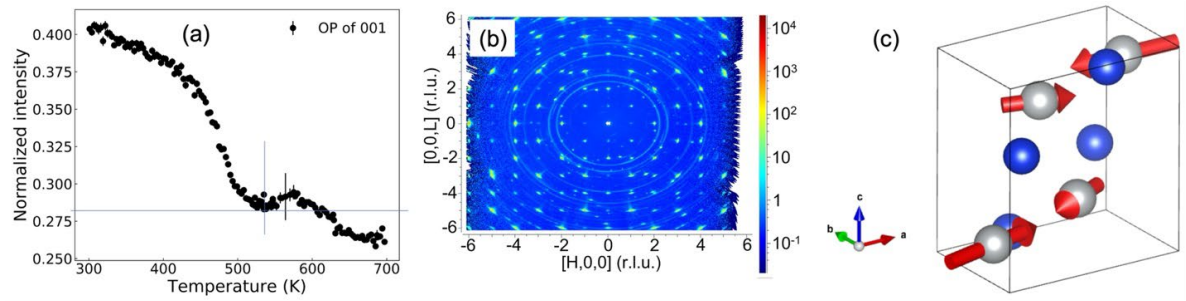
Fig. 1: (a) Magnetic order parameter as a function of temperature of NiSi (measured on CORELLI) with onset temperature of T ~ 520 K. Paramagnetic fluctuation persists to higher temperature, exceeding 700 K. (b) Representative mesh scan of elastic data at T = 300 K. Magnetic peaks are detected at q values given by h+k+l = 2n+1. (c) Modeling of magnetic data reveals AFM order with moments aligned in a-b plane, rotated by ~ 10 degree from the c-axis.

Fig. 2: Magnetic hysteresis measurements at T = 350 K, manifesting one-step switching transition between two field-aligned saturated magnetic states at H ~ 900 Oe.
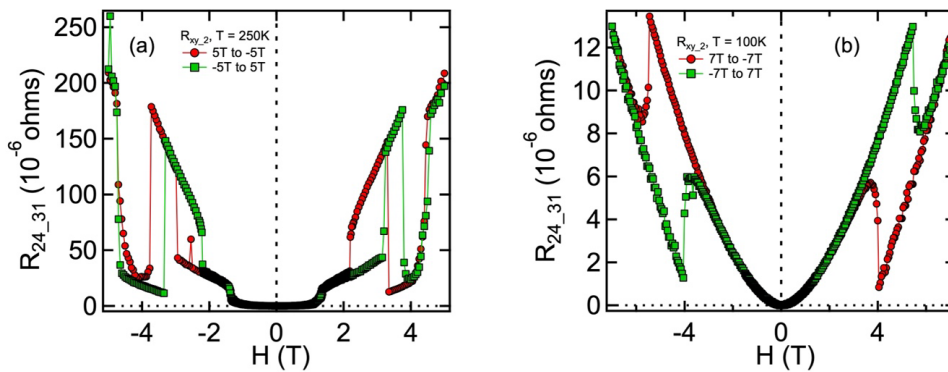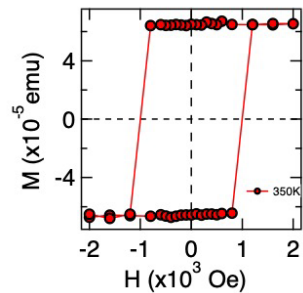
Fig. 3: Magnetoresistance (MR) data as a function of magnetic field at two representative temperatures of T = 250 K (fig. a) and 100 K (fig. b). Hall measurements reveal strong asymmetry in MR data, causing hysteresis, at all measurement temperatures. The asymmetry is pronounced at higher magnetic fields compared to the magnetic hysteresis data, suggesting strong coupling between the underlying electronic and magnetic properties.

Theory of Exchange Spin-Orbit Coupling

K. Hayashida[1], and H.Akera[2]

[1]Division of Applied Physics, Graduate School of Engineering, Hokkaido University, Sapporo, Hokkaido, 060-8628, Japan

[2]Division of Applied Physics, Faculty of Engineering, Hokkaido University, Sapporo, Hokkaido, 060-8628, Japan

learning-penguin802@eis.hokudai.ac.jp

Relativistic spin-orbit coupling is a fundamental interaction and attracts much attention for spintronics applications and physics. However, recent theoretical [1] and experimental [2] studies have found exchange spin-orbit coupling (ESOC) that comes from the exchange interaction between carriers and localized spin. The ESOC generates k(wavevector)-dependent and non-relativistic spin splitting of the energy bands, and the splitting is much larger than that of relativistic SOC due to its origin. The ESOC is a potentially powerful resource for spintronics. However, the theoretical studies for the ESOC have just performed the first-principles or complicated Hubbard model calculation to propose the ESOC. The understanding of ESOC mechanism based on a band structure has been still lacking.

We propose a mechanism that can describe both relativistic and exchange SOC in a unified manner based on a band structure, and apply the mechanism to the ESOC of an *n*-type ferromagnetic semiconductor (*n*-type FMS) to calculate the ESOC spin splitting, anomalous Hall conductivity [3], and Curie temperature T_c. The *n*-type FMS that we consider is suitable for our calculation method (a $k \cdot p$ method with mean-field approximation) and the carrier-mediated ferromagnet with a host III-V semiconductor and iron magnetic impurities [4].

The proposed mechanism for a general SOC is the following: the SOC in the conduction band (CB) emerges from the inter-band process [Fig.1(1,3)] and the spin-dependent interaction (*p-d* exchange interaction of the valence band for ESOC of an *n*-type FMS and LS coupling for relativistic SOC) which rotates the electron spin in the intermediate state [Fig. 1(2)].

The calculated energy bands [Fig.2] show the spin splitting in the CB due to *p-d* ESOC for a typical *n*-type FMS (InFeAs at Fe 6%). Surprisingly the spin splitting is ten times larger than the spin splitting (several meV) due to the relativistic SOC in typical III-V semiconductors.

The intrinsic anomalous Hall conductivity of the *p-d* ESOC [black line in Fig.3] increases with the iron concentration in contrast to the relativistic Dresselhaus SOC with *s-d* exchange. Finally, we obtain the spin polarization and the T_c to find that the *p-d* ESOC is crucial to the T_c since the *p-d* absent T_c largely deviates from experimental values.

The theory [Fig.1] will open up new SOC for condensed matter physics and spintronics.

[1] M. Naka *et al*, Nat. Commun. **10**, 4305 (2019). [2] H. Bai *et al*, Phys. Rev. Lett. **128**, 197202 (2022), A. Bose *et al*, Nature Electronics **5**, 267 (2022). [3] K. Hayashida and H. Akera, Phys. Rev. B **105**, 235203 (2022). [4] L. D. Anh *et al*, Nat. Commun. 7:13810 (2016).
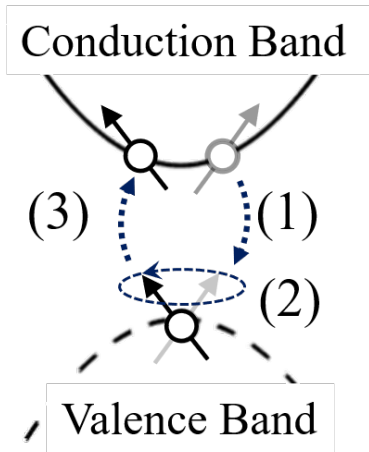
Fig.1: Mechanism of spin-orbit coupling in the conduction band. (1) The conduction electron spin moves to the valence band. (2) The spin rotates by a spin-dependent interaction, and (3) the effective rotation appears after the electron goes back to the conduction band.
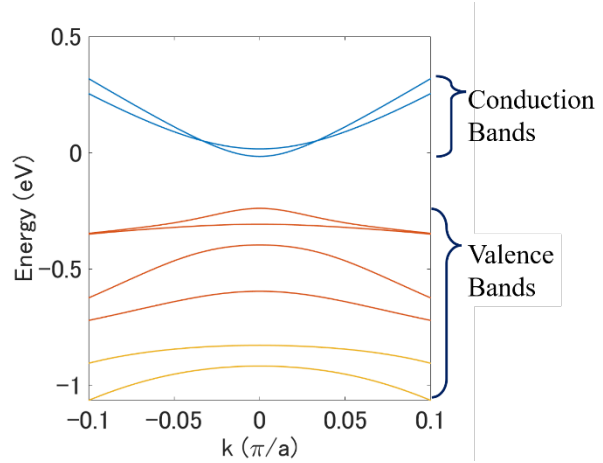
Fig.2: Energy bands of InFeAs (Fe 6%) along the [100] direction of the host InAs. The band structure is the III-V semiconductor type with spin splitting by exchange interactions.
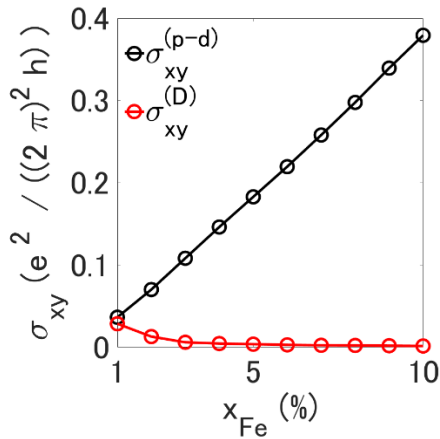
Fig.3: Intrinsic anomalous Hall conductivity and iron concentration dependence. For comparison, we show p-d exchange (black) and Dresselhaus SOC with s-d exchange cases (red) [3].

Nonreciprocity in Spin Transport

Sadamichi Maekawa[1,2]

1. *RIKEN Center for Emergent Matter Science (CEMS), Wako, 351-0198, Japan,*

2. *Kavli ITS at University of Chinese Academy of Sciences, Beijing, China,*

Sadamichi.maekawa@riken.jp (e-mail address)

"Nonreciprocity" means "not going the same way backward as forward". The well-known is the rectification by using PN junctions in electronics where electrons flow in one direction but not the other. The spin Hall effect and its inverse are the interconversion mechanism between electron current and spin current. It has been shown that the interconversion is reciprocal and described by the Onsager reciprocal relation [1]. On the contrary, many of the spin transport phenomena are nonreciprocal. Here, the nonreciprocity in spin transport is discussed together with various examples. The key is that the spin current is a flow of spin angular momentum, in contrast to the electric current. A flow of electrons can have the orbital angular momentum , which is called "vorticity", and may be interconverted with spin current [2]. However, since the vorticity of electron flow is highly nonlinear, the conservation mechanism, i.e., the spin-vorticity coupling, is also nonlinear [1]. As a result, we find a variety of nonreciprocal phenomena in spin transport. The nonreciprocity of surface acoustic waves in magnetic films [3], the magnetic skyrmion generation and annihilation by electric current in magnetic films with notch structure [4], and the spin current generation in the graded materials [5] will be discussed.

[1] T. Kimura, Y. Otani, T. Sato, S. Takahashi and S. Maekawa: Phys. Rev. Lett. **98**, 156601 (2007),

[2] M.Matsuo, E.Saitoh and S.Maekawa, Chapter 25 in "Spin Current" ed. S.Maekawa et al. (Oxford University Press, 2017).

[3] M. Xu, K. Yamamoto, J. Puebla, K. Baungaert, B. Rana, K. Miura, H. Takahashi, D. Grundler, A. Maekawa and Y. Otani: Sci. Adv. **6**, eabb1724 (2020),

[4] J.Fujimoto, W.Koshibae, M.Matsuo and S.Maekawa, Phys. Rev. B*103*, L220404 (2021).

[5] G.Okano, M.Matsuo, Y.Ohnuma, S.Maekawa, and Y.Nozaki, Phys. Rev. Lett. *122*, 217701 (2019).
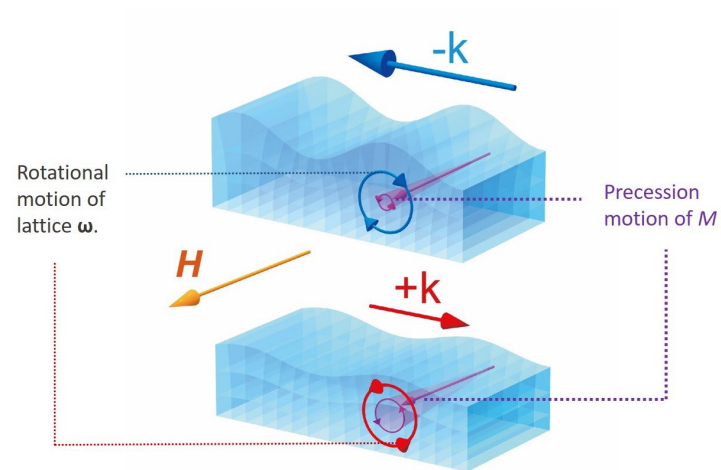
*Fig. 1. Surface acoustic waves (SAWs) are rotational lattice (ω) vibrations localized at the surface. Magnetization precession is unidirectional motion. Therefore, their coupling is Nonreciprocal! c.f., S. Maekawa and M. Tachiki, API Proc., **29**, 542 (1976).*

Superfluid Spin Transistor

Alexey A. Kovalev[1]

[1]*Department of Physics and Astronomy and Nebraska Center for Materials and Nanoscience, University of Nebraska, Lincoln, Nebraska 68588, USA*

An ability to control spin currents is important for probing many spin related phenomena in the field of spintronics, and for designing logic and memory devices with low dissipation. Spin-orbit torque is an important example in which spin current flows across magnetic interface and helps to control magnetization dynamics. In this talk, I will discuss the spin superfluid transport associated with collective modes in magnetic insulators. We observe that in two dimensional systems at finite temperatures spin superfluidity is affected by the presence of topological defects. We further propose to use the Hall response of topological defects, such as merons and antimerons, to spin currents in 2D magnetic insulator with in-plane anisotropy for identification of the Berezinskii-Kosterlitz-Thouless (BKT) transition in a transistor-like geometry. Our numerical results relying on a combination of Monte Carlo and spin dynamics simulations show transition from spin superfluidity to conventional spin transport, accompanied by the universal jump of the spin stiffness and exponential growth of the transverse vorticity current. We propose a superfluid spin transistor in which the spin and vorticity currents are modulated by tuning the in-plane magnet across BKT transition, e.g., by changing the exchange interaction, magnetic anisotropy, or temperature [1-2].

[1] Bo Li and Alexey A. Kovalev, Phys. Rev. B 103, L060406 (2021).
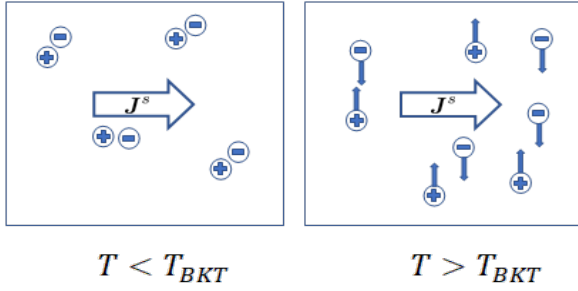[2] Edward Schwartz, Bo Li, Alexey A. Kovalev, arXiv:2112.14241

Fig.1: Superfluid spin current exerts the Magnus force on magnetic defects, such as merons and antimerons, resulting in the vorticity Hall effect. The vorticity Hall effect is suppressed below BKT temperature due to binding of defects with opposite vorticity.

Fig.3: The vorticity Hall response as a function of temperature. Circles show numerical results for the vorticity Hall response as a function of temperature in arbitrary dimensionless units. Lines show fit to analytical predictions. (a) Fitting to analytical predictions for easy-plane anisotropy $K = 0.1J$ leads to estimate $k_B T_{BKT} \approx 0.61J$ where J is the exchange interaction. (b) Fitting to analytical predictions for easy-plane anisotropy $K = 0.2J$ leads to estimate $k_B T_{BKT} \approx 0.65J$.
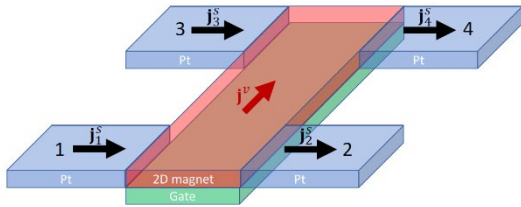

Fig.2: A schematic plot of superfluid spin transistor. Spin current injected through lead 1 can propagate to lead 2 in the spin superfluidity regime below BKT transition while injected spin current will exponentially decay above BKT transition. In addition, the presence of transverse vorticity current above BKT transition can be detected in the nonlocal geometry using leads 3 and 4. The spin superfluid current can be modulated by tuning in-plane magnet below or above BKT transition via modifications of exchange interactions and anisotropy, e.g., by the gate modulated electrical-field-induced strain or direct electrical-field-induced modifications of exchange interactions and anisotropy.

Fig.4 Spin current $j^s(L)$ for different system sizes when spin current $j^s(0)$ is injected on the left. We consider in-plane anisotropy $K= 0.2J$ and take $T = 0.62\ J/k_B < T_{BKT}$ for the upper plot and $T = 0.71\ J/k_B > T_{BKT}$ for the lower plot. Lines are the fit to analytical predictions. Curves demonstrate crossover from exponential to algebraic decay.

Evaluating Spin Transfer Torques
in Multilayered Magnetic Tunnel Junctions and Spin Valves

S. Fiorentini[1,2], M. Bendra[1,2], J. Ender[1,2], W. Goes[3], V. Sverdlov[1,2], and S. Selberherr[1]

[1] *Christian Doppler Laboratory for Nonvolatile Magnetoresistive Memory and Logic at the*
[2] *Institute for Microelectronics, TU Wien, Gußhausstraße 27-29/E360, 1040 Vienna, Austria*
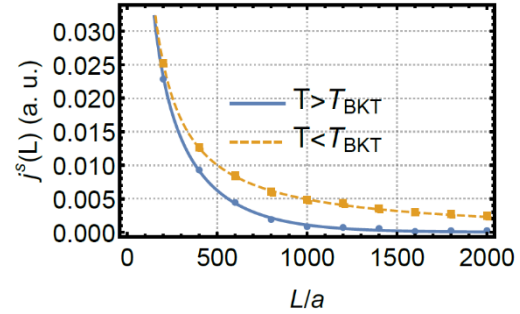[3] *Silvaco Europe Ltd., Cambridge, United Kingdom*
{sverdlov|selberherr}@iue.tuwien.ac.at

Emerging nonvolatile spin-transfer torque (STT) magnetoresistive random access memory (MRAM) offers high speed and endurance. An MRAM cell consists of several layers, including a CoFeB magnetic reference layer and a free layer (RL and FL) separated by an MgO tunnel barrier (TB) (Fig. 1a). To increase the perpendicular magnetic anisotropy, the FL, typically composed of two CoFeB layers and a thin metal buffer, is interfaced with a second MgO layer. Introducing several MgO layers in the FL and elongating it allows to boost the perpendicular anisotropy even further, while reducing the FL diameter. For an accurate design of an ultra-scaled MRAM cell (Fig. 1b) it is necessary to describe the torques acting on elongated FLs with the inclusion of metal buffers and MgO TBs. We incorporated all phenomena in a three-dimensional finite element method (FEM) based modeling approach. We numerically solve the Landau-Lifshitz-Gilbert equation describing the magnetization dynamics. The demagnetization field is evaluated only on the disconnected magnetic domain by a hybrid boundary element method and the FEM [1]. The coupled spin and charge drift-diffusion (DD) method accurately describes the spin and charge and transport through a nanometer sized metallic magnetic valve.

We extended the method to magnetic tunnel junctions (MTJs). First, we model the tunnel barrier as a poor conductor with a local resistance dependent on the relative orientation of the magnetization [2]. However, the continuity of the spin accumulation and spin current at the TB interfaces results in an incorrect angular dependence of the torque acting on the FL (Fig. 2). To reproduce the angular dependence expected in an MTJ, novel boundary conditions for the spin current at the TB interfaces must be introduced [3]. The spin-transfer torque is then perfectly reproduced (Fig. 3). Introducing voltage-dependent interfacial spin current polarizations, the experimentally observed voltage dependencies of the filed-like and damping-like torques are reproduced (Fig. 5). The approach was successfully applied to demonstrate the switching of a composite elongated FL (Fig. 5). The time-dependent magnetization in the FL is shown in Fig.6.

[1] J. Ender *et al., Proc. SISPAD,* pp. 213-216, 2020.

[2] S. Fiorentini *et al.*, Solid-State Electronics **186**, 108103, 2021.

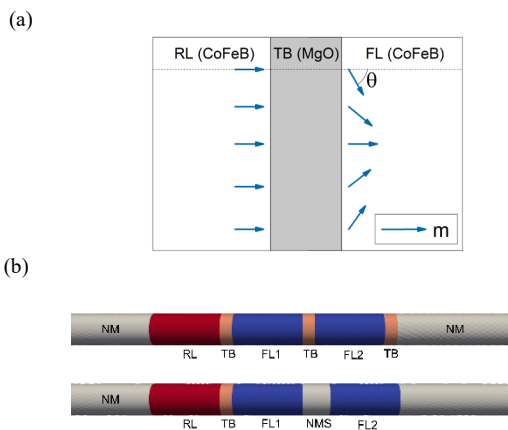[3] S. Fiorentini *et al.*, submitted to Sci. Reports.

(a)

(b)

Fig.1: (a) Magnetic tunnel junction with nonuniform magnetization of the FL; (b) Ultra-scaled MRAM cell with a composite elongated FL. The parts of the FL are separated by a TB or a metal layer.

Fig.2: Angular dependence of the torque acting on a semi-infinite FL based on the DD (dotted line) and on the Slonczewski expression (dashed line).

Fig.3: Angular dependence of the torque with the spin-current boundary conditions, for a 2 nm thick FL. The expected angular dependence specific to an MTJ is reproduced, for several values of the spin polarization parameter.

Fig.4: Comparison between the simulated and the experimental field-like and damping-like spin transfer torques.

Fig.5 Switching snapshot of the MRAM cell (Fig.1) switching for initial, intermediate, and final state. Arrows indicate the magnetization directions, and the color-coding represents the average magnetization in x-direction.
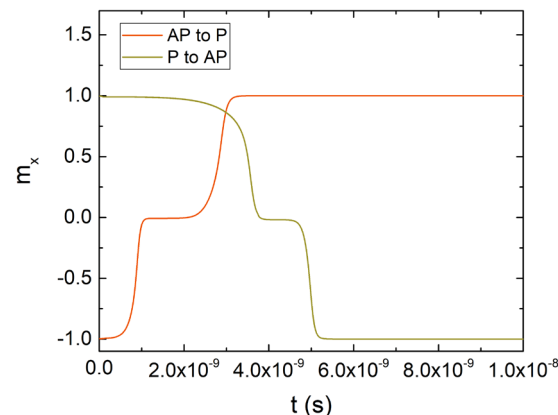
Fig.6: FL (Fig.1) magnetization reversal from anti-parallel to parallel and from parallel to anti-parallel configuration relative to the reference layer. An intermediate state is observed for both switching directions.

Singular Angular Magnetoresistance in a Nodal Semimetal

Takehito Suzuki

Department of Physics, Toho university, Funabashi, Japan
takehito.suzuki@sci.toho-u.ac.jp

Coupling between conduction electrons and localized magnetic moments gives rise to various magnetotransport phenomena. A spin-orbit coupled anisotropic scattering leads to angular magnetoresistance, a variation of lon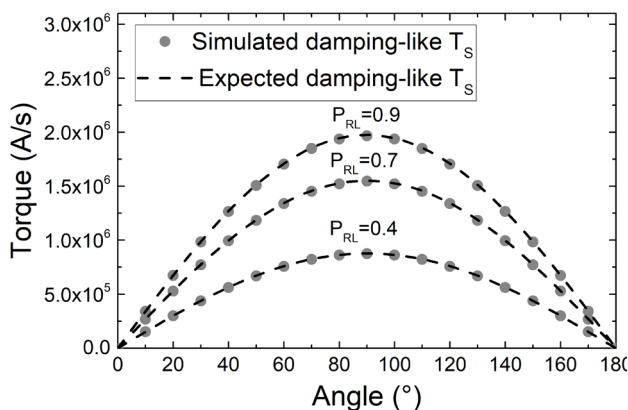gitudinal resistivity in magnetic field depending on the angle between the magnetic moment and the electric current directions. The angular dependence shows a smooth variation that typically varies as the square of the cosine of the angle and is generally described by the magnetic point group symmetry of the material. This is widely utilized for a magnetic field sensor.

Magnetic Weyl semimetals have a distinct electronic structure with nodal Fermi surface as well as magnetic ordering. Their coupling is expected to lead to novel magnetotransport properties. Here, we show singular angular magnetoresistance, angular magnetoresistance with an unprecedented sharp response to the applied magnetic field direction where the full-width-half-maximum of the feature reaches to less than one degree, in a topological semimetal candidate CeAl(Ge,Si) [1]. The resistivity enhancement occurs in the magnetically ordered phase with intermediate strength of magnetic field applied along the crystallographically high symmetry direction. This originates from scattering at the boundary of the magnetic domains that have Fermi surface at different locations in the momentum space depending on the magnetic moment direction. Such an effect is intensified in the system with stronger conduction electron-localized moment coupling and smaller Fermi surfaces that lead to larger Fermi surface mismatch between the magnetic domain, indicating that nodal semimetal with magnetic ordering, including magnetic Weyl and nodal line semimetals, can be a potential platform for a singular angular magnetoresistance behavior.

[1] T. Suzuki *et al.*, Science 365, 377 (2019).

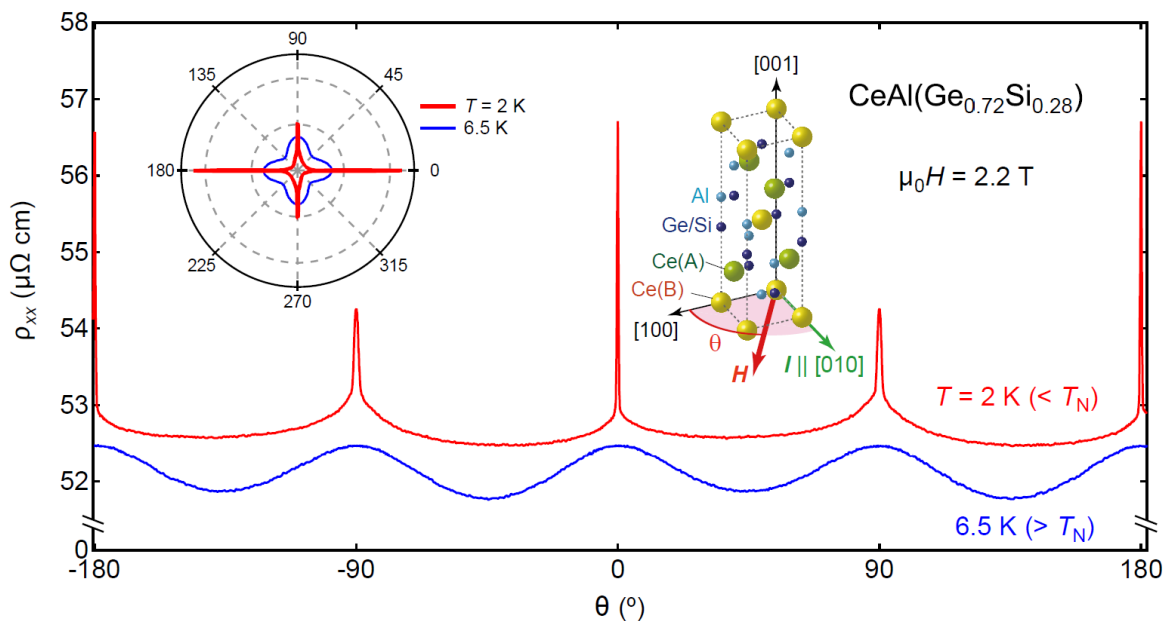Fig.1: *Singular angular magnetoresistance in a nodal semimetal CeAl(Ge,Si). The longitudinal resistivity shows the sharp enhancement with magnetic field along the [100] (θ = -180, 0, and 180°) and the [010] directions (θ = -90 and 90°). The left inset is the corresponding polar plot. The right inset displays the measurement configuration, where the magnetic field is rotated in the (001) plane.*

Edge State Band Gap Dependences on the Width of Transition Metal Dichalcogenide Nanoribbons in the 1T′ Topological Phase

V. Sverdlov[1,2], A. El-Sayed[2,3], H. Seiler[2], and H. Kosina[2]

[1] *Christian Doppler Laboratory for Nonvolatile Magnetoresistive Memory and Logic at the*
[2] *Institute for Microelectronics, TU Wien, Gußhausstraße 27-29/E360, 1040 Vienna, Austria*
[3]*EU Patent Office, Munich, Germany*

sverdlov@iue.tuwien.ac.at

Monolayers of two-dimensional transition metal dichalcogenides in the 1T′ phase possess an unusual dispersion. Due to its double honeycomb lattice structure the band dispersion exhibits two Dirac cones broken with an inverted fundamental band gap. Within the fundamental gap highly conductive edge states protected against back-scattering by nonmagnetic impurities exist [1]. The normal electric field induces a phase transition between the phases with and without the edge states. The transition is promising for building ultra-scaled electron switches [1].

The edge states at opposite edges start interacting in a narrow nanoribbon. It results in the opening of a tiny bandgap in the edge states spectrum. The bandgap is expected to increase if the nanoribbon width d is reduced. Here, we investigate the dependence of this bandgap on the nanoribbon's width for armchair edges (Fig.1) using *ab initio* calculations. The atomic and electronic structures were calculated using VASP. The exchange and correlations were described by the generalized PBE pseudopotentials. The spin-orbit interaction was calculated as the zeroth order coupling of a spinor wave function. For the nanoribbon calculations, a vacuum gap of 2nm was added to all non-periodic dimensions. The number of grid points was $12 \times 1 \times 1$.

The edge of a nanoribbon after the energy relaxation is slightly modifed. The metal atoms at the edge are pushed inward the structure, chalcogenide atoms outwards. For several materials the dependences of the bandgap between the edge states on the nanoribbon's width (in unit cells) were calculated. Surprisingly, the dependences are nonuniform. Although a trend to increase at narrow widths is observed, an oscillating behavior is observed for MoS_2 and $MoSe_2$. To understand the dependences, **k·p** calculations [2] were performed. A comparison with with the *ab initio* results were performed. Based on the comparison, we explain the oscillatory behavior in MoS_2, $MoSe_2$ and WSe_2 and its absence in WS_2 nanoribbons.

[1] X. Quan *et al*., Science **346**, 1344 (2014).
[2] V. Sverdlov *et al*., Solid-State Electronics **193**, 108266 (2022).

Figures are not printed due to the authors' request

Robust Resistive and Mem-devices for Neuromorphic Circuits

T. Venkatesan

Center for Quantum Research and Technology, University of Oklahoma, Norman OK, USA

venky@ou.edu

Artificial intelligence (AI) has been heralded as the flagbearer of the fourth industrial revolution but comes with a cost and that is computing power. It is projected that by 2040, we will need more computing energy than the total energy we can produce now. So, we need devices that can offer higher computing/ storage density with low energy consumption like neurons. We are addressing these challenges using oxide and molecular-electronic based memristors, which enable us to overcome the von Neuman bottleneck by co-locating the memory and computing functions on the same device, as in neuromorphic computing.

I will discuss a variety of strategies for forming oxide based memristors using different phenomena- band filling and creating a quasi-conduction band, using oxygen vacancies to create conductive percolation, using metal-insulator transitions, or using asymmetric tunneling at a ferroelectric barrier. The relative merits of the various approaches will be detailed.

In addition, I will touch upon memristive devices and circuits made from an azo-aromatic complex with extra-ordinary reproducibility, robustness, and scalability. These devices have been shown to switch with energies approaching atto-joules with measured switching times shorter than 5 ns. By using a simple cross bar array, we have shown that these devices perform with an energy-speed product 5000 times that of a state-of-the-art CMOS circuit.

[1]   Sreetosh Goswami*, Rajib Pramanick, Abhijeet Patra, Santi Prasad Rath, Ariando, Damien Thomson, T. Venkatesan*, Sreebrata Goswami* and R Stanley Williams*, <u>Decision Trees within a Molecular Memristor</u>, Nature, Sep. 3, 2021

[2]   Sreetosh Goswami, Adam J. Matula, Santi P. Rath, Svante Hedstrom, Surajit Saha Meenakshi Annamalai, Debabrata Sengupta, Abhijeet Patra, Siddhartha Ghosh, Hariom Jani, Soumya Sarkar, Mallikarjuna Rao Motapothula, Christian A. Nijhuis' Jens Martin, Sreebrata Goswami*, Victor S. Batista*, T. Venkatesan*, <u>Robust resistive memory devices using solution-processable metal-coordinated azo-aromatics</u>, Nature Materials, 16, 1216 (2017). News and views on this article: I. Valev and M. Kozicki, Non-volatile Memories: Organic Memristors come of age, Nature Materials, 16, 1170 (2017)

[3] Rui Guo, Weinan Lin, Xiaobing Yan, T Venkatesan, Jingsheng Chen, <u>Ferroic tunnel junctions and their application in neuromorphic networks</u>, Applied Physics Reviews, 2020/3/6

Interface Characteristics of Ferroelectric $Hf_{1-x}Zr_xO_2$ on Si with an Al_2O_3 Interface Layer

J. Lee, D. Eom, W. Lee, J. Oh, C. Park, and H. Kim

School of Advanced Materials Science & Engineering, Sungkyunkwan University,

Suwon 16419, Republic of Korea

hsubkim@skku.edu

The recent discovery of ferroelectric HfO_2 films with excellent process compatibility and thickness scalability has prompted vigorous research for their applications in ferroelectric field-effect transistor (FeFET) memories. One of the gate stack structures used in FeFETs, a metal–ferroelectric–insulator–semiconductor (MFIS) structure, is well suited to the modern device fabrication processes. However, an ultra-thin interfacial layer (typically, metal-silicate) with a lower dielectric constant than SiO_2 is inevitably formed between the ferroelectric film and the Si substrate. Because this insulating layer with poor quality generates many interface traps during operation [1], several intentional layers, such as SiON and ZrO_2 [2–3], have been introduced to improve the endurance characteristics.

In this study, to improve the reliability characteristics of the FeFETs with a MFIS structure, an ultra-thin Al_2O_3 film was used as an insulating layer between the Zr-doped HfO_2 (HZO) film and Si. Both Al_2O_3 and HZO films were deposited at 280 °C via an in situ atomic-layer-deposition process. The MFIS capacitors with and without an Al_2O_3 insulating layer were fabricated, and their electrical properties, such as polarization, transfer characteristics, endurance, and interface trap density were compared. As one of the advantages using the ultra-thin Al_2O_3 layer, the interface state generation by voltage pulse cycling was largely suppressed (Fig. 1).

[1] K. Ni *et al.*, IEEE Trans. Electron Devices **65**, 2461 (2018).

[2] T. Ali *et al.*, IEEE Trans. Electron Devices **65**, 3769 (2018).

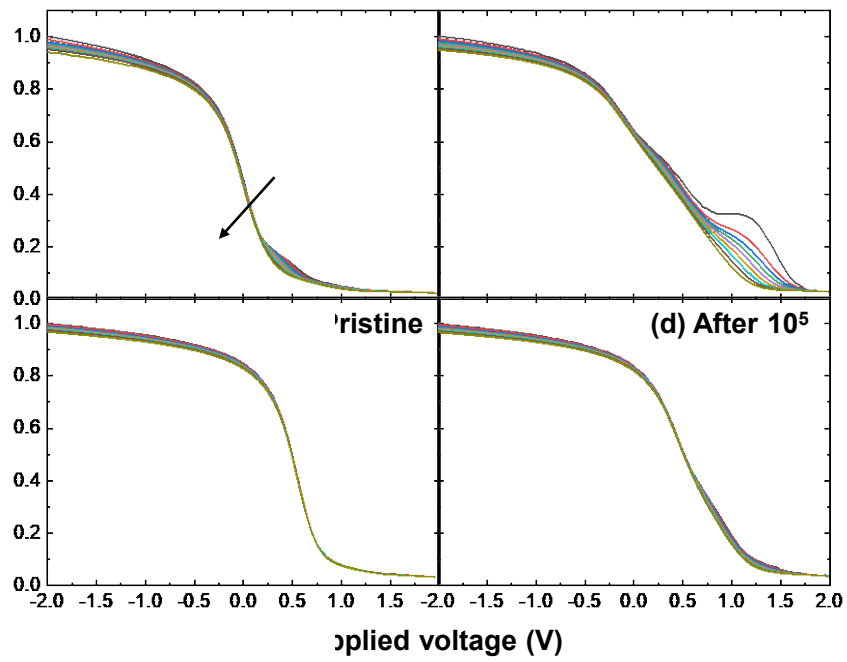[3] W. Xiao *et al.*, Nanoscale Res. Lett. **14**, 254 (2019).

Fig. 1. Multi-frequency C–V characteristics of HZO capacitors (a, b) without and (c, d) with an Al_2O_3 interface layer for varying numbers of voltage pulse cycling.

Ferroelectric Microelectronic Devices Utilizing NbN and Nb Electrodes with Thin Film Ferroelectric (Hf,Zr)O$_2$

<u>M. David Henry</u>[1], Shelby Fields[2], Samantha Jaszewski[2], Giovanni Esteves[1], Travis Young[1], Steve Wolfley[1], and Jon Ihlefeld[2]

[1]*Microsystems Engineering, Science and Applications, Sandia National Laboratories, Albuquerque, New Mexico, 87123, USA*

[2]*Department of Materials Science and Engineering, University of Virginia, Charlottesville, Virginia, 22904*

mdhenry@sandia.gov

Technological advancement of microelectronics utilizing the ferroelectric phase of hafnia (HfO$_2$) and hafnium zirconium oxide (HZO) have renewed interests in ferroelectric nonvolatile memories (NVM) due to its high compatibility with CMOS technologies. Well past the thickness scaling limitations of PZT, this ferroelectric has demonstrated stability down to just a few nanometers in thickness offering increased integration potential and new device architectures. The material science of the metastable orthorhombic (o) and tetragonal (t) phases has been widely scrutinized and studied with questions about how to take the amorphous atomic layer deposited film and encourage the o-phase to emerge over that of the equilibrium monoclinic (m) phase. High o/t phase volume fractions have been observed to have higher remanent polarizations (Pr) and increased lifetime. Much of the recent progress has centered around oxygen vacancies and their movement through the oxide and interactions with the electrode interface. Device design, including deposition conditions and annealing parameters, are critical to the integration and stabilization of hafnia, but extend to factors extrinsic to hafnia, including the metal electrodes and linear dielectrics surrounding the film. Past work has demonstrated that hafnia can achieve high fractions of the o/t phase on TiN, Pt, TaN, Ta, RuO$_2$ and W, each with its own interactions and vacancy forming potentials. These interactions can be modulated with surface oxides, chemical interface interactions, and presence of the electrode. Extraction of the film ferroelectric behavior can be observed by electrical interrogation of these fabricated devices. This work details our efforts to investigate ferroelectric HZO with on NbN and Nb as viable electrodes for microelectronic ferroelectric memory. We first demonstrate stabilization of HZO on Nb and NbN symmetric electrodes with 20 nm thick HZO and thin alumina over the bottom electrode. For these metal-ferroelectric-metal (MFM) devices we note maximum $2P_r$ of 36 and 28 $\square$C/cm^2 respectively with P_r reduction consistent with expected depolarization fields from the linear dielectric layer thicknesses. Establishment of the ferroelectric phase, as noted by the P_r, is observed to be strongly dependent on the cycling voltage for each alumina barrier thicknesses. Other parameters for the MFM devices, including current leakage and memory retention times, will be discussed. We then investigate efforts to establish thinner ferroelectric barriers with our development of ferroelectric tunnel junctions (FTJ) composed of thin HfO$_2$ and HZO films at 4 nm on antisymmetric electrodes of NbN as the bottom electrode and Nb as the top electrode.

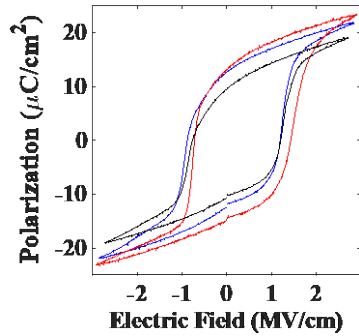For very thin films ON:OFF ratios of 3 and 5 for the HfO_2 and HZO films, respectively, are observed.

Fig.1: Stabilization of ferroelectric $Hf_{0.5}Zr_{0.5}O_2$ on symmetric NbN electrodes with 0.5 (red), 1.0 (blue), 2.0 (black) nm alumina over the bottom electrode after 190 cycles of 5V. Reduction of P_r for the 2 nm alumina is due to the retarding potential of the linear dielectric.

Fig.2: Stabilization of ferroelectric $Hf_{0.5}Zr_{0.5}O_2$ on symmetric Nb electrodes with 0.5 (red), 1.0 (blue), 2.0 (black) nm alumina over the bottom electrode after 190 cycles of 4V. Reduction of P_r for the 2 nm alumina is due to the retarding potential of the linear dielectric.
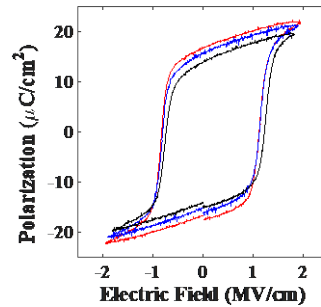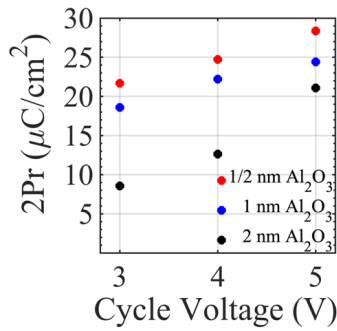

Fig.3: Remanent polarization dependance on the cycling voltage is noted after 500 cycles of wake up for each of the alumina barrier thicknesses for the $NbN/Al_2O_3/Hf_{0.5}Zr_{0.5}O_2/NbN$ FeRAM devices.
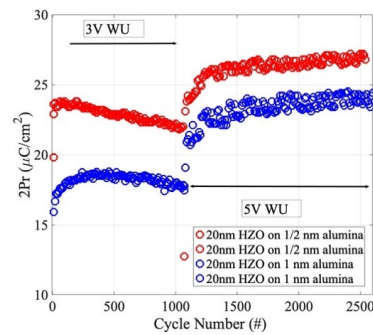
Fig.4: Remanent polarization dependance on the cycling voltage is observed. After lower voltages wake the devices up, a higher cycling voltage recovers higher polarization for the FeRAM devices.
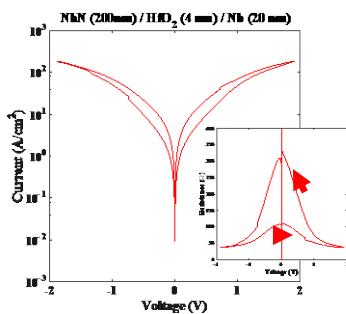

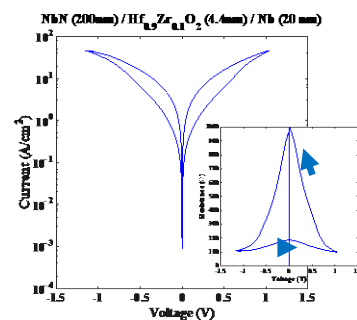Fig.5: FTJ I-V characteristics of a $NbN/HfO_2/Nb$ device with resistance performance inset. OFF/ON ratio of ~3.

Fig.6 FTJ I-V characteristics of a $NbN/Hf_{0.9}Zr_{0.1}O_2/Nb$ device, with resistance performance inset. OFF/ON ratio of ~5.2.

Internal Photoemission (IPE) Spectroscopy Measurement of Electrode Energy Barriers in Pristine, Woken, and Poled Ferroelectric HZO Devices

J. Peterson,[1] T. Mimura,[2] Jon Ihlefeld,[2] and J.F. Conley, Jr. [1,*]

[1]School of EECS, Oregon State University, Corvallis, OR, 97331

[2]Depts. of MSE and ECE, University of Virginia, Charlottesville, Virginia 22904

*jconley@eecs.oregonstate.edu

Ferroelectric $Hf_{0.5}Zr_{0.5}O_2$ (HZO) has attracted interest for CMOS memory and logic due to due to the current widespread use of HfO_2 and potential ease of integration. Optimal use of HZO in these applications requires knowledge of the interfacial energy barriers with the electrodes in the specific device structure used. Internal photoemission (IPE) spectroscopy is the only method of measuring barrier heights "in-situ" in working devices. IPE measurements of energy barriers have been reported recently for pristine HZO with various electrodes.[1] However, a "waking" process entailing repeatedly sweeping a field across the device is required to induce strong ferroelectric behavior in HZO.[2] Here we investigate the impact of waking and poling on barriers in operating ferroelectric MIM capacitors.

20 nm thick HZO films were deposited on a TaN coated Si substrates via atomic layer deposition (ALD) using 102 supercycles of HfO_2 and ZrO_2. After coating with 20 nm of TaN, the stack was annealed at 600°C for 30 seconds. This top TaN layer was then stripped and an optically transparent top electrode of 5 nm TaN / 5 nm Pd was deposited. TaN/HZO/TaN devices were woken by performing 5000 $\pm$5V cycles at 1 kHz (Fig. 1). Woken devices were poled by applying a 0 to +4 V or 0 to -4 V square pulses. IPE measurements were taken by applying voltage to the bottom electrode while grounding the top and then simultaneously sweeping incident photon energy from 2 to 5 eV. Positive (negative) polarity was used to assess the top (bottom) barrier. Extracted spectral thresholds were plotted vs. square root electric field and extrapolated to zero to account for any Schottky field induced barrier lowering.

For unwoken devices, the top and bottom HZO/TaN barriers were 2.6 and 2.9 eV, respectively, indicating the influence of processing (Fig. 2). After waking, the top barrier was increased to 2.9 eV while the bottom barrier was unchanged (Fig. 3). Poling caused a roughly 0.7 eV reduction in both electrode barriers, independent of polarity. The reduced barrier heights are consistent with a report on the impact of voltage cycling on the effective work function of TiN on HZO, and suggest a role for oxygen vacancies, to be discussed.[3] This work provides important insight into the impact of waking and poling on barriers in ferroelectric HZO devices.

[1]Grimley et al., AEM 2, 1600173, (2016).; [2]Jenkins et al., ACS AMI 13, 14634 (2021).

[3]Hamouda et al., APL 120 202902 (2022).
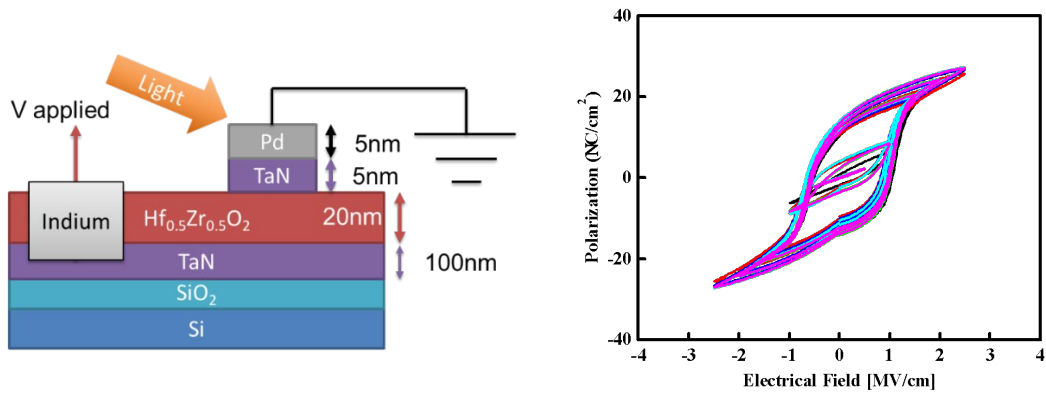
Fig. 1. (a) Schematic cross section of MIM devices used in this work illustrating bias scheme of terminals used for IPE and (b) plot of polarization vs. electric field sweeps illustrating the wake-up process.

Fig. 2. IPE (a) yield plots and (b) Schottky plots for top and bottom electrode barriers of pristine devices for positive and negative sweeps.

Fig. 3. IPE (a) yield plots and (b) Schottky plots for top and bottom electrode barriers of woken devices for positive sweeps.

Si-integrated Ferroelectric Thin Films for Optical Computing

A. A. Demkov, A. B. Posadas and M. Reynaud
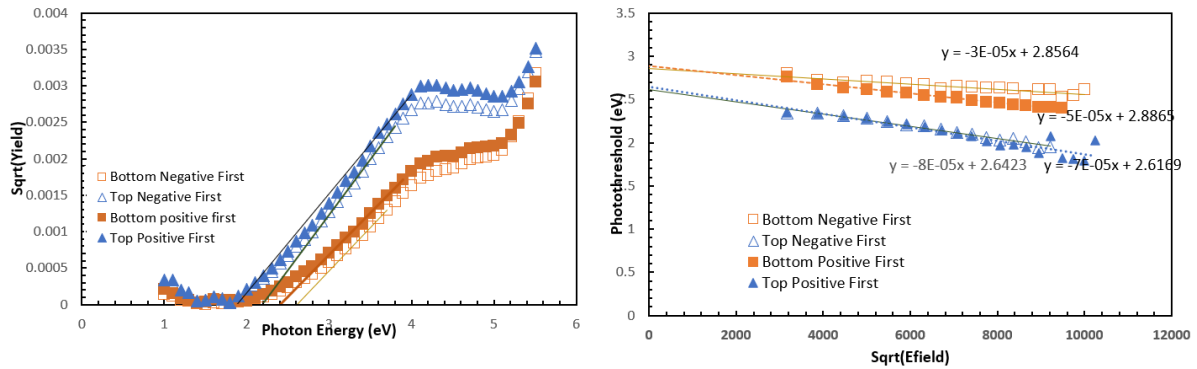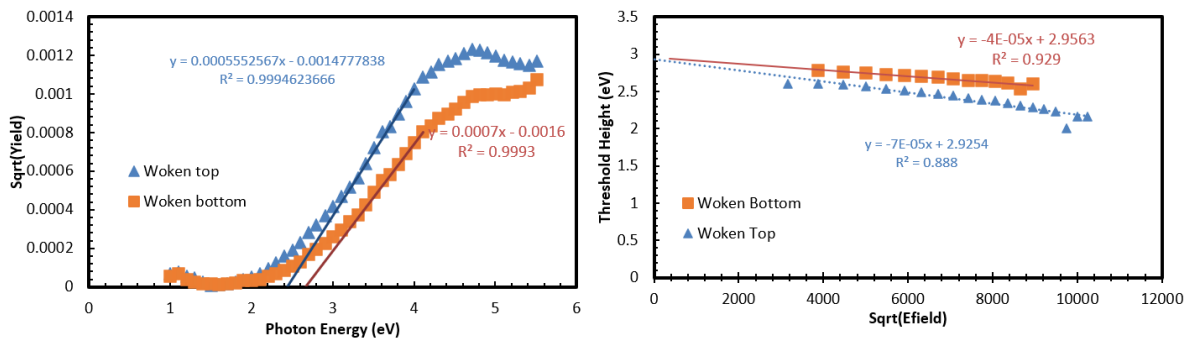
Department of Physics, The University of Texas at Austin, Austin, Texas, 78712, USA

As the von Neumann computer architecture is experiencing difficulties with both scaling and power consumption requirements, new computing paradigms are being actively explored. Even more revolutionary would be a complete or partial switch from electrons to photons. Infrared silicon photonics is one possible avenue for realizing such an alternative computing paradigm [1,2]. This technology will ultimately require integration of active and passive photonic elements on a single chip. One key photonic element is an optical modulator. I will first review the recent progress in integrating ferroelectric $LiNbO_3$ and $BaTiO_3$ with silicon photonics for the purpose of fabricating ultra-small and efficient electro-optic modulators exploiting the linear electro-optic effect [2]. I will focus on the fabrication of thick films of ferroelectric perovskite $BaTiO_3$ capable of providing a robust electro-optic (EO) response via the Pockels effect. While the majority of reports to date discusses the integration of $BaTiO_3$ with silicon using molecular beam epitaxy [3,4], I will talk about our recent success with epitaxial integration of single crystal $BaTiO_3$ with silicon using rf-sputtering (see Figs. 1 and 2). I will discuss the relation of the film microstructure to its EO properties. EO measurements performed in free space as well as using Si waveguides, deposited atop the film, correlate well with the microstructural analysis and demonstrate the potential of Si-integrated $BaTiO_3$ for silicon photonics. In conclusion I will briefly introduce applications of EO modulators based on Si-integrated $BaTiO_3$ in optical neuromorphic computing.

[1] A. A. Demkov, C. Bajaj, J. G. Ekerdt, C. J. Palmström, and S. J. B. Yoo, "Materials for emergent silicon-integrated optical computing," J. Appl. Phys. **130**, 070907 (2021).

[2] A. A. Demkov and A. B. Posadas, "Si-integrated ferroelectrics for photonics and optical computing," MRS Bulletin **47**, 1 (2022).

[3] W. Guo, A. B. Posadas and A. A. Demkov, "The Epitaxial Integration of $BaTiO_3$ on Si for Electro-Optic Applications," J. of Vac. Sci. Technol. A **39**, 030804 (2021).

[4] M. Reynaud, Z. Dong, H. Park, et al., "Microstructural analysis and electro-optic properties of thick epitaxial $BaTiO_3$ films integrated on silicon (001)," Phys. Rev. Materials **6**, 095201 (2022).

[5] A. B. Posadas, H. Park, M. Reynaud, et al., "Thick $BaTiO_3$ epitaxial films integrated on Si by RF sputtering for electro-optic modulators in Si photonics," ACS Appl. Mat. & Interfaces **13**, 51230 (2021).
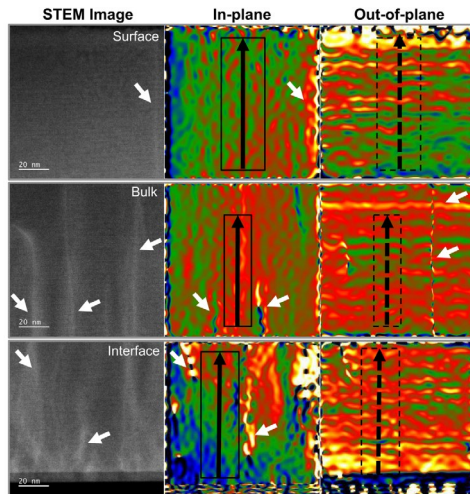
Fig.1: Geometric phase analysis of STEM images of three regions of the film. The top row corresponds to the near surface region; the middle row corresponds to the bulk region; and the bottom row corresponds to the near interface region. The STEM images used are shown in the left column; GPA results for the in-plane strain are shown in the middle column; and GPA results for the out of plane strain are shown in the right column. Dislocations are indicated by white arrows (from Ref. 5).
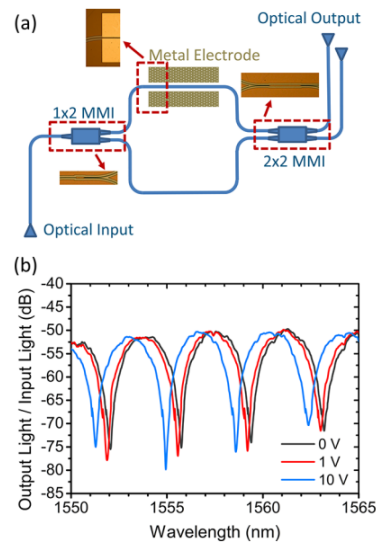
Fig.2: (a) Schematic diagram of the Mach-Zehnder Modulator (MZM), with optical microscope images showing 1 × 2 Multimode Interferometer (MMI), 2 × 2 MMI, and a section of the active region with electrodes. (b) MZM modulation response under various DC voltages (from Ref. 5).

BCl₃ Plasma Treatment of Mos₂ For Atomic-Layer-Deposition of High-K Dielectrics

H. Lee[1], H. Kim[1], K. Kim[1], K. Jeong[2], G. Y. Yeom[1], and H. Kim[1]

[1] *School of Advanced Materials Science & Engineering, Sungkyunkwan University, Suwon 16419, Republic of Korea*

[2] *Division of Physics and Semiconductor Science,, Dongguk University, Seoul 04620, Republic of Korea*

hsubkim@skku.edu

As the scaling of Si-based logic devices continues, two-dimensional (2D) transition metal dichalcogenide semiconductors with excellent carrier mobility even at sub-nanometer thicknesses have been considered as novel channel material candidates for next-generation gate-all-around field-effect transistors [1]. However, it is difficult to form a uniform dielectric film on the surface of a 2D material using an atomic layer deposition (ALD) process [2]. Therefore, it is essential to develop a surface treatment capable of forming reactive sites in all directions on the 2D materials. Although various surface treatments, such as UV-ozone and seed layer insertion [3, 4], have been reported, studies on the surface treatment applicable to three-dimensional (3D) structures are very scarce.

This presentation introduces a BCl₃ remote plasma treatment, which enables the formation of reactive sites on the MoS₂ surface for the facile subsequent growth of high-k dielectrics via ALD. The surface coverage improvement of ALD dielectrics was confirmed by SEM and AFM measurements, and the absence of physical damages to MoS₂ was demonstrated through electrical measurements of bottom-gate field-effect transistors (FETs) with monolayer MoS₂. To confirm the applicability of BCl₃ remote plasma treatment for the top-gate FETs, an ALD-Al₂O₃ gate dielectric was deposited on the pretreated thick MoS₂ flakes and the electrical properties of the fabricated devices were characterized. In addition, the feasibility of uniform treatment on the 3D structure was demonstrated by depositing ALD-Al₂O₃ films on the MoS₂ bridge structure floating on the substrate.

[1] D. Akinwande *et al*., Nature **573**, 507 (2019).

[2] S. McDonnell *et al*., ACS Nano. **7**,11, 10354 (2013).

[3] A. Azcatl *et al*., Appl. Phys. Lett. **104**, 111601 (2014).

[4] S. Son *et al*., Appl. Phys. Lett. **106**, 021601 (2015).

Graphene Bioimpedance Tattoos for Blood Pressure Monitoring

Deji Akinwande[1], Dmitry Kireev[1], Kaan Sel[2], Bassem Ibrahim[2], Roozbeh Jafari[2]

[1]The University of Texas at Austin, TX, USA
[2]Texas A&M University, College Station, TX USA
dejii@ece.utexas.edu

Monitoring complex health-related electrophysiological signals such as arterial blood pressure (BP) in ambulatory settings is essential for a proper understanding of health conditions, predominantly cardiovascular diseases [1]. Moreover, continuous long-term monitoring of BP for patients with sleep apnea, stroke, or hypertension is essential to understand their health risk factors and build preventative care routines. While conventional ambulatory BP monitoring devices exist, they are uncomfortable, bulky, and intrusive. The common drawbacks of all these systems are their bulkiness and incompatibility with skin's elastic properties, causing sensor's displacement during usage, consequently requiring frequent system re-calibration.

Here, we present a unique wearable BP monitoring platform that leverages imperceptible atomically-thin and electrically conductive graphene electronic tattoos (GETs) as the main building block [2]-[4]. The GETs are placed over the radial and ulnar arteries on the wrist and subsequently used as current injection and voltage sensing electrodes, measuring arterial bioimpedance. In contrast to any other wearable system, the atomically thin, lightweight, and skin-conformable GETs do not apply any external tension onto the skin during the operation, and able to perform long-term and nocturnal measurements without discomforting the subjects. Using bioimpedance modality allows us to disregard the tattoo-skin interface, which is typically 2-4 orders of magnitude larger compared to tissue impedance, and record only from the areas of interest. Employing a machine learning regression model on the recorded bioimpedance value, we yield effective beat-to-beat detection of diastolic and systolic BP values with IEEE grade-A accuracy. Besides BP, we show that the same Bio-Z signal can be post-processed to estimate person's RR in an entirely wearable and non-invasive manner.

[1] D. Kireev, K. Sel, B. Ibrahim, N. Kumar, A. Akbari, R. Jafari, and D. Akinwande, "Continuous cuffless monitoring of arterial blood pressure via graphene bioimpedance tattoos," Nature Nanotechnology, 2022.

[2] D. Kireev, E. Okogbue, R. T. Jayanth, T.-J. Ko, Y. Jung, and D. Akinwande, "Multipurpose and Reusable Ultrathin Electronic Tattoos Based on PtSe2 and PtTe2," ACS Nano, 2021.

[3] D. Kireev, S. K. Ameri, A. Nederveld, J. Kampfe, H. Jang, N. Lu, and D. Akinwande, "Fabrication, characterization and applications of graphene electronic tattoos," Nature Protocols, vol. 16, 2021.

[4] S. Kabiri Ameri, R. Ho, H. Jang, L. Tao, Y. Wang, L. Wang, D. M. Schnyer, D. Akinwande, and N. Lu, "Graphene Electronic Tattoo Sensors," ACS Nano, vol. 11, 2017.

Fig. 1: Illustration of blood pressure wave and monitoring with wearable graphene tattoo electrodes.

Effective Voltage Control of Two-Dimensional Magnetic Insulator

S. Liang and C. Gong

Department of Electrical and Computer Engineering and Quantum Technology Center,
University of Maryland, College Park, MD 20742, USA
gongc@umd.edu (e-mail address of the corresponding author)

Magnetic insulators (MI), possessing long-range magnetic order while being electrically insulating, allow spin propagation without electrons' motion and thus promise a unique paradigm of next-generation dissipationless magnetoelectric and magneto-optical devices. While two-dimensional (2D) MIs [1] usher the prospects into the atomic-thin region, efficient electrical control as an essential prerequisite for practical devices remains elusive; fundamental obstacles arise from the difficulty of electrostatically doping insulators and the inability of external electric fields to effectively modify materials' crystal fields [2]. Here, by constructing a heterostructure consisting of functional thin film and a 2D magnetic insulator, we achieved a strong and reversible electrical control of magnetism. The wavefunction overlap at the heterostructure interface differs greatly under opposite voltages applied, leading to effective control of the coercivities in magnetic hysteresis loops of the 2D magnets. The layered dependence study confirmed that this effective control occurs exclusively for 2D magnets instead of the bulk counterpart, owing to the electrically controllable interfacial wavefunction overlap that could effectively alter the interfacial crystal field. Our work opens up new avenues to usher 2D MIs towards future nanoscale spintronic, magnonic, and magneto-optical applications.

1. Gong, C. *et al.*, *Nature* **546**, 265–269 (2017).
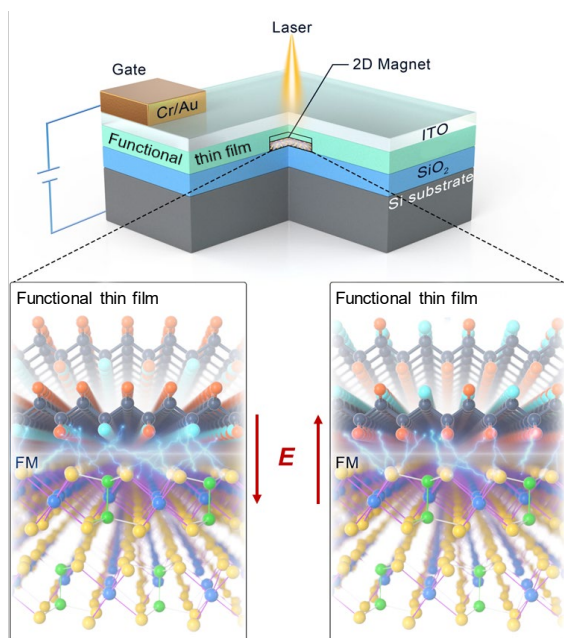2. Gong, C. *et al.*, *Nat. Commun.* **10**, 2657 (2019).

Fig.1: Device schematic and side view of the magnetoelectric interfacial coupling between the functional thin film and 2D ferromagnet (FM) under opposite voltages applied.
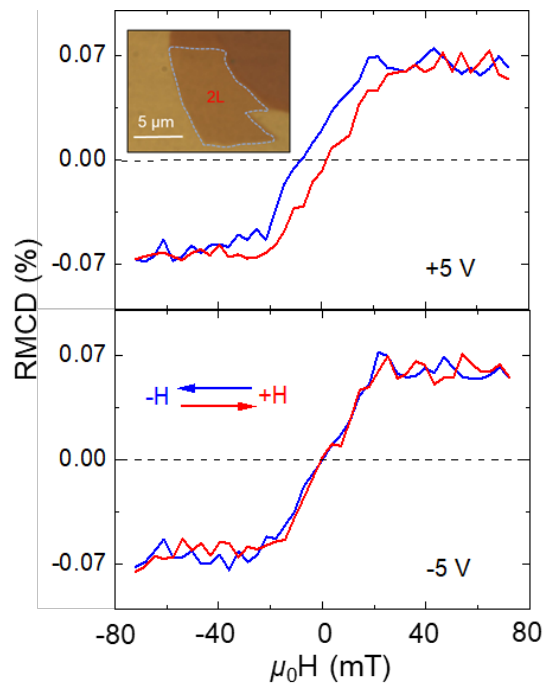

Fig.2: Voltage control of the magnetism of the 2D magnet in the heterostructure.

Hexcitons and Oxcitons in Monolayer WSe$_2$

Hanan Dery and Dinh Van Tuan

Department of Electrical and Computer Engineering, University of Rochester, Rochester, New York 14627, USA

hanan.dery@rochester.edu

Hydrogen-like bound states of photoexcited electron-hole pairs in semiconductors -- that is, excitons -- have been a focus of considerable study for more than half a century. In undoped direct-gap semiconductors, neutral excitons comprise the photogenerated electron and hole in the conduction and valence bands (CB and VB), respectively, and typically manifest as discrete optical resonances below the free-particle band-gap energy. More interesting states arise when electron-hole (*e-h*) pairs are photoexcited into doped semiconductors containing a Fermi-sea of mobile carriers.

In the archetypal monolayer semiconductor WSe$_2$, the distinct ordering of spin-polarized valleys (low-energy pockets) in the CB allows for studies of not only simple neutral excitons and charged excitons (i.e., trions), but also more complex many-body states that are predicted at higher electron densities. We discuss magneto-optical measurements of electron-rich WSe$_2$ monolayers and interpret the spectral lines that emerge at high electron doping as optical transitions of 6-body exciton states ("hexcitons") and 8-body exciton states ("oxcitons"). These many-body states emerge when a photoexcited electron-hole pair interacts simultaneously with multiple Fermi seas, each having distinguishable spin and valley quantum numbers.

I will discuss composite excitonic states in cases that the exciton binding energy of the semiconductor exceeds the Fermi energy. The composite state is made of one or more electron-hole pairs, where the hole of at least one pair is from the VB. Other electron-hole pairs are made of CB holes (missing electron in the Fermi-sea) and electrons with distinct spin-valley configuration. The possible number of pairs in a composite excitonic state is determined by the spin-valley space at the edge of the CB (or VB by reversing the discussion to *p*-type doping).

[1] D. Van Tuan et al., Hexcitons and oxcitons in monolayer WSe$_2$, arXiv:2202.08375.
[2] D. Van Tuan and H. Dery, Composite excitonic states in doped semiconductors, arXiv:2202.08374.
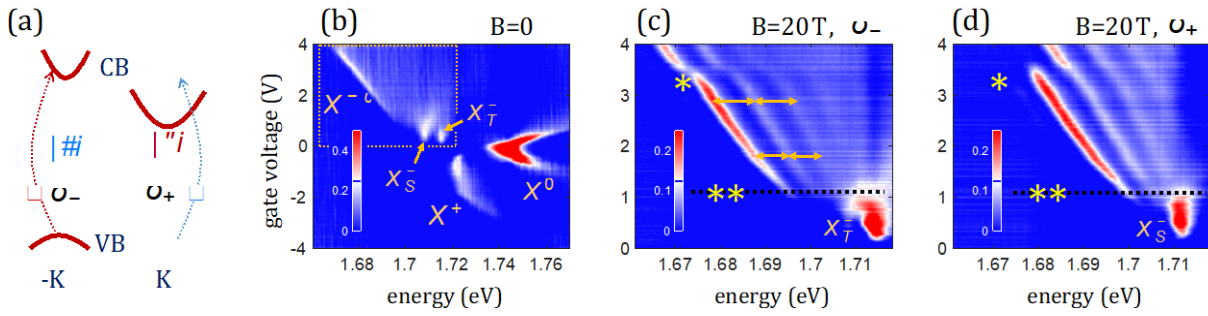
(a) Helicity resolved optical transitions in ML-WSe₂. Light excitation with right-handed (left-handed) helicity corresponds to optical transitions at the K (-K) valley. Resident electrons occupy the bottommost valleys, whereas photoexcited electrons belong in the top valleys. (b) Optical reflectance spectra at 4K as a function of gate voltage and photon energy. (c) and (d) Helicity resolved magneto-optical reflectance spectra when the out-of-plane magnetic field is 20T, shown in the spectral and voltage windows that are marked by the dotted box in (b).
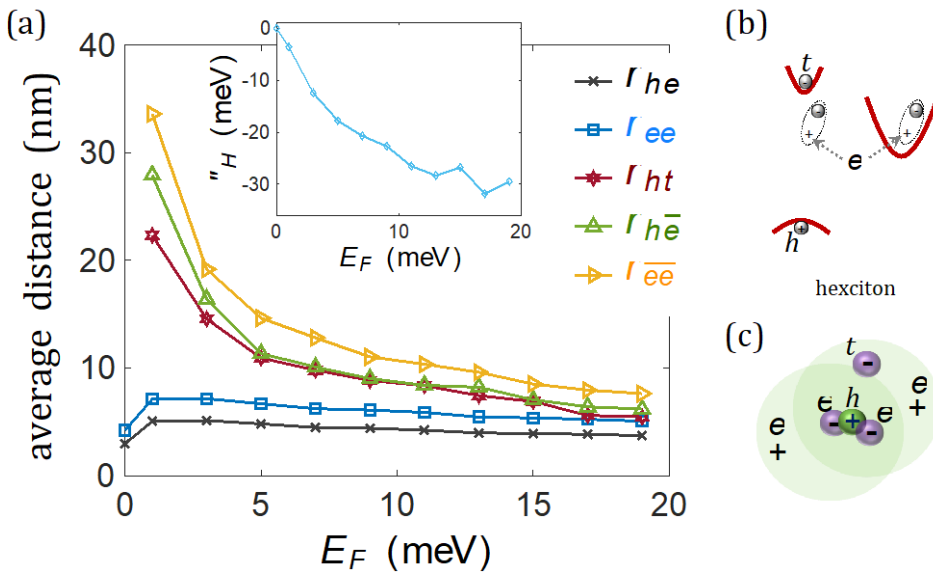

Fig. 1. (a) Calculated inter-particle distances in the hexciton as a function of the Fermi energy ($E_F \sim$ 5meV amounts to $n = 10^{12}$ cm⁻²). The Hexciton corresponds to the resonance X-' in Figure 1. Results are shown for average distances between the CB electron and VB hole (r_{he}), between the two CB electrons of the core trion (r_{ee}), between the VB hole and the outer top-valley electron (r_{ht}) or CB holes ($r_{h\bar{e}}$), and between the CB holes ($r_{\bar{e}\bar{e}}$). Inset: Calculated binding energy of the satellite electron to the hexciton. (b) and (c) Schemes of the hexciton in k-space and real-space, respectively. The trion at the core of the hexciton binds to two CB holes and a satellite electron.

Growth of Single-Crystal Hexagonal Boron Nitride by Chemical Vapor Deposition

Hyeon Suk Shin

Department of Chemistry, Ulsan National Institute of Science and Technology (UNIST), Ulsan 44919, Republic of Korea

shin@unist.ac.kr

Large-area single-crystal monolayers of two dimensional (2D) materials such as graphene, hexagonal boron nitride (hBN) and transition metal dichalcogenides have been successfully grown. Among them, hBN has been demonstrated to be the "ideal" dielectric substrate for 2D materials-based field effect transistors (FETs). Although hBN thicker than a monolayer is more desirable as substrate for 2D semiconductors, the growth of highly uniform and single-crystal few- or multi-layer hBN has not yet been demonstrated. Here we report the epitaxial growth of wafer-scale single-crystal tri-layer hBN by a chemical vapour deposition method. Uniformly aligned tri-layer hBN islands are found to grow on a 2 cm × 5 cm single-crystal Ni (111) at early stage of growth and finally to coalesce into a single-crystal film [1]. Cross-sectional transmission electron microscopy (TEM) results show that a $Ni_{23}B_6$ interlayer is formed (during cooling) between the single-crystal tri-layer hBN film and Ni (111) substrate by boron dissolved in Ni (111) and that there is epitaxial relationship between tri-layer hBN and $Ni_{23}B_6$ and between $Ni_{23}B_6$ and Ni (111). We further find that the tri-layer hBN film acts as a protective layer that remains intact during catalytic evolution of hydrogen – suggesting continuous and uniform single-crystal tri-layer hBN in large area. This tri-layer hBN transferred onto the SiO_2 (300 nm)/Si wafer acts as a dielectric layer to reduce electron doping from the SiO_2 substrate in MoS_2 FETs. Our results demonstrate that it is possible to achieve high quality multi-layered hBN over large areas by CVD – opening up new pathways for making it a ubiquitous substrate for 2D semiconductors and other purposes.

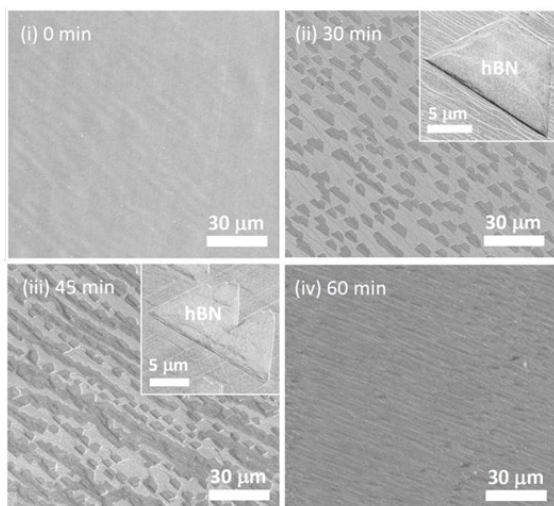*[1] K. Y. Ma et al., Nature. **606**, 88 (2022).*

Fig.1: SEM images showing the time evolution of tri-layer hBN on a Ni (111) foil surface at 1220 ºC. Insets show two different high-magnification SEM images each showing hBN islands. In the first, a single hBN island is parallel to the surface steps. The second shows two hBN islands that have joined along one edge.
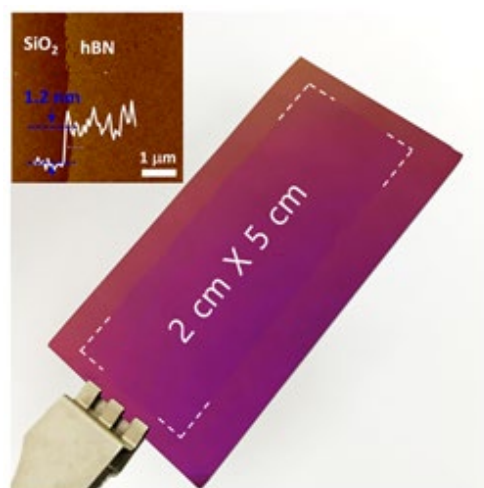

Fig.2: Photograph of 2 cm × 5 cm hBN film transferred onto the SiO₂ (300 nm)/Si substrate. Inset shows an AFM image of an edge of the hBN film transferred onto the SiO₂ (300 nm)/Si substrate. The average thickness at 24 positions (in the film edges) is 1.27 ± 0.06 nm.
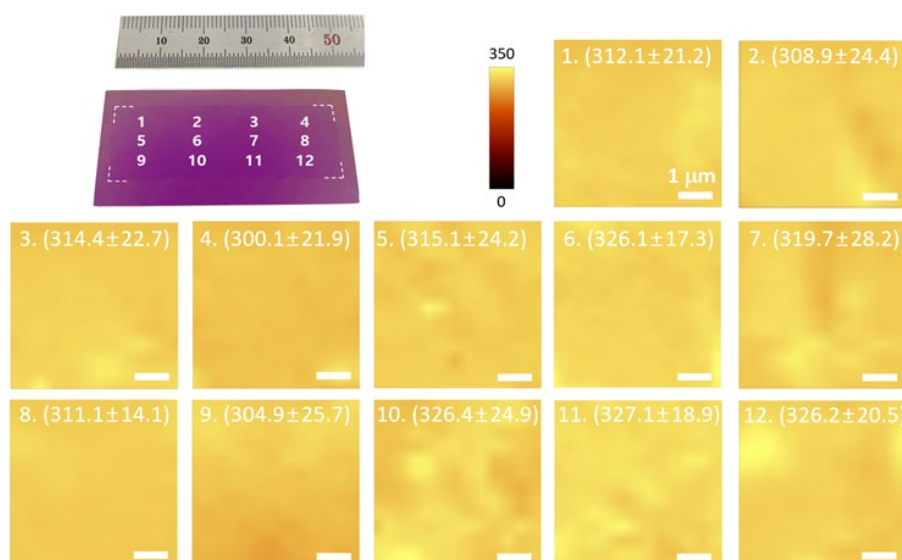

Fig.3: Raman mapping images of normalized E_{2g} intensity at the 12 marked positions on the tri-layer hBN film on SiO₂ (300 nm)/Si. The mapped area at each position is 5 mm x 5 mm. Average intensities in each image are marked in the mapping images. The mean and standard deviation of Raman intensity is 314.4±23.5.
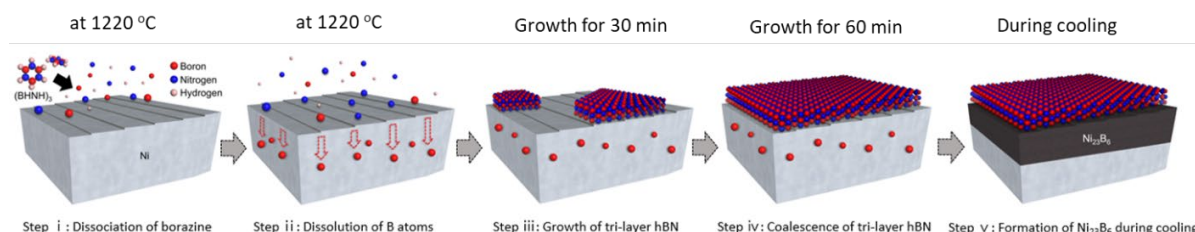

Fig.4: Schematic illustration of the proposed growth pathway of tri-layer hBN film on Ni (111) and the subsequent appearance of $Ni_{23}B_6$ at the Ni (111)/hBN interface. The final structure from top to bottom is tri-layer hBN/$Ni_{23}B_6$/Ni (111). The tri-layer hBN/$Ni_{23}B_6$ and $Ni_{23}B_6$/Ni (111) layers show epitaxial relationship, respectively.

Phonon Limited Mobility and Phonon Drag in H-BN Encapsulated Monolayer and AB-Stacked Bilayer Graphene

Vasili Perebeinos[1]

[1]*Department of Electrical Engineering, University at Buffalo, The State University of New York, Buffalo, New York 14260, USA.*

vasilipe@buffalo.edu (e-mail address of the corresponding author)

We report the electrical transport in h-BN encapsulated AB-stacked bilayer graphene theoretically and experimentally. Using the perturbation theory within the tight-binding model approach, we identify the dominant role of the shear phonon mode scattering on the carrier mobility in AB-stacked graphene bilayer at room temperature, as shown in Fig. 1. The shear phonon mode is absent in free-standing monolayer graphene, which explains high mobilities in monolayer devices fabricated under similar conditions resulting in minimal Coulomb impurity scattering. At temperatures above 200 K, the surface polar phonon scattering from the boron-nitride substrate contributes significantly to the experimental mobilities of 15,000 -20,000 cm^2/Vs at room temperature and carrier concentration n~10^{12} cm^2 reported here. A screened Surface Polar Phonon (SPP) potential for a dual gated bilayer and transferable tight-binding model allows us to predict mobility scaling with temperature and bandgap for both electrons and holes in agreement with the experiment [1].

The resulting electron-SPP coupling is used to predict that, by exploiting the strong coupling of their electrons to surface polar phonons, van der Waals heterostructures can offer a suitable platform for phonon sensing, capable of resolving energy transfer at the single-phonon level. The geometry we consider is one in which a drag momentum is exerted on electrons in a graphene layer, by a single out-of-equilibrium phonon in a dielectric layer of hexagonal boron nitride, giving rise to a measurable induced voltage. Our numerical solution of the Boltzmann Transport Equation in Fig. 2 shows that this drag voltage can reach a level of a few hundred microvolts per phonon, well above experimental detection limits. Furthermore, we predict that drag voltage should be largely insensitive to the mobility of carriers in the graphene layer and increase the temperature up to at least 300 K, offering the potential of a versatile material platform for single-phonon sensing.

[1] C. Tan, D. Adinehloo, J. Hone, and V. Perebeinos, Phys Rev. Lett. **128**, 206602 (2022).
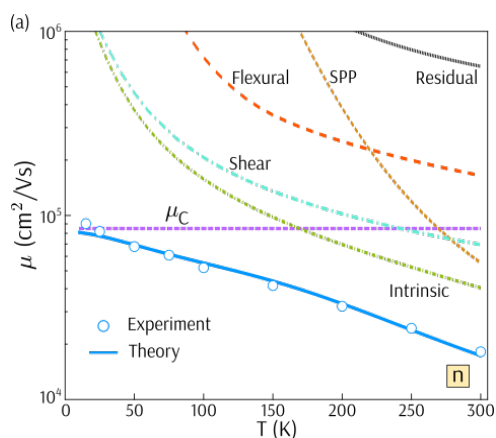
Fig. 1. Experimental and theoretical temperature dependence of mobility in bilayer graphene (blue) and calculated contributions due to different vibrational modes: intrinsic and extrinsic SPP in h-BN substrate [1].
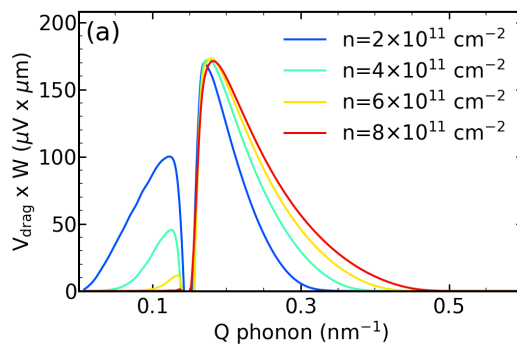

Fig. 2. Phonon drag voltage times width of graphene monolayer as a function of the h-BN SPP wavevector, and for various carrier densities shown in the legend. The calculations assume T=50 K and infinitely thick h-BN substrate.

Mobility-fluctuations Mechanism of 1/f Noise in Graphene

S. Rumyantsev[1], A. Rehman[1], J. A. D. Notario[1], J. S. Sanchez[2], Y. M. Meziani[2], G. Cywiński[1], W. Knap[1], A. A. Balandin[3]

[1]*CENTERA Labs, Institute of High Pressure Physics, PAS, Warsaw, Poland*
[2]*Nanotechnology Group, Universidad de Salamanca, Salamanca, Spain*
[3]*Nano-Device Laboratory, University of California, Riverside, California, USA*
e-mail: roumis4@gmail.com

Although the history of the 1/f noise research goes back almost a century, the answers to even fundamental questions are still being discussed (f is the frequency). Among them is the fundamental question of whether the mobility or the number-of-carriers fluctuations cause the resistance fluctuations with the 1/f spectrum. Here, we report results of our experimental investigation of 1/f noise in graphene field-effect transistors under condition of geometrical magnetoresistance. In the sample geometry with a length (L) much smaller than its width (W), the magnetic field perpendicular to the electrical field causes the well-known effect of geometrical magnetoresistance. The resistivity and its fluctuations under the assumption of the mobility fluctuations are given by [1]:

$$\rho_{\mathrm{xx}} = \rho_0[(1 + (\mu_0 B)^2], \; \frac{\delta\rho_{\mathrm{xx}}}{\rho_{\mathrm{xx}}} = \frac{\delta\mu_0}{\mu_0}\frac{(\mu_0 B)^2 - 1}{(\mu_0 B)^2 + 1}.$$

As seen, if the 1/f noise is caused by the mobility fluctuations one can expect a strong decrease of the noise at $\mu_0 B \cong 1$. We used high-quality single-layer graphene encapsulated in h-BN to fabricate back-gated FETs with the electron mobility of ~3 m^2/Vs at room temperature. Figures 1 and 2 show the schematic of the h-BN encapsulated transistor and current-voltage characteristics at different temperatures, respectively. To avoid complications due to quantum confinement effects the measurements were performed at T= 100 K - 300 K. Figure 3 shows the current-voltage characteristics at 100 K and 300 K at different magnetic fields. Figure 4 shows examples of the noise spectra and the dependences of noise on the magnetic field at different temperatures. The symbols are the experimental dependences of noise at the frequency of the analysis f = 10 Hz. The continuous solid and dashed-dotted lines represent the results of the calculations assuming the mobility and number-of-carriers fluctuations, respectively. These results prove that the mobility fluctuations are the dominant mechanism of the low-frequency noise in graphene. In conclusion, we succeeded in the first direct experimental demonstration that the mobility fluctuations can indeed cause the 1/f noise in certain materials [2].

[1] M. Levinshtein, S. Rumyantsev, Soviet Physics of Semiconductors, **17**, 1167 (1983).

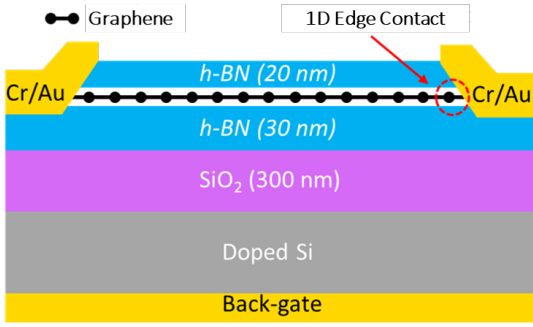[2] A. Rehman, *et al*., Nanoscale, **14**, 7242 (2022).

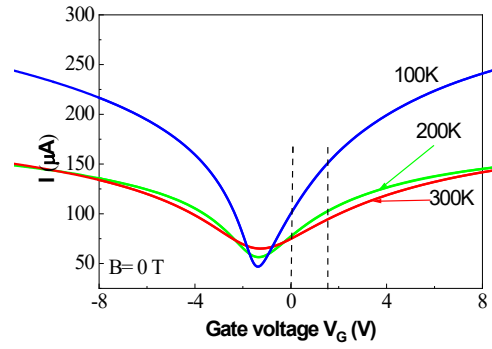*Fig. 1: Schematic of the graphene device design.*

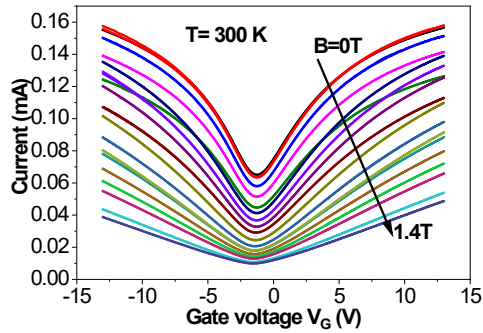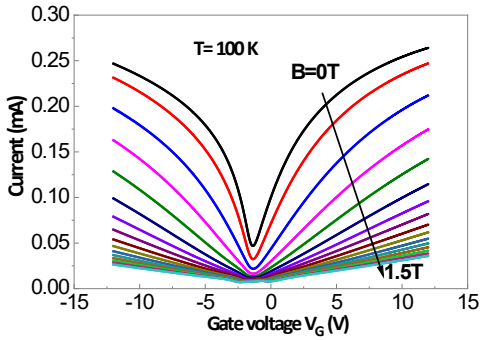*Fig. 2: Current-voltage characteristics at different temperatures.*

Fig. 3: Current-voltage characteristics at different magnetic fields plotted at 100 K (left panel) and 300 K (right panel).
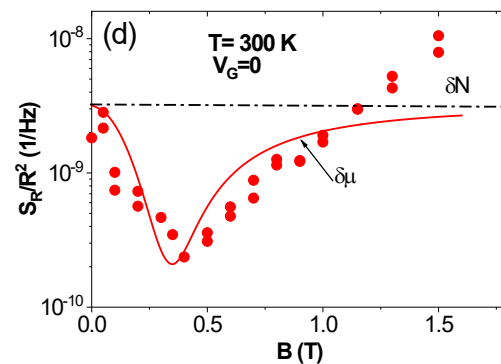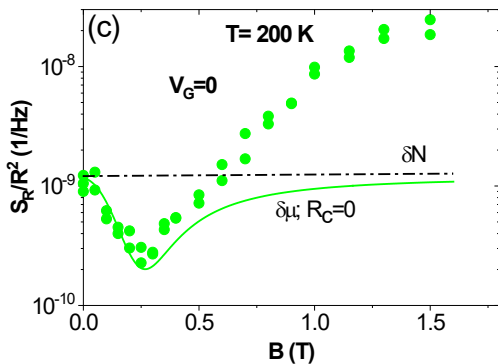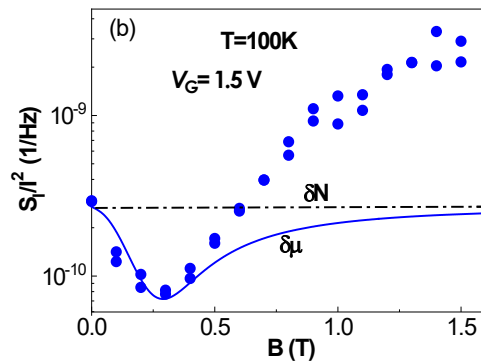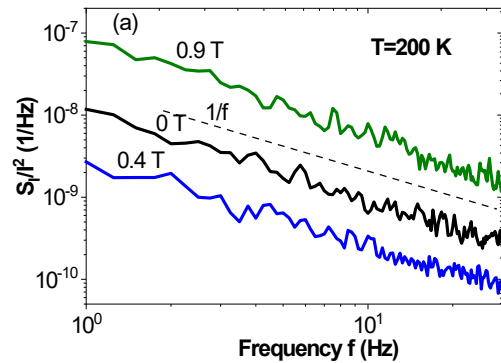

Fig. 4: Example of the noise spectra (a) and relative noise spectral density as a function of the magnetic field at (b) T = 100 K, (c) T = 200 K, and (d) T=300 K under the condition of the geometrical magnetoresistance in FETs with the channel's aspect ratio W/L = 4. The symbols show the experimental results (frequency of analysis f = 10 Hz). The solid lines are the calculations assuming the mobility fluctuations as a source of the 1/f noise. The dash-dotted lines show the hypothetical noise behavior in the cases of the noise due to the fluctuations in the number of carriers.

Quantum Emitters in Hexagonal Boron Nitride

N. Mendelson[1], and I. Aharonovich[2,3]

[1] Pritzker School of Molecular Engineering, University of Chicago, Chicago, Illinois 60637, United States

[2]Faculty School of Mathematical and Physical Sciences, University of Technology Sydney, Ultimo, New South Wales 2007, Australia

[3]ARC Centre of Excellence for Transformative Meta-Optical Systems (TMOS), University of Technology Sydney, Ultimo, New South Wales 2007, Australia

nmendelson@uchicago.edu

Single defects in solids have become some of the most promising frontrunner hardware constituents of applications in quantum information technologies and integrated quantum photonics. A world-wide effort to engineer these systems requires a deep understanding of the structure and underlying level structures of these defects. Knowledge of these details in some systems has led to proof of principle demonstrations ranging from quantum networks to spin-photon interfaces.

Recently, multiple classes of single photon emitters (SPEs) have been identified in hexagonal boron nitride (hBN) and have garnered significant attention due to their superior optical properties[1]. They exhibit remarkable properties: extremely bright emission, a strong response to applied strain and electric fields (Stark shifts), stability under high pressure and elevated temperatures, potential for resonant excitation above cryogenic temperatures, and addressability via spin-selective optical transitions[2].

The talk covers our recent work on single photon emitters in hexagonal boron nitride (hBN), focusing on visible region SPEs and the newly identified negatively charged boron vacancy[3]. Optical and spin properties of different hBN SPEs will be discussed (figure 1), and the current understanding of their chemical identity and relevant level structures are covered highlighting what remains to be investigated. I will discuss our novel methods for hBN SPE fabrication/creation *via* both bottom-up and top down methods as well as the integration of these defects in van der Waals heterostructures and nanophotonic resonators using both hybrid and monolithic approaches (figure 2). A range of emission tuning methods *via* both Stark and strain tuning have been demonstrated, with red and blue shifts up to 65meV as well as changes to other photophysical properties such as the rotation of the optical dipole are observed (figure 3). The role of hBN SPEs in quantum technologies, and the future of the field are mentioned.

[1] S. Castelletto., *et al.,* Beilstein J. Nanotechnol. **11**, 740–769 (2020).

[2] N. Mendelson., *et al.,* Nat. Mater. **20**, 321-328 (2021).

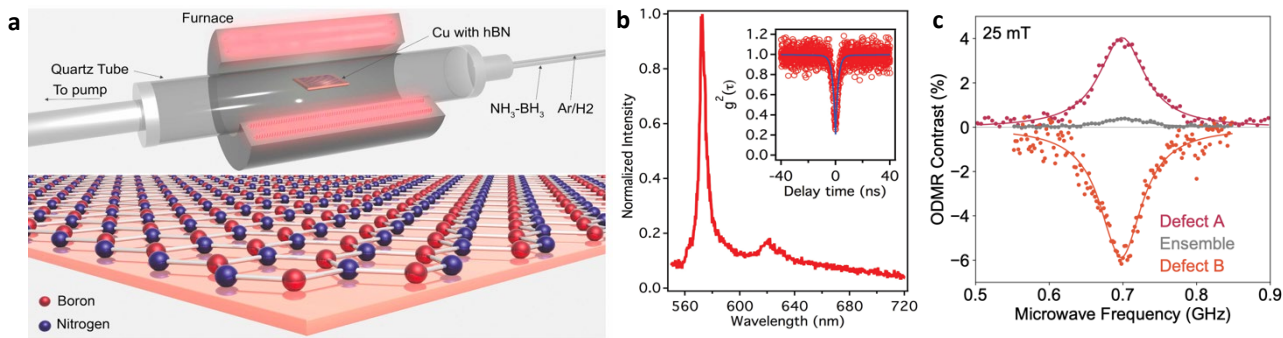[3] A. Gottsscholl., *et al.,* Nat. Mater. **19**, 540-545 (2020).

Fig.1: hBN SPE fabrication, optical, and spin properties. a. Schematic of chemical vapor deposition growth of hBN. b. Typical photoluminescence of hBN SPE, and associated 2nd order autocorrelation. c. Optically detected magnetic resonance spectroscopy on different hBN defects.
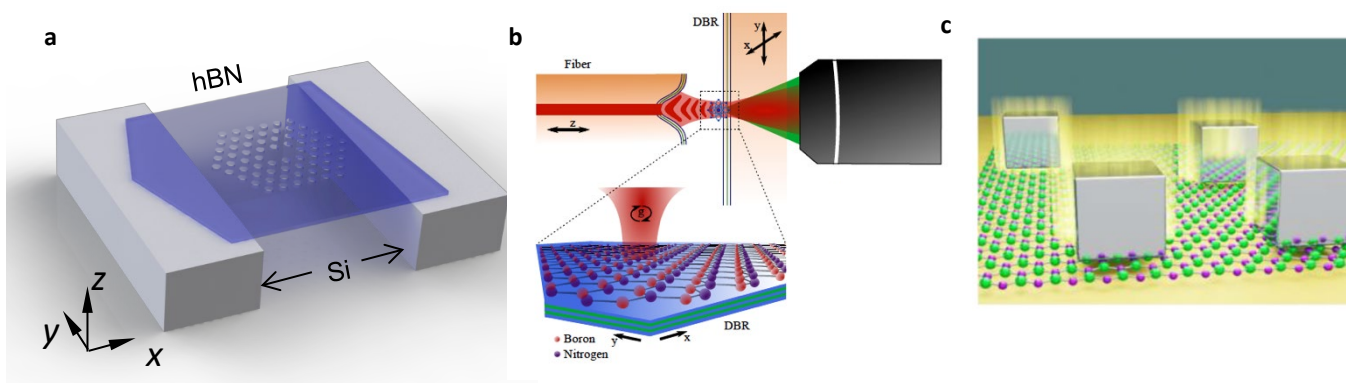

Fig.2: Integration of hBN SPEs with nanophotonic structures. a. Schematic of a 2D suspended hBN photonic crystal cavity. b. Schematic of an hBN thin film integrated with tunable fiber cavity. c. Schematic representation of hBN sandwiched between a plasmonic cavity.
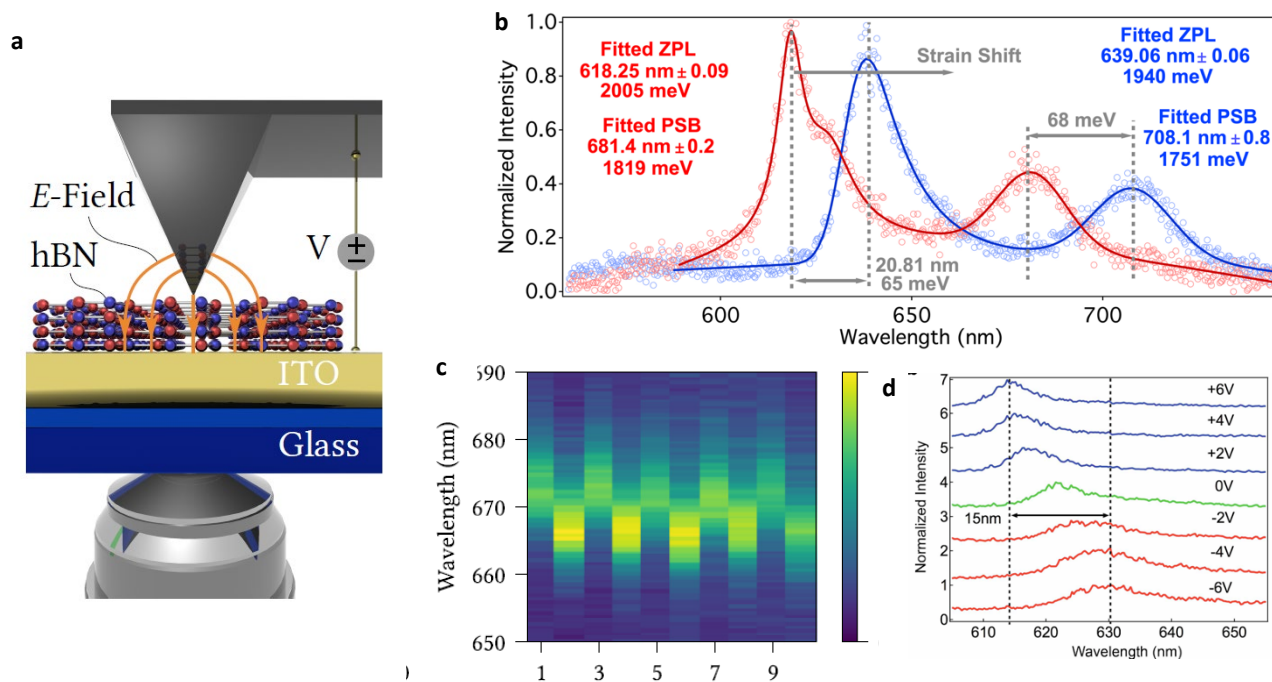

Fig.3: Emission tuning of hBN SPEs. a. Schematic of setup for Stark shift of hBN SPEs. b. Emission tuning via strain engineering. c. Reversible stark shift of a hBN SPE using the setup in a. d. Stark shift of a single SPE at different applied voltages.

Electrical Gating of the Charge-Density-Waves in Two-Dimensional 1T-TaS$_2$ Devices – Prospects of Memory Applications

M. Taheri[1], J. Brown[1], A. Rehman[2], N. R. Sesing[3], F. Kargar[1,4], T. T. Salguero[3], S. Rumyantsev[2], and <u>A. A. Balandin</u>[1,4]

[1]*Nano-Device Laboratory, Department of Electrical and Computer Engineering, Bourns College of Engineering, University of California, Riverside, California 92521 U.S.A.*
[2]*CENTERA Laboratories, Institute of High-Pressure Physics, Polish Academy of Sciences, Warsaw 01-142 Poland*
[3]*Department of Chemistry, University of Georgia, Athens, Georgia 30602 U.S.A.*
[4]*Phonon Optimized Engineered Materials Center, Materials Science and Engineering Program, University of California, Riverside, California 92521 U.S.A.*
Email: balandin@ece.ucr.edu

The charge-density-wave phase is a macroscopic quantum state consisting of a periodic modulation of the electronic charge density accompanied by a periodic distortion of the atomic lattice. Recent years witnessed a rebirth of the charge-density-wave field driven by research on layered quasi-2D van der Waals materials with charge-density-wave phase transitions above room temperature [1]. The work reported to date utilized two-terminal devices without electrical gating. Here, we report on the electrical gating of the charge-density waves and current in three-terminal 1T-TaS$_2$ devices. It is demonstrated that the application of a gate bias can shift the current-voltage hysteresis associated with the transition between the nearly commensurate and incommensurate charge-density-wave phases (see Figures 1 and 2). The evolution of the hysteresis and current, while sweeping the gate voltage, suggests that the effect is electrical rather than self-heating. The transition between the nearly commensurate and incommensurate phases can be induced by both the source-drain current and the electrostatic gate (see Figures 3 and 4). Since the charge-density-wave phases are persistent in 1T-TaS$_2$ at room temperature, one can envision memory applications of such devices when scaled down to the dimensions of individual commensurate domains and few-atomic plane thicknesses.

[1] A. A. Balandin, S. V. Zaitzev-Zotov, and G. Grüner, Appl. Phys. Lett., 119, 170401 (2021).
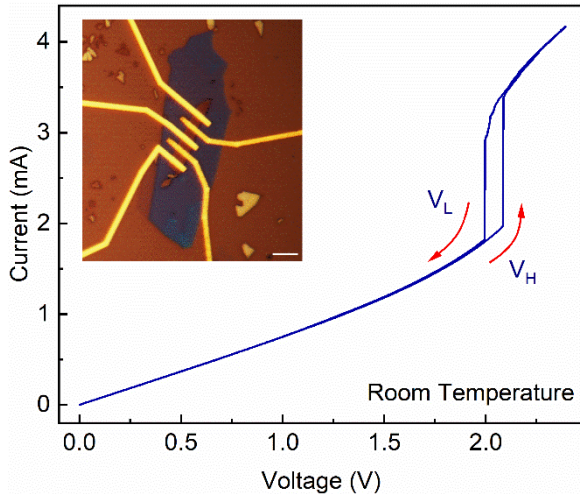
Fig. 1: I-V characteristics of the 1T-TaS$_2$ device, capped with hexagonal boron nitride at room temperature. The hysteresis corresponds to the NC to IC-CDW transition with the threshold voltages of V_H and V_L in the forward and reverse bias sweep, respectively. The inset shows the optical image of a typical 1T-TaS$_2$ device, with channel dimensions of 3μm by 2 μm. The purple strip a is 1T-TaS$_2$ layer with a thickness of ~ ≤ 15 nm and the blue region is the capped thin film of h-BN. The scale bar is 5 μm.
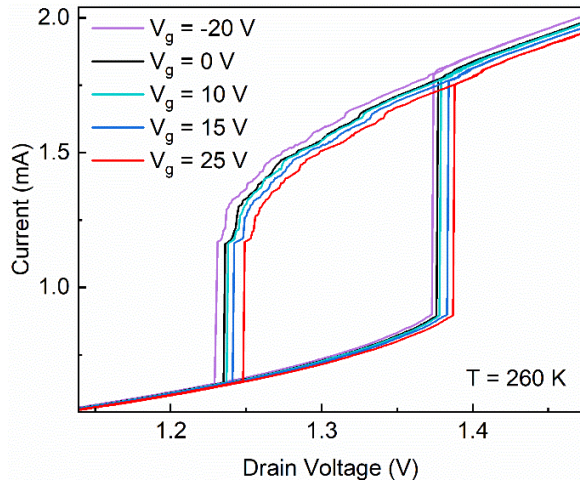
Fig. 2: Hysteresis under the applied back-gate bias, V_g, at T = 260 K for a tested device with a channel length of ~1 μm. The onset of hysteresis, V_H and V_L, shifts non-monotonically with the gate bias. The area of hysteresis remains unchanged suggesting the electrical rather than self-heating process. At T = 260 K, the 1T-TaS$_2$ channel is in the NC-CDW state. The voltage sweeps were performed with sufficient time intervals in between to avoid heat accumulations.
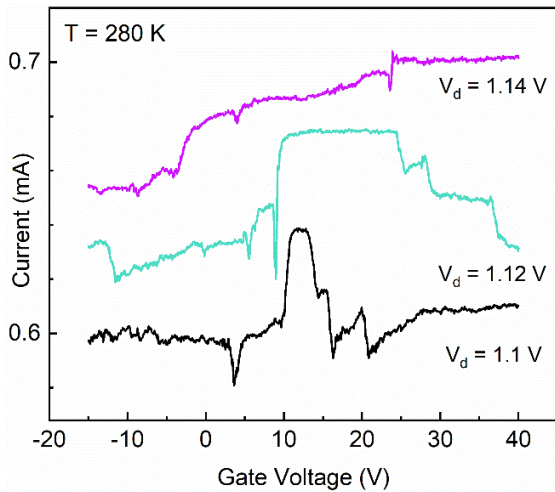
Fig. 3: Current as a function of gate bias for fixed drain voltages, V_d. At T = 280 K, 1T-TaS$_2$ is in the at NC-CDW state. V_d is set to fixed values in the super-linear region close to the V_H and the current is monitored under the continuous gate voltage sweep. The peaks and dips in the current are attributed to the electric field effect on the commensurate domains in the channel.
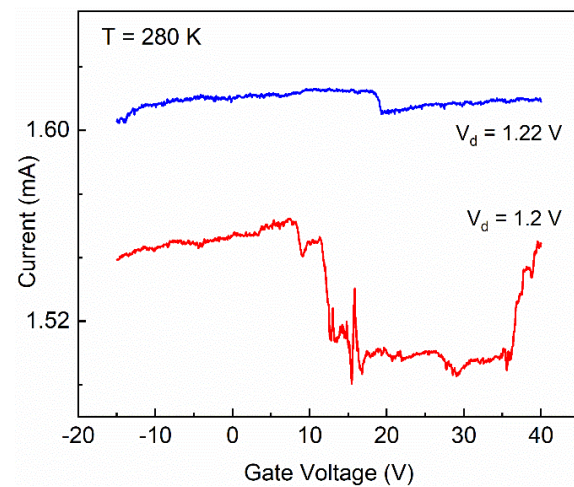
Fig. 4: Current as a function of gate bias for fixed drain voltages, V_d. The 1T-TaS$_2$ channel has entered the IC-CDW state, which can be observed by the level of current fluctuation of ~ 1.52 mA. The largest fluctuation occurs in the vicinity of V_H which indicates the instability of the melted commensurate domains in the proximity of the transition point. The change in the current level is damped down as the channel stabilizes deeper in the metallic IC-CDW state at V_d = 1.22 V.

Emerging Memory Devices from AlScN Ferroelectric

Deep Jariwala[1]

[1]*University of Pennsylvania*

dmj@seas.upenn.edu

Ferroelectric materials have been the subject of continued research interest since their discovery > 100 years ago. The spontaneous electric polarization in these crystals which is non-volatile and programmable is very appealing for a range of information technology, sensing, as well as catalysis applications. Recent discovery of ferroelectricity in Wurtzite structure AlScN has renewed enthusiasm and opened new opportunities for their deployment in commercial scale devices, particularly in microelectronics hardware. This talk will focus on the most recent results on AlScN materials and devices from our lab. I will present our recent work on non-volatile memories based on Ferroelectric Field Effect Transistors (FE-FETs) made using a heterostructure of MoS_2/AlScN[1, 2] and also introduce our work on Ferroelectric Diode devices also based on thin AlScN.[3] I will further present our work on extending these devices into computing circuits and new approaches to in-memory computing hardware.[4] Relevant comparison and contrasts with existing materials will be appropriately made in addition to providing a thorough futuristic roadmap of ferroelectric materials and devices.

[1]. Liu, X.; Wang, D.; Kim, K.-H.; Katti, K.; Zheng, J.; Musavigharavi, P.; Miao, J.; Stach, E. A.; Olsson, R. H.; Jariwala, D., Post-CMOS Compatible Aluminum Scandium Nitride/2D Channel Ferroelectric Field-Effect-Transistor Memory. *Nano Letters* **2021,** *21* (9), 3753-3761.

[2]. Kim, K.-H.; Oh, S.; Fiagbenu, M. M. A.; Zheng, J.; Musavigharavi, P.; Kumar, P.; Trainor, N.; Aljarb, A.; Wan, Y.; Kim, H. M.; Katti, K.; Tang, Z.; Tung, V.; Redwing, J. M.; Stach, E. A.; Olsson III, R.; Jariwala, D., Scalable CMOS-BEOL compatible AlScN/2D Channel FE-FETs. *arXiv preprint arXiv:2201.02153* **2022**.

[3]. Liu, X.; Zheng, J.; Wang, D.; Musavigharavi, P.; Stach, E. A.; Olsson III, R.; Jariwala, D., Aluminum scandium nitride-based metal–ferroelectric–metal diode memory devices with high on/off ratios. *Applied Physics Letters* **2021,** *118* (20), 202901.

[4]. Liu, X.; Ting, J.; He, Y.; Fiagbenu, M. M. A.; Zheng, J.; Wang, D.; Frost, J.; Musavigharavi, P.; Esteves, G.; Kisslinger, K.; Anantharaman, S. B.; Stach, E. A.; Olsson III, R.; Jariwala, D., Reconfigurable Compute-In-Memory on Field-Programmable Ferroelectric Diodes. *Nano Letters* **2022,** *(in press)*.

An Exploration of Liquid Electrolytes to Enable Graphene Electrical Switches with High On-Off Ratios

C. Hayashi[1], C. Aguilar[1], L. Hsu[1], C. Torres Jr[2],
T. Schranghamer[3], A. Dodda[3], S. Das[3], and R. Ordonez[1],
[1]Naval Information Warfare Center Pacific, Pearl City, Hawaii, USA
[2]Naval Information Warfare Center Pacific, San Diego, California, USA
[3]Pennsylvania State University, State College, Pennsylvania, USA
cody.k.hayashi.civ@us.navy.mil

Traditionally, graphene devices have been limited to non-digital applications due to the lack of a bandgap in graphene and minimum conductivity of graphene: $4e^2/h$ [1]. We demonstrated that an electrical voltage can be applied to an electrolyte on graphene to induce electrolysis, electrochemically produce molecular hydrogen, form an electrical double layer on the surface of graphene, and dope graphene with molecular hydrogen to reduce the minimum conductivity significantly below $4e^2/h$ [2]. An electrical voltage of opposite polarity can be applied to the electrolyte to reverse the polarity of the electrical double layer, release dopants on the surface of graphene, and reset graphene back to a semi-metallic state. The fabricated electrochemical device consisting of a commercial honey electrolyte exhibited an on-off ratio $> 10^4$. However, the device failed within ten switching cycles—likely due to the large voltage ($> 5V$) needed to induce the electrochemical reaction and the resulting mechanical perturbations from electrolysis.

We present results of a variety of liquid electrolytes with graphene, including dilute acetic acid (i.e. vinegar) and the ionic liquid, bis(trifluoromethanesulfonyl)imide (TFSI) dissolved in polyethylene glycol (PEG). Due to the toxicity and/or reactivity of many electrolytes, a rapid-prototyping process is presented to deposit and hermetically seal electrolytes on graphene while maintaining electrical access to electrodes. We demonstrate that a promising electrolyte from literature, TFSI-PEG [3], is able to achieve more than 300 switching cycles with graphene, and the improved endurance is believed to be due to the large magnitude of intercalation anions (TFSI-) and lower voltage threshold required (3V). A set of sequential switching experiments illustrates that, even if a sufficient voltage is applied to the electrolyte, several switching cycles are required before the device exhibits minimum conductivities significantly below $4e^2/h$. The presented method and devices can be explored further for potential applications in digital, asynchronous, and domino logic.

[1] Y. Tan *et al*., Phys. Rev. Lett., **99**, 246803 (2007).

[2] C. Hayashi *et al.*, IEEE Access, **8**, 92314-92321 (2020). ieeexplore.ieee.org/document/9093841

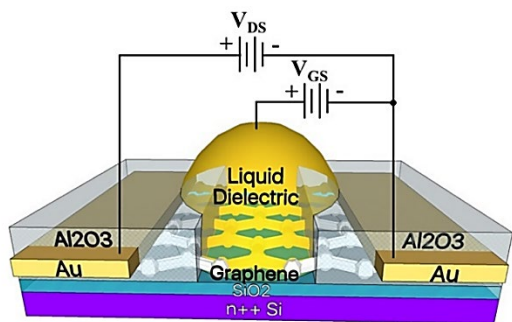[3] S. Li *et al.*, Nature Electronics, **4**, 254-260 (2021).

Fig.1: Schematic of Device. Graphene on Silicon/Silicon Dioxide (Si/SiO$_2$) with Gold (Au) Electrodes, Aluminum Oxide (Al$_2$O$_3$) Passivation Layer, and Liquid Dielectric. Adapted from [2]
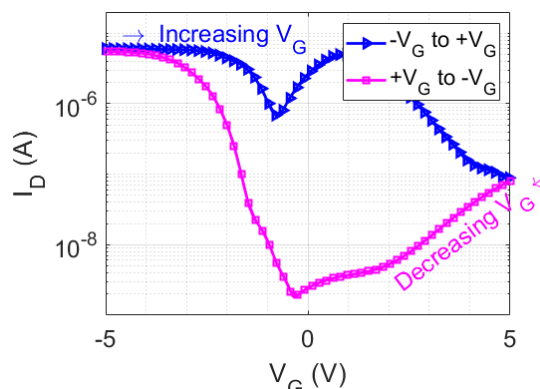

Fig.4: Semi-Logarithmic Transfer Curve of Graphene-with-Honey Device (with hysteresis). Adapted from [2]. Graphene-with-Vinegar Device (not shown here) Exhibited On-Off Ratio > 10^2

Fig.2: Sealed Electrolytes on Graphene Devices. Graphene Field-Effect Transistors Acquired Commercially from Graphenea, Consists of 2x6 Array of 100um x 100um Graphene Transistors with an Unpassivated Gold Side-Gate. Sealed with NOA71 Epoxy

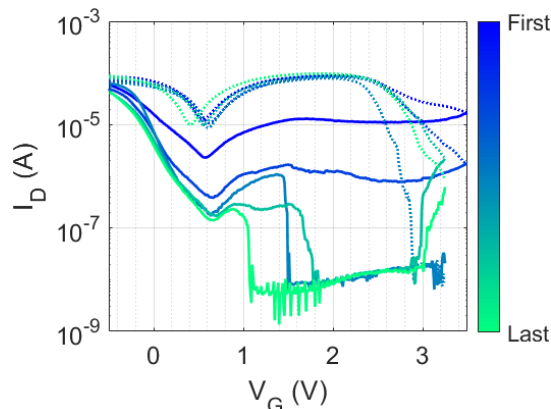Fig.5: Series of Transfer Curve Sweeps of Graphene-with-TFSI-PEG Device. Illustrates that Larger Resistivity Values are Attainable in Later Measurements
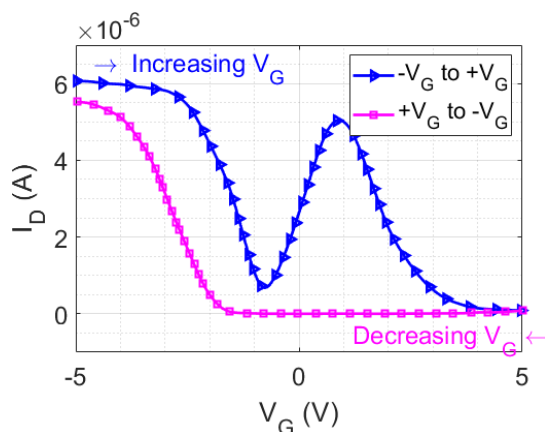

Fig.3: Transfer Curve of Graphene-with-Honey Device Showing Dependence of Drain Current vs. Gate Voltage (with hysteresis). Adapted from [2]
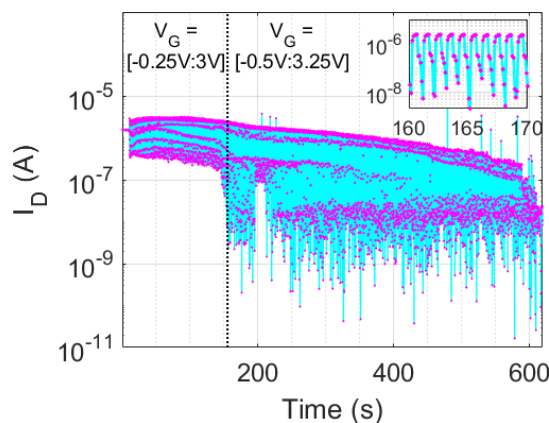

Fig.6: Transient Response to 1 Hz Square-Wave Gate-Voltage Input Showing Repeatability of 300+ Cycles with TFSI-PEG

Adiabatic Resonance for Fast and Robust Quantum Control

Xinyu Zhao[1], Yan Xia[1], and Xuedong Hu[2]

*[1]Department of Physics, Fuzhou University, Fuzhou, Ibaraki 305-8571, China*
[2]Department of Physics, University at Buffalo, Buffalo, NY 14260-1500, USA
xhu@buffalo.edu

Adiabatic passage is a useful technique to realize quantum control and quantum gates. It is in general robust, albeit slow. Motivated by interesting but special examples we studied before [1,2] and various efforts to accelerate adiabatic passage, we explore a universal scheme to achieve fast adiabatic passage with high-fidelity based on having the system returning to the instantaneous eigenstates periodically, which we call adiabatic resonance [3]. We find that by designing a cyclic evolution in the adiabatic frame, the evolution path of the system could periodically cross the adiabatic path, leading to high operation fidelity near these crossing/resonance points. We derive the general condition for adiabatic resonance, and apply it to a two-level system, specifically to the problem of single electron transfer in a double quantum dot. We show that with such a designed detuning pulse we can realize adiabatic Landau-Zener transition rapidly. Compared to other schemes aiming at accelerating adiabatic passage, such as transitionless quantum driving, the adiabatic resonance scheme has the advantage that it does not require any additional control Hamiltonian. Lastly, we discuss the possibility of optimization and built-in robustness against noise.

[1] S. Oh, Y.-P. Shim, J. Fei, M. Friesen, and X. Hu, Physical Review A **87**, 022332 (2013).

[2] S. Oh, X. Hu, F. Nori, and S. Kais, Scientific Reports **6**, 20824 (2016).

[3] X. Zhao et al, preprint in preparation.
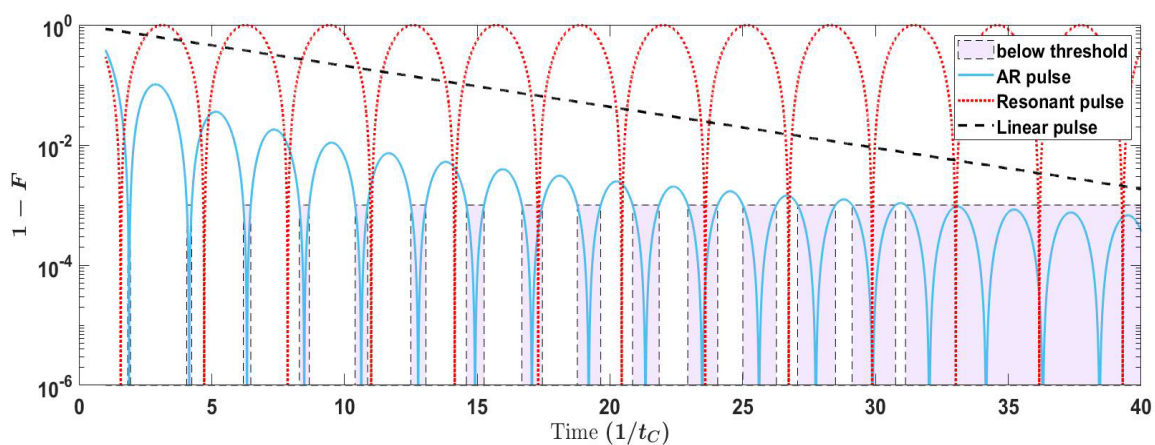
Fig.1. Here we plot electron transfer fidelity in a double quantum dot based on different schemes. The black dashed line represents a linear change in interdot detuning, the red dotted line represents a resonant protocol (change the detuning from a finite value favoring the initial state to zero suddenly, stay there for a period of time, then suddenly switch the detuning to a value where the destination dot has the ground state), and lastly the blue solid line presents results of an AR pulse.

Rabi Frequency and Fidelity of Strongly Driven Electric Dipole Spin Resonance

Yasuhiro Tokura

Faculty of Pure and Applied Sciences, University of Tsukuba, Tsukuba, 305-8571, Japan
Tsukuba Research Center for Energy Materials Science (TREMS), Tsukuba 305-8571, Japan
tokura.yasuhiro.ft@u.tsukuba.ac.jp

Coherent control of a single spin confined in a quantum dot (QD) by the microwave electric field (electric dipole spin resonance; EDSR) is an active field of recent research. One of the required mechanisms to couple the orbital motion to the spin degree of freedom is to utilize the slanting magnetic field [1]. This approach has enabled recent experimental studies, including fast Rabi oscillation [2], coupling with microwave photon [3], and fast Si-QD spin manipulation [4]. In the fast-driving condition of the Rabi frequency more than 100MHz, it is observed that the deviation from the expected linear dependence with the microwave amplitude [4,5] and the fidelity of the Rabi oscillation becomes degraded. One of the possible origins of the deviation from the linear behavior of Rabi frequency on the microwave amplitude is the non-parabolicity of the confinement potential. Other possible origin is the non-linearity of the field gradient. In this report, we study the effect of non-parabolicity of the QD confinement potential and non-linearity of the field gradient on the fidelity of the coherent control of spin states. We derived an effective Hamiltonian on the rotating frame and applied Schrieffer-Wolff transformation to obtain a Hamiltonian of the spin, which is parametrized with the driving field amplitude, non-parabolicity and non-linearity of the field. Under the condition that sub-linear dependence of the Rabi frequency on the applied microwave amplitude appears, the fidelity becomes worse, which is attributed to the enhanced entanglement of the spin degree of freedom with the electron orbital. We also study the effect of the electron-phonon couplings on the fidelity of the strongly driven spin system. Part of this work is supported by JSPS Kakenhi (18k03479) and JST's Moonshot R&D (Grant No. JP- MJMS2061).

[1] Y. Tokura, W. G. van der Wiel, T. Obata, and Seigo Tarucha, Phys. Rev. Lett. **96**, 047202 (2006).

[2] M. Pioro-Ladriere, T. Obata, Y. Tokura, Y. -S. Shin, T. Kubo, K. Yoshida, T. Taniyama, and S. Tarucha, Nature Physics, **4**, 776 (2008).

[3] X. Mi, M. Benito, S. Putz, D. M. Zajac, J. M. Taylor, G. Burkard, and J. R. Petta, Nature **555**, 599 (2018). [4] J. Yoneda, T. Otsuka, T. Nakajima, T. Takakura, T. Obata, M. Pioro-Ladriere, H. Lu, C. J. Palmstrom, A. C. Gossard, and S. Tarucha, Phys. Rev. Lett. **113**, 267601 (2014).

[5] F. N. M. Froning, L. C. Camenzind, O. A. H. van der Molen, A. Li, E. P. A. M. Bakkers, D. M. Zumbuhl, and Floris R. Braakman, Nature Nanotechnology, **16**, 308 (2021).

Speed Limits for Two-Qubit Gates with Weakly Anharmonic Qubits

Sahel Ashhab[1], Fumiki Yoshihara[1,2], Tomoko Fuse[1], Naoki Yamamoto[3], Adrian Lupascu[4],
& Kouichi Semba[1,5]

[1]*National Institute of Information and Communications Technology,*
4-2-1, Nukui-kitamachi, Koganei, Tokyo 184-8795, Japan
[2]*Department of Physics, Tokyo University of Science,*
1–3 Kagurazaka, Shinjuku, Tokyo 162–0825, Japan,
[3]*Quantum Computing Center and Department of Applied Physics and Physico-Informatics ,*
Keio University, 3-14-1 Hiyoshi, Kohoku-ku, Yokohama, Kanagawa 223-8522, Japan
[4]*Institute for Quantum Computing, Department of Physics and Astronomy, and Waterloo*
Institute for Nanotechnology, University of Waterloo, Waterloo, Ontario, Canada N2L 3G1
[5]*Institute for Photon Science and Technology,*
The University of Tokyo, 7-3-1 Hongo, Bunkyo-ku, Tokyo 113-0033, Japan
e-mail: ashhab@nict.go.jp

We consider the implementation of two-qubit gates when the physical systems used to realize the qubits possess additional quantum states in the accessible energy range [1]. We use optimal control theory to determine the maximum achievable gate speed for two-qubit gates in the qubit subspace of the many-level Hilbert space, and we analyze the effect of the additional quantum states on the gate speed. We identify two competing mechanisms. On one hand, higher energy levels are generally more strongly coupled to each other. Under suitable conditions, this stronger coupling can be utilized to make two-qubit gates significantly faster than the reference value based on simple qubits. On the other hand, a weak anharmonicity constrains the speed at which the system can be adequately controlled: faster operations require stronger control fields, which leads to faster decoherence and uncontrolled leakage outside the qubit space. In order to account for this constraint, we modify the pulse optimization algorithm to avoid pulses that lead to appreciable population of the higher levels. Then we find that the presence of the higher levels can lead to a significant reduction in the gate speed. We compare the optimal-control gate speeds with those obtained using the cross-resonance/selective-darkening protocol. We find that the latter, with some optimization, can be used to achieve relatively fast CNOT gates. These results can help the search for optimized gate implementations and provide guidelines for desirable conditions on anharmonicity to enable the utilization of the higher levels in realistic systems.

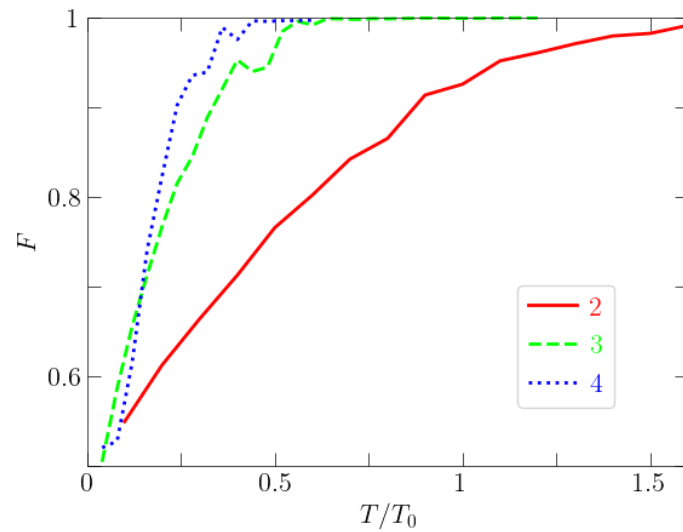[1] S. Ashhab *et al*., Phys. Rev. A **105**, 042614 (2022).

Fig.1: Two-qubit CNOT gate fidelity as a function of pulse time for numerically optimized pulses. The minimum gate time is identified as the pulse time at which the fidelity exceeds a preset threshold, e.g. 99.9%. The different symbols correspond to different models of the qubits in which each qubit is replaced by a multi-level system with 2, 3 or 4 energy levels. The more the levels, the faster the CNOT gate.
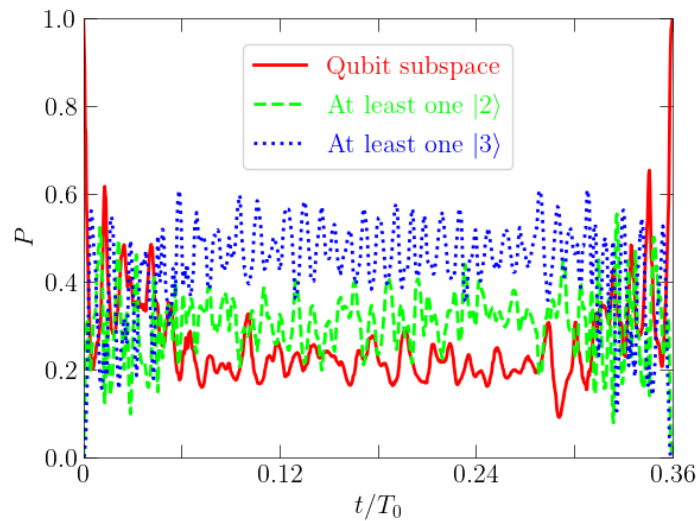

Fig. 2: Populations in different subspaces of the Hilbert space during the implementation of a CNOT gate. This figure shows that higher energy levels are populated during the CNOT gate implementation.

Dimension-adaptive Quantum State Tomography with Machine Learning

<u>Sangita Regmi</u>[1, *], Sanjaya Lohani[1], Joseph M. Lukens[2], Ryan T. Glasser[3], Brian T. Kirby[3,4], and Thomas A. Searles[1]

[1]*Department of Electrical and Computer Engineering, University of Illinois Chicago, Chicago, IL 60607, USA*

[2]*Quantum Information Science Section, Oak Ridge National Laboratory, Oak Ridge, TN, 37831, USA*

[3]*Tulane University, New Orleans, LA 70118, USA*

[4]*DEVCOM US Army Research Laboratory, Adelphi, MD 20783, USA*

*sangita@uic.edu

We introduce an approach for performing quantum state reconstruction on systems of n qubits using a machine-learning-based reconstruction system trained exclusively on m qubits, where $m \geq n$. This approach removes the necessity of exactly matching the dimensionality of a system under consideration with the dimension of a model used for training. We demonstrate our technique by performing quantum state reconstruction on randomly sampled systems of one, two, and three qubits using machine-learning-based methods trained exclusively on systems containing at least one additional qubit. The reconstruction time required for machine-learning-based methods scales significantly more favorably than the training time; hence this technique can offer an overall savings of resources by leveraging a single neural network for dimension-variable state reconstruction, obviating the need to train dedicated machine-learning systems for each Hilbert space.
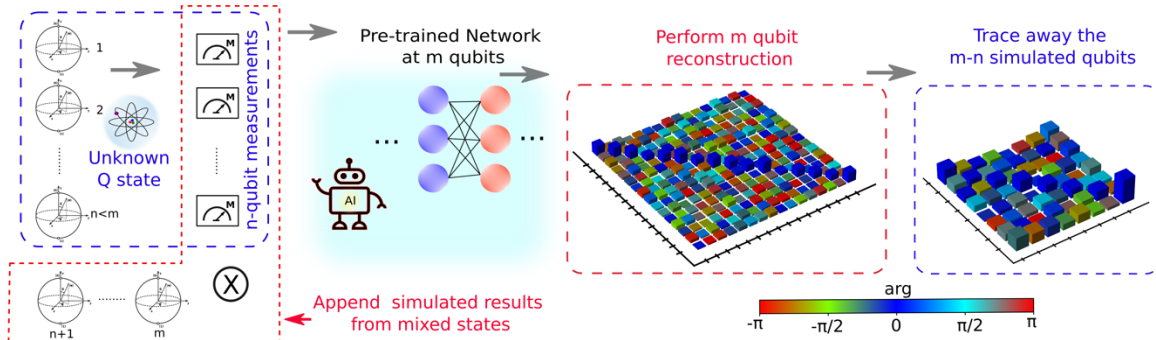
Fig. 1. A schematic of our approach for dimension-adaptive quantum state reconstruction. The estimation of n-qubit quantum states uses a machine-learning-based reconstruction system trained on m qubits, where m>=n. First, we append virtual results for m-n qubits via engineered padding (red dotted box) to n-qubit measurements (blue dotted box) and feed the padded measurements into a network pre-trained for m qubits. At the output, the network returns an m-qubit density matrix, which is partially traced to return an estimate of the unknown quantum system of n qubits.
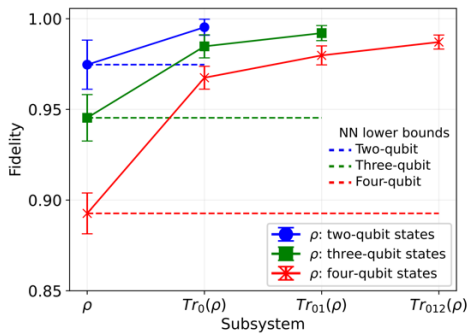

Fig. 2. Reconstruction fidelity versus subsystem of predicted density matrix. For example, when ρ represents a four-qubit system, then the subsystems $Tr(\rho_0)$, $Tr(\rho_{01})$, $Tr(\rho_{012})$ represent a three-qubit, two-qubit, and one-qubit quantum system, respectively. The markers 'cross', 'square', and 'circle' respectively, denote reconstructions with the network pre-trained on m=4, m=3, and m=2 qubits. The dotted lines indicate the average reconstruction fidelity for an m-qubit system reconstructed with a network pre-trained on m qubits.
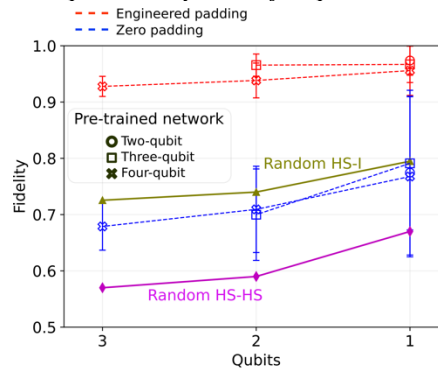

Fig. 3. Reconstruction fidelity with engineered padding and zero padding are respectively shown by red and blue dotted lines. The magenta line shows the average fidelity between two random density matrices sampled from the Hilbert-Schmidt (HS) measure, whereas the olive line represents the average fidelity between a maximally mixed state and a random density matrix sampled from the HS measure for a system of n qubits.

https://arxiv.org/abs/2205.05804

Implementation of Quantum Algorithms for THz Metasurfaces

A. Blackwell, R. Yahiaoui, Y-H. Chen, P-Y. Chen, Z.A. Chase, and T.A. Searles*

Department of Electrical and Computer Engineering, University of Illinois at Chicago, Chicago, IL 60607, USA (tsearles@uic.edu)
*tsearles@uic.edu

Quantum computing offers significant speed and efficiency advantages over classical computing via the exploitation of the superposition of quantum states.[1] The design and development of "computational metamaterials" is crucial for this to be realized in order to perform wave-based quantum search algorithms for signal processing applications.[2] Presented here is the use of a Gradient Index (GRIN) lens metamaterial, as the Fourier Transform subblock of the quantum algorithm emulator system, that uses the Deutsch-Jozsa algorithm for such an application in the THz region where most of the previous work has concentrated in the microwave region. Figures 1a and 1b show the dimensions of a singular aperture and the whole GRIN lens, of varying aperture size, made entirely of a highly flexible Kapton polyimide material, respectively. The GRIN lens manipulates the incoming light to achieve electromagnetic properties that do not occur naturally by varying the index of refraction within a lens itself giving it an advantage over flat lenses (Fig. 1c). When different THz signals are introduced to the GRIN lens there are notable changes to the outgoing spectral profile (Fig. 1d and Fig. 2) where the electric field intensity increases with the THz wavelength on the focal plane. The design allows for the flexibility to manipulate the incoming light along the desired focal point by changing the geometry of the individual apertures.

[1] Cheng, K. *et al*., Optics Express **28**, 16230 (2020).
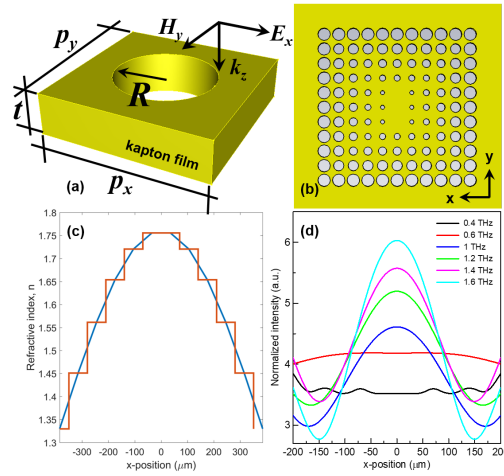[2] Zhang, W. *et al*., Advanced Materials **30**, 1703986 (2018).

Fig.1: (a) Structural design of the unit cell with the relevant geometrical dimensions: px= py = 70 m, t = 127 m and R varies 10, 15, 20, 25 and 30m, respectively. b, (c) Schematic view of the GRIN lens. The aperture size of the lens is about 1mm. (c) Refractive index in dependence of the radial distance from the center of the GRIN lens. (d) Simulated electric field intensity on the focal plane for different frequencies.
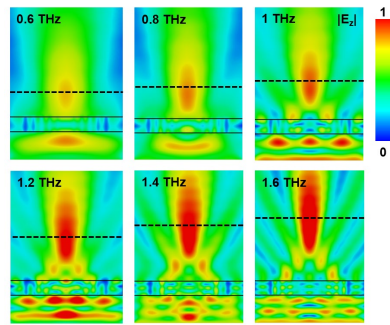

Fig.2: Simulated z-component of the normalized electric field for different working frequencies. The dash line corresponds to the cross-section shown in Figure 1d .

Reservoir Computing with Spin Waves in a Skyrmion Crystal

M.-K. Lee* and M. Mochizuki

Department of Applied Physics, Waseda University, Okubo, Shinjuku-ku, Tokyo 169-8555,
Japan
* irlight203@hotmail.com

Magnetic skyrmions are nanometric spin textures characterized by a quantized topological invariant in magnets and often emerge in a crystallized form called a skyrmion crystal in an external magnetic field. We propose that skyrmion crystals possess high potential for application to reservoir computing, which is one of the state-of-the-art derivative frameworks of recurrent neural networks. Our skyrmion reservoir exploits precession dynamics of magnetizations, i.e., spin waves, propagating in the crystal. Benefited from the nonlinear interferences and slow relaxations of spin waves, the skyrmion reservoir attains several important characteristics required for reservoir computing, e.g., the generalization ability, nonlinearity, and short-term memory. We first investigate these properties by performing three standard tasks, i.e., the input-estimation task, short-term memory task, and parity-check task, to demonstrate that skyrmion crystals are promising materials for spintronics reservoir devices [1]. Second, we extend our study to more nontrivial tasks, such as the nonlinear autoregressive moving average task and handwritten digit recognition task. A high digit recognition rate larger than 95% can be achieved by the skyrmion crystal with the number of virtual nodes being less than one thousand, which further consolidates the practical potential of the skyrmion reservoir. Importantly, since skyrmion lattices emerge spontaneously in magnets via a self-organization process under application of a static magnetic field, the proposed skyrmion reservoir requires neither advanced nanofabrication nor complicated manufacturing for production, in contrast to other previously proposed magnetic reservoirs constructed with spintronics devices, e.g., spin-torque oscillators. Our work is expected to realize a breakthrough in the research of spintronics reservoir computing.

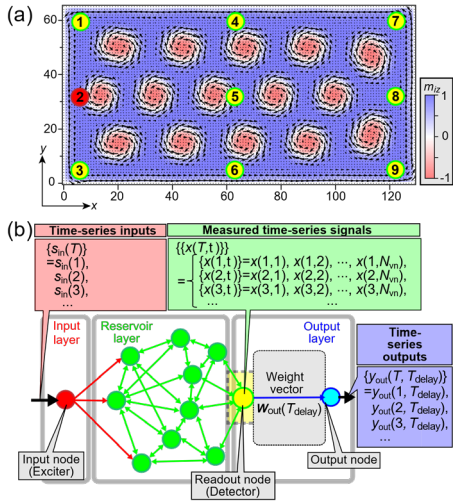[1] M.-K. Lee and M. Mochizuki, Phys. Rev. Applied **18**, 014074 (2022) (Editor's Suggestion)

Fig.1: (a) Proposed reservoir in a skyrmion crystal (b) Architecture of the reservoir computing.
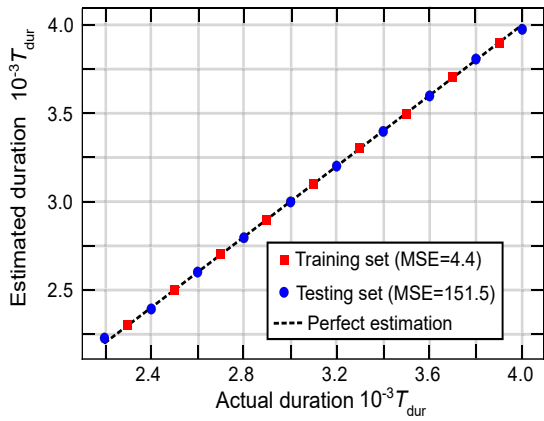

Fig.2: Results of the input-estimation task. The horizontal (vertical) axis labels the actual (estimated) duration of the input ac magnetic field. The dashed line is the perfect estimation line, indicating highly accurate estimations.
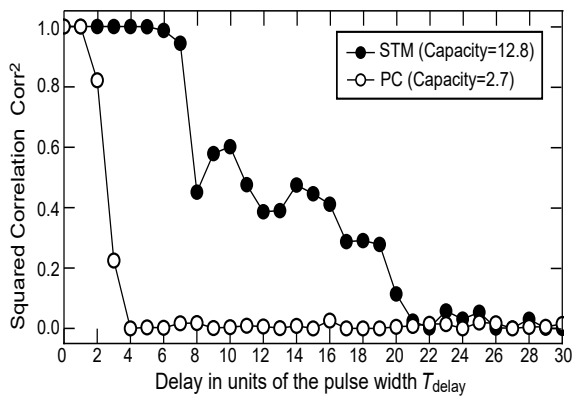

Fig.3: Squared correlations of short-term memory (STM) and Parity-check (PC) tasks as functions of the delay time. Capacities of both tasks correspond to the areas below the respective curves, which quantify the performance of the reservoir for these tasks.
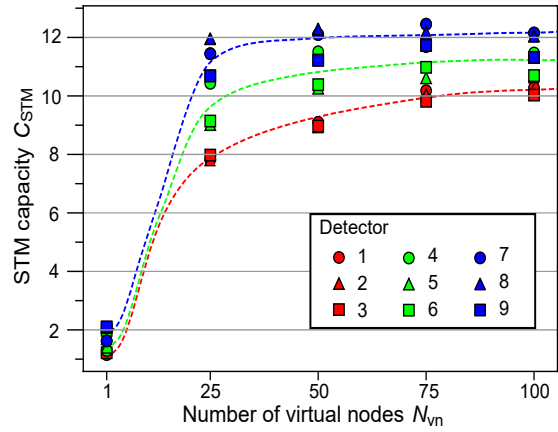

Fig.4: Short-term memory (STM) task capacity as a function of virtual node number for nine detectors in Fig.1(a) on the skyrmion lattice.
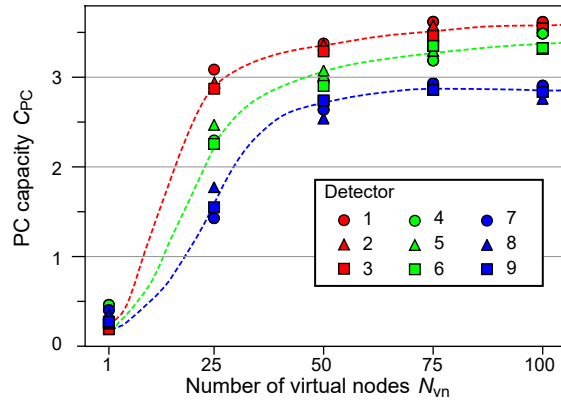

Fig.5: Parity-check (PC) task capacity as a function of virtual node number for nine detectors in Fig.1(a) on the skyrmion lattice.

Fraunhofer Pattern in The Presence of Majorana Zero Modes

F. Dominguez[1], E.G. Novik[2], and P. Recher[1,3]

[1]Institut für Mathematische Physik, Technische Universität Braunschweig, 38106 Braunschweig, Germany

[2]Institute of Theoretical Physics, Technische Universität Dresden, 01062 Dresden, Germany

[3]Laboratory of Emerging Nanometrology, 38106 Braunschweig, Germany

p.recher@tu-braunschweig.de

Topological states are recent concepts in condensed matter physics that have important implications for example in metrology, due to their robust transport properties or in topological quantum computation through the braiding of Majorana bound states. Here, we propose a novel topological Josephson junction with the normal region being a quantum spin Hall insulator. Using the BHZ model and numerical tight-binding simulations, we show that the Fraunhofer pattern in the presence of Majorana edge modes in the superconductors behaves dramatically different with respect to size and period as compared to the situation without Majorana edge modes [1]. The two regimes are connected to each other by the application of a Zeeman field. By investigating the different scattering processes in the junction by means of an analytical scattering model, we can show that the presence of Majorana edge modes can induce strong crossed Andreev reflection via the two edges (leading to non-local triplet pairing) that is otherwise strongly suppressed by virtue of the spin-momentum locking of the helical edge states. We further argue that the effect originates from a truly non-local feature of separated Majoranas that can be measured in equilibrium and at finite temperature. Together with predictions for the two-terminal conductance [2], the present setup offers unique and experimentally accessible signatures of topological superconductivity.

[1] F. Dominguez, E.G. Novik, P. Recher, to be submitted (2022).
[2] E.G. Novik, B. Trauzettel, P. Recher, Phys. Rev. B **101**, 235308 (2020).
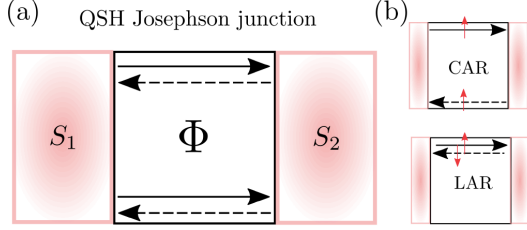
Fig.1: (a) Planar quantum spin Hall based Josephson junction with superconducting (S_1, S_2) areas and normal region threaded by a magnetic flux Φ. Solid and dashed arrows denote electron- and hole-like helical edge states, respectively. (b) Sketches of crossed Andreev reflection (CAR) and local Andreev reflection (LAR) processes for helical edge states transporting Cooper pairs between S_1 and S_2. Arrows denote electron spin directions.

Fig.3: Critical current I_c as a function of flux Φ (Fraunhofer pattern) calculated with the numerical Green's function method illustrated in Fig. 2. (a) Color plot of I_c as a function of in-plane magnetic field with Zeeman energy $B_{||}$ that drives a topological phase transition from topologically trivial to topologically non-trivial superconductors with Majorana bound states. The critical Zeeman field $\sim 0.5 meV$. (b) Two line-cuts for different Zeeman energies: $B_{||}$ =0 meV (blue, trivial regime), $B_{||} = 1.1$ meV (red dashed, non-trivial regime). The different periodicities originate from different dominant electron-hole reflection probabilities in the presence or absence of Majorana bound states. Here, we used the parameters (cf. Fig. 2): $L_n = 0.74$ μm, W=0.14 μm, Δ_0=0.15 meV, and Φ_0=h/2e.
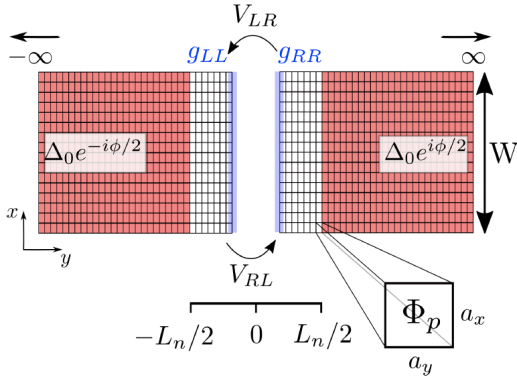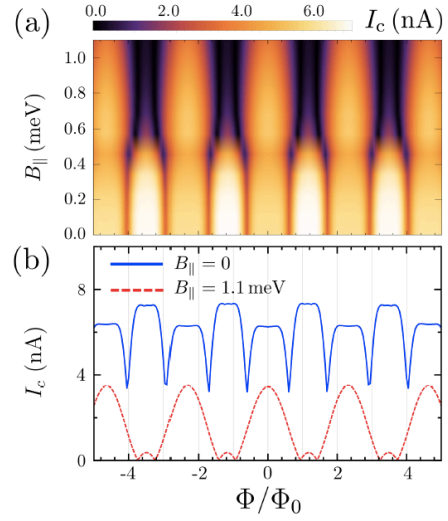

Fig.2: Sketch of the tight-binding implementation of the setup and Josephson current based on surface Green's functions g_{LL} and g_{RR} (blue areas) defined on a lattice with spacing $a_x = a_y \equiv a$. The two separate parts illustrate the recursive method where neighboring slices are coupled by $V_{LR/RL}$. The two superconducting regions (red) have a phase difference of ϕ.
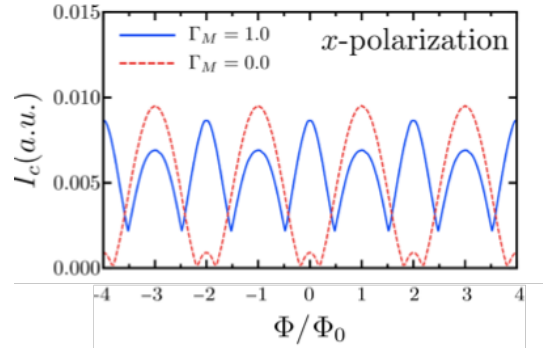

Fig.4: Result of an analytical scattering matrix calculation where the different periods of Fig. 3 (b) could be reproduced qualitatively, assuming Majorana bound states with spinor polarization in x-direction (cf. Fig. 2) for the red dashed curve, whereas the blue curve has no coupling to Majorana bound states (corresponding to the trivial regime with no Majorana bound states).

Topological Insulator Josephson Junctions integrated in superconducting Qubit Circuits

A. Schmidt[1], T.W. Schmitt[1], C. Liu[2], A. Hertel[1], C. Dickel[3], K. Moors[1], M. Schleenvoigt[1],

Yoichi Ando[3], M.R. Connolly[2,4], D. Grützmacher[1] and P. Schüffelgen[1]

[1]Peter Grünberg Institute, Forschungszentrum Jülich & Jülich-Aachen Research Alliance

(JARA), Forschungszentrum Jülich and RWTH Aachen, Jülich, Germany

[2] Blackett Laboratory, Imperial College London, London, UK

[3] Institute of Physics II, University of Cologne, Cologne, Germany

[4] London Centre for Nanotechnology, University College London, London, UK

a.schmidt@fz-juelich.de (e-mail address of the corresponding author)

A very promising research topic for the development of novel quantum devices is the study of hybrid material systems with a conventional superconductor (S) in proximity to a topological insulator (TI). The predicted potential of such devices to host exotic phenomena such as topological superconductivity and Majorana zero modes makes them interesting for the realization of topological quantum computing. [1] Recently, we achieved the integration of S-TI-S Josephson junctions with superconducting microwave circuits (see Fig. 1). This was demonstrated via circuit quantum electrodynamics measurements (see Fig. 2) which has unlocked new techniques to study TI-based Transmon qubits potentially hosting MZMs. [2] In this work, I will present the implementation of Transmon qubits with our in situ device fabrication which is possible through selective area growth of our $(Bi,Sb)_2Te_3$-TI nanoribbons in combination with stencil lithography of the superconductor using molecular beam epitaxy. Thanks to this method, we can generate highly transparent S-TI interfaces, which already showed first signatures of Majorana bound states in TI based Josephson junctions by a missing first Shapiro step. [3] In our TI-based Transmon device it was possible to conduct coherence measurements at zero magnetic field. [4] However, entering the topological phase requires magnetic field strengths of up to 1T applied parallel to the junction. Here we demonstrate that our quantum circuit is compatible with such fields and that also coherent qubit control is possible in these high magnetic fields (see Fig. 3 and Fig. 4). We present initial results on the magnetic field dependence of the T_1 lifetime and the qubit's anharmonicity which can be found in Fig. 5 and Fig. 6.

[1] A. Cook and M. Franz, Phys. Rev. B, **84**, 201105 (2011).

[2] E. Ginossar and E. Grosfeld, Nat. Commun. **5**, 4772 (2014).

[3] P. Schüffelgen et al., Nat. Nanotechnol. **14**, 825-831 (2019).

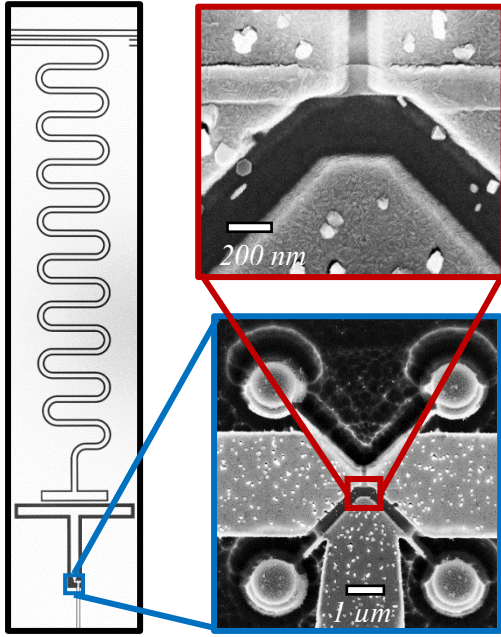[4] T. W. Schmitt et al., Nano lett. **22**, 2595−2602 (2022).

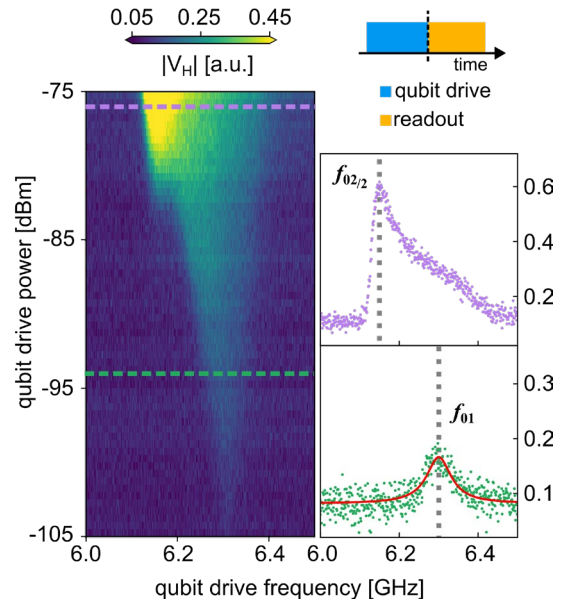Fig. 1: SEM picture of a Ti-based Transmon qubit

Fig. 2: Power dependence of the two-tone spectroscopy of the TI-based Transmon qubit at zero magnetic field from Ref. [4]
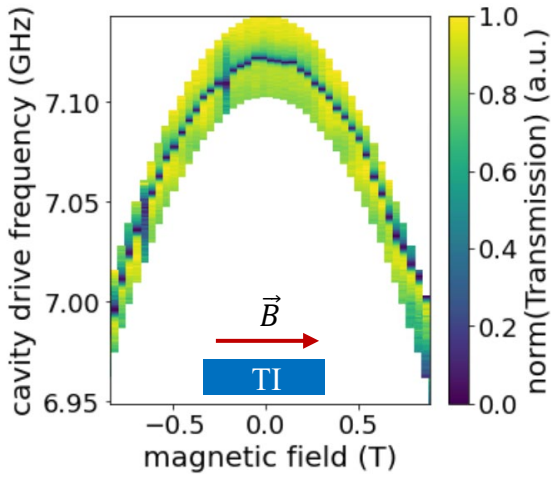

Fig. 3: Resonator spectroscopy measurement at different magnetic field values applied along the TI wire
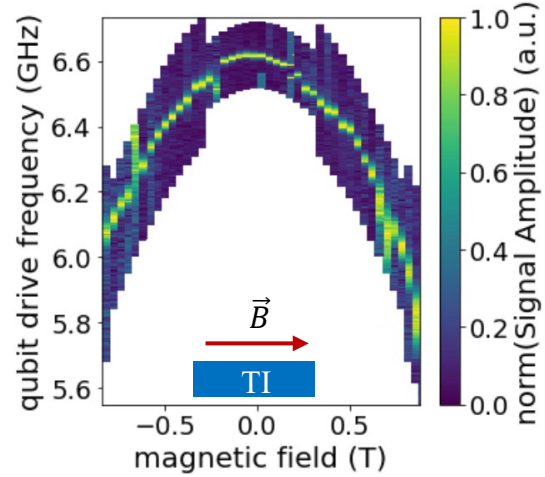

Fig. 4: Qubit spectroscopy measurement at different magnetic field values applied along the TI wire
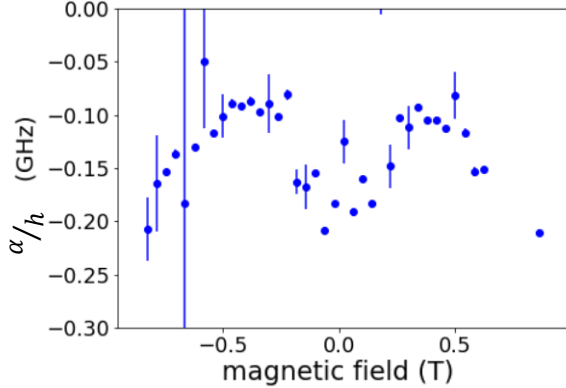

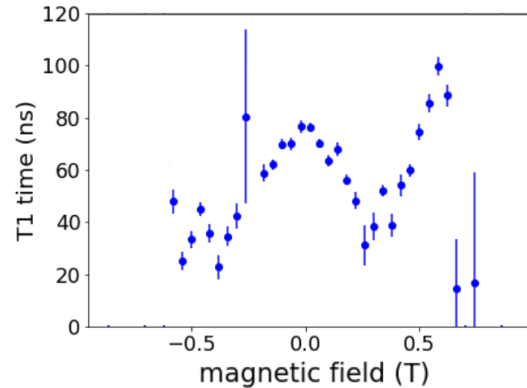Fig. 5: Qubit anharmonicity against magnetic field applied along the TI wire

Fig. 6: Qubit lifetime against magnetic field applied along the TI wire

Topological Superconductivity in Phase-Controlled Josephson Junctions

B. Scharf[1,2]

[1]*Institute for Theoretical Physics and Astrophysics, University of Würzburg, Germany*
[2]*Department of Physics, University at Buffalo, State University of New York, USA*
Benedikt.Scharf@physik.uni-regensburg.de

The prospect of non-Abelian statistics and fault-tolerant quantum computing has made the search for Majorana bound states one of the most intense topics of research in condensed matter physics during the past decade. In this context, experimental efforts have been mostly directed to one-dimensional (1D) systems such as hybrid structures of semiconductor nanowires and superconductors. Despite promising results, these 1D systems suffer from several drawbacks, such as requiring large magnetic fields and an intricate fine-tuning of the chemical potential.

Recent experimental progress in proximity-inducing superconductivity in two-dimensional systems, however, points to a possible route for overcoming these obstacles, and different setups based on two-dimensional electron gases and various geometries have been proposed as alternatives to 1D wires [1]. Among these proposals, those based on phase-controlled Josephson junctions with strong spin-orbit coupling (SOC) offer an attractive alternative [2]. A key advantage of this proposal is the tunable superconducting phase difference, which serves as an additional knob to control the topological transition and offers the prospect of avoiding experimentally difficult fine-tuning like the one required in wires.

Here, we first discuss the conditions for the formation of a topological superconducting phase hosting Majorana bound states in phase-controlled Josephson junctions. We elucidate how Josephson junctions with an arbitrary combination of SOC can host crystalline anisotropic topological superconductivity with Majorana bound states for a wide range of parameters as long as an appropriately oriented in-plane magnetic field is applied [3]. Moreover, we investigate the topological phase diagram and gap protecting the Majorana bound states as well as the optimal conditions to observe these states. Finally, we discuss experiments that point to the observation of such a topological phase transition in HgTe-based Josephson junctions [4].

[1] B. Scharf, et al., Phys. Rev. B 91, 144505 (2015); G. Fatin, et al., Phys. Rev. Lett. 117, 077002 (2016).
[2] F. Pientka, et al., Phys. Rev. X 7, 021032 (2017); M. Hell, et al., Phys. Rev. Lett. 118, 107701 (2017).
[3] B. Scharf et al., Phys. Rev. B 99, 214503 (2019); J. Pakizer, et al., Phys. Rev. Res. 3, 013198 (2021)
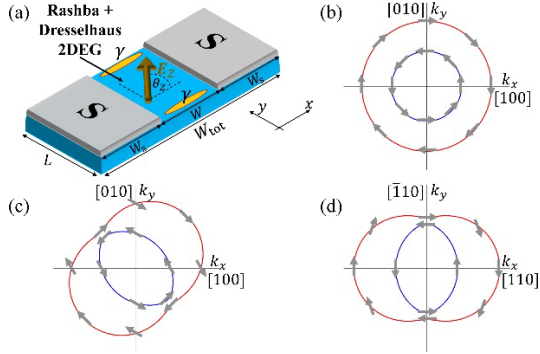[4] H. Ren, et al., Nature 569, 93 (2019).

Fig.1: Schematic setup of a phase-controlled Josephson junction. The position of the Majorana bound states γ that appear at the ends of the normal region in the topological phase is also indicated. Depending on the direction of the in-plane magnetic field E_Z (parametrized by the angle $θ_Z$) and the in-plane crystallographic axes along which the superconducting phase difference is applied, SOC affects the formation of a topological phase differently. Fermi contours for 2DEGs formed in quantum wells with [001] growth direction: (b) 2DEG with Rashba SOC and 2DEGs with Rashba as well as Dresselhaus SOC if the x axes are chosen along the (c) [100] and (d) [110] directions, respectively. Taken from Ref. [3].
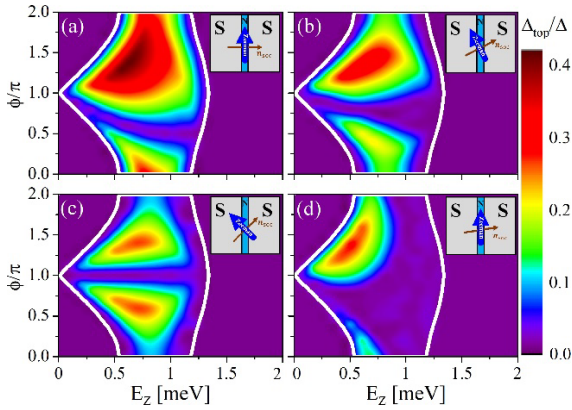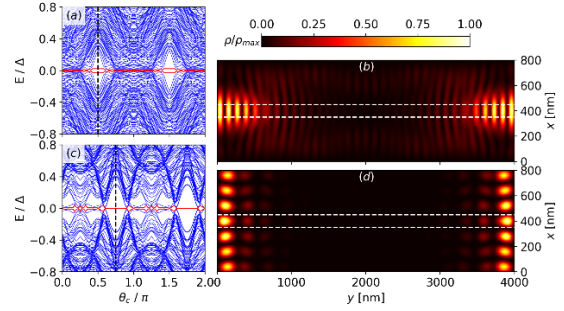

Fig.3: Energy spectrum as a function of $θ_c$ (characterizing the angle between the [100] crystallographic axis and the axis along which the superconducting phase difference φ is applied) for (a) a junction with only Rashba SOC, $θ_Z = 0$ and $φ = π$, and (c) a junction with equal Rashba and Dresselhaus SOC, $θ_Z = π/4$ and $φ = 0$. Red lines indicate the states with energies closest to zero, while black dashed vertical lines indicate the crystallographic orientation resulting in a maximal topological gap. (b) and (d) show the probability density (normalized to its maximum value) of the Majorana bound states in (a) and (c), respectively, at $θ_c$ values specified by the vertical dashed lines. Taken from Ref. [3].

Fig.2: Topological phase diagrams for different configurations of SOC and the Zeeman field E_Z. The white lines indicate the phase boundaries and $Δ_{top}$ only measures the gap inside the topological phase, whereas gaps outside the topological phase have been set to zero. The insets illustrate the directions of n_{soc} and E_Z. Taken from Ref. [3].

Fig.4 Development of a zero-bias peak and reconstructed phase diagram in HgTe-based Josephson junctions: a–h, Progression of tunneling conductance color plots (in units of e^2/h) as the magnetic field B_x varies from $−1.0$ T to 1.2 T. i, Color plot showing the extracted zero-bias curvature (in units of $e^2h^{−1}μeV^{−2}$) as a function of both the in-plane magnetic field B_x and the phase difference offset $Δφ$. The blue region in the phase diagram shows where a well-defined zero-bias peak is present in the tunneling conductance. Taken from Ref. [4].

Enhanced Spin-Triplet Superconductivity Induced by Spin-Orbit Coupling

Chenghao Shen[1,*], Jong Han[1], Thomas Vezin[1], Ranran Cai[2], Wei Han[2], and Igor Žutić[1]

[1]Department of Physics, University at Buffalo, State University of New York, USA

[2]International Center for Quantum Materials, School of Physics, Peking University, 100871 Beijing, P. R. China.

**cshen6@buffalo.edu*

A common path to superconducting spintronics, Majorana bound states, and topologically protected quantum computing relies on spin-triplet superconductivity. While naturally occurring spin-triplet pairing is elusive, and even common spin-triplet candidates, such as Sr_2RuO_4, support alternative explanations, proximity effects in heterostructures can overcome these limitations. There is a growing effort to realize proximity-induced equal-spin triplet superconductivity in junctions with magnetic regions or an applied magnetic field and common s-wave superconductors. To enhance such spin-triplet contribution, it is expected that junctions with a weak interfacial barrier and strong spin-orbit coupling (SOC) are desirable. Intuitively, a weak interfacial barrier enables a robust proximity-induced superconductivity and strong SOC promotes spin mixing, converting spin-singlet into spin-triplet superconductivity. In contrast, we reveal a nonmonotonic spin-triplet contribution with the strength of the interfacial barrier and Rashba SOC by calculating zero-bias conductance contributions from equal-spin Andreev reflection and superconducting correlations in ferromagnet/s-wave superconductor junctions [1,2]. In junctions with magnetic regions and SOC, we reveal that the predicted [3] and measured large magnetoresistance [4] is the manifestation of an enhanced spin-triplet superconductivity [1,2]. Our explanation for the enhanced spin-triplet superconductivity, which is nonmonotonic in the interfacial barrier strength [1], is experimentally demonstrated in quasi-two-dimensional van der Waals ferromagnet/s-wave superconductor junctions [5]. This peculiar behavior arises from an effective perfect transparency: interfacial spin-orbit coupling counteracts the native potential barrier for states of a given spin and wave vector. A huge increase in the magnetoresistance is observed at an intermediate junction resistance [5], which we predict can be even further enhanced at a finite bias [2].

[1] T. Vezin, C. Shen, J. E. Han, and I. Žutić, Phys. Rev. B **101**, 014515 (2020).

[2] C. Shen, J. E. Han, T. Vezin, M. Alidoust, and I. Žutić, preprint.

[3] P. Högl, A. Matos-Abiague, I. Žutić, and J. Fabian, Phys. Rev. Lett. **115**, 116601 (2015).

[4] I. Martinez et al., Phys. Rev. Applied **13**, 014030 (2020).

[5] R. Cai, Y. Yao, P. Lv, Y. Ma, W. Xing, B. Li, Y. Ji, H. Zhou, C. Shen, S. Jia, X. C. Xie, I. Žutić, Q.-F. Sun, and W. Han, Nat. Commun. **12**, 6725 (2021).
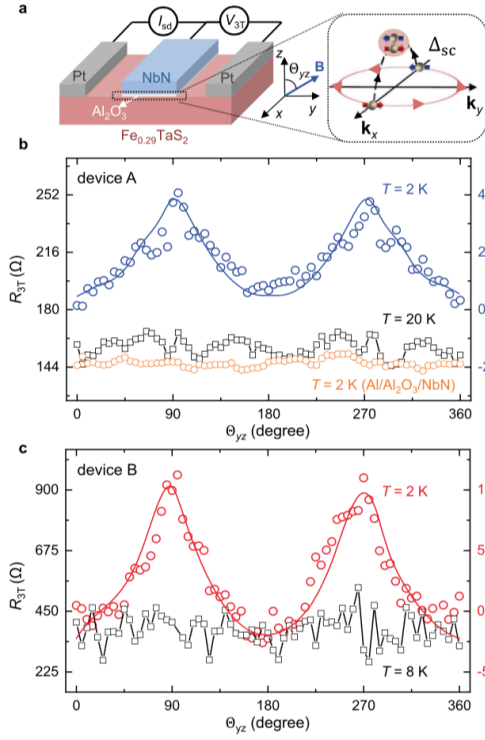
Fig.1: Large magnetoresistance of the quasi-2D van der Waals (vdW) $Fe_{0.29}TaS_2$/NbN junction. (a) Illustration of the quasi-2D vdW $Fe_{0.29}TaS_2$/NbN magnetoresistance (MR) device and the measurement geometry. The right panel shows the schematic of the spin-triplet pairing component resulting from Rashba SOC at the ferromagnet/superconductor interface. (b) The interfacial resistance ($R_{3T} = V_{3T}/I_{sd}$) and MR ratio as a function of the magnetic field angle measured on the typical quasi-2D vdW $Fe_{0.29}TaS_2$/NbN device (device A) under B = 9 T. The orange curve represents the resistance measured on a typical control device (Al/Al_2O_3/NbN) under B = 9 T. (c) The interfacial resistance and MR ratio as a function of the magnetic field angle on device B under B = 9 T. Large MR can be attributed to the spin-triplet superconductivity and the magneto-anisotropic Andreev reflection (MAAR). The solid lines in (b) and (c) are guides to the eye. Taken from Ref. [5].
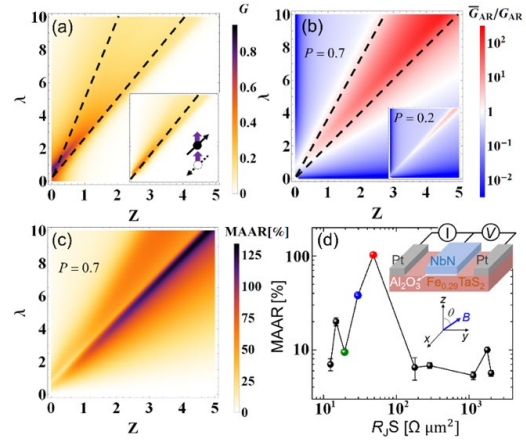
Fig.2: The total zero-bias conductance, G, as a function of barrier Z and Rashba SOC strength λ for out-of-plane magnetization, M, with spin polarization P = 0.7. Inset: G from the dominant spin-flip Andreev reflection, solid (dashed) arrows: incoming electrons (reflected holes), violet arrows: spin parallel (up) and antiparallel (down) to M. (b) The conductance ratio between the spin-flip and conventional Andreev reflection as a function of Z and λ for P = 0.7 (inset: P = 0.2). (c) Amplitude of out-of-plane magneto-anisotropic Andreev reflection (MAAR) as a function of Z and λ for P = 0.7. (d) Dependence of the MAAR amplitude on the interface resistance area product (R_JS, which plays the role of Z in the low-bias measurement. Inset: schematic of the experimental $Fe_{0.29}TaS_2$/Al_2O_3/NbN device Taken from Refs. [1] and [5].

All-nitride Superconducting Qubits Epitaxially Grown on Silicon Substrate

Sunmi Kim[1], Hirotaka Terai[1], Taro Yamashita[2,*], Wei Qiu[1,†], Tomoko Fuse[1],

Fumiki Yoshihara[1,‡], Sahel Ashhab[1], Kunihiro Inomata[3] & Kouichi Semba[1,§]

[1]*National Institute of Information and Communications Technology,*

4-2-1, Nukui-kitamachi, Koganei, Tokyo 184-8795, Japan

[2]*Graduate School of Engineering, Nagoya University, Furo-cho, Chikusa-ku,*

Nagoya, Aichi, 464-8603, Japan

[3]*Research Center for Emerging Computing Technologies, Advanced Industrial Science and*

Technology (AIST), Central 2, 1-1-1 Umezono, Tsukuba, Ibaraki 305-8568, Japan.,

[*]*Present address: Graduate School of Engineering, Tohoku University,*

Sendai, Miyagi 980-8579, Japan

[†]*Present address: IQM Quantum Computers, Keilaranta 19, 02150 Espoo Finalnd,*

[‡]*Present address: Department of Physics, Tokyo University of Science,*

1–3 Kagurazaka, Shinjuku, Tokyo 162–0825, Japan,

[§]*Present address: Institute for Photon Science and Technology,*

The University of Tokyo, Tokyo 113-0033, Japan.

e-mail: kimsunmi@nict.go.jp; terai@nict.go.jp; semba@ipst.s.u-tokyo.ac.jp

We have developed superconducting qubits based on NbN/AlN/NbN epitaxial Josephson junctions on silicon substrates [1] which promise to overcome the drawbacks of qubits based on Al/AlO$_x$/Al junctions. The all-nitride qubits have great advantages such as chemical stability against oxidation, feasibility for epitaxial tunnel barriers that reduce energy relaxation and dephasing, and a larger superconducting gap of 5.2 meV for NbN, compared to 0.3 meV for aluminum, which suppresses the excitation of quasiparticles. By replacing conventional MgO by a silicon substrate with a TiN buffer layer for epitaxial growth of nitride junctions [2], we demonstrate a qubit energy relaxation time T_1 ~16.3 μs and a Hahn-echo phase relaxation time $T_2 \sim$ 21.5 μs. These significant improvements in quantum coherence are explained by the reduced dielectric loss compared to the previously reported $T_1 \sim T_2 \sim$ 0.5 μs of NbN-based qubits on MgO substrates [3]. These results are an important step towards constructing a new platform for superconducting quantum hardware. This work was supported by JST CREST (Grant No. JPMJCR1775), JSPS KAKENHI (JP19H05615), JST ERATO (JPMJER1601), and partially by MEXT Quantum Leap Flagship Programs (JPMXS0120319794 and JPMXS0118068682).

[1] S. Kim, H. Terai, T. Yamashita *et al.*, Commun Mater **2**, 98 (2021).

[2] K. Makise, H. Terai, and Y. Uzawa, IEEE Trans. Appl. Sup **26**, 1100403 (2016).

[3] Y. Nakamura, H. Terai, K. Inomata *et al.*, Appl. Phys. Lett. **99**, 212502 (2011).
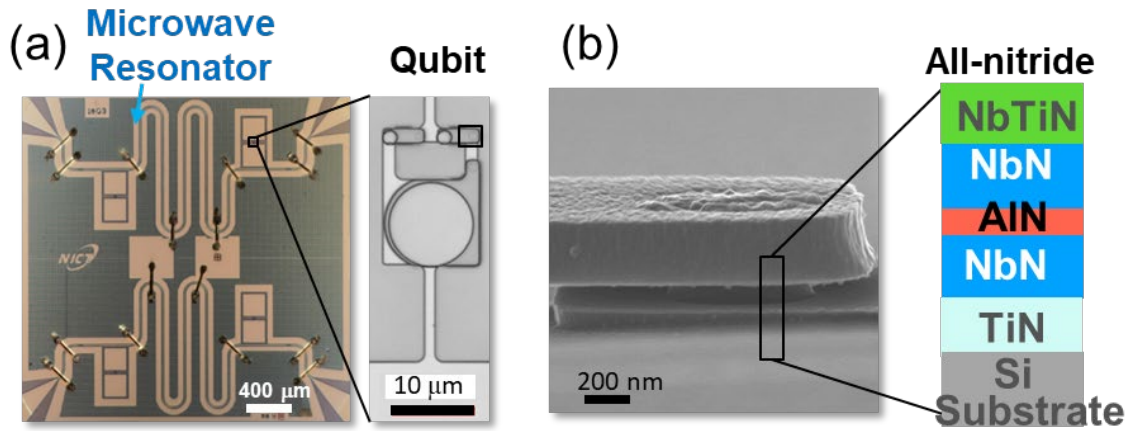
Fig.1: (a) Optical micrograph of nitride superconducting qubit circuit
(b) Electron micrograph of nitride superconducting qubit (part) and cross-sectional view of the device
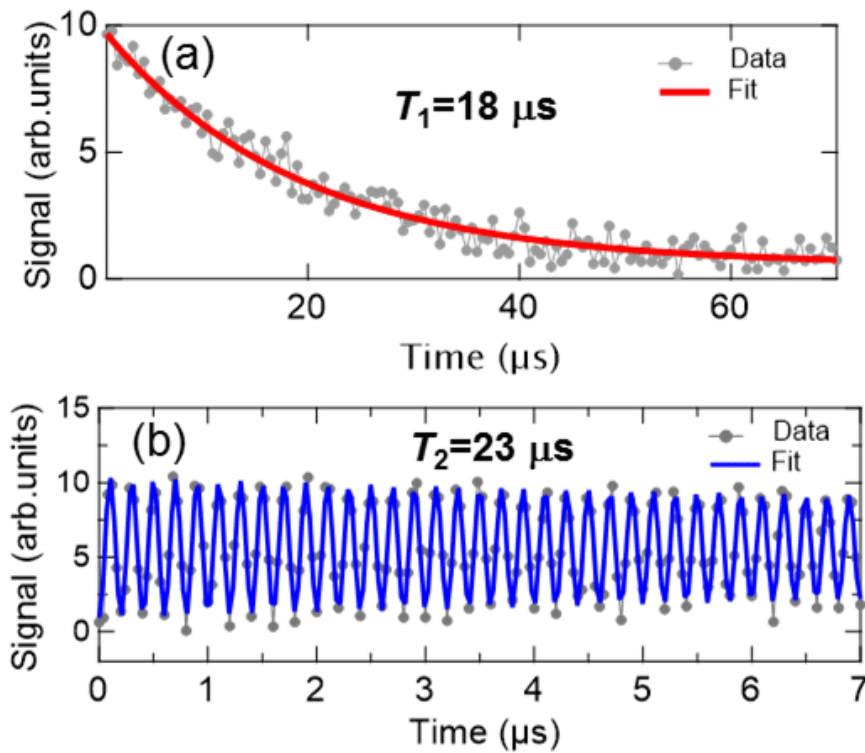

Fig. 2: Measured coherence times (a) Energy relaxation time T_1=18 microseconds (b) Phase relaxation time T_2=23 microseconds

99

Efficient Control of Two-Dimensional Magnets

C. Gong

Department of Electrical and Computer Engineering and Quantum Technology Center,
University of Maryland, College Park, MD 20742, USA
gongc@umd.edu

The emergent two-dimensional (2D) layered magnets [1, 2] provide ideal platforms to enable the atomic-thin magneto-optical and magnetoelectric devices. Though many have envisioned that 2D magnets should allow an efficient control of magnetism by a variety of external stimuli, true breakthroughs are still lacking, with only proof-of-concept reports. There appear to be fundamental obstacles for efficient control, e.g., through electrical and optical approaches. In this talk I will analyze the challenges, and present our theoretical and experimental progress on efficient electrical and optical control of 2D magnets [3-8]. Specifically, our results show that the laser shinning of tens of uW/um^2 can effectively affect magnetic domain behaviors of 2D magnets, in stark contrast to the conventional adoption of intensive ultrafast laser pulses of ~10^7 uW/um^2. We also demonstrated that the voltage of a few volts can effectively change the magnetic anisotropy of 2D magnets. These efficient controls of 2D magnets potentially open up new avenues towards low-power spintronics and photonics.

[1] C. Gong *et al.*, Nature **546**, 265-269 (2017).

[2] C. Gong *et al.*, Science **363**, eaav4450 (2019).

[3] C. Gong, *et al.*, Nat. Commun. **10**, 2657 (2019).

[4] S.-J. Gong, *et al.*, PNAS **115**, 8511 (2018).

[5] E.-W. Du, *et al.*, Nano Lett. **20**, 7230 (2020).

[6] Y. Gong, *et al.*, npj 2D Mater. Appl. **6**, 9 (2022).

[7] T. Xie, *et al.*, under review (2022).
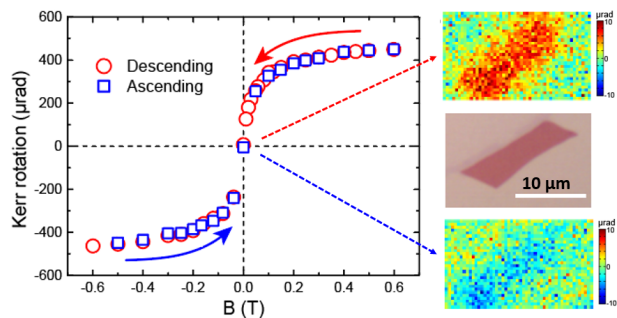
[8] S. Liang, *et al.*, under review (2022).

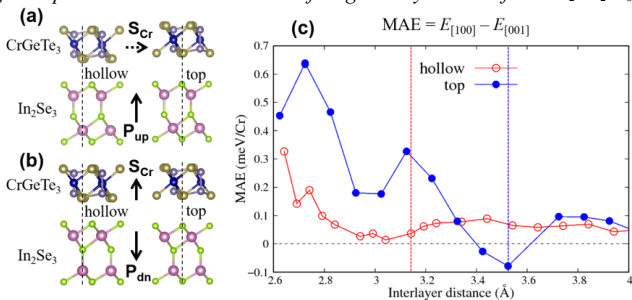*Fig.1: Experimental characterization of magnetic hysteresis of 2D Cr₂Ge₂Te₆.*

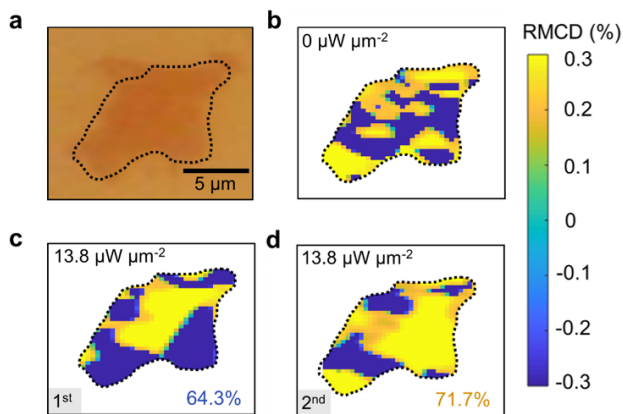*Fig.2: DFT calculation of van der Waals heterostructure multiferroicity.*

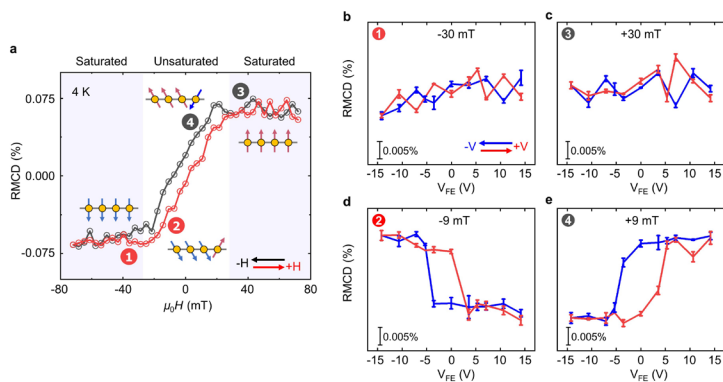*Fig.3: Experimental optical control of magnetic domains in 2D magnets.*

Fig.4: Experimental electrical control of magnetizations of 2D magnets.

Zener-Klein Tunneling and Transit-Time Effects in Cascade Periodic Graphene P-I-N Structures: Amplification and Emission of Terahertz Radiation

V. Ryzhii[1], M. Ryzhii[2], V. Mitin[3], M. S. Shur[4], and T. Otsuji[1]

[1]Research Inst. of Electrical Communication, Tohoku University, Sendai 980-8577, Japan
[2]Dept. of Computer Science and Eng., University of Aizu, Aizu-Wakamatsu 965-8580, Japan
[3]Dept. of Electrical Eng., University at Buffalo, SUNY, Buffalo, NY 14260, USA
[4] Dept. of Electrical, Computer, and Systems Eng., Rensselaer Polytechnic Inst.,
Troy, NY 12180, USA
v-ryzhii@riec.tohoku.ac.jp

The Zener-Klein (ZK) interband tunneling in graphene layers (GLs) with the lateral n-i-n and p-i-n junctions [1-3] results in the nonlinear I-V characteristics that can be used for the rectification and detection of the terahertz (THz) signals. The transit time (TT) delay of tunneling electrons and holes in the junctions in question leads to the phase shift between the THz current and THz voltage causing the negative dynamic conductance in a certain frequency range (resulting in the so-called TT instability). The combination of the ZK tunneling and the TT negative dynamic conductivity enables resonant THz detection [4] and the amplification and emission of THz radiation.

In this presentation, we propose and evaluate the THz devices based on periodic cascade GL p-i-n structures with ungated (chemically doped) p- and n-regions using the ZK tunneling and TT resonances (GPIN-TTs). Figures 1 and 2 show the device structure and the band diagram of one of the device sections. Figures 3 – 6 display the GPIN-TT characteristics. As seen, the real part of the GPIN-TT impedance can be negative at the frequencies where its imaginary part turns to zero due to the TT resonance enabling the THz radiation emission. Figure~6 shows the resulting absorption coefficient of the incident THz radiation, which is negative in the frequency range corresponding to the ZK-TT instability. The instability can be used in the THz sources with the GPIN-TT structure coupled to an antenna, forming the ring circuit configuration, or placed within a Fabri-Perot cavity.

[1] V. V. Cheianov and V. I. Fal'ko, Phys. Rev. B **74**, 041103 (2006).

[2] A. Ossipov *et al.*, Phys. Rev. B **75**, 241401 (2007).

[3] D. Jena, Proc. IEEE **101**, 1585 (2013).
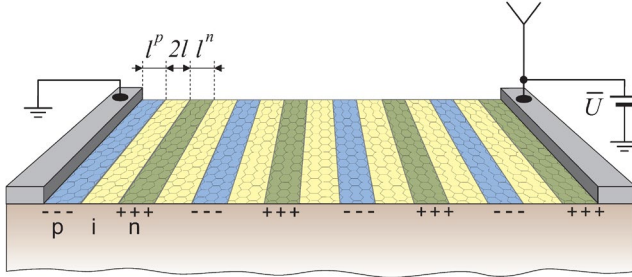
[4] V. Ryzhii *et al.*, Phys. Rev. Appl. (2022), in press.

Fig.1: Cascade periodic ungated GPIN-TTD structure with chemically doped p- and n-regions and undoped i-regions .
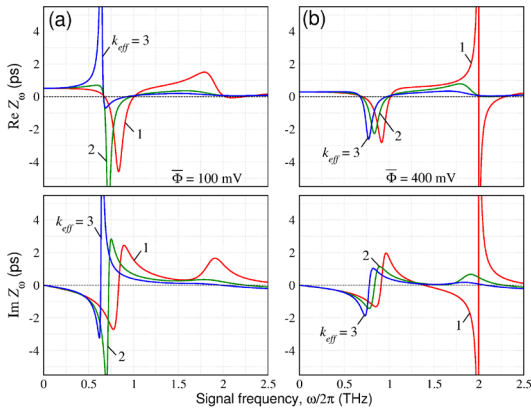

Fig.2: Potential profile of the p-i-n junction in one of the device sections at the dc reverse bias and ac signal voltages.

Fig.3: Real and imaginary parts of GPIN-TTD impedance versus signal frequency for 2l = 0.75μm, L = 0.5μm and different effective dielectric constants k_{eff} and different bias voltages across i-region:
(a) 100mV and (b) 400mV.
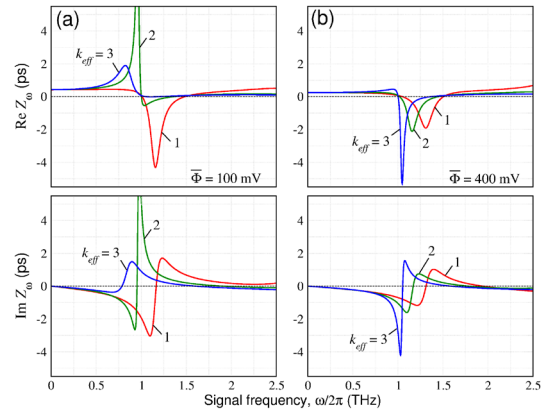
Fig.4: The same as in Fig.3 but for 2l = 0.5μm and L = 0.5μm.

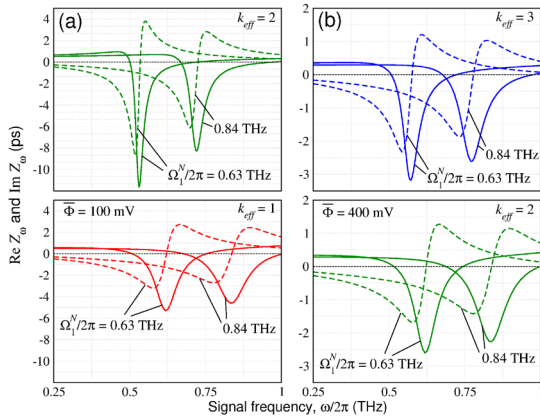

Fig.5: Frequency dependences of real (solid lines) and imaginary (dashed lines) parts of GPIN-TTDs with parameters corresponding to TT resonant frequencies 0.63THz and 0.84THz and different effective dielectric constants at different bias voltages.
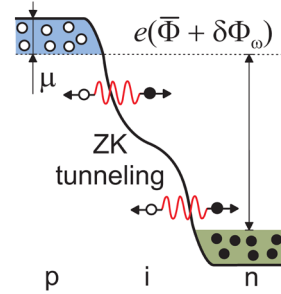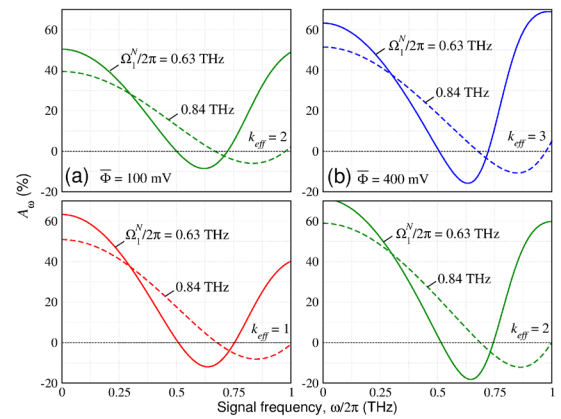

Fig.6: Frequency dependences of the absorption coefficient of the incident THz radiation of GPIN-TTDs with the same parameters as in Fig.5.

Mixed-dimensionality Metal Halide Perovskite Semiconductor Interfaces for Optical Switching and Memory Devices

Jeff Blackburn

National Renewable Energy Laboratory, USA

Hybrid metal halide perovskite (MHP) materials have recently made a rapid and dramatic impact on the world of opto-electronics, exemplified predominantly by their rise to the forefront of next-generation photovoltaic devices. These versatile semiconductors combine organic charge-balancing cations with inorganic metal halide frameworks to create hybrid materials with a wide variety of attractive and novel properties. Beyond their impact in the PV arena, MHPs also have unique and highly desirable properties for both quantum and neuromorphic information processing, where the coupling between light, charge carriers, ions, and the spin degrees of freedom can enable novel opto-electronic devices. These mixed ionic and electronic conducting materials exhibit large dynamic responses of electrons and ions to external stimuli (voltage, current, temperature, light, strain), which could be useful for neuromorphic information processing. Recent studies have also demonstrated that the use of chiral organic cations can open up new avenues for detecting and emitting circularly polarized light, which opens up applications in quantum information science.

In this talk, I will discuss our recent efforts at exploring new opto-electronic functionalities for perovskite-based interfaces, focusing on interfaces with other low-dimensional materials like semiconducting single-walled carbon nanotubes (s-SWCNTs) and layered 2D materials. In recent studies, we have paired highly enriched s-SWCNTs with low-dimensional quantum-confined MHP semiconductors to produce versatile mixed-dimensionality thin-film heterojunctions. These hybrid interfaces capitalize upon the attractive properties of each individual material to enable efficient photoinduced conductance switching with properties and performance metrics that exceed either material alone. Thin-film device studies demonstrate novel functionalities with implications for optically initiated information processing. As examples, we realize room-temperature optical synapse-like devices that can be optically initiated at very low input energies (i.e., fJ/pulse), read either electrically or optically, and electrically erased or habituated.[1] Heterostructures with chiral MHPs can transduce circularly polarized photons into electrical current with current density that is sensitive to the incoming light polarization, enabling chiral photodetectors.[2, 3] Complimentary static and time-resolved optical spectroscopy and electrical transport techniques provide insights into the mechanisms underlying these unique functionalities.

[1] Hao, J.; Kim, Y.-H.; Habisreutinger Severin, N.; Harvey Steven, P.; Miller Elisa, M.; Foradori Sean, M.; Arnold Michael, S.; Song, Z.; Yan, Y.; Luther Joseph, M.; Blackburn Jeffrey, L. Low-Energy Room-Temperature Optical Switching in Mixed-Dimensionality Nanoscale Perovskite Heterojunctions. *Science Advances* **2021,** *7*, eabf1959.

[2] Hao, J.; Lu, H.; Mao, L.; Chen, X.; Beard, M. C.; Blackburn, J. L. Direct Detection of Circularly Polarized Light Using Chiral Copper Chloride–Carbon Nanotube Heterostructures. *ACS Nano* **2021,** *15*, 7608-7617.

[3] Kim, Y.-H.; Song, R.; Hao, J.; Zhai, Y.; Yan, L.; Moot, T.; Palmstrom, A. F.; Brunecky, R.; You, W.; Berry, J. J.; Blackburn, J. L.; Beard, M. C.; Blum, V.; Luther, J. M. The Structural Origin of Chiroptical Properties in Perovskite Nanocrystals with Chiral Organic Ligands. *Advanced Functional Materials* **2022**, 2200454.

Evidence of Hot Carriers in Metal Halide Perovskite Solar Cells

S. Sourabh,[1] H. Afshari,[1] V.R Whiteside,[1] Giles, E. Eperon,[2] Rebbeca A. Schiedt,[3] M. C. Beard,[3] and I. R. Sellers[1]

[1] *Department of Physics & Astronomy, University of Oklahoma, Norman, OK 73019*
[2] *Swift Solar, San Carlos, CA 94070*
[3] *National Renewable Energy Laboratory, Golden, CO 80401 United States*
sellers@ou.edu

Metal halide perovskite an intriguing emerging class of solution-based semiconductors with significant potential for photovoltaics. In this study we investigate the triple halide perovskite $(FA,Cs)Pb(I,Br,Cl)_3$, which is known to be amongst the most stable metal halide perovskite systems available. This stability allows a comprehensive study of the hot carrier dynamics to be assessed under steady-state conditions at high fluence and various temperatures in a device structure.

A systematic set of measurements including simultaneous power-dependent (PDPL) and temperature-dependent photoluminescence (TDPL), and current-voltage (JV) measurements were performed to probe the hot carriers and electron-phonon coupling in operational solar cells. These measurements support the presence of hot carriers in the device in advance of any negative effects due to halide segregation or decomposition. At 100 K, clear evidence of hot carriers was observed via increasing carrier temperatures in the high energy tail of the PL coupled with signatures of hot photocarriers in J-V measurements. At room temperature, however, the blue shift in the PL and high energy broadening characteristic of hot carrier generation at higher laser excitation are shown to compete with a gradual redshift in the PL peak energy as photo induced halide segregation begins to occur at higher lattice temperature.

Ultrafast Carrier Relaxation in Type I and Type II InAs Based Quantum Wells

I. Baranowski[1], Y. Zou[2], D. Vasileska[1],and S. M. Goodnick[1]

[1]*School of Electrical Computer and Energy Engineering, Arizona State University, Tempe, AZ 85287, USA*
[2] *First Solar, Perrysburg, OH 43551, USA*
stephen.goodnick@asu.edu

The ultrashort time scale carrier dynamics of photoexcited carriers in semiconductor nanostructures is critical in controlling energy loss processes, fundamental to the realization of advanced concept photovoltaic devices. In the present work, we compare ensemble Monte Carlo (EMC) simulation of carrier dynamics in semiconductor multi-quantum well (MQW) structures with continuous wave photoluminescence studies performed in type I [1] and type II [2] In(Ga)As mutli-quantum wells (MQWs). The EMC simulations include nonquilibrium hot phonon effects, intervalley scattering, carrier-carrier scattering and degeneracy effects, as well as the conventional scattering mechanisms in III-V materials, all within a multi-subband framework for MQW structures. Nonequilibrium phonons are modeled assuming an anharmonic lifetime for LO modes into acoustic modes. The dependence of carrier temperature with pump power is shown to be primarily due to the build-up of a nonequilibrium LO phonon population that slows the energy loss rate. The LO population is directly related to the carrier generation rate and excess carrier energy, leading to higher steady state carrier temperatures for higher pump powers and shorter wavelength excitation. Intervalley scattering plays a role for short wavelengths while carrier degeneracy leads to reduced energy loss rates at high injected densities. The differences in type I and type 2 MQW systems primarily occurs through the spatial separation of electrons and holes which suppresses electron-hole scattering which is an energy loss mechanism for type I MQWs, which are discussed in this talk.

[1] H. Esmaielpour *et al.*, Nat. Energy **5**, 336–343 (2020).
[2] H. Esmaielpour *et al.,* Scientific Reports 8:12473 (2018).

Enhanced Transmission by Surface Plasmon Antenna for Single Photoelectron Trapping in A Lateral GaAs Quantum Dot

R. Fukai,[1] Y. Sakai,[1] T. Fujita,[1,2,3] H. Kiyama,[1,2,3] A. Ludwig,[4] A. D. Wieck,[4] and <u>A. Oiwa</u>[1,2,3,*]

[1] *SANKEN, Osaka University, Osaka, Japan*
[2] *Center for Spintronics Research Network, Osaka University, Osaka, Japan*
[3] *Center for Quantum Information and Quantum Biology, Osaka University, Osaka, Japan*
[4] *Lehrstuhl für Angewandte Festkörperphysik, Ruhr-Universität Bochum, Bochum, Germany*
*corresponding author: oiwa@sanken.osaka-u.ac.jp

Quantum networks are expected to provide absolutely secure communication, distributed quantum computation and advanced quantum processing [1]. The development of quantum networks for long distances requires quantum repeaters. The spins confined in gate-defined quantum dots (QDs), which have been studied for realizing fault-tolerant quantum computers, have a great potential for the quantum repeaters because of their high electrical tunability, heralding charge sensors and the feasibility of implementing quantum error correction [2,3]. Indeed, recently, the transfer of a photon polarization superposition state to an electron spin superposition state has been demonstrated using a gate-defined QD [4]. However, the efficiency of the trapping of single electrons generated by an absorption of photons in a QD is limited to approximately 0.01 %. To improve the efficiency by reducing the size mismatch between the focused light spot and the QD in the dilution refrigerator, we fabricate a surface plasmon antenna (SPA) on a gate-defined QD and successfully demonstrate an enhancement of the probability of single photoelectron trapping in the QD.

A double QD and nearby charge sensor QD were formed in a Si-delta doped AlGaAs/GaAs single heterostructure. An SPA was fabricated on the left QD of the double QD (Fig.1). The light emitted from a supercontinuum light source was first monochromated and then chopped by mechanical shutters to create light pulses with a 200-μs duration. The attenuated pulse was impinged to the sample in a dilution refrigerator through an objective lens placed in front of the device at low temperature. Then, we performed real-time charge sensing synchronized with the pulsed-light illumination. Figure 2 (a) shows various charge sensing photoresponses (CSPs). The bottom trace accompanied by an abrupt decrease at the illumination and a return to the initial level indicates the trapping of a single photoelectron in the QD and the tunneling of this photoelectron off the QD. The probability of such single photoelectron detection (SPD) in the QD was estimated to be 0.014%. We deduced 5~9 times enhancement of the SPD probability from a comparison with the SPD probability reported for a QD formed in a quantum well [5]. Furthermore, we discuss the impact of the SPA on the photon transmission to the QD from the wavelength dependence of the total probability of both SPD and other types of CSP due to photon absorptions other than the QD.

[1] S. Wehner, D. Elkouss and R. Hanson, Science **362**, eaam9228 (2018).
[2] A. Oiwa et al., J. Phys. Soc. Japan **86**, 011008 (2017).
[3] L. Gaudreau et al., Semicond. Sci. Technol., **32**, 093001 (2017).

[4] K. Kuroyama et al., Phys. Rev. B **99**, 085203 (2019).
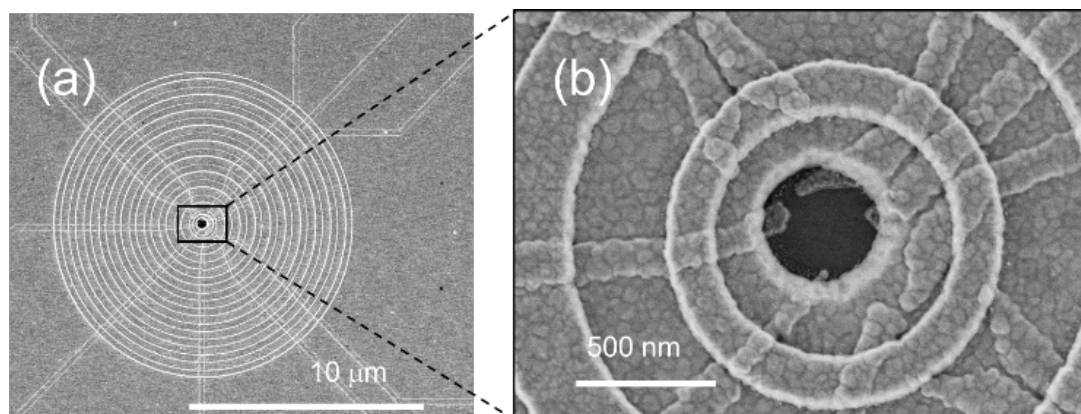[5] K. Kuroyama et al., Sci. Rep. **7**, 2045 (2017).

Fig.1 (a) Scanning electron micrograph image of surface plasmon antenna fabricated on a gate-defined QD. (b)Magnified image of the center aperture and surrounding concentric rings.
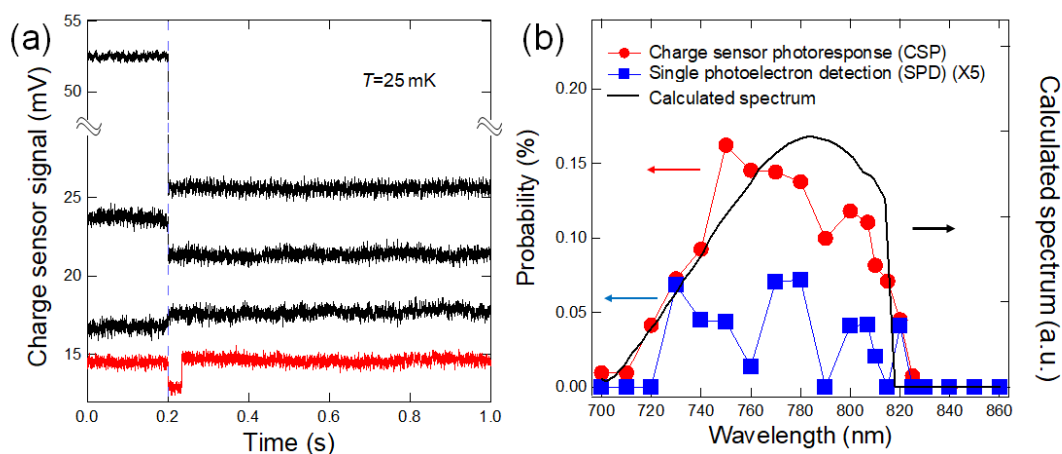

Fig.2(a) Typical real-time charge sensor photoresponse (CSP) signals measured in the QD with SPA. The bottom trace shows the single photoelectron detection (SPD) by the QD. The traces are shifted vertically for clarity. (b) Spectra of CPS and SPD. The SPD spectrum is magnified by 5 times. The solid line is a calculated spectrum.

Electrically and Optically Pumped SiGeSn Laser on Si

D. Buca[1], O. Concepción[1], T. Liu[1], M. Oehme[3], M. El Kurd[4], J Witzens[5], <u>D. Grützmacher[1,2]</u>

[1]Peter Grünberg Institute- 9 and JARA-FIT, Forschungszentrum Jülich, 52425 Jülich,

[2]Peter Grünberg Institute- 10 and JARA-FIT, Forschungszentrum Jülich, 52425 Jülich,

[3]Institut für Halbleitertechnik, University of Stuttgart, Stuttgart, Germany

[4]Université Paris-Saclay, CNRS, C2N, Paris, France

[5]Institute of Integrated Photonics, RWTH Aachen University, Aachen, Germany

d.gruetzmacher@fz-juelich.de

The discovery of the direct bandgap of GeSn alloys with Sn concentrations exceeding 8% led to the development of Si based group-IV optoelectronic devices, such as optically pumped lasers [1,2,3] and photodiodes in the SWIR to MIR range [3]. Improvements in the epitaxial control of the material, in band engineering, and in the understanding of carrier dynamics led to laser devices with very low pumping thresholds at low temperatures [2] and to the design of two color Ge/GeSn imagers [3]. Here we report on the successful fabrication of GeSn optically pumped microdisc lasers operating at room temperature and electrically pumped microdisks lasers with a maximum operation temperature of 100K.

Microdisk lasers were fabricated from GeSn layers with Sn concentrations up to 14 at.%. The fabrication involves bonding the GeSn microdisks to an Al coated substrate, under-etching and subsequent an "all-around" SiN_x stressor layer to induce about 1% of tensile strain into the microdisk cavity [4]. The latter will increase the energy spacing between electrons in the Γ and the L-valleys, hampering thermal escape of electrons from the Γ-valley and thus allow high temperature operations. Fig. 1 shows the performance of these GeSn lasers excited by optically pumping where lasing up to 300 K is clearly demonstrated.

In a second step, the GeSn layer was imbedded in SiGeSn cladding layers to provide electrical and optical confinement as well as a p-i-n diode structure. Here, phosphorous is used as n-dopant and the p-type background doping of the SiGeSn layers have been used for the electrical contacts. Despite this non-optimized laser design, lasing under electrical pumping is observed. Figs. 2-5 show culminated viewgraphs of the properties for ring-shaped microdisc lasers measured at different temperatures in the range from 4-100K and a threshold current around 45 kA/cm^2 at low temperatures. The results document the substantial progress achieved on the path towards electrically pumped GeSn lasers operating at room temperature and at low threshold currents.

[1] S. Wirths et al., *Nature Photonics* **9**, 88 (2015).

[2] A. Elbaz et.al. *Nature Photonics* **14,** 375 (2020)

[3] D. Stange et.al. *ACS Photonics* **3**, 1279 (2016)

[4] E.T. Simola et.al. *ACS Photonics* **8,** 2166 (2021)

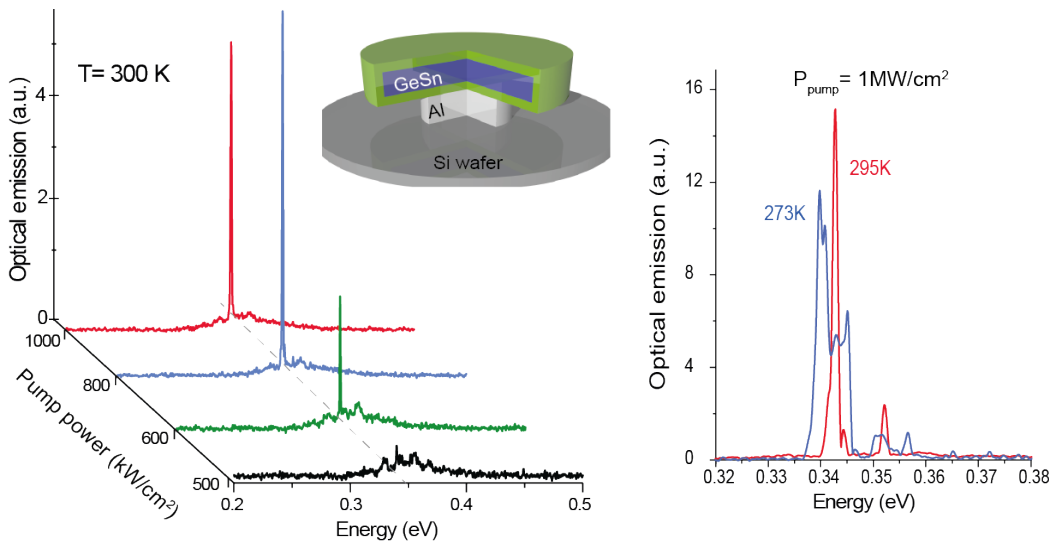Fig.1: Spectra of GeSn microdisc lasers obtained by optical pumping at room temperature. The dependence on pumping is show in the left figure where lasing is obtained for pump powers exceeding 500 kW/cm². The right figure, depicts high resolution spectra, shows multimode emission and its temperature dependence.
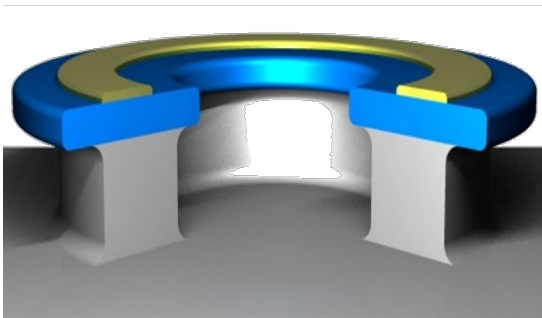

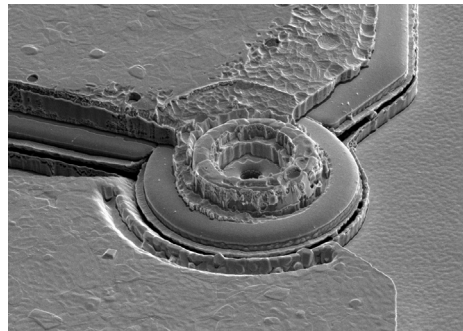Fig.2: Schematic view of the ring-shaped laser fabricated for electrical pumping.

Fig.3: SEM image of the laser prepared for electrical pumping having a diameter of 11µm and a diameter of the inner hole of 2 µm.
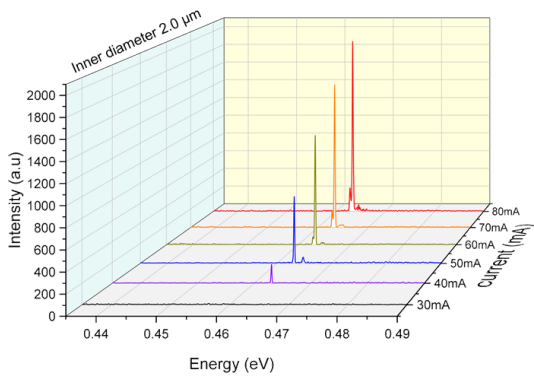

Fig.4: Spectra of SiGeSn/GeSn laser in dependence on pump currents. The intensity grows exponentially with the pumping power.
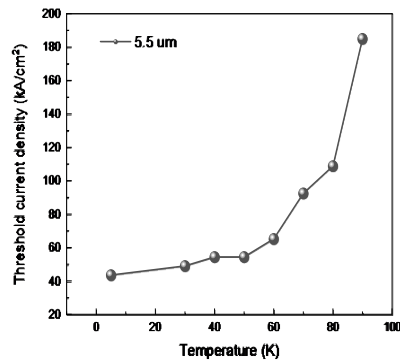

Fig.5: Dependence of the threshold currents on the temperature.

Extended Ultraviolet (EUV) Programmable High-Efficiency Grating Based on a Structural Metastability in Charge-Configuration Devices Based on 1T-TaS₂

Igor Vaskivskyi[1], Emil Bozin[2], Ricardo Mincigrucci[3] and Dragan Mihailovic[1]

[1] *Jozef Stefan Institute, Jamova 39, 1000 Ljubljana, Slovenia*

[2] *Condensed Matter Physics and Materials Science Division, Brookhaven National Laboratory, Upton, NY 11973, USA*

[3] *Elettra Sincrotrone Trieste S.C.p.A., Strada Statale 14, km 163.5, 34149 Basovizza, Italy.*

dragan.mihailovic@ijs.si

Metastable electronic states in quantum materials such as the prototypical dichalcogenide tantalum disulphide offer many potential uses in diverse devices, ranging from computer memories [1–3] to nonlinear devices, such as oscillators [4–6] and detectors [7]. Metastability in such materials is primarily discussed in terms of electronic ordering phenomena, and topologically protected electronic states in particular. Yet the driving force behind such phenomena is intimately tied to the interaction of charge with the lattice. This leads to carrier localization and electronic correlation-induced ordering, that also causes a local *structural* metastability with an exceptionally large amplitude along the direction perpendicular to the layers in 1T-TaS₂. Using scanning tunneling microscopy, x-ray PDF techniques of local structural deformations and supporting theoretical modeling, we show that the lattice response associated with metastable topologically protected charge ordering is anomalously large. The effect can be used to construct controllable optical modulators for EUV radiation. Here we demonstrate the creation of a metastable programmable nanoscale transient grating by interfering two sub-picosecond EUV beams generated at the Fermi FEL facility (Fig. 1). The metastable grating is found to exhibit unprecedented efficiency for modulating EUV radiation enhance by large interlayer expansion (Fig.2) The grating can be repeatedly written by interfering EUV beams and erased thermally, or with a single EUV laser beam (Fig.3).

[1] D. Mihailovic *et al.*, APL **119**, 013106 (2021).

[2] R. Venturini *et al.*, APL **120**, 253510 (2022)

[3] A. Mraz *et al.*, Nano Letters **22**, 4814 (2022).

[4] G. Liu *et al.*, Nat Nanotechnol **11**, 845 (2016).

[5] A. Geremew *et al.*, Acs Nano **13**, 7231 (2019).

[6] A. Mohammadzadeh *et al.*, Appl Phys Lett **118**, 093102 (2021).

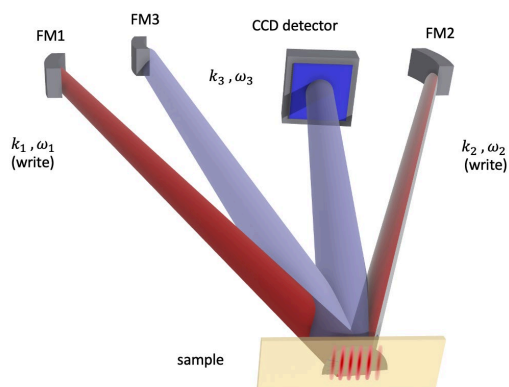[7] X. Wang *et al.*, Advanced Materials **30**, 1800074 (2018).

Fig.1: The EUV metastable grating on 1T-TaS$_2$ is created by the two 'write' beams with different k. The third beam is deflected by the grating. The excitation wavelength $\lambda_{exc} = 39.9$ nm, 31.3 eV is resonant with Ta transitions. The probe wavelength $\lambda_{pr} = 13.3$ nm (93.2 eV) is non-resonant.
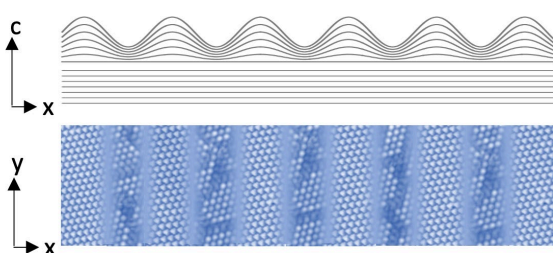

Fig.2: A schematic representation of the structural modulation caused by the nanoscale electronic modulation. The pitch is given EUV wavelength, and is not intrinsic to the material. The uniform regions correspond to the commensurate CDW, while the domain wall regions correspond to the nearly commensurate phase.
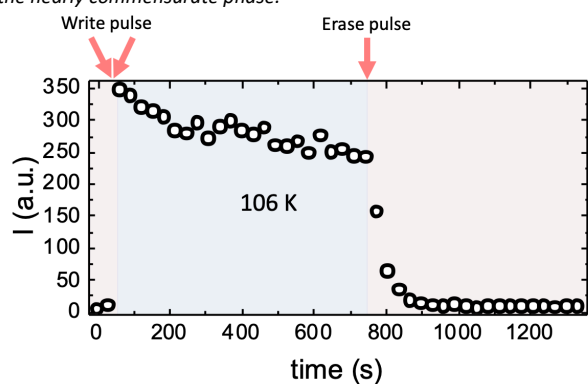

Fig.3: Intensity of the deflected EUV beam measured at 100K. The grating is erased by spatially uniform illumination of one of the EUV beams.

Silica Based Nanomaterials for Sensors Applications: Challenges, Opportunities and Risks

<u>A. Lobnik</u>[1,2], T. Lobnik[2], A. Košak[1,2], A. Hadela[2], L. Popović[2],

[1]*DUniversity of Maribor, Faculty of Mechanical Engineering, Center of Sensor Technology, Smetanova 17, 2000 Maribor, Slovenia*

[2]*IOS, Institute of Environmental Protection and Sensors, Beloruska ulica 7, 2000 Maribor,*

Aleksandra.lobnik@um.si

Due to the increased *specific area - to - volume* ratio (*S/V*), silica based nanomaterials may have different and in many cases better chemical and physical characteristics than bulk materials. Many of these properties can be improved by surface modification and functionalization of nanomaterials, which can be done by altering their functionality and characteristics of their surfaces, such as roughness, hydrophilicity/hydrophobicity, surface charge, biocompatibility, and reactivity. In this way, the functionality of nanomaterials can be adapted to the desired application. Due to the extremely fascinating and useful chemical and physical properties, nanomaterials exhibit an interest in many fields of applications such as sensor technology, biomedicine and biotechnology, environmental protection, photonics and, production of paints and varnishes, textiles, footwear, packaging, electronics, aerospace and automotive, etc. Although nanomaterials, on the one hand, offer technical and commercial opportunities and challenges, on the other hand, they can pose a risk to the environment and raise concerns about the health and safety of humans and animals, as regulation of nanomaterials is debated and many questions related to the risks of exposure to nanomaterials are still unanswered.

This presentation will introduce some recent examples from our Sensor Research Group demonstrating the use and challenges that may be tackled by functional nanomaterials, and some risks will be briefly mentioned:

(a) In the "*Safety and protection*" as an optical chemical sensors for food quality control, detection and protection against UV radiation, and toxic organophosphates. Optical chemical sensors based on mesoporous silica (SiO_2) and titania (TiO_2) nanomaterial became very widespread in the last decades and rely on the use of "sol-gel" materials, which include e.g. indicators, dyes and other additives. Our group recently developed a variety of novel "sol-gel" materials in the form of spherical nanoparticles and thin films containing specific dyes which enable more reliable sensing of important parameters such as UV radiation, oxygen, temperature, pH, etc., which will be presented together with the sensing requirements of sensitivity, selectivity, stability, etc. [1, 2]

(b) In the "*Health*" as an optical chemical sensors for the detection of disease states *in vitro* and *in-vivo*, as well as superparamagnetic hollow spherical nanostructures for sensors as

well drug delivery, etc.. Hollow-type nanostructures of superparamagnetic iron-oxide shell containing antitumor therapeutic drug "doxorubicine" (DOX) in the cavity as well indicator dyes, were prepared by using new modified hard-template method where mesoporous SiO$_2$ particles served as the templates. This new method of preparing hollow spheres was patent protected granted by the Intellectual Property Office, London [3].

[1] N. Frančič, A. Košak, A. Lobnik. J. of Sol-Gel Sci. and Technol. 79 (2016) 3.

[2] P. Nedeljko, M. Turel, A. Košak, A. Lobnik. J. of Sol-Gel Sci. and Technol. 79 (2016) 3,

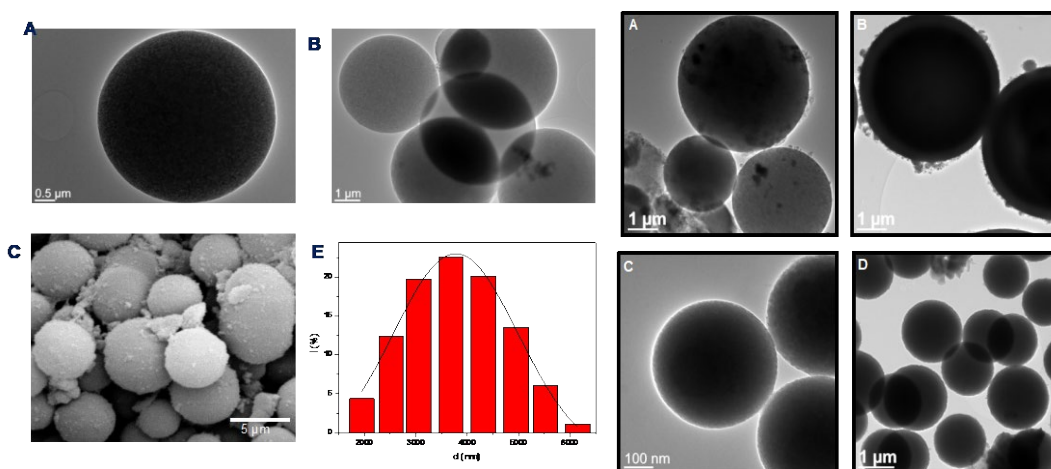[3] A. Košak, M. Lakić, A. Lobnik. GB2526659 (B). London: Intellectual Property Office, (2017).

Fig. 1: TEM micrographs of silica particles. (A-B), SEM microgram (C), and particle size distribution (E) of MPS 5 particles
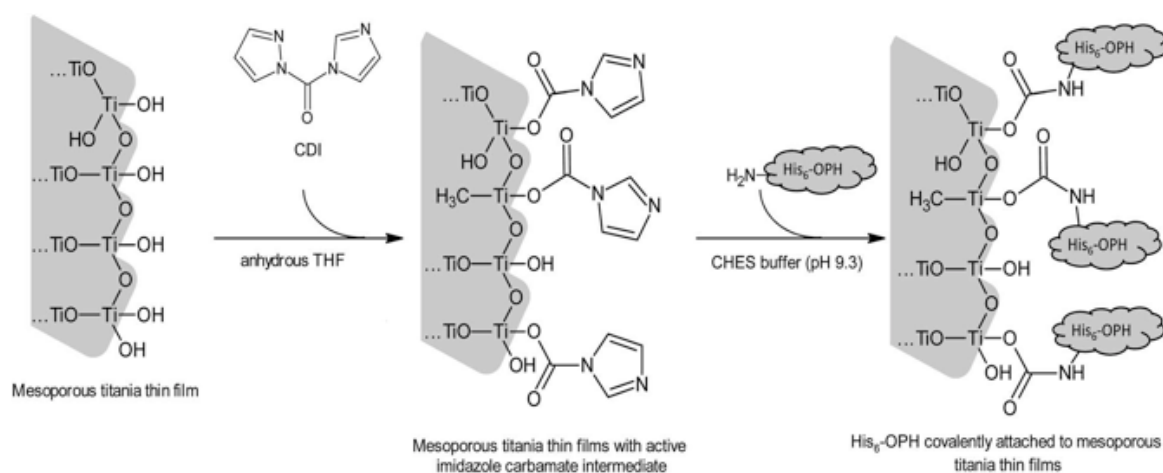

Fig. 2:. Schematic representation of the preparation route of His6-OPH-conjugated mesoporous titania thin films trough CDI mediated reaction.

Two-dimensional Material Transfer Station for Twisted Bi-Layer Graphene and Heterostructures

<u>A. Gasbarro</u>[1,2], R. Ordoñez[1], C. Hayashi[1], C. Torres[1], K. Liotta[1], J. Weldon[2]
[1]Graphene Microfluidics Laboratory,
Naval Information Warfare Center Pacific, Pearl City, Hawaii
[2]Department of Electrical Engineering, College of Engineering,
University of Hawaiʻi at Mānoa, Honolulu, Hawaiʻi
agasbarr@hawaii.edu

To make twistronics research more available to the masses, we demonstrate two-dimensional (2D) material stacking with a custom in-house 2D material transfer station. In 2018, researchers from MIT discovered unconventional superconductivity employing two stacked layers of graphene with ~1.1˚ offset between the layers producing a Moiré pattern [1]. More importantly, twisted nanomaterial bilayers exhibit ability to be tuned from superconducting, metallic, or insulating states simply by adjusting voltages such as in a hall bar structure. However, to this day, twisted bilayer research has been limited to a few laboratories and any explanation of the transfer station is limited. To make this research more accessible to standard research labs, we disclose a 2D transfer station utilizing a traditional laboratory microscope and optomechanical components. With our setup, we transferred hexagonal Boron Nitride (hBN) to and from and silicon substrate to produce a stack of 2D material. This research is part of the first year's effort by the Naval Information Warfare Center Pacific to fabricate qubit circuits using applied magic angle graphene.

[1] Cao, Y., Fatemi, V., Fang, S. et al. Unconventional superconductivity in magic-angle graphene superlattices. Nature 556, 43–50 (2018). https://doi.org/10.1038/nature26160
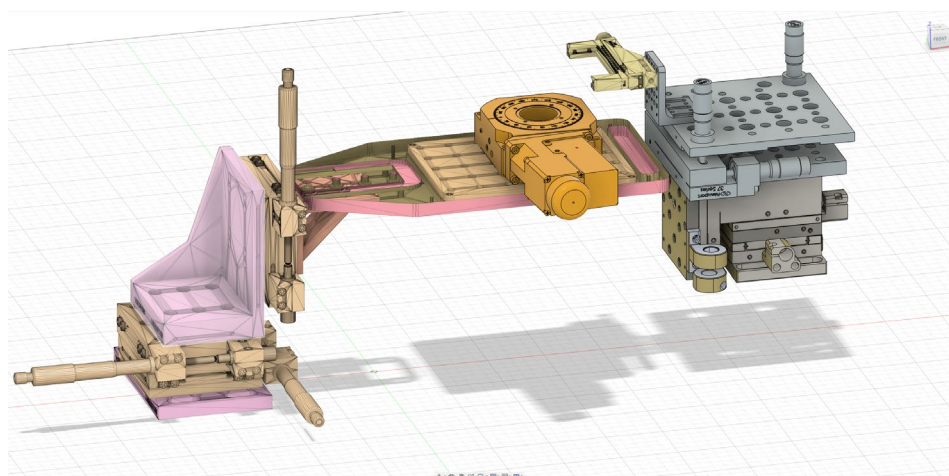
Fig.1: 3D Model of the 2D material transfer station, the system is comprised of 2 X-Y-Z translation stages, a tip, tilt and spin stage, a micro controlled rotational stage, and a heating element.
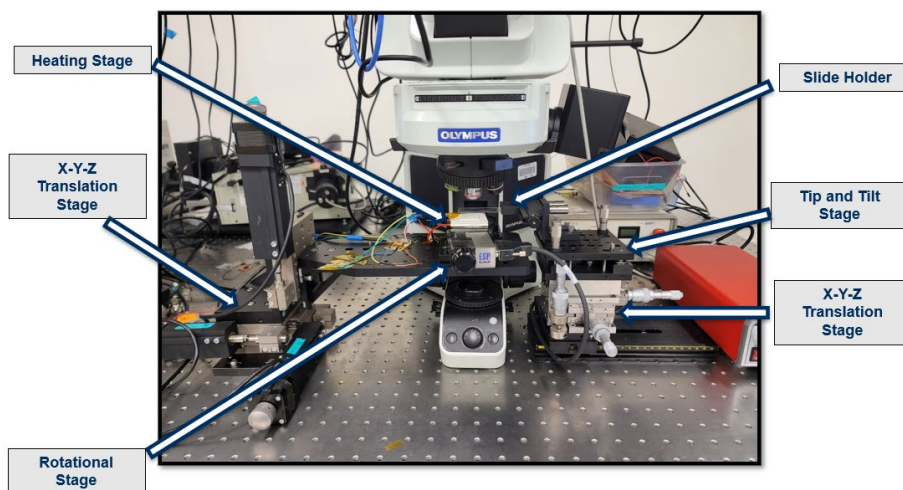

Fig.2: Labeled image of 2D material transfer station. (Left) Thorlabs XYZ translation stage with 50mm linear actuators, (Center) MKS Newport rotational stage, Olympus BX upright microscope with 20x, 50x, and 100x objective lenses, Thorlabs heating stage, and (Right) MKS Newport XYZ translation stage, MKS Newport tip, tilt, spin stage, Thorlabs slide holder.

Fig.3: Exfoliated 2D hexagonal Boron Nitride (hBN) on Nitto SPV224 PVC Vinyl tape.
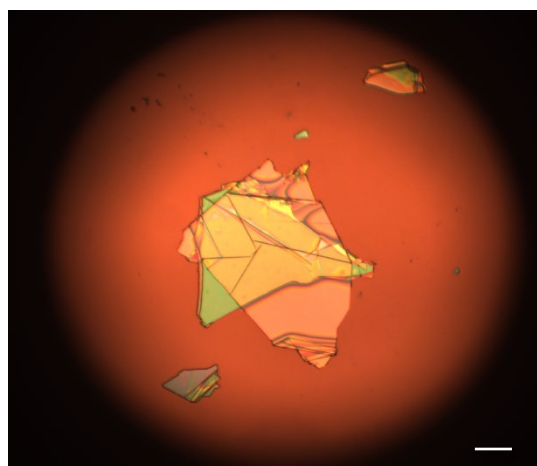

Fig.4: 2D hexagonal Boron Nitride (hBN) flakes stacked and rotated using 2D transfer station. Scale bar = 200 microns.

Optimized Fabrication of Graphene-Based Device Patterns Via Low Power, Low Pressure Oxygen Plasma Etching

S. Olson[1], K. Hood[1], and J. Jiao[1]

[1]Department of Mechanical and Materials Engineering, Portland State University, Portland, OR, USA

jiaoj@pdx.edu

The fabrication of graphene-based field effect transistors and other devices necessitates the ability to pattern and etch the 2D material reliably at the micro- and nanoscale, without imparting damage that would negatively impact device performance. The standard method for creating graphene microstructures is patterning via electron beam lithography (EBL) with a polymethyl methacrylate (PMMA) resist, followed by development of the resist and etching of exposed graphene via oxygen plasma [1]. Frequently, this method results in damage to covered graphene, as well as undercutting of the plasma resulting in poor representation of features [2]. In this work, low power oxygen plasma etching was investigated. The results demonstrate the ability to fully etch exposed graphene, while keeping resist-covered graphene safe from damage.

The graphene used in this work was sourced commercially from Grolltex on a 4" SiO_2 wafer. The wafers were exposed to oxygen plasma in a KJL AXXIS PVD system with an asher filament unit. Oxygen flow was maintained at 3 sccm, which resulted in a chamber pressure of 1 mTorr. Filament voltage and current levels were adjusted to achieve the desired power output.

Fig 1. shows optical images and average Raman spectra of graphene films post-exposure to varying powers and durations of oxygen plasma [3]. Fig 2 shows the 50 W 30 sec plasma etching scheme as used on an actual patterned device (a graphene FET). Graphene channel width is maintained with minimal undercutting, as shown by the SEM micrograph in comparison to the lithography file. The Raman map (the magnified area of Fig 2c) shows a clear delineation of etched and protected zones. The protected zones show minimal increase in D:G peak intensity ratio, confirming the lack of significant damage to the film. These results demonstrate the ability of low-power plasma to prevent damage to resist-covered graphene films, combined with the use of low-pressure environments to prevent undercutting during etching to maintain device dimensional integrity.

[1] I. Childres *et al.* New Journal of Physics **13**, 025008 (2011).

[2] J. Sun *et al.* Applied Physics Letters **106**, 033509 (2015)

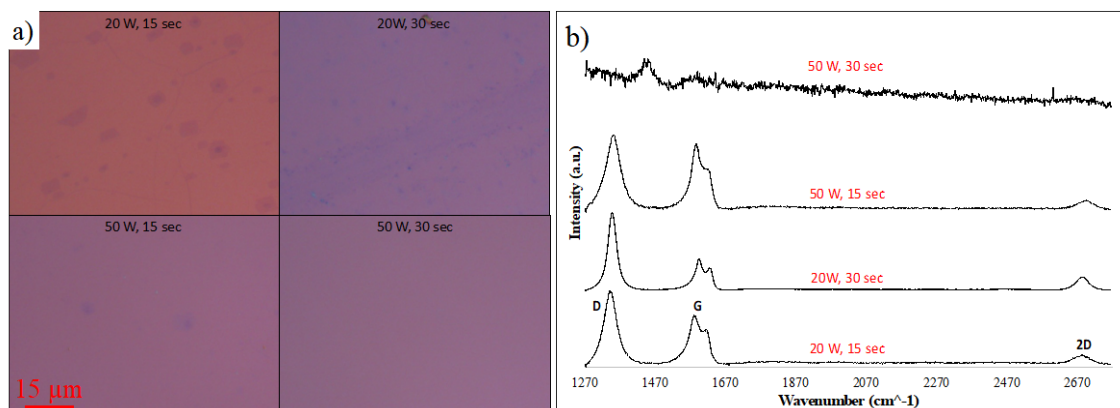[3] A. Ferrari *et al.* Physical Review Letters **97**, 187401 (2006).

Fig.1: Plasma tests were conducted at 20 W and 50 W for 15 sec and 30 sec exposure times. (a) Optical images of exposed wafer surface post-etch, showing minimal film removal at 20 W even with extended duration. 50 W at low exposure time etches most of the film but adlayers remain, etching for longer completely removes the graphene film. (b) Average Raman spectra from 10 μm x 10 μm maps of wafer surfaces post-etch. 20 W tests show damage imparted to graphene (increase in D:G peak ratio), but graphitic films still remain. The 50 W 30 sec etching recipe showed no signs of graphitic material on the exposed surface.
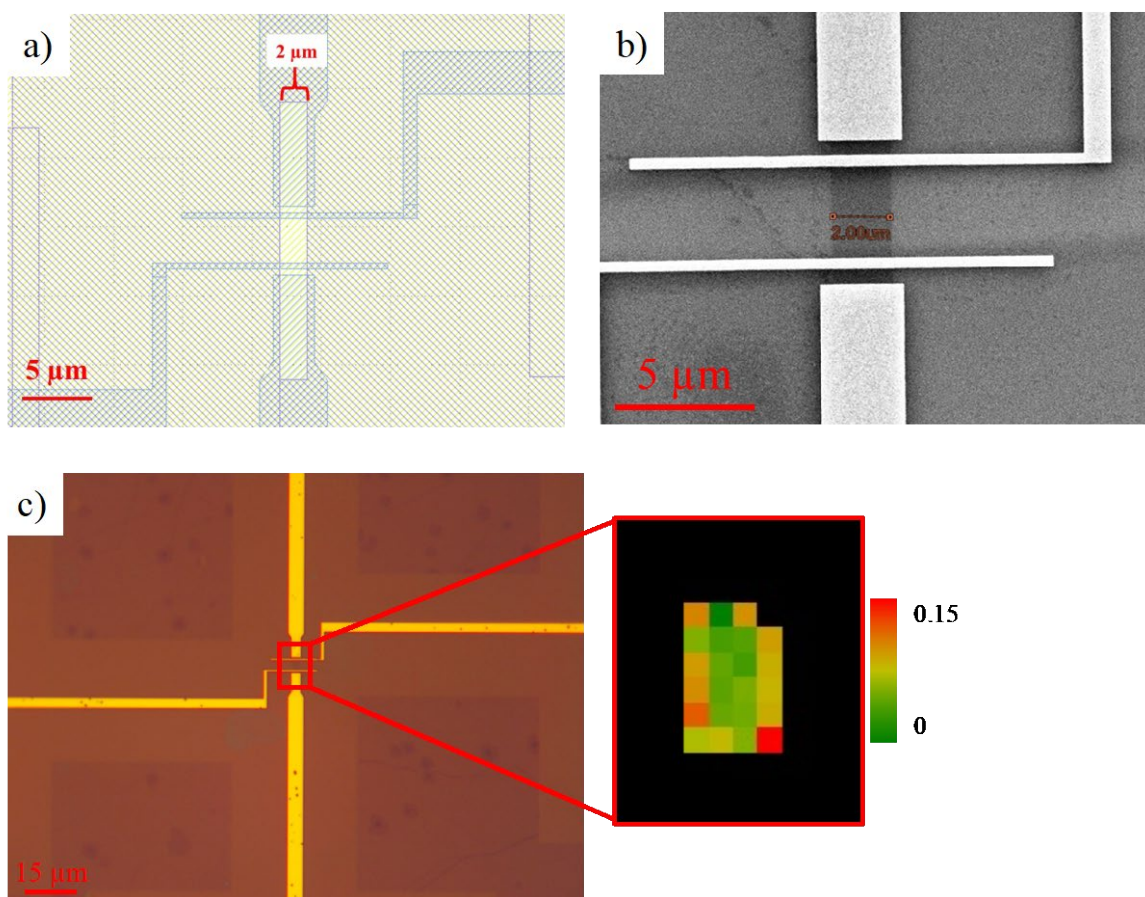

Fig.2 (a) Lithography file of GFET device showing 2 μm channel width target, (b) An SEM image of a GFET device showing pattern dimensional integrity post-etch at 50 W for 30 sec, (c) Optical image of a typical GFET device pattern showing clear delineation between etched and non-etched graphene. Corresponding D:G peak ratio map (an indicative parameter for defects: the smaller the D:G ratio the less defective the area measured). Raman map of channel shows max ratio of 0.15, with the majority of the channel <0.1. Most graphene damage occurs at the edge of the channel pattern, which is to be expected. All black pixels are below the signal to noise threshold of 15 (i.e., no significant peaks).

Data-centric Artificial Intelligence in Quantum Information Science

Sanjaya Lohani[1, *], Joseph M. Lukens[2], Ryan T. Glasser[3], Brian T. Kirby[3,4], and Thomas A. Searles[1]

[1]Department of Electrical and Computer Engineering, University of Illinois Chicago, Chicago, IL 60607, USA

[2]Quantum Information Science Section, Oak Ridge National Laboratory, Oak Ridge, TN, 37831, USA

[3]Tulane University, New Orleans, LA 70118, USA

[4]DEVCOM US Army Research Laboratory, Adelphi, MD 20783, USA

*slohan3@uic.edu

Artificial Intelligence (AI) has found broad applicability in quantum information science, where existing AI techniques are often applied without significant alterations to network architectures. However, the concept of data-centric AI suggests that incorporating domain-specific knowledge related to the underlying structure of quantum mechanics could further improve performance. Here we propose physics-inspired data-centric heuristics for AI systems used in quantum information science and demonstrate their efficacy using a neural network trained for the task of quantum state reconstruction. While some presented heuristics are translations of well-known concepts, such as the importance of diversity in training sets, we also find it is not always optimal to engineer training sets to match the expected distribution of a target scenario. Instead, performance improves when training sets are biased to be more mixed than the target distribution. We argue this is due to the heterogeneity in the number of free variables required to describe states of different purity.
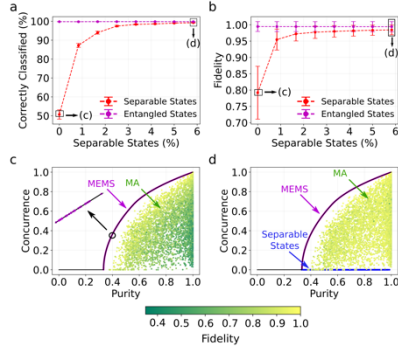
Fig. 1. (a) Entanglement-separability classification accuracy and (b) network reconstruction fidelity versus the percentage of separable states added to a training set containing entangled states. Reconstruction fidelity for test states from the MA distribution for (c) a MEMS-only trained network and (d) after adding a small fraction of separable states into the training set. MEMS (separable) training states are shown by magenta (blue) dots. A small portion of the MEMS line is magnified and shown in the top-left inset. The MA distribution test sets are shown by the inner dots, with shading indicating their reconstruction fidelity. The rectangular boxes in (a,b) represent the pre-trained networks that are used for results in (c,d).

Fig. 2. (a) Reconstruction fidelity for NISQ-sampled states. The use of various training distributions constitutes a data-centric approach and is shown by an arrow pointing upwards, whereas varying number of trainable parameters is an example of a model-centric approach as indicated by the arrow pointing to the right. The domain from 10^6 to 10^7 parameters is magnified in the left inset. The rectangular box in the inset indicates the network architecture used for the results described in Fig. 4. (b) Joint purity-concurrence distributions for the engineered and IBMQ sets, shown by brown and green dots, respectively.
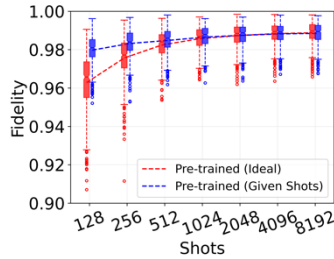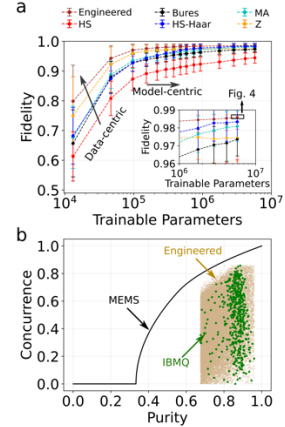

Fig. 3. Reconstructing the NISQ-sampled distribution with simulated measurements performed with shots ranging from 128 to 8192. The red line is the reconstruction fidelity when performed using a network trained on ideal measurements which themselves have no statistical error. The blue line is the reconstruction fidelity when a separate network has been trained for each shot level such that the training set was simulated at the same shot level as the test set.
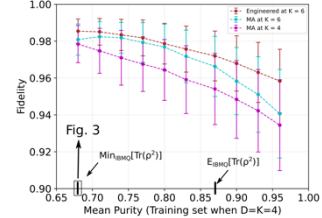

Fig. 4. The two vertical tick marks along the x-axis emphasized with arrows correspond to the scenarios where the mean purity of the training set matches the minimum and mean purity of the NISQ-sampled states when D = K = 4. The mean purity of the states (labeled with subscripts IBMQ) is shown by a vertical line on the x-axis as indicated by an arrow. The error bars represent one standard deviation from the mean.
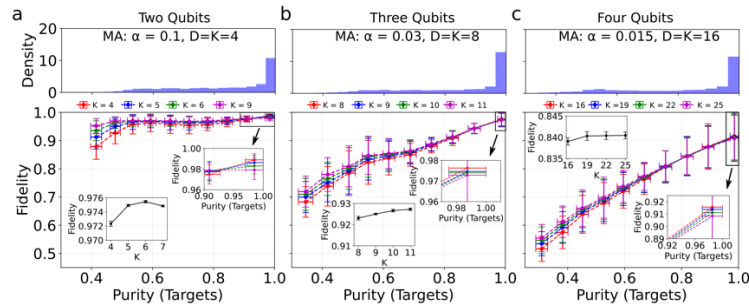

Fig. 5. Reconstruction fidelities versus test state purity for (a) two-qubit, (b) three-qubit, and (c) four-qubit quantum systems. The histograms for the purity distributions of the target states are shown at the top. In the lower plots, the red lines indicate reconstruction when the network has been trained using the same distribution (sampled separately) as the test set. Each other curve (blue, green, purple) represents the reconstruction fidelity when the network is instead trained on a more mixed version of the test distribution. The reconstruction fidelities averaged over all test states are shown in the insets, for each K.

https://arxiv.org/abs/2201.09134

Tunable Infrared Detector for Object Recognition

V. Mitin[1], S. Tulyakov[1], G. Biswal[2], M. Yakimov[2], V. Tokranov[2], and S. Oktyabrsky[2]

[1]EE Department, University at Buffalo, SUNY, Buffalo, NY, USA
[2]Faculty SUNY Polytechnic Institute, Albany, NY, USA
vmitin@buffalo.edu

With the goal to build tunable infrared (IR) camera for object recognition controlled by artificial intelligence, we are developing a tunable infrared detector. Fig. 1 shows an example where IR images even during the daytime can reveal some features that are not available on conventional RGB cameras for the visible spectrum. Moreover, there is an advantage to getting images at least in two different IR wavelengths. The two-color IR focal plane arrays were demonstrated multiple times, but they typically utilize two stacks of quantum well (QW) infrared photodetectors (QWIPs) with the fixed spectral response, contrary to our design that offers continuous control of the spectral response in asymmetrically doped double QW structures.

The design, growth, and characterization of QWIPs with different GaAs QWs width and depth (through x-concentration of the $Al_xGa_{1-x}As$ barrier) of GaAs/AlGaAs structure was performed to obtain the 8 to 12 μm wavelength detection. An example of QWIP epitaxial layer design is shown in Fig.2. The structures were grown by molecular beam epitaxy with a QWIP section sandwiched between two highly n-type doped ($2x10^{18}$ cm^{-3}) GaAs contact layers. The QWIP section consisted of 25 periods of double GaAs QW layers, one of which was δ-doped to the sheet density of $5x10^{11}$ cm^{-2} and separated by a 3.1nm thin $Al_{0.2}Ga_{0.8}As$ barrier from the other. An example of the QWIP spectral response at various biases is shown in Fig. 3 and reveals two bands at 5.5 and 8 μm with tunable sensitivity. The measurements confirm the results of simulations: the spectrum reveals two bands determined mostly by the splitting of the ground-state level in a double QW structure (Fig. 4). The asymmetric double QW design allows for control of electron population on the split ground-state level by the external electric field. The ratio of the responsivities of the two bands is controlled over an order of magnitude (Fig. 5).

We investigated the benefits of the proposed sensor by collecting a dataset of 603 IR image pairs (Fig.1, IR1, IR2) and performing a task of object detection (1,305 person and 608 car annotations). Due to the increased noise of the camera with filter, additional statistical denoising was applied and we used YOLOv4 [1] as an object detection network (Fig. 6). Fusion of the detection results of two cameras was performed by merging detection candidates and selecting ones with best scores. The results indicate the improved performance of two spectrally offset IR sensors, which confirms our hypothesis on the benefits of the tunable IR sensor (see Table).

[1] Bochkovskiy, C.-Y. Wang, and H.-Y. M. Liao, "YOLOv4: Optimal Speed and Accuracy of Object Detection," https://arxiv.org/abs/2004.10934, 2020.

Fig. 1. Sample triplet of collected images consisting of RGB, wide band (8-14 μm) LWIR IR1 image, and 9.5 μm (0.5 μm band) IR2 image. Note hot brakes and muffler under the car on the IR images.
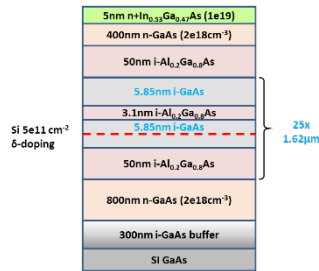

Fig. 2. Schematic epitaxial layer structure of QWIP with asymmetrically doped detection elements (epi growth N1845 with the results shown below).
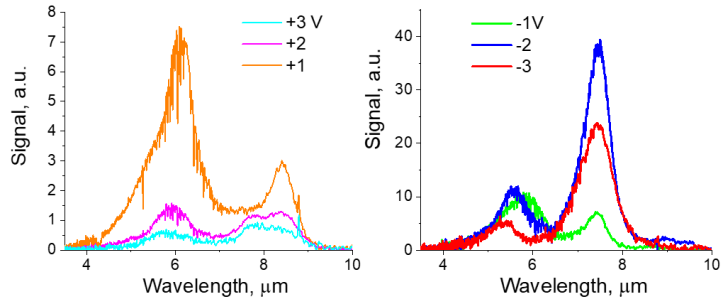

Fig. 3. Experimental FTIR spectral response of QWIPs at 77K as a function of applied bias for positive and negative voltage.
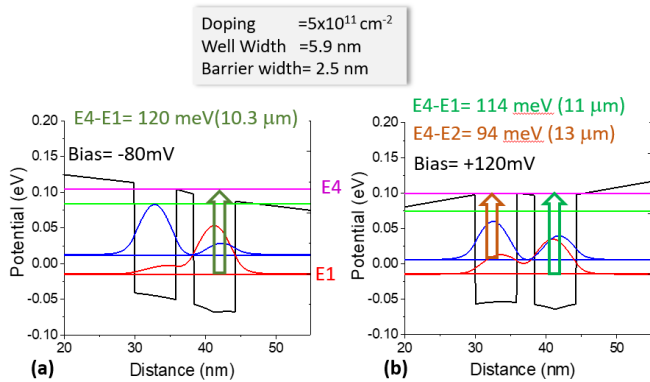

Fig. 4. Example of calculated potential and wavefunctions in the double quantum well under bias (a) -80 mV and (b) +120mV. The strongest transitions with their energies are indicated. The biases correspond approximately to -1.7V and +2.6V, respectively, applied to the 25-period structure.
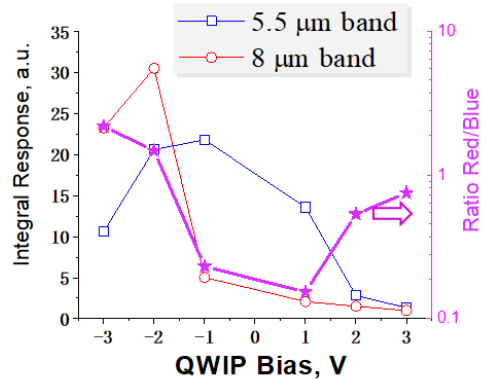

Fig. 5. Experimental integral response of the two bands controlled by the applied bias to the QWIP structure, and the sensitivity ratio of the two bands.
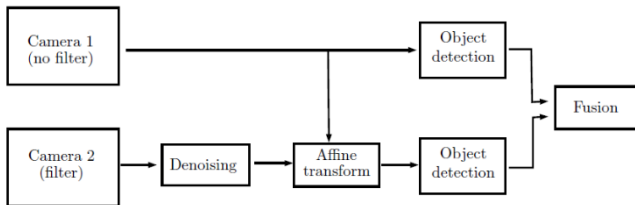

Fig. 6. Developed object recognition system.

Table. System performance for object detection task; performance for each class (person, car) is provided along with overall performance. Numbers are AP@[.5:.05:.95] (primary performance metrics for MSCOCO dataset); a bigger number is better.

	person	*car*	*all*
IR1	19.32	**20.93**	20.12
IR 2	20.27	1.58	10.93
usion	**21.67**	19.27	**20.47**

Nd-Gd Nanoparticles for Multi-Functional Bioimaging

J. Echeverria[1], and T. Sztynda[1]

[1] *Faculty of Sciences, University of Technology, Sydney, NSW, Australia*

Jacqueline.Loyola-Echeverria@uts.edu.au

Novel nanoparticles (NPs) have immense promise in the fields of biomedical imaging, diagnostics, and theragnostic agents [1]. Significant progress has been made in this area, however, given the diverse composition, shapes, and sizes of NPs which can be synthesized we have only begun to scratch the surface of their potential. Of special interest are inorganic functionalized lanthanide ions (Ln3+) nanoparticles (NPs), such as Neodymium and Gadolinium, which provide stable and optically active transitions for bio-medical applications, as well as the potential to synthesize magnetic nanoparticles for enhanced non-invasive imaging techniques, such a magnetic resonance imaging (MRI).

Gadolinium-doped nanoparticles (Gd NPs) have been shown to function as contrast imaging agents for magnetic resonance imaging (MRI) [2], surpassing the performance of traditional molecular gadolinium based sources due to the high level of Gd doping in the nanoparticles. Such nanoparticles can be functionalized with organic polymers to make them bio-compatible and hydrophilic. By increasing the effectiveness of the MRI contrast agent during a scan, we can for instance improve the detection of early onset Alzheimer's.

Here we demonstrate, the synthesis of 20 nm hexagonal Nd-F nanocrystals (figure 1), which can then be doped with up to 30% Gd through an ion exchange process. The resulting particles display strong photoluminescence due to the f-shell Nd transitions (figure 2), which can be leveraged for direct imaging applications. Additionally, we test the magnetic properties of the nanoparticles to determine their potential as MRI contrast agents. We observe that the NPs are extremely promising as both R1 and R2 based contrast agents [3], showing a three-fold increase in relaxivities (figure 3). We also developed an efficient polymer coating process for the NPs, and demonstrate they are non-toxic to human neuronal cell lines and demonstrate negligible leaking of lanthanide ions in-vitro (figure 4). Our particles are extremely promising as a multi-functional bio-sensors, and further study will provide an in-depth look at their in-vivo and in-vitro behavior.

[1] X. Han *et al.,* Nanoscale, **11**, 799-819 (2019).

[2] M. Bottrill *et al.,*. Chem. Soc. Rev. **6,** 557-71 (2006).

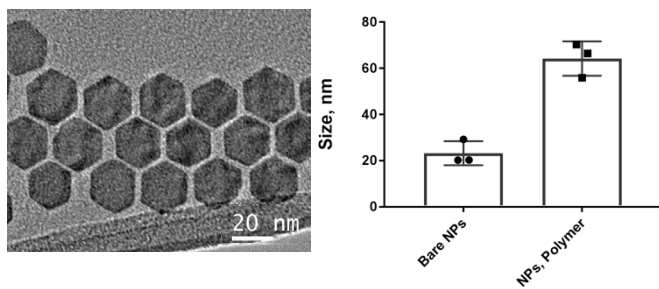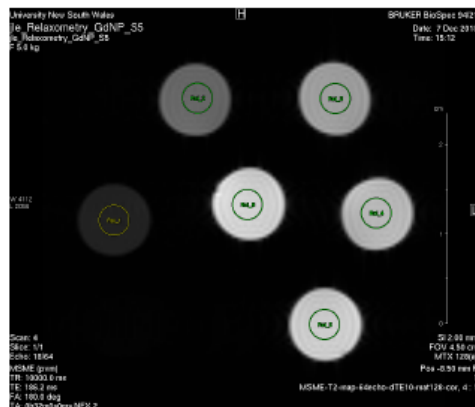[3] S. Laurent, *et al*. J. Nucl. Med. Mol. Imaging., **6,** 586-603 (2009).

Fig.1: Nanoparticle synthesis. a. Schematic of synthesis of Gd, Nd-doped sodium fluoride NCs. b. TEM image of bare hexagonal NPs of 20 nm. c. Nanoparticle size distribution determined by Dynamic Light Scattering.
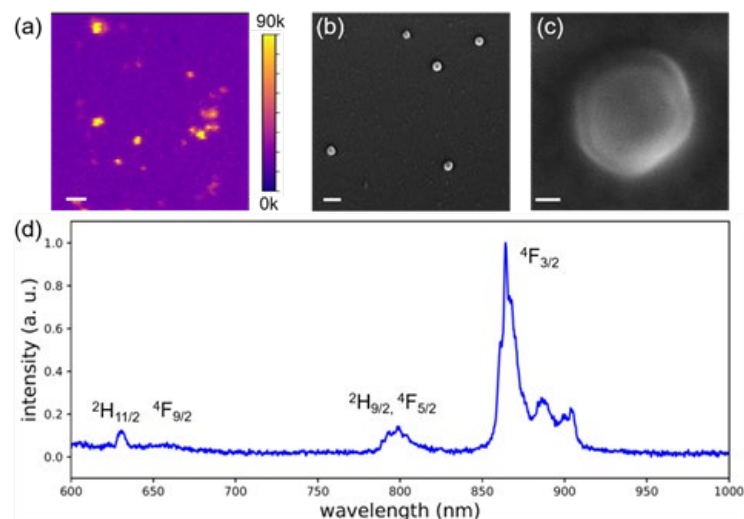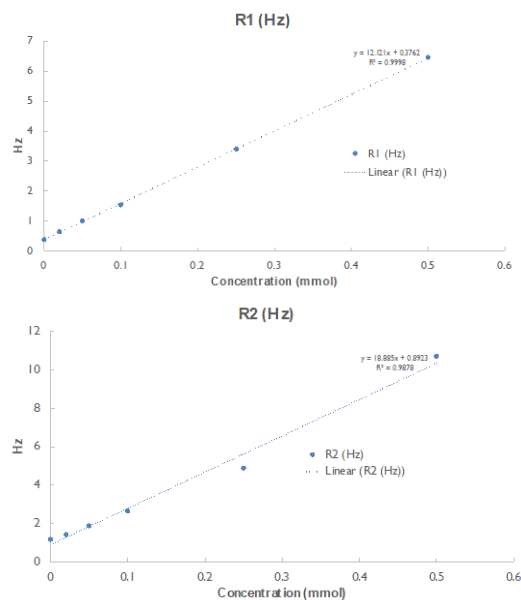

Fig.2: PL and SEM images of synthesized Gd,Nd-doped sodium fluoride NPs. a. Confocal PL map. b,c. SEM image of polymer functionalized bare NPs. d. PL Spectra of NPs excited with 532 nm laser.

Gd doped Nd

Sample	Conc mmol	T2 (ms)	R2 (Hz)	T1 (ms)	R1 (Hz)
1	0.5	93.3	10.71811	155	6.451613
2	0.25	205	4.878049	295	3.389831
3	0.1	378	2.645503	650	1.538462
4	0.05	528	1.893939	991	1.009082
5	0.02	704	1.420455	1560	0.641026
Ref H2O	0	853	1.172333	2640	0.378788

Fig.3: NPs as MRI contrast agent. a. Signal as a function of the magnetic field for several T2/T1. b. Linear correlation of R1 results for the concentration series of Nd(Gd) NCs. c. Linear correlation of R2 results for the concentration series of Nd(Gd) NCs.
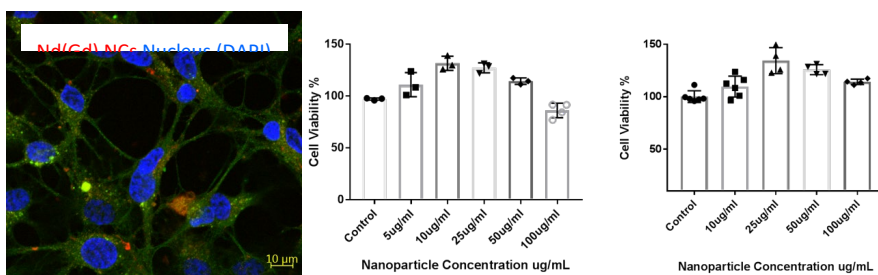

Fig.4: In-Vitro testing of NPs. a. Confocal Microscope images showing the NCs (red) are up-taken by Astrocyte cells. b,c. cell viability tests with increasing NP dosing in b. SY5Y cells and c. Astroglia Cells.

Electrical characteristics of HfO$_2$/Y$_2$O$_3$ on p-Si$_{1-x}$Ge$_x$ with Various Ge Concentrations

W. Lee, J. Lee, D. Eom, J. Oh, C. Park, J. Kim, H. Shin and H. Kim

School of Advanced Materials Science and Engineering, Sungkyunkwan University,

Suwon 16419, Republic of Korea

hsubkim@skku.edu

To continue improving the performance of metal–oxide–semiconductor (MOS) field-effect transistors, traditional Si channels must be replaced with new semiconducting materials with higher carrier mobility. Among the many emerging candidates, the Si$_{1-x}$Ge$_x$ layer epitaxially grown on Si is the most promising due to its high compatibility with current device manufacturing processes [1]. However, the poor interfacial properties of high-k dielectric/Si$_{1-x}$Ge$_x$ are a fatal drawback that prevents the implementation of Si$_{1-x}$Ge$_x$ transistors. More specifically, the formation of thermodynamically unstable interfacial GeO$_x$ deteriorates the electrical properties [2, 3]. Recently, it has been reported that an yttrium (Y)-doped GeO$_2$ layer improves thermal stability by suppressing GeO$_x$ formation on Ge [4]. A single Y$_2$O$_3$ layer also improved the interfacial properties with pure Ge by reducing the interface state density (D_{it}) [5]. However, the dielectric constant of Y$_2$O$_3$ is somewhat lower than that of HfO$_2$ [6], which is unfavorable for reducing the capacitance-equivalent thickness (CET).

In this presentation, we will discuss the effect of ultrathin Y$_2$O$_3$ intercalation on the electrical properties of HfO$_2$/Si$_{1-x}$Ge$_x$ (x = 0, 0.15, and 0.3), which is expected to be beneficial in reducing the CET while lowering the D_{it}. The HfO$_2$/Y$_2$O$_3$ gate stack was deposited via an in situ atomic layer deposition process. Using the fabricated MOS capacitors (TaN/HfO$_2$/Y$_2$O$_3$/Si$_{1-x}$Ge$_x$ structures), various electrical properties (CET, flatband voltage, D_{it}, and gate leakage current) were systemically investigated while varying the Ge concentration of Si$_{1-x}$Ge$_x$ substrates. As shown in Fig. 1, the introduction of ultrathin Y$_2$O$_3$ layers on Si$_{0.15}$Ge$_{0.85}$ and Si$_{0.3}$Ge$_{0.7}$ was beneficial in significantly reducing the interface state response.

[1] P. Hashemi et al., ECS Trans. **66**, 17 (2015).

[2] M. Rabie et al., J. Appl. Phys. **98**, 074904 (2005).

[3] Y. Kamata, Mater. Today, **11**, 30 (2008).

[4] C. Lu et al., Appl. Phys. Lett. **104**, 092909 (2014).

[5] M. Ke et al., Microelectron. Eng. **178**, 132 (2017).

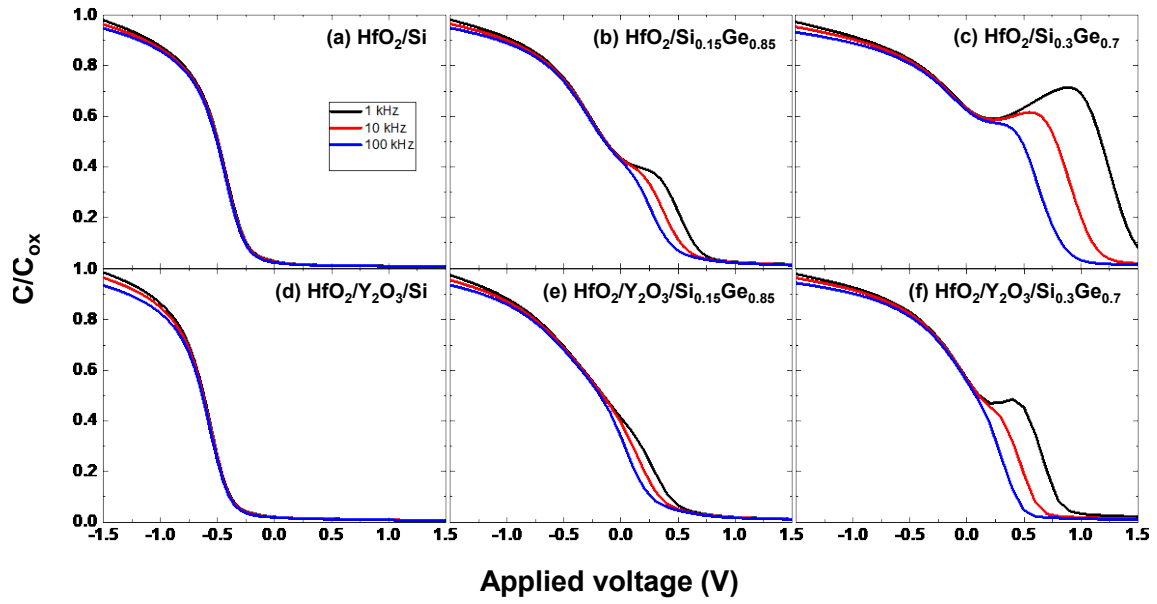[6] J. Robertson et al., Mater. Sci. Eng. R Rep. **88**, 1 (2015).

Fig. 1. Normalized multi-frequency C–V responses measured from (a) HfO₂/Si, (b) HfO₂/Si₀.₁₅Ge₀.₈₅, (c) HfO₂/Si₀.₃Ge₀.₇, (d) HfO₂/Y₂O₃/Si, (e) HfO₂/Y₂O₃/Si₀.₁₅Ge₀.₈₅, and (f) HfO₂/Y₂O₃/Si₀.₃Ge₀.₇ capacitors.

nanoHUB.org: How to enable Rapid Curriculum Innovation through Translation of Research-Based Simulation Tools into Apps

Gerhard Klimeck[1], Tanya Faltens[1], Daniel Mejia[1], Alejandro Strachan[1],
Lynn Zentner[1], Michael Zentner[2]

[1]*Division Network for Computational Nanotechnology, Purdue University, USA*
[2]*San Diego Supercomputing Center, University of California San Diego, USA*
gekco0@gmail.com

Over 150,000 nanoHUB users have run over 7 million simulations in browsers. Most nanoHUB apps deal with semiconductor device and materials modeling. These apps provide very simple and intuitive interfaces to community and research codes that are hard to install, operate, and to maintain even for experts. As such nanoHUB created the first end-to-end scientific cloud enabling users to focus on solving problems rather than installing and maintaining software. Any portal provides access, installation, and compute cycles, however, usability is most often neglected. Most scientific tools focus on solving "any" simulation problem in a specific problem range. Such comprehensiveness makes these tools usable by experts only, typically after intensive training. nanoHUB has instead focused on delivering a spectrum of apps that individually have a limited capability compared to the underlying toolset, but as a whole set cover a vast swath of problems. Hundreds of community members have contributed over 700 Apps into nanoHUB.

The results are stunning. Our user analytics prove that over half of the simulation users participate in structured education through homework/project assignments. Over 90,000 students have nanoHUB tools and apps in over 3,600 structured classrooms. We can identify classroom sizes and detailed tool usage [1,2]. We can begin to build mind-maps of design explorations and assess depth of explorations for individuals and classes. While parts of academia has struggled to innovate curricula we have measured the median first-time app insertion into a class to be less than six months. Over 180 institutions have utilized nanoHUB in their curriculum innovation in over 5,000 classes. 2 million nanoHUB visitors explore lectures and tutorials annually. With such a community presence we believe **nanoHUB is the platform of choice** to deliver online modeling, simulation, virtual environments, and lectures for the US initiative **for semiconductor workforce development**.

[1] Krishna Madhavan, Michael Zentner, Gerhard Klimeck, "Learning and research in the cloud", Nature Nanotechnology 8, 786–789 (2013)

[2] TEDx Talk, Klimeck, "Mythbusting Scientific Knowledge Transfer with nanoHUB.org", https://www.youtube.com/watch?v=PK2GztIfJY4

Figure 1 (a) nanoHUB user map. Red circles designate users viewing lectures, tutorials, or homework assignments. Yellow dots are simulation users. Green dots indicate 4,100+ authors of 1,700+ scientific publications citing nanoHUB through 2016. Dot sizes correspond to number of users, and lines show author-to-author connections proving research collaboration networks. (b) U.S. enlarged. (c) a collage of typical nanoHUB interactive tool sessions and 3D-rendered interactively explorable results (quantum dots, carbon nanotubes, nanowires).
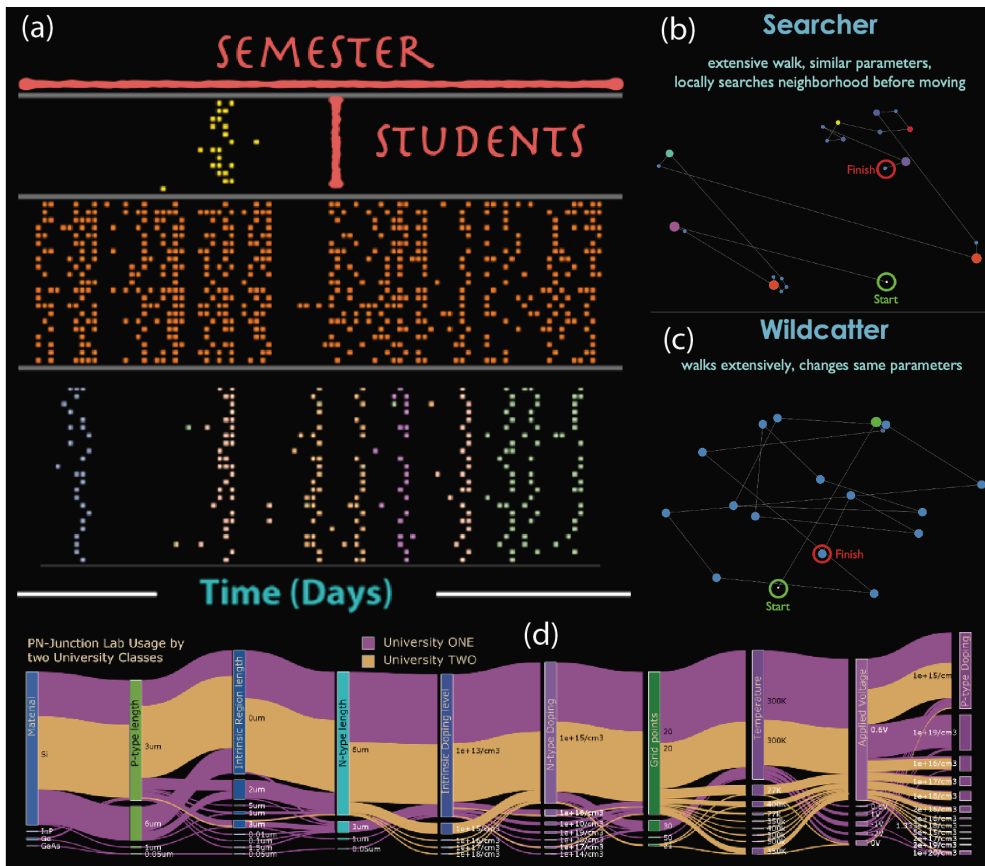

Figure 2 (a) nanoHUB user behaviors over time identified as classes. (b,c) Specific behavior of 2 PN Junction Lab users classified as Searcher and Wildcatter. (d) Collective behavior of 2 classes using PN Junction Lab.

Some news about the insulating phases in twisted bilayer graphene

Nicolas Regnault

Laboratoire de Physique de l'Ecole Normale Supérieure, CNRS, Paris

The twisted bilayer graphene near the first magic angle hosts topological flat moiré electron bands, and exhibits a rich tunable strongly interacting physics. Correlated insulators and Chern insulators have been observed at various integer fillings. In this talk, we will discuss the enhanced U(4) or U(4)xU(4) symmetries of the projected TBG Hamiltonian with Coulomb interaction in various combinations of the flat band and chiral limits. These enlarged symmetries allow us to identify exact or approximate ground or low-energy (Chern) insulator states at all the integer filling factors under a weak assumption that we justify numerically. The exact expressions of charge and neutral excitations allow us to compute the expected signatures in scanning tunneling microscopy experiments. Finally, we will present self-consistent Hartree-Fock results that unveil the fate of these exact insulating phases away from the chiral limit. In particular at integer filling nu=−3, we will discuss a competing phase characterized by a spin and valley polarized, translation symmetry breaking, state with C2zT symmetry, a charge gap and a doubling of the moiré unit cell, dubbed the C2zT stripe phase.

Phase transitions in topological materials

Maia G. Vergniory

Max Planck for Chemical Physics of Solids, 01067 Dresden, Germany

maia.vergniory@cpfs.mpg.de

Phonons play a crucial role in many properties of solid-state systems, such as thermal and electrical conductivity, neutron scattering and associated effects or superconductivity. Hence, it is expected that topological phonons will also lead to rich and unconventional physics and the search of materials hosting topological phonons becomes a priority in the field. In this talk I will present a methodology to identify topological phonons in materials as well as charge-density waves instabilities. We identify vdW layered material as possible candidate for CDW and we explore the coupling of Dirac fermions with it. Finally, we theoretically study the effect of low-frequency light pulses in resonance with phonons in the topological and magnetically ordered two-septuple layer (2-SL) MnBi2Te4 (MBT) and MnSb2Te4 (MST).

[1] Yuanfeng Xu, MG Vergniory, Da-Shuai Ma, Juan L Mañes, Zhi-Da Song, B Andrei Bernevig, Nicolas Regnault, Luis Elcoro, arXiv:2211.11776 (2022)

[2] Martin Rodriguez-Vega, Ze-Xun Lin, Aritz Leonardo, Arthur Ernst, Maia G Vergniory, Gregory A Fiete, The journal of physical chemistry letters 13, 4152-4158 (2022)

Modification of Bulk and Surface Phonons in Single-Crystal Diamond *via* Substitutional Boron Doping

E. Guzman,[1] F. Kargar,[1] F. Angeles,[2] R. V. Meidanshahi,[3] T. A. Grotjohn,[4] A. Hardy,[5] M. Muehle,[5] R. B. Wilson,[2] S. M. Goodnick,[3] and A. A. Balandin[1]

[1]*Phonon Optimized Engineered Materials Center, Department of Electrical and Computer Engineering, University of California, Riverside, California 92521 USA*

[2]*Department of Mechanical Engineering and Materials Science and Engineering Program, University of California, Riverside, California 92521 USA*

[3]*School of Electrical, Computer and Energy Engineering, Arizona State University, Tempe, Arizona 85281 USA*

[4]*Department of Electrical and Computer Engineering, Michigan State University, East Lansing, Michigan 48824 USA*

[5]*Fraunhofer USA Center Midwest, East Lansing, Michigan 48824 USA*

E-mail: *fkargar@ece.ucr.edu* *https://balandingroup.ucr.edu*

Recent years witnessed a rapid growth of interest in ultra-wide bandgap (UWBG) semiconductors for applications in power electronics. Among UWBGs, diamond attracts the most attention as it holds a record-high current density, thermal conductivity, mechanical stiffness, chemical stability, and the critical electric field. Intrinsic diamond is doped by boron (B) to become suitable for electronic applications. In diamond, bulk acoustic phonons with high group velocities and long lifetimes are the main heat carriers. While boron substitutional doping improves the electrical conductivity of diamond, it adversely affects its excellent intrinsic phonon heat conduction characteristics. Although the phonons in pristine diamond have been investigated extensively, the data on the surface and bulk acoustic phonons in doped diamond are scarce and rather controversial. In this work, we used Raman and Brillouin-Mandelstam spectroscopy to investigate the optical and bulk and surface acoustic phonons in the undoped high-pressure high temperature (HPHT) diamond and boron-doped CVD-grown diamond films. It was found that the frequency and group velocity of acoustic phonons decrease non-monotonically with the increasing boron doping concentration [1]. The observed changes in the acoustic phonon properties of B-doped diamond have important implications for heat conduction and electron-phonon interactions in UWBG materials.

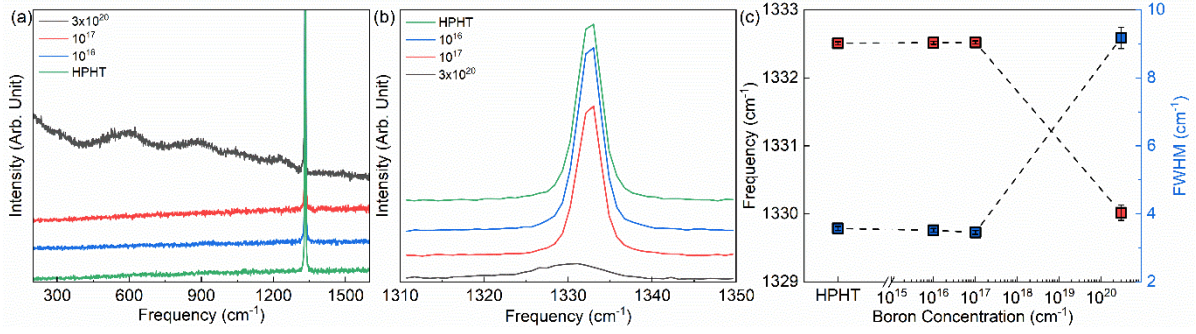[1] E. Guzman, *et al*., ACS Appl. Mater. Interfaces (2022).

Fig.1: (a) Raman spectra of the boron-dope diamond samples and a reference undoped HPHT diamond recorded under a 633-nm excitation laser. (b) Raman spectra for the same samples in the vicinity of the diamond's zone-center optical phonon peak at ~1332 cm⁻¹. (c) Spectral position (red squares) and FWHM (blue squares) of the zone-center peak as a function of the boron concentration. The spectral position of the peak decreases by 2 cm⁻¹ while its FWHM increases significantly for the highly doped diamond.
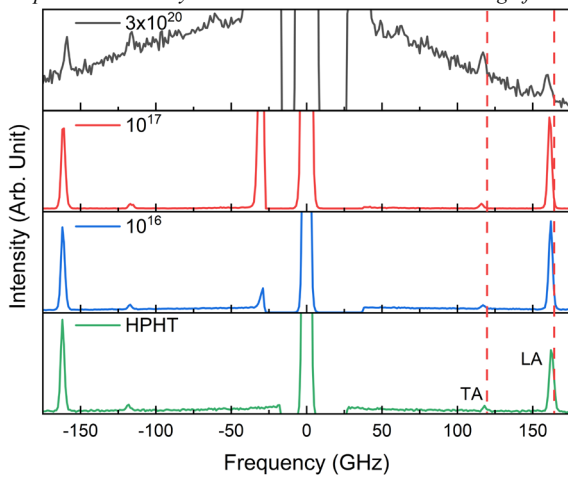

Fig.2: Brillouin light scattering spectra of the boron-doped diamond samples in the backscattering geometry performed at a 20° incidence angle. The dashed lines are guides to the eye to show the decrease in the acoustic phonon frequency as the doping level increases. The peaks labeled as LA and TA correspond to the longitudinal acoustic and the transverse acoustic bulk phonons.
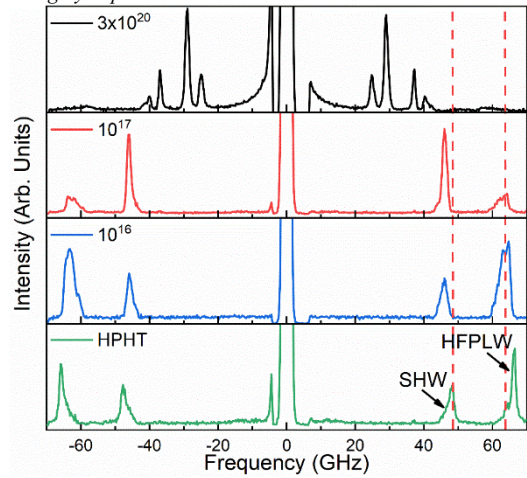

Fig.3: Brillouin light scattering spectra of the boron-doped diamond samples and a reference HPHT diamond substrate accumulated at $\theta = 75°$. The shear-horizontal surface wave and high-frequency pseudo-longitudinal wave are labeled as SHW and HFPLW, respectfully. The frequency of types of phonons decreases as the boron concentration increases.
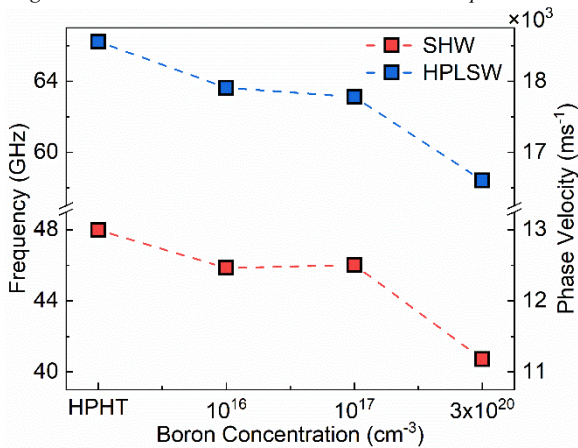

Fig.4: Frequency and velocity of surface phonons in diamond as a function of the boron concentration. The data for the SHW and HPLSW phonon branches are shown at $q_{||} = 0.0228\ nm^{-1}$.
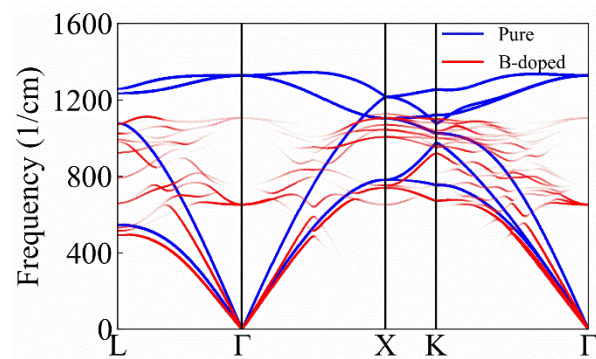

Fig.5: Calculated phonon band structure of the pristine (blue) and B-doped (red) diamond. The softening of all acoustic phonon modes as a result of boron doping is clearly observed.

Epitaxial Growth of c-BN on Diamond and Strategies for Power and RF Applications

Avani Patel[1], Saurabh Vishwakarma[1], Jesse Brown[2], David J. Smith[2] and Robert J. Nemanich[2*]

[1] School for Eng. of Matter, Transport and Energy, Arizona State University, Tempe, AZ 85287, USA

[2] Department of Physics, Arizona State University, Tempe, AZ 85287, USA

*Email: robert.nemanich@asu.edu

Cubic boron nitride (c-BN) is an ultra-wide bandgap semiconductor with properties appropriate for high power, high frequency electronics for extreme environments (high temperature, high radiation, and corrosive environments) [1]. The 6.4 eV bandgap of c-BN projects a breakdown field > 12 MV/cm. Moreover, n-type doping with S and Si (~0.3eV) and p-type doping with Be and Mg (~0.24 eV) have been demonstrated. The measured electron mobility of 825 cm^2/V-s agree reasonably with theoretical values of 956 to 1680 cm^2/V-s. There is uncertainty in the experimental hole mobility, which has been theoretically projected between 80 and 280 cm^2/V-s [2,3]. Native c-BN substrates are not available but the 1.4% lattice mismatch with diamond enables diamond as a substrate for epitaxial growth of c-BN. Epitaxial c-BN on diamond structures have recently been demonstrated at ASU and by other groups that employ ion beam assisted deposition processes. This study employs ECR plasma enhanced CVD based on a fluorine chemistry and a low substrate bias (~60V) to achieve low stress, epitaxial layers. The *in situ* three step process employs a hydrogen plasma clean, a c-BN nucleation step with an enhanced hydrogen concentration, and a film growth step that optimizes the ratio of hydrogen and fluorine to achieve epitaxial growth. A growth rate of ~50 nm/hr is achieved, which is much greater than the rate typically obtained with ion assisted MBE deposition. The 150 nm thick c-BN films grown on single crystal diamond substrates are stable against delamination. After growth the BN / diamond sample is transferred in UHV to a photoemission system, which is used to determine the sp^2 content by measuring the relative intensity of the π-peak. With optimized growth chemistry, the sp^2 π-peak was not detected indicating the presence of c-BN.

TEM investigation shows a near epitaxial interface. Figure 1 presents a high-resolution image of c-BN grown on a p-type diamond (111) substrate. The diffraction pattern of the substrate and the layer confirm epitaxy. Examination of the boron electron energy loss spectrum (EELS) shows sp^3 bonding throughout the film with a very small π-peak only evident near the interface.

A unique aspect of c-BN / diamond heterostructure is that the band offset between diamond and c-BN is expected to depend on the interface bonding [4] as indicated in Figure 2. The potential of epitaxial c-BN for different device configurations will be discussed.

[1] N. Izyumskaya, D. O. Demchenko, S. Das, Ü. Özgür, V. Avrutin, and H. Morkoç, Adv. Electron. Mater. 3, 1600485 (2017).

[2] N. Sanders and E. Kioupakisa, Appl. Phys. Lett. 119, 062101 (2021).

[3] S. Poncé, F. Macheda, E. R. Margine, N. Marzari, N. Bonini, and F. Giustino, Phys. Rev. Res. 3, 043022 (2021).

[4] Dehe Zhao, Wei Gao, Yujing Li, Yuyuan Zhang and Hong Yin, RSC Adv. 9, 8435 (2019).
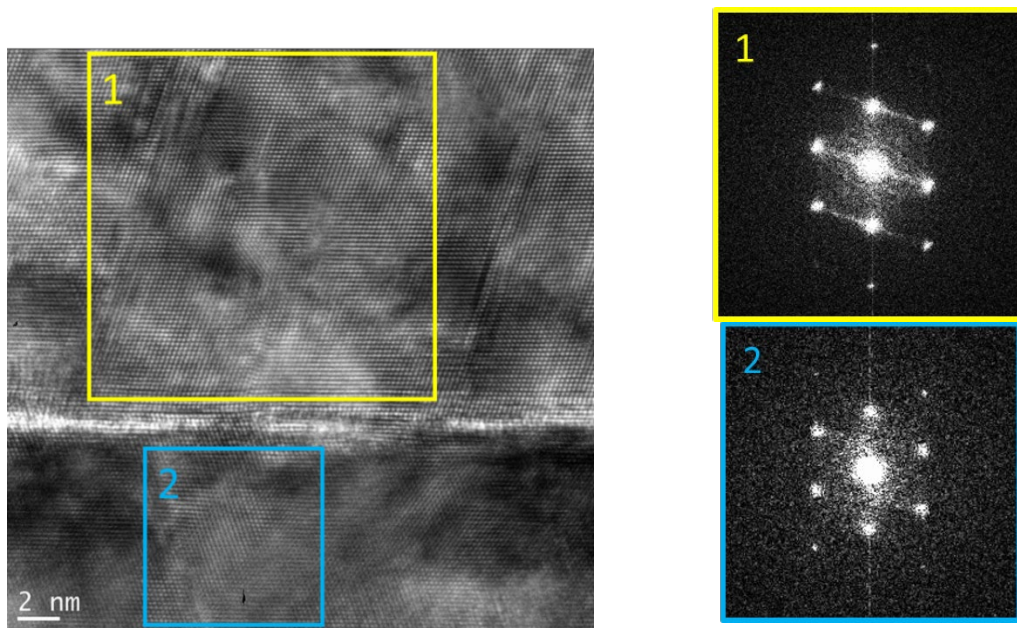
Figure 1. *High resolution TEM image of c-BN on diamond (111). Diffraction patterns calculated from the indicated regions are included. A separate study of the electron energy loss spectra (EELS) indicated a small fraction of sp^2 bonded BN only near the interface.*
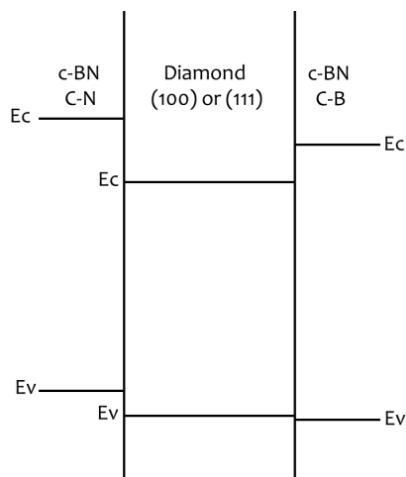
Figure 2. *Theoretical studies [4] have indicated that the band alignment of c-BN / diamond heterostructures would depend on the specific interface bonding which could be C-B or C-N or a mixture depending on the orientation.*

V-defects in InGaN Quantum wells: Influence on Carrier Dynamics

S. Marcinkevičius[1], R. Yapparov[1], Y. C. Chow[2], F. Wu[2], S. Nakamura[2], and J. S. Speck[2]

[1]*Department of Applied Physics, KTH Royal Institute of Technology, AlbaNova University Center, 10691 Stockholm, Sweden*

[2]*Materials Department, University of California, Santa Barbara, California 93106, USA*

sm@kth.se

GaN-based RGB (red-green-blue) lighting is expected to have more functionalities and higher efficiency compared to traditional blue LED and phosphor devices. For that, efficient green and red LEDs are required. In such LEDs the InGaN/GaN quantum wells (QWs) are deep, which prevents a uniform carrier distribution in multiple QWs that form the active region and increases the nonradiative Auger recombination. Recently it has been suggested that this issue could be resolved by using volumetric carrier injection into all QWs via V-defects [1,2], which are hexagonal pyramids terminating threading dislocations in polar nitride QW structures. The key property here is semipolar QWs that form on the V-defect sidewalls and can serve as channels for the hole transport. Nevertheless, the V-defects are still defects and can, for instance, accumulate point defects increasing the nonradiative Shockley-Read-Hall (SRH) recombination. To reveal the possible drawbacks that the V-defects can have on the efficiency of LED emission, we have studied spatial variations of the optical, structural, and chemical properties of single InGaN QWs emitting in a broad range, from 410 nm to 570 nm. To that end, various scanning techniques, including energy-dispersive x-ray spectroscopy, atomic force microscopy, and time- and spectrally-resolved scanning near-field optical microscopy (SNOM) were used.

Photoluminescence (PL) spectra and carrier dynamics experience considerable differences in the V-defect rich and defect-free regions. For instance, the radiative lifetimes show spatial variations up to a factor of 3 higher around the V-defects, which is a signature of deeper nm-scale band potential fluctuations and increased carrier localization. On the other hand, the nonradiative lifetime at the defects is shorter showing that, indeed, there is some point defect agglomeration around the V-defects. The areas with the efficient nonradiative recombination, however, are limited to the immediate vicinity of the dislocations, which occupy no more than a few percent of the sample area. Thus, the fast nonradiative recombination at dislocations does not substantially affect the overall internal quantum efficiency of the QWs, and the advantages of V-defects as volumetric injectors should prevail over the drawbacks of the slightly increased nonradiative recombination.

[1] Li *et al*., AIP Advances **6**, 055208 (2016).

[2] C.-H. Ho, J. S. Speck, C. Weisbuch, and Y.-R. Wu Phys. Rev. Appl. **17**, 014033 (2022).
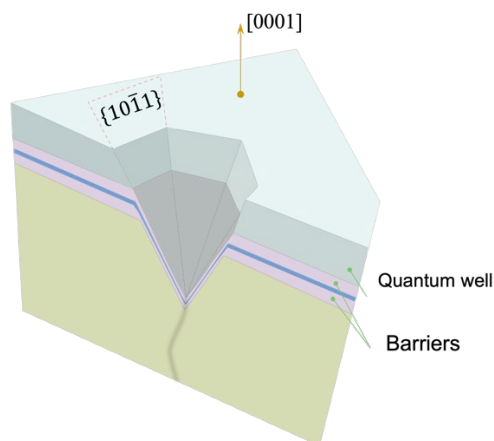
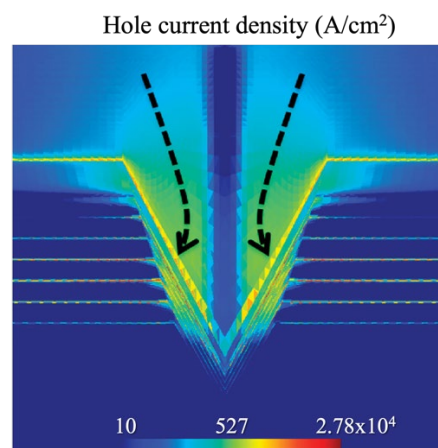Fig.1: Schematics of a V-defect terminating a threading dislocation.

Fig.2: Simulated hole injection into all QWs via semipolar QWs at the V-defect facets. From Li et al., AIP Advances **6**, 055208 (2016).
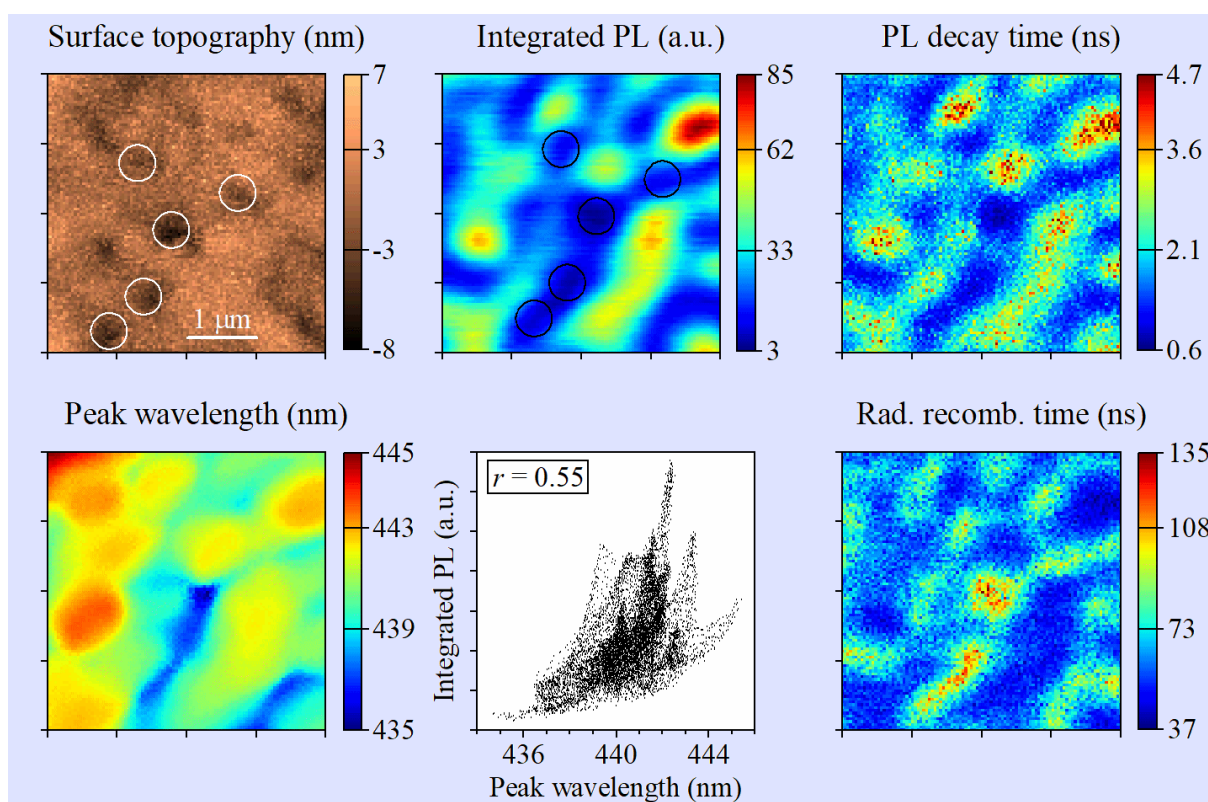

Fig.3: SNOM maps of the surface topography, integrated PL intensity, PL decay time, peak wavelength, and radiative recombination time for the blue-emitting QW. The circles in the topography and PL intensity maps indicate regions with agglomerated V-defects and help to correlated topography and optical maps. Correlation plot for the PL peak wavelength and integrated intensity shows that areas emitting at longer wavelengths (and having a larger In content in the $In_xGa_{1-x}N$ alloy) produce a higher PL intensity due to a slower SRH recombination.

Tight-Binding and Full-Band Monte Carlo
Analysis of the Strain Effects in wurtzite GaN

W. Miyazaki, H. Tanaka, and N. Mori

Graduate School of Engineering, Osaka University

2-1 Yamada-oka, Suita, Osaka 565-0871, Japan

E-mail: miyazaki@si.eei.eng.osaka-u.ac.jp

GaN is attracting much attention for use in power devices. In this study, we calculate the strain-induced change in the band structure and the electron transport to predict the potential for improvement of the device performance due to strain. We calculate the band structure of wurtzite GaN under uniaxial and biaxial strain using the empirical tight-binding (TB) method. As the TB parameters, we adopted values given in [1]. To derive the displacement of an atom from the unstrained state to the strained state, we use the elastic stiffness constants and internal strain given in [2]. Using the computed band structure, we calculate the bandgap, effective mass, and group velocity. Fig. 1 shows the uniaxial strain dependence of the bandgap. Bandgap becomes larger under the uniaxial compressive strain. The uniaxial strain dependence of the effective mass along the $\langle 0001 \rangle$ direction is shown in Fig. 2. The most significant change is the effective-mass exchange between LH and SH. Fig. 3 shows the orbital-projected valence band structure focusing on the p_z orbitals of N atoms. Focusing on the bands dominated by the p_z orbitals, we can see that the orbital components are exchanged between LH and SH. This change of orbital characteristics is the cause of the effective-mass exchange. Fig. 4 shows the average group velocity which is defined as the average of the group velocities weighted by the density of states [3]. We find that the group velocity of the valence band in the range of 0 eV to -3.5 eV is smaller under uniaxial tensile strain. According to previous studies, holes have a greater effect on the impact ionization in GaN than electrons [4]; Smaller group velocity leads to a reduction in the impact ionization and the effect of which is suggested to be more dominant than the effect of the bandgap [5, 6]. For these reasons, we conclude that uniaxial tensile strain may be beneficial for achieving higher breakdown voltage. Using the obtained band structure, we calculate electron transport properties by full-band Monte Carlo simulation. As scattering mechanisms, we consider acoustic, nonpolar optical, and polar optical phonon scattering. Figs. 5 and 6 show the electron drift velocity along the $\langle 0001 \rangle$ direction. We find that uniaxial tensile strain may lead to higher electron drift velocity.

[1] J.-M. Jancu et al., APL 81, 4838 (2002). [2] J.-M. Wagner et al., PRB 66, 115202 (2002).

[3] E. Gnani et al., PRB 66, 195205 (2002). [4] T. Maeda et al., JAP 129, 185702 (2021).

[5] H. Tanaka et al., JAP 131, 225701 (2022). [6] H. Tanaka et al., APEX 13, 041006 (2020).
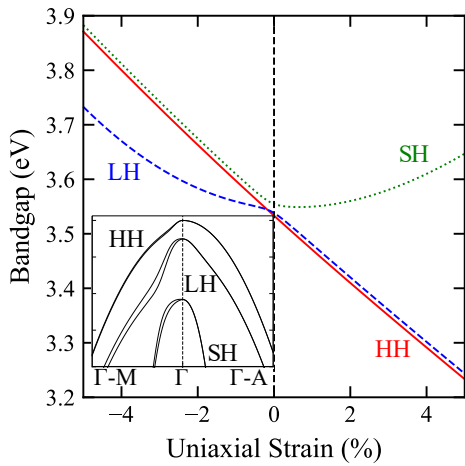
Fig.1: The bandgap of GaN as a function of uniaxial strain along the ⟨0001⟩ direction. The bandgap is calculated as the energy gap between the lowest conduction band and heavy hole (HH), light hole (LH), split off hole (SH) bands at the Γ point. The inset shows the valence band structure of unstrained GaN.

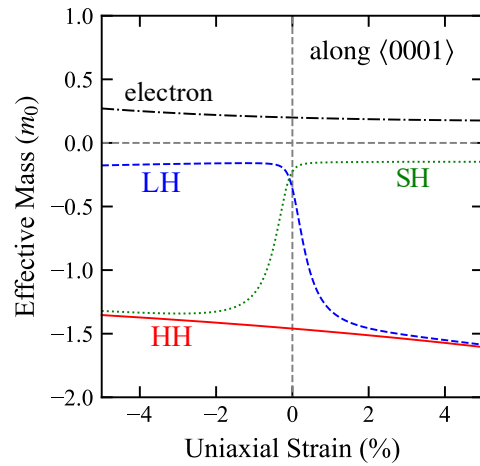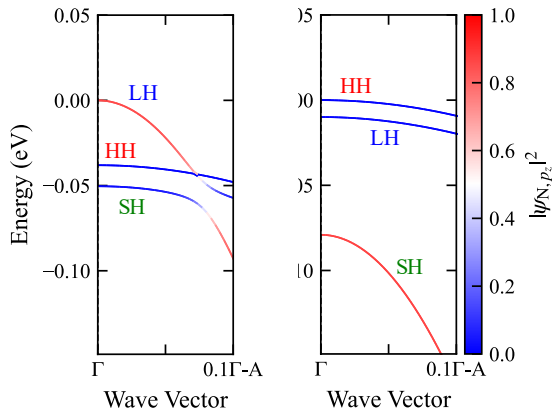Fig.2: Effective mass of the electron, HH, LH, and SH along the ⟨0001⟩ direction as a function of uniaxial strain.

Fig.3: Orbital-projected valence band structure of uniaxially strained GaN focusing on the p_z orbitals of N-atoms. The color indicates the contribution of the p_z orbitals; Red shows that p_z orbitals of N-atoms are dominant.
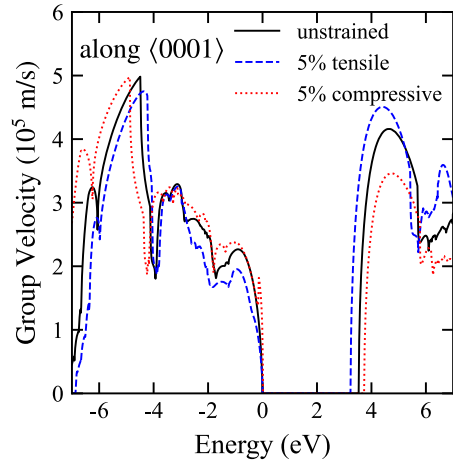
Fig.4: Energy dependence of the average group velocity of GaN along the ⟨0001⟩ direction. Results for unstrained (black solid line), 5% tensile (blue dashed line), and 5% compressive uniaxial strain (red dotted line) are compared.
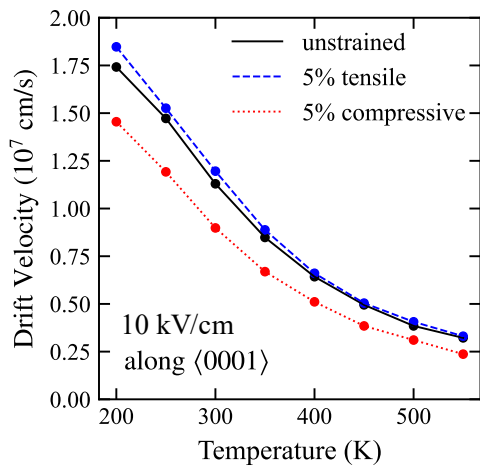

Fig.5: Temperature dependence of the electron drift velocity along the ⟨0001⟩ direction at 10 kV/cm.

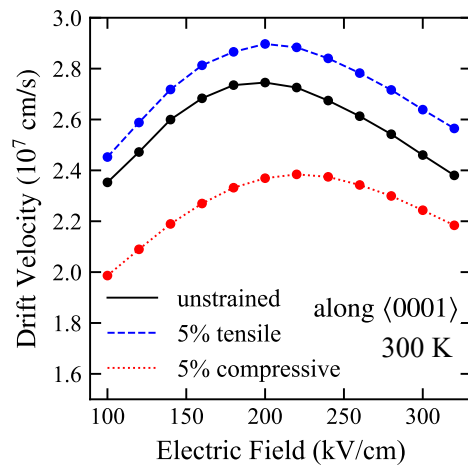Fig.6: Electric field dependence of the electron drift velocity along the ⟨0001⟩ direction at 300 K.

Ultrafast Microwave Spectrum Analysis Using Sweep-Tuned Spin-Torque Nano-Oscillators

A. Litvinenko[1] , S. Louis[2], V.S. Tyberkevych[2], B.Dieny[1], <u>A.N. Slavin</u>[2], and U. Ebels[1]

[1]Univ. Grenoble Alpes, CEA, CNRS, Spintec, 38000 Grenoble, France

[2]Department of Physics, Oakland University, Rochester Michigan 48309, USA

slavin@oakland.edu

Modern applications in radar and communication technologies often use frequency-agile signals, the spectral analysis of which requires sub-μs temporal resolution. Such a speed of the spectral analysis can be achieved with a sweep-tuned spectrum analyzer only if the local oscillator of the analyzer has a nano-scale size, and very low time constants, so that its frequency can be swept on the time scale of the targeted temporal resolution. It was theoretically predicted in [1, 2] that such an ultrafast analysis can be performed using spin-torque nano-oscillators (STNO) both in microwave (MHz to GHz) [1] and THz [2] frequency ranges.

Recent experimental studies [3, 4] performed on the vortex-magnetic-state [3] and uniform-magnetic-state [4] STNOs, rapidly sweep-tuned by a bias voltage, fully confirmed these theoretical predictions, and proved that ultrafast time-resolved spectral analysis of frequency-agile microwave signals is possible. The critical reduction in the time of the spectral analysis comes from the naturally small (1−100 ns) temporal constants of the nano-sized STNOs. The advantage of an ultrafast frequency-tunability of STNOs, that have a large (>100 MHz) relaxation frequency of amplitude fluctuations, is exploited to realize ultrafast wide-band time-resolved spectral analysis at nanosecond time scale with a frequency resolution limited only by the sweeping frequency through the "bandwidth" theorem.

The demonstration of the time-resolved (*T*~50 ns) spectral analysis in the GHz frequency range (frequency interval of 1.0 GHz around a central frequency of 9.1 GHz with a scanning speed of 50 MHz/ns) was performed on an STNO comprised of a perpendicular polarizer and a perpendicularly and uniformly magnetized "free" magnetic layer [4]. It was shown in [4] that such a uniform-state STNO-based spectrum analyzer can efficiently perform spectral analysis of frequency-agile signals with rapidly varying frequency components, and that a relatively wide (~10 MHz) generation linewidth of the STNO does not significantly affect the frequency resolution of the spectral analysis, which is determined by the speed of the frequency sweeping.

[1] S. Louis *et al.*, Appl. Phys. Lett. **113,** 112401 (2018).

[2] P. Yu. Artemchuk *et al.*, J. Appl. Phys. **127**, 063905 (2020).

[3] A. Litvinenko *et al.*, Nano Lett. **20**, 6104 (2020).

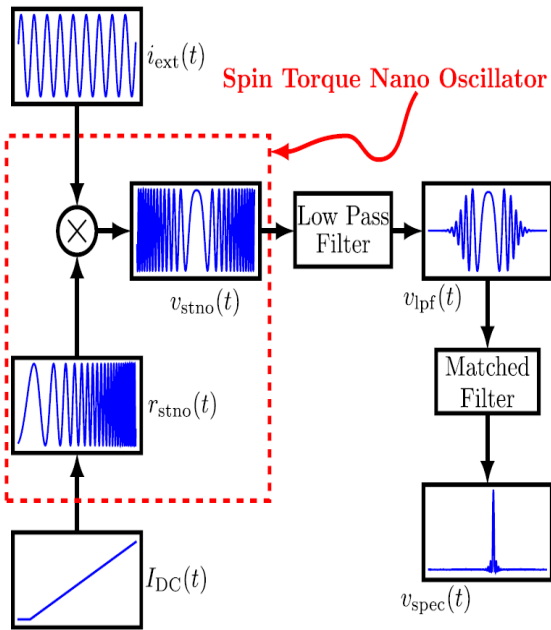[4] A. Litvinenko *et al.*, Nano Lett., **22**, 1874–1879 (2022).

Fig.1: Block diagram of an ultrafast spectrum analyzer based on a spin-torque nano-oscillator (STNO) (see [1]). An external microwave signal $i_{ext}(t)$ is mixed with the frequency-chirped signal $r_{stno}(t)$ generated by the STNO, that is driven by the ramped (sweep-tuned) current I_{DC}. The resultant signal $v_{stno}(t)$ is passed through a low pass filter and a matched filter to form the output signal $v_{spec}(t)$ representing the spectrum of the input microwave signal.
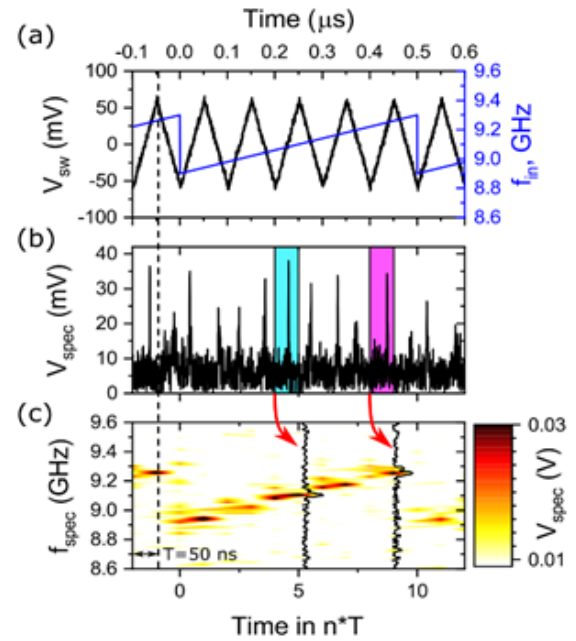

Fig.2: Example of a spectrum analysis of a complex external input signal V_{in}, whose frequency is varying in a sawtooth manner between 8.9 and 9.3 GHz with a period of $T_{in} = 10T$, where T is the sweeping period of T = 50 ns (see [4]): (a) STNO sweeping signal V_{sw} (with the period T), and the time variation of the input signal frequency (with the period 10T); (b) resultant peaks $V_{spec}(t)$ with temporal positions varying within each sweeping period; (c) temporal variation of the external signal frequency obtained as a result of the time-resolved spectral analysis.

Manipulation of Fractional Charge on The Nanoscale in Charge Configuration Memory Devices Using Multi-Tip Scanning Tunneling Microscopy

Yevhenii Vaskivskyii[1], Anže Mraz[1], Andrej Kranjec[1], Peter Karpov[3], Igor Vaskivskyi[1], and <u>Dragan Mihailovic</u>[1]

[1] *Jozef Stefan Institute, Jamova 39, 1000 Ljubljana, Slovenia*
[2] *Condensed Matter Physics and Materials Science Division, Brookhaven National Laboratory, Upton, NY 11973, USA*

Nanoscale charge ordering dynamics in charge configuration memory (CCM) devices cannot be easily investigated using time-resolved X-rays, electron diffraction, ARPES or optics, because of lack of the necessary spatial resolution. On the other hand, high-resolution investigation of nanoscale ordering dynamics with scanning tunnelling microscopy is possible when the relaxation timescale of metastable states can be tuned by temperature (Fig. 1). Here we present investigations of fractionally charged dislocation dynamics created by charge injection in a polaronic Wigner crystal system $1T\text{-}TaS_2$ (Fig. 2). The microscopic defect dynamics is topologically protected and the dynamics is sufficiently slow to be observable at low temperature. We show that spontaneous fractional charge annihilation dynamics can be excited thermally, or by quantum fluctuations. They can also be manipulated by a surface current (Fig. 3). The investigations show how microscopic topological defects in the electronic crystal structure play a role in the metastability of quantum matter, and are of the utmost importance in governing the behaviour of energy efficient fast electronic devices based on Wigner crystal manipulation [1-7].

[1] D. Mihailovic *et al.*, APL **119**, 013106 (2021).

[2] R. Venturini *et al.*, APL **120**, 253510 (2022).

[3] A. Mraz *et al.*, Nano Letters **22**, 4814 (2022).

[4] G. Liu *et al.*, Nat Nanotechnol **11**, 845 (2016).

[5] A. Geremew *et al.*, Acs Nano **13**, 7231 (2019).

[6] A. Mohammadzadeh *et al.*, Appl Phys Lett **118**, 093102 (2021).

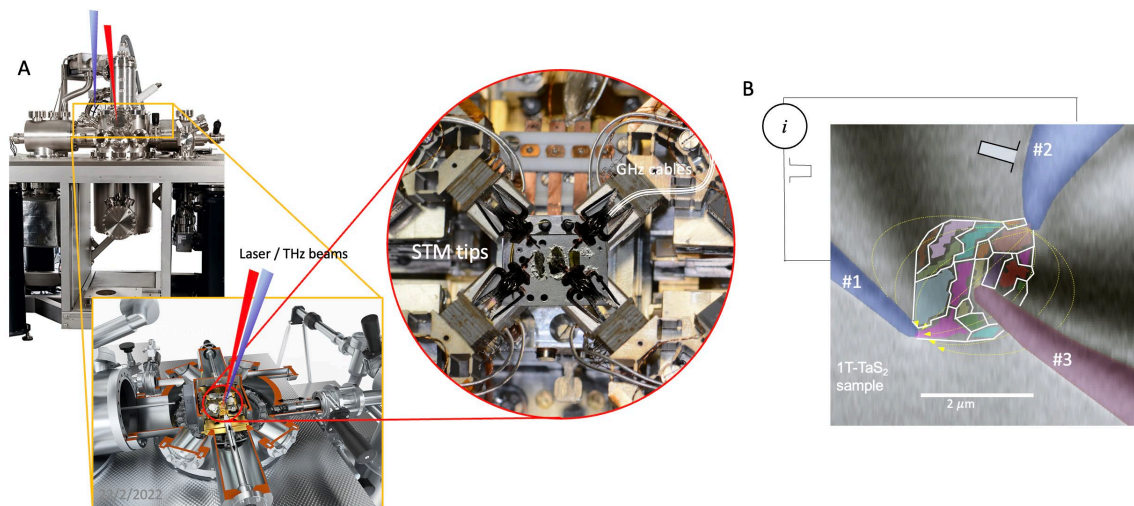[7] X. Wang *et al.*, Advanced Materials **30**, 1800074 (2018).

Fig.1: A) A 4-probe UHV LT STM microscope with integrated SEM column. B) Three STM probe setup indicating the current injection by outer STM tips #1 and #2, and probing by the middle STM tip #3. The fractionally charged topological defects (dislocations) can be manipulated by current or by laser beams incident on the sample.
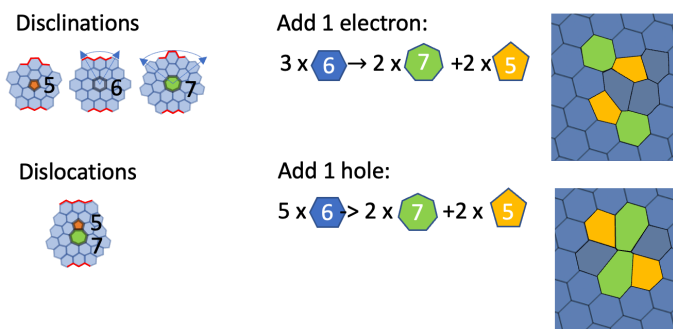

Fig.2: Formation of topological defects (disclinations and dislocations) in a hexagonal Wigner crystal lattice upon injection of electrons or holes. Note that a single electron, or hole creates two dislocations, each with an electronic charge ½e. Experiments show that the fractional charges pinned to vertices are connected by domain walls. (See Fig. 3 A).
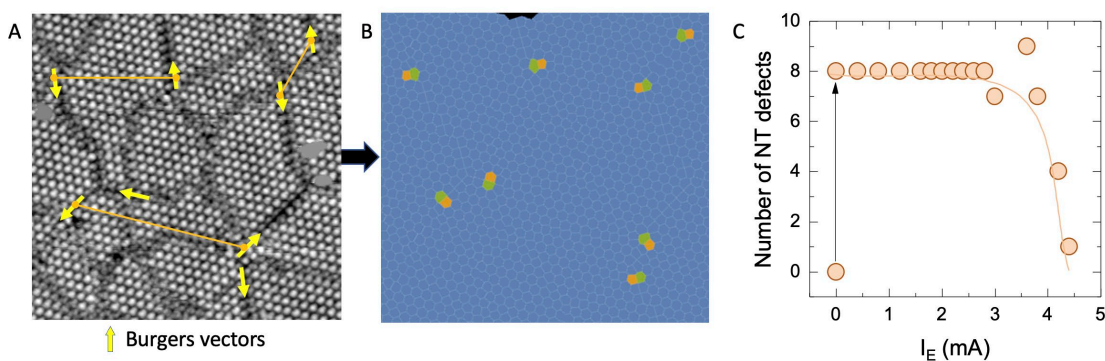

Fig.3: A) An STM image of the domain structure created from a uniform commensurate Wigner crystal phase by carrier injection. The yellow arrows show Burger's vectors associated with dislocations at the vertices. Dislocations with equal an opposite Burgers vectors are joined by orange lines. B) The equivalent dislocation picture on a Wigner-Seitz cell construction of the Wigner crystal from the same STM image. C) Manipulation of the number of nontrivial (NT) defects (dislocations) by external current I_E on the outer STM tips in a CCM device.

Temperature Dependence of A Capacitorless Cryogenic CMOS Memory Based on Impact Ionization

Curt A. Richter[1], Pragya R. Shrestha[1], Brian Hoskins[1], Son T. Le[1,2], Advait Madhavan[1,2], Jabez J. McClelland[1], and Alexander Zaslavsky[1,3]

[1]Nanoscale Device Characterization Division, National Institute of Standards and Technology, Gaithersburg, MD 20899 USA

[2]University of Maryland, College Park, MD USA

[3]School of Engineering, Brown University, Providence, RI USA

curt.richter@NIST.gov

Cryogenic complementary metal oxide semiconductor (CMOS) silicon transistors are crucial for integration with emerging nanoscale systems for quantum information science, high-performance computing, and advanced sensors. Bistability and dramatic hysteretic loops have been observed in the drain current as a function of gate voltage, $I_D(V_{GS})$ of 180 nm technology node CMOS transistors (Fig. 1) operated at low temperatures (T < 30 K)[1]. The hysteretic loops - which have a $>10^7$ ratio of high to low I_D states at the same V_{GS} - can be used as a capacitorless single-transistor cryogenic memory. The bistable behavior occurs when the transistors are operated at voltages exceeding 1.3 V at cryogenic temperatures (Fig. 2) for both n-type and p-type transistor polarities. The device bistability arises from impact ionization charging of the transistor body, which leads to effective back-gating of the inversion channel. This physical mechanism can be used as the "WRITE 1" process for memory operation. It was verified by independent measurements of the body potential as large as ≈1 V. The measured body charge remains trapped with an exponential decay time greater than 10 minutes. We report here that the impact ionization induced body charge can be removed in an efficient "WRITE 0" process by forward biasing the body-drain junction sufficiently to evacuate the trapped charges. By simultaneously applying an appropriate gate bias the transistor will remain off so that this erase is a lower power step than WRITE 1. The memory state can easily be read out with a V_{SD} within the hysteresis region. The full write/read/erase/read cycle is illustrated at quasi-static rates in Fig. 3. The substrate conductance was measured as a function of temperature (Fig. 4) and the expected dramatic increase in the resistance was observed for carrier freeze-out below ≈40 K. Impact ionization substrate current hysteresis is only observed in this substrate freeze-out regime (Fig. 5). The temperature dependence of the impact-ionization-based write/read/erase/read cycle was measured to determine the temperature range of operation. It was found that the process works well above the base temperature of our measurements (≈3 K).

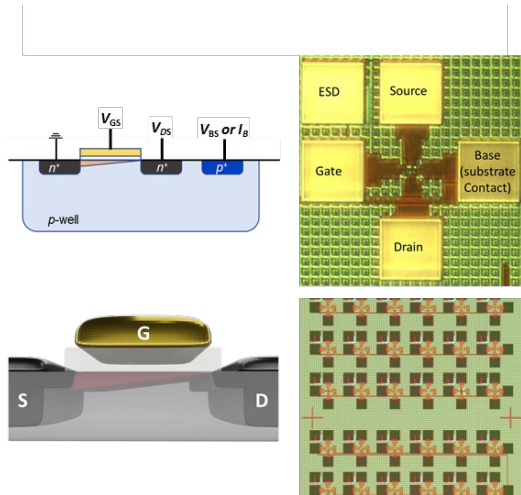[1] A. Zaslavsky, *et al.*, Appl. Phys. Lett. **119**, 043501 (2021).

Fig.1: Schematic drawings and optical images of the 180 nm technology node CMOS transistors characterized at cryogenic temperatures in this study.
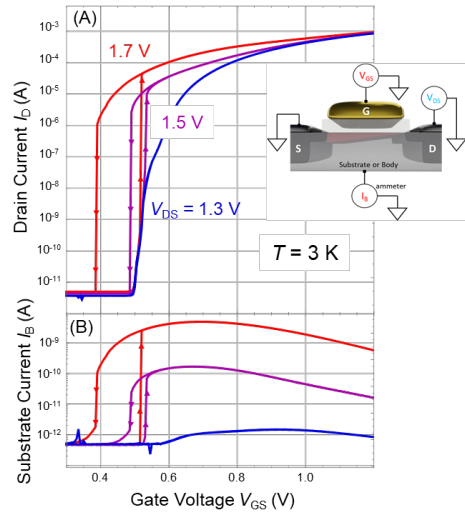

Fig.2: (A) NMOS $I_D(V_{GS})$ for V_{DS} = (1.3, 1.5, and 1.7) V at $T \approx 3$ K showing hysteresis for $V_{DS} > 1.3$ V; (b) Corresponding I_B. insert: Schematic diagram of the transistor measurement set-up.
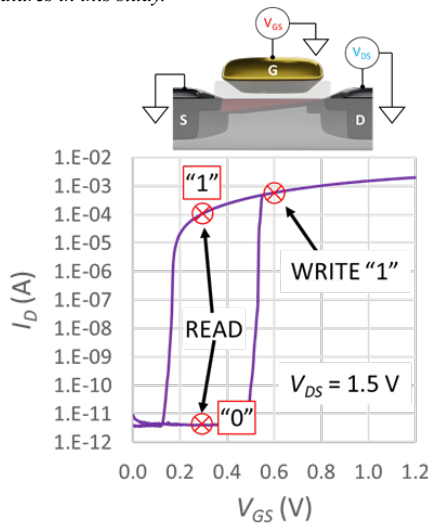

Fig.3: Demonstration of capacitorless cryogenic CMOS memory at $T \approx 3.1$ K. Top left, schematic diagram of the floating base transistor measurement set-up. Bottom left, $I_D(V_{GS})$ for V_{DS} = 1.5 V at showing the WRITE 1 and read bias points. Right, the full write/read/erase/read cycle measured at quasi-static rates.
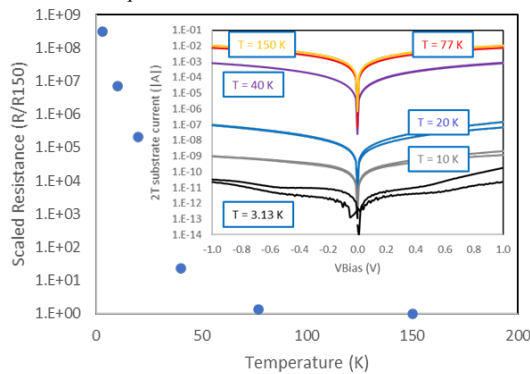

Fig. 4: Substrate resistance vs. T. inert: p-substrate current between two p^{++} contacts vs. bias voltage at various temperatures.
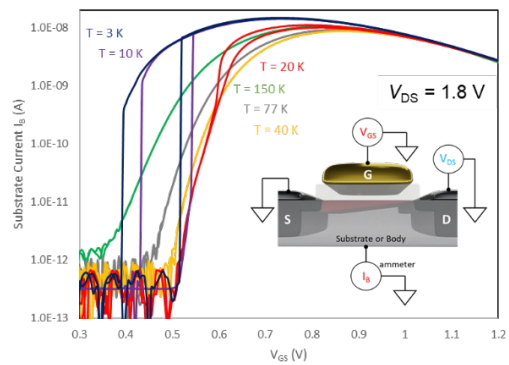

Fig. 5: Impact ionization current vs. T, NMOS $I_B(V_{GS})$ for V_{DS} = 1.8 V at various temperatures showing hysteresis for $T < 20$ K. insert: Schematic diagram of the transistor measurement set-up.

Combinatorial Logic Devices Based on a Multi-Path Active Ring Circuit

Alexander Khitun and Michael Balinskiy

Electrical Engineering Department, University of California - Riverside, Riverside, CA, USA, 92521

akhitun@engr.ucr.edu

In this work, we describe a logic device in which an act of computation is associated with finding a path connecting input and output ports [1]. The device is based on an active ring circuit comprising electric and magnetic parts. The electric part includes an amplifier, a phase shifter, and an attenuator. The magnetic part is a multi-port magnetic matrix comprising delay lines and frequency filters. Signals propagating on different paths may accumulate different phase shifts. Auto-oscillations occur in the circuit when the magnetic and electric parts match each other to meet the resonance amplitude and phase conditions. The system naturally searches for a resonance path that depends on the position of the electric phase shifter and amplification level. The path is detected by the set of power sensors. The proposed logic device can be used for solving a variety of computational problems. We present the results of numerical modeling illustrating prime factorization and finding the shortest path connected selected points on the mesh. We also present experimental data on the proof-of-the-concept experiment for the two-path device. The magnetic part consists of two waveguides made of single-crystal yttrium iron garnet $Y_3Fe_2(FeO_4)_3$ (YIG) films. Different phase shifts per delay line are achieved by adjusting the magnitude and direction of the bias magnetic field. The auto-oscillation signal changes the propagation path in the magnetic matrix depending on the position of the outer electric phase shifter. The power difference between the active and passive paths exceeds 40 dBm at room temperature. The described logic devices are robust, deterministic, and operate at room temperature. The number of possible paths increases factorial with the size of the mesh. It may be possible to encode information in paths and retrieve it using the external phase shifters and attenuators. Potentially, combinatorial logic devices may compete with quantum computers in functional throughput. Physical limits and constraints are also discussed.

[1]   A. Khitun and M. Balinskiy, *Scientific Reports,* vol. 12, no. 1, Jun 2022, Art no. 9482, doi: 10.1038/s41598-022-13614-2.
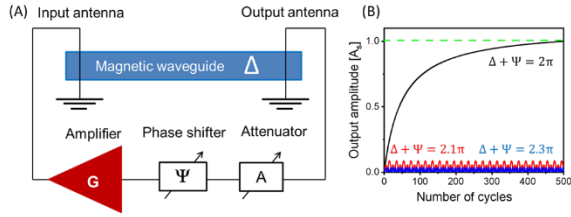
Fig.1: (A) Schematics of an active ring system comprising a broadband amplifier G, a magnonic waveguide – a delay line providing phase shift Δ, a variable attenuator A, and a variable phase shifter Ψ connected in series. (B) Results of numerical modeling illustrating the amplitude evolution with a number of rounds for different phase correlations
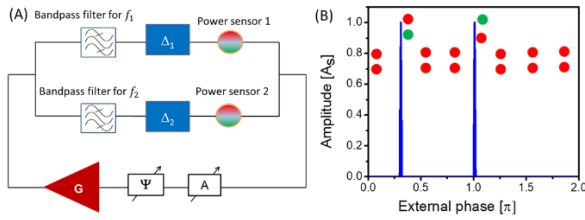

Fig.2: (A) Schematics of an active ring circuit with two passive paths. Each path includes a bandpass filter, a delay line providing a phase shift Δ to the propagating signal, and a power meter. The power meter is aimed to detect whether the power of the signal flowing through the path exceeds the noise level. (B) Results of numerical modeling showing the amplitude of the auto-oscillations depending on the position of the external phase shifter Ψ.
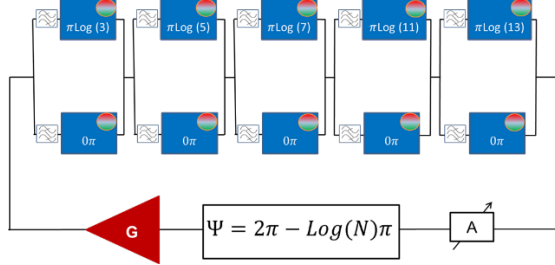

Fig.3: . Schematics of the device for prime factorization. The delay lines in the upper paths provide phase delays proportional to the logarithms of prime numbers 3,5,7,11, and 13, respectively. The delay lines in the lower paths provide no phase shift for the propagating signal. The external phase shifter Ψ is setup to $\Psi = 2\pi - \pi \cdot \log (N)$, where N is the number to be factorized.
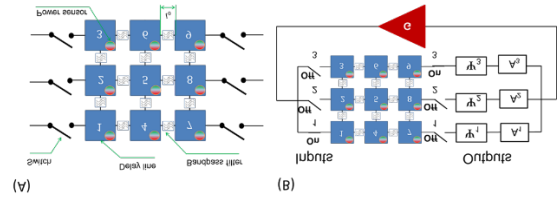

Fig.4: Schematics of 3×3 magnetic matrix comprising nine delay lines marked as 1,2,...9. The delay lines are connected through the bandpass filters. There is a power sensor included in each delay line to detect the energy flow. (B) Matrix connection to the electric part. There are three input and three output ports.
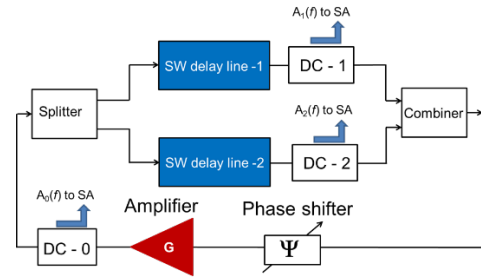

Fig.5 Schematics of the experimental setup for the proof-of-the-concept experiment with a two-path circuit. It is an active ring circuit with two delay lines made of YIG. Delay line one is based on YIG-film with thickness $d_0 = 9.6$ μm, width 2 mm, length 9 mm, saturation magnetization $4\pi M_0 = 1750$ G. Delay line two is based on YIG-film with thickness $d_0 = 21.3$ μm, width 6 mm, length 12 mm, saturation magnetization $4\pi M_0 = 1750$ G.
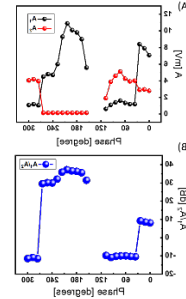

Fig.6: Experimental data on the energy through the upper and lower paths measured separately using DC-1 and DC-2. The black markers correspond to the signal propagating through delay line 1. The red markers correspond to the signal propagating through delay line 2. (A) Experimental data on the power A_s [mV] depending on the position of the external phase shifter. (B) The ratio in dB between the power flow flowing through the upper and lower paths. All experiments are done at room temperature.

Circuit-level Device Modeling for Erase Failure Analysis in Vertical Gate-all-around Charge Trapping Flash Memories

Sunghwan Cho[1,2] and Byoungdeog Choi[3]

[1]*Department of Semiconductor and Display Engineering, Sungkyunkwan University, Suwon, Korea*

[2]*Samsung Electronics Company, Ltd., Hwaseong 445-701, Korea*

[3]*Department of Electrical and Computer Engineering, Sungkyunkwan University, Suwon, Korea*

bdchoi@skku.edu

In order to scale down the memory devices, charge trapping flash memory devices with gate-all-around structure gradually replace conventional NAND flash memories with a larger storage area and less capacitive coupling rather than planar-structured NAND flash memories [1]. However, as the number of vertically stacking layers is getting higher and demands for high capacity and performance are continued to grow, accurate prediction for various behaviors during program/erase execution in circuit-level analysis is necessary to optimize circuit design. This brings an essential requirement of accurate circuit-level device model to analyze various characteristics and failure mechanisms. Although several works for circuit-level device model using BSIM-CMG model have been reported previously [2], it is mainly focused on program operation which is not related to vertically hole accumulation from p-well. In this work, we have developed an accurate circuit-level device model for erase operation in gate-all-around-structured string which is vertically connected to p-well. Fig. 1 shows general circuit model for erase operation in gate-all-around structured charge trapping flash memory device using conventional BSIM-CMG model. By forcing positively to V_{BODY} and using voltage-controlled-current-source in this general model, erase execution can be easily implemented. However, as shown in Fig. 2(a), body is floated unlike planar NAND flash memory and holes are should be accumulated vertically from p-well to erase the charge trapping layer. Fig. 2(b) illustrates circuit schematic for proposed model using voltage-controlled-current-source for describing hole accumulated current through the vertical cell string, which can determine the electrostatic potential of V_{CH} and electric field between V_{CH} and V_{NIT} during erase operation. With our circuit-level device model, less hole accumulation by barrier between poly-Si channel of GSL transistor and p-well and corresponding V_{CH} lowering can be predicted unlike conventional model, as shown in Fig.3(a) and (b). Consequently, our model makes it available for circuit designer to analyze erase failures by good agreement with measurement, as shown in Fig. 4, and furthermore, allows accurately predicting the characteristics in various behaviors and optimizing the performance in ultra-scaled charge trapping flash memory devices.

[1] Akira Goda, IEEE Transactions on Electron Devices, vol. 67, no.4, pp. 1373-1381 (2020).

[2] M.Kim *et al.*, IEEE Transactions on Electron Devices, vol. 67, no.8, pp. 3095-3101 (2020).
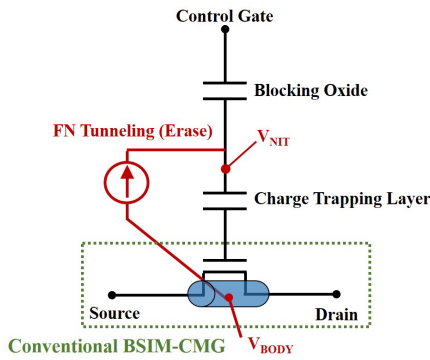
Fig.1: Circuit schematic for general device model describing erase operation by voltage controlled current source between charge trap layer (V_{NIT}) and body (V_{BODY}) which is not the real
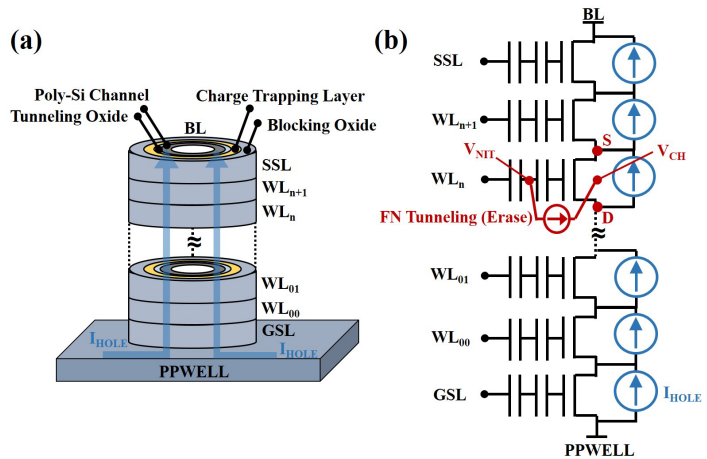

Fig.2: (a) Schematic for structure and hole current from p-well in vertical gate-all-around charge trapping flash memory (b) Schematic for equivalent circuit of proposed model describing hole accumulation from p-well and electrostatic potential (V_{CH}) for erase execution.
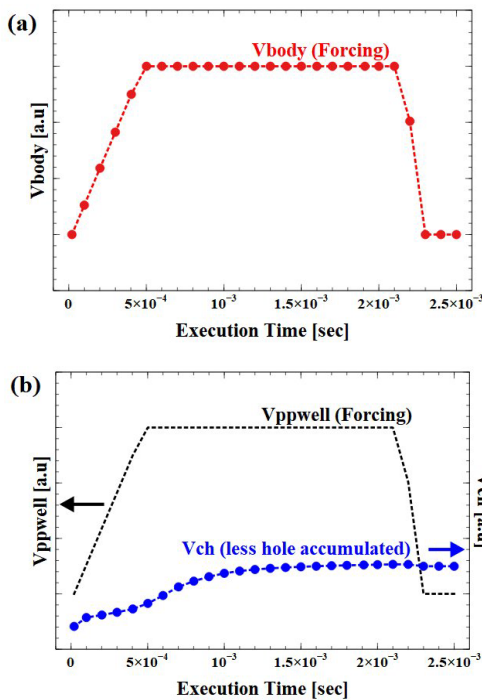

Fig.3: Circuit simulation results for (a) V_{BODY} using conventional model and (b) V_{CH} using the proposed model. Note that V_{CH} can be lowered using our model which is attributed to less hole accumulation by barrier between poly-Si channel of GSL transistor and
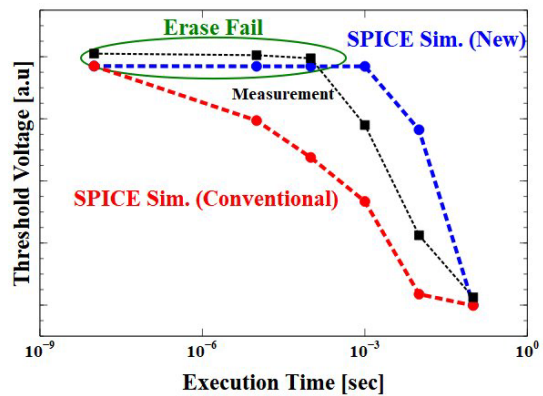

Fig.4: Erase speed results of measurement and circuit simulations (conventional and proposed model). Note that simulation result by our model have good agreement with measured behavior which contributes to analyze erase failure and optimize performance of ultra-

Modeling and Design of Atomic Precision Advanced Manufacturing (APAM) Enabled Bipolar Devices

X. Gao[1], J. P. Mendez[1], S. Misra[1], J. N. Randall[2], J. H. G. Owen[2], and W. P. Kirk[3]

[1] Sandia National Laboratories, 1515 Eubank SE, Albuquerque, NM 87123, USA

xngao@sandia.gov

[2] Zyvex Labs LLC, 1301 N. Plano RD, Richardson, TX 7508, USA

[3] 3D Epitaxial Tech., LLC, 999 E. Arapaho Rd, Richardson, TX 75081, USA.

In recent years, p-type dopants (e.g., B and Al) have been successfully incorporated in atomic precision advanced manufacturing (APAM) devices [1-2], in addition to the more mature n-type P dopant [3-5], which enabled the first experimental demonstration of APAM *pn* junction device [1]. Sharp doping profile and high doping density obtained from APAM provide the possibility of designing new devices with superior performance. With that in mind, we are exploring the design and fabrication of APAM bipolar devices including *pn* diodes and bipolar junction transistors (BJT) [6]. To understand the operation of APAM bipolar devices, we simulated an APAM *pn* diode (Fig.1, right) based on the device in Ref. [1], using Sandia's open-source TCAD code Charon (Fig.1, left). To model the band-to-band tunneling (B2BT) due to high doping, we developed a modified Hurkx B2BT model (Fig. 1, left) to achieve robust numerical convergence as well as negligible tunneling current at equilibrium. As shown in Fig. 2, the peak current of the negative differential conductance (NDC) region depends strongly on the parameter B, which acts as a threshold field for B2BT. Note, the simulated valley voltage (~ 0.9 V) where normal diode behavior turns on is much larger than the measured value (~ 0.6 V). There can be multiple reasons why the measured valley voltage is smaller than the simulated value. One of them is band-to-trap tunneling (B2TT) [7] that can enhance valley current and reduce valley voltage as shown in Fig. 3. Another possibility is that high delta doping causes significant band gap narrowing (BGN) in the delta layer, leading to reduction of the valley voltage as shown in Fig. 4. We expect that a combination of B2TT and BGN can capture the forward I-V data quite well except at low voltages (< 0.2 V). For reverse biases, Fig. 5 shows B2BT alone can model the main features in the measured data despite the need for further study. Finally, we simulated APAM *pn* junctions with various gaps (bottom inset in Fig. 6) and plotted the resulting I-V curves in Fig. 6. Currently, we are fabricating APAM *pn* junctions with various gaps to compare fabricated device I-V characteristics with these simulations.

[1] T. Škereň *et al.* Nat. Electron. **3**, 524-530 (2020). [2] J. H. G. Owen *et al.*, J. Phys.: Cond. Matt. **33**, 464001 (2021). [3] F. J. Ruess *et al.*, Nano Lett. **4** (10), 1969-1973 (2004). [4] L. Fricke *et al.*, Nat. Commun. **12**, 3323 (2021). [5] C. Halsey *et al.*, IEEE Trans. Device Mater. Rel. **22** (2), 169-174 (2022). [6] J. H. G. Owen *et al.*, talk at Fall MRS, Dec. 2021. [7] X. Gao *et al.*, J. Appl. Phys. **125**, 054503 (2019).
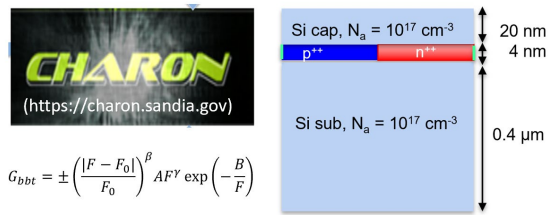
Fig.1: (left) Sandia's open-source TCAD Charon tool and the modified Hurkx model for B2BT. F_0 and F are the electric field strengths at equilibrium and non-equilibrium respectively. A, B, β, γ are adjustable parameters. B2BT can be modeled as generation (+) or recombination (-) depending on applied bias. (right) Not-to-scale schematic of the simulated APAM pn junction. Doping values in the Si cap and substrate layers were arbitrarily chosen since they are not expected to affect the current. Doping in the p++ and n++ delta layer was set to $3x10^{20}$ cm^{-3}, corresponding to a sheet density of $1.2x10^{14}$ cm^{-2}, which is close to the delta doping in Ref. [4].
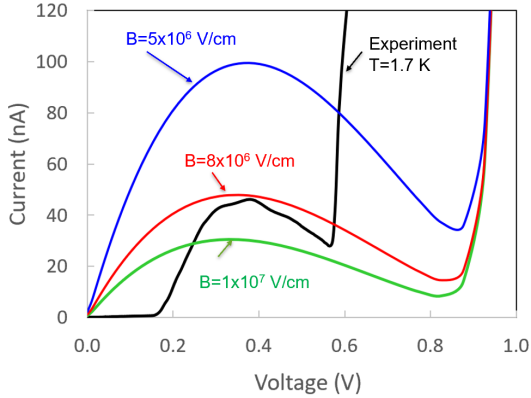

Fig.2: Simulated current-voltage (I-V) curves for different B2BT parameter B values as compared to the experimental data in Ref. [4]. Since the parameter B acts like a threshold field in the model, a smaller B value leads to a higher tunneling current. In addition, because our B2BT model does not contain temperature, the simulated NDC response is insensitive to temperature.
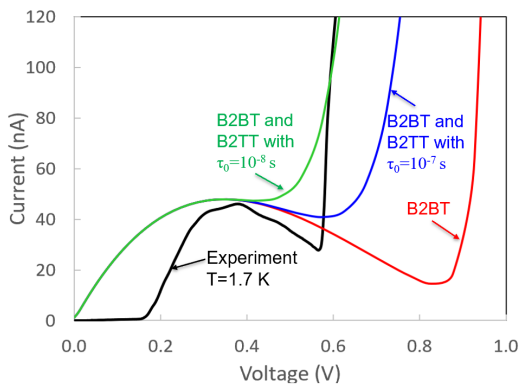

Fig.3: Simulated current-voltage curves for B2BT only (red), B2BT and B2TT with different zero-field lifetimes (blue and green) as compared to the experimental data (black). The red curve is the same as the red one in Fig. 2. As expected, inclusion of B2BT does not affect the NDC response, but decrease the valley voltage and increase the valley current.
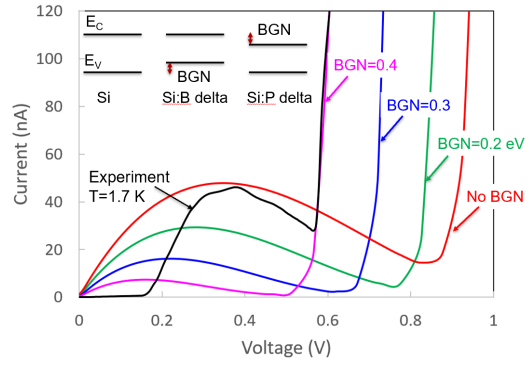

Fig.4: Simulated I-V curves for different band gap narrowing (BGN) values as compared to the experimental data. The red curve is the same as in Fig. 2. Inset: schematics showing the locations of BGN for the Si:B (p-type) and Si:P (n-type) delta layers. Due to high doping in delta layers, BGN is expected; but its value depends on process conditions and doping density. The same BGN value was applied to Si:B and Si:P delta layers.
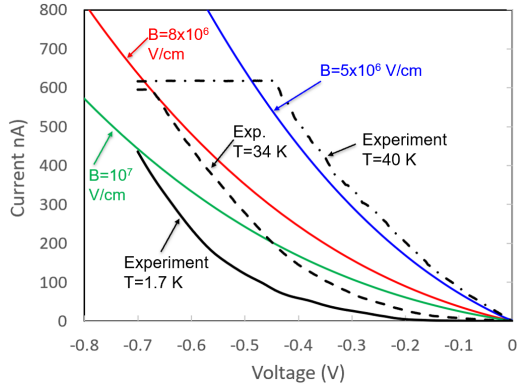

Fig.5: Simulated reverse I-V curves for different B2BT parameter B values as compared to the experimental data which show a strong temperature dependence. Since our B2BT model does not have a temperature dependence, we modified the B value to approximately account for this effect.
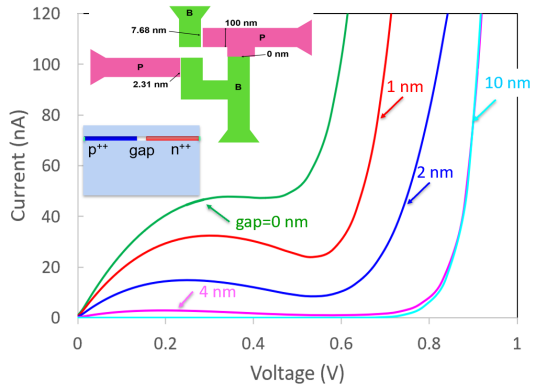

Fig.6: Simulated I-V curves for different gap widths denoted by the schematic in the bottom inset. The green curve is the same as in Fig. 3. When the gap width is larger than 4 nm, the NDC behavior nearly vanishes. The top inset shows the layout of APAM pn junctions that were designed based on these simulations. These results will be compared to the devices being fabricated.

Hot-carrier Dynamics and Transport in Type-II Quantum Wells

H. P. Piyathilaka,[1] V. R. Whiteside,[2] M. Santos,[2] I. R. Sellers[2] and A. D. Bristow[1]

[1]*Department of Physics and Astronomy, West Virginia University, Morgantown, West Virginia, 26506-6315 USA*

[2]*Home L. Dodge Department of Physics and Astronomy, University of Oklahoma, Norman, Oklahoma, 73019 USA*

alan.bristow@mail.wvu.edu

InAs/AlAsSb superlattice heterostructures have type-II band alignment and are a model system for enhancing hot-carrier dynamics, which for example remains a viable way to overcome the detailed balance limit of single-junction photovoltaic cells [1,2]. Using pump-probe spectroscopy with a tunable near-infrared excitation pulse and a terahertz frequency probe, transient absorption, terahertz conductivity and terahertz photoconductivity allow for a full exploration of the charge carrier dynamics and transport in these devices. Control parameters include the pump-probe delay time, the terahertz delay time, the excitation photon energy and the lattice temperature of the sample. Overall, the photon excitation dependence shows the existence of a metastable state shortly after photoexcitation, particularly visible at cryogenic temperatures; see Fig 1 [1]. This metastability exhibits a clear onset at ~100 meV excess photon energy at <120 K. This onset is energy dependent and appears to vanish at ambient temperatures, when valence bands are expected to completely delocalized throughout the superlattice structure. The decay mechanism exhibit strong Auger scattering at high excitation densities, which gives way to strong radiative recombination and then Shockley-Reed-Hall dynamics as the photocarrier density decreases; see Fig 2(a) and Fig 3. Moreover, the fastest recombination time correlates to specific peaks on the absorption spectrum and is highly temperature dependent as expected from a changing band structure; see Fig 2(b). The metastable regime corresponds to strong Auger scattering. AC photoconductivity shows that as the photocarrier density decreases so does the conductivity; see Fig 4(a). In the metastable regime, there is an increase photocarrier density and conductivity; see Fig 4(b). Interestingly, this corresponds to a slight reduction in mobility (not shown) as the carriers scatter more strongly. Overall, the mobility for the samples is exceptionally high and as the lattice temperature increases the fast mechanism of Auger scattering gives way to an increased ambipolar diffusion; see Fig 5. The combination of decay and transport characteristics suggest that the metastability doesn't vanish at high temperature, but remains a mechanism for hot-carrier extraction temper by diffusion process that seek to reduce excessive photocarrier densities, meaning that these III-V superlattice structures could be engineered for hot-carrier extraction in photovoltaic devices.

[1] H. P. Piyathilaka *et al.*, Sci. Rep. **11**, 10483 (2021).

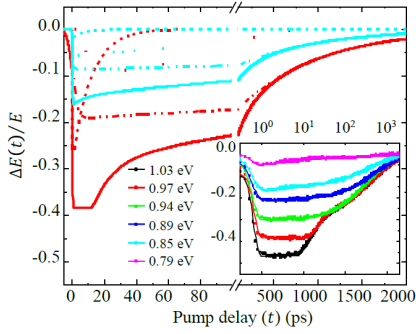[2] H. P. Piyathilaka et al, Phys. Rev. Appl. **18**, 014001 (2022).

Fig.1 Transient absorption of the InAs/AlAsSb heterostructures as a function of photon energy with fitting contributions. Inset shows the data on a semilog scale, highlighting existence of a metastable state at early delay times.
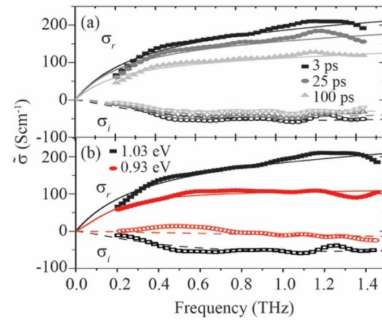

Fig.4 AC photoconductivity as a function of (a) pump-probe delay time and (b) excitation energies above and below the P_3 excitation threshold for metastability (Δ_{plt}).
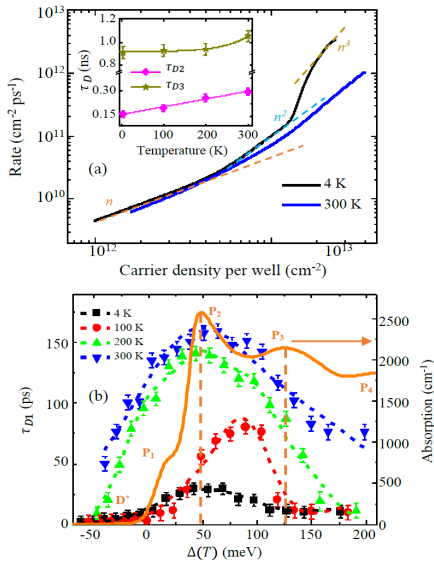

Fig.2 (a) Rate-equation for high and low temperature at 1.03 eV excitation, with gradients indicating mechanisms [SRH ~n, radiative ~n^2 and Auger ~n^3]. Inset shows slow decay times. (b) Fast decay time versus excess photon energy (Δ) and temperature. [D*=defect states, P_x =significant points in simulated absorption (orange).]
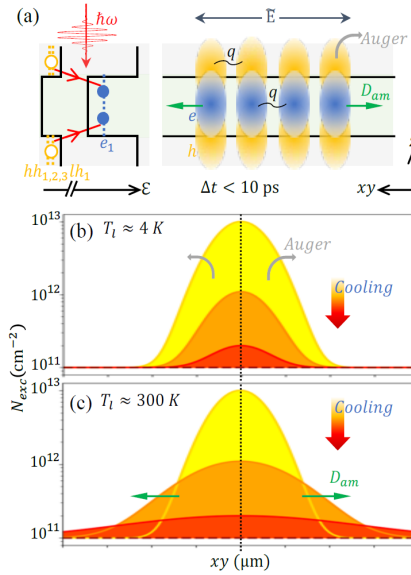

Fig.5 (a) Schematic diagram of excitation of electrons and holes and their resulting dynamics and AC transport. Schematic distribution of carriers undergoing cooling at lattice temperatures of (a) 4 K and (b) 300 K. [D_{am} = Diffusion coefficient]
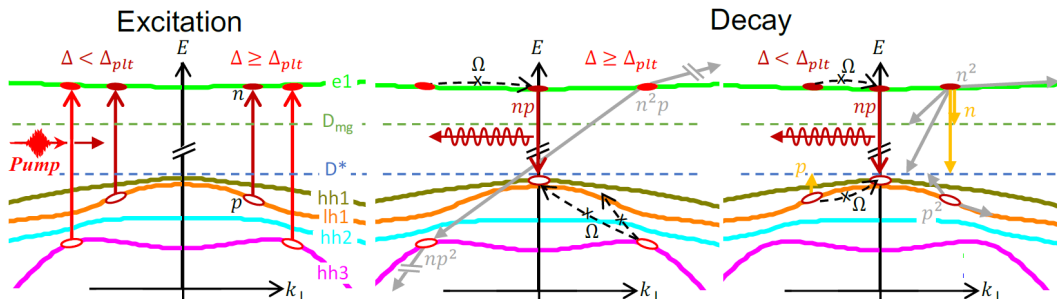

Fig.3 Excitation and decay mechanisms to explain the recombination dynamics with the metastable state at low-temperature and high excess photon energy (Δ). [Δ_{plt} = threshold for excitation to metastable state, e1 = conduction band, hh =heavy hole band, lh = light hole band, D = defect bands , n = electron density and SRH dynamics, p = hole density and SRH dynamics, np = radiative recombination, n^2 and p^2 = intraband scattering, n^2p and np^2 = Auger scattering.]

Prediction of two conductivity regimes in δ-layer tunnel junctions

D. Mamaluy[1], and J.P. Mendez[1]

[1]Cognitive & Emerging Computing, Sandia National Laboratories, Albuquerque, USA,

mamaluy@sandia.gov

We present an open-system quantum-mechanical charge self-consistent 3D real-space study of the conduction band structure and conductive properties of phosphorus delta-layer tunnel junctions in silicon shown in Fig. 1. These structures serve as basic building blocks for beyond-Moore (classical digital) (e.g. [1]) and quantum computing applications (e.g. [2]). Recent high resolution ARPES experiments [3, 4] demonstrated that the traditional band structure calculation methods that are based on either periodic or Dirichlet boundary conditions fail to describe the existence of 3Γ subband without adjusting the dielectric constant of Si to 40. Recently we demonstrated that using the open system boundary conditions (for the charge self-consistent Schrodinger equation) that preserve the quantum-mechanical flux allows to explain the existence of 3Γ subband without any fitting parameters and accurately reproduce the sheet resistance values for a wide range of delta-layer doping densities and different experimental groups [5]. Here we extend the open-system charge self-consistent quantum transport analysis to delta-layer tunnel junctions. The performed numerical analysis predicts that the strong conduction band quantization leads to the existence of two distinct Ohmic conductivity regimes as shown in Fig. 2. The corresponding mechanism can be understood from Figure 3, where the computed local density of states is shown. For cryogenic temperatures only the states below Fermi level are occupied. As can be seen from Figure 3, the strong delta-layer confinement leads to the conduction band quantization. For low voltages, there is a mismatch between the quasi-discrete states on the left that have to tunnel to the quasi-discrete states on the right side, which reduces the conductivity. For higher applied drain voltages, the quasi-continuum states on the right side become available to tunnel into from the left side that eliminates the mis-match and increases conductivity [6]. Recent experimental data [2] for the I-V characteristics in Si:P delta-layer tunnel junctions support the existence of the two conductivity regimes. The "threshold" voltage (around 0.05-0.07 V in Fig. 2) is a function of doping level and doping thickness, and could be controlled for device applications.

[1] He, Y. et al., Nature 571, 371–375 (2019).

[2] M. B. Donnelly, J. G. Keizer, Y. Chung, and M. Y. Simmons, Nano Letters 21, 10092 (2021).

[3] A. J. Holt et al., Phys. Rev. B 101, 121402 (2020).

[4] F. Mazzola, CY. Chen, R. Rahman et al., npj Quantum Mater. 5, 34 (2020).
[5] D. Mamaluy, J.P. Mendez, X. Gao, et al. Commun Phys 4, 205 (2021).
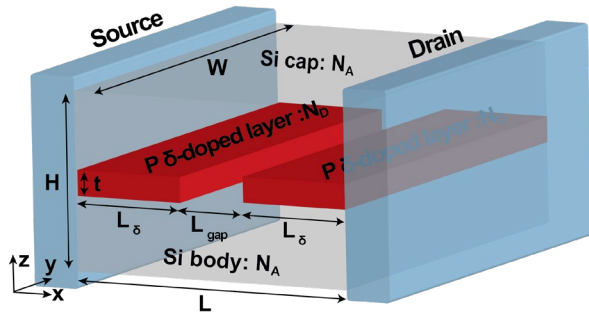[6] J.P. Mendez, D. Mamaluy, Scientific Reports (accepted) (2022).

Fig.1: Fig.1: Ideal Si:P δ-layer tunnel junction (TJ) devices. The ideal device consists of a semi-infinite source and drain, in contact with the channel. The channel is composed of a lightly doped Si body and Si cap and a very thin, highly P doped-layer with an intrinsic gap of length L_{gap}.
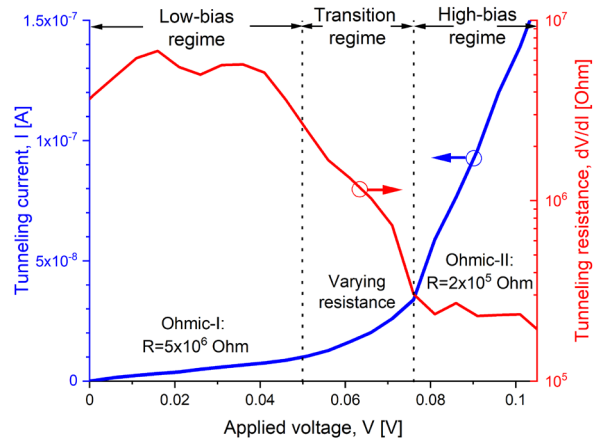
Fig.2: Two conductivity regimes in δ-layer tunnel junctions. Total current vs voltage (blue curve, linear scale) and the corresponding differential resistance dV/dI (red curve, logarithmic scale) are shown for L_{gap}=10nm, N_D=1.0×10^{14}cm^{-2}, N_A=5.0×10^{17}cm^{-3} and t=1nm.

Fig.3: Local Density of States for δ-layer tunnel junctions. The LDOS(E,x) for a tunnel junction of L_{gap}=10 nm is shown in (a) and (b) when a voltage of 1 mV and 100 mV is applied to the drain contact, respectively. The Fermi levels indicated in the figures correspond to the Fermi levels of the source and drain contacts. In (a) and (b), the corresponding effective 1D potentials are also shown, calculated by integrating over the (y,z)-plane the actual charge self-consistent 3D potentials weighted with the electron density. N_D=1.0×10^{14} cm^{-2}, N_A=5.0 ×10^{17} cm^{-3}, and t=1nm.
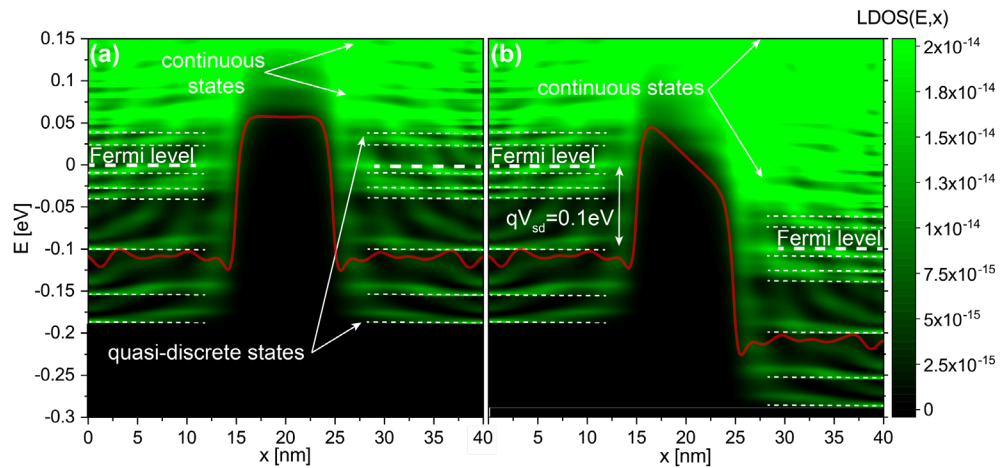
Atom-Defined Silicon Device Elements for Quantum Devices and Ultra-Fast, Ultra-Low Power Classical Circuits

R.Wolkow[1,2] , J.Pitters[2], J. Onada[1,2], A.Khademi[1,2], T.Chutora[1], C.Leon[1], F.Altincicek[1], J.Croshaw[1], L.Livadaru[1], M.Yuan[1], R.Achal[1], S.Yong[1]

[1]*Department of Physics, University of Alberta, Edmonton, Alberta, Canada*
[2]*National Research Council of Canada Nanotechnology Research Centre*

Most all atom-defined structures that have been built to date have been held together by extremely weak dispersion interactions and are therefore unstable at room temperature. Moreover, most systems of study have been fabricated on metal substrates that entirely mask any interesting/useful electronic properties of atomic (or molecular) assemblies. Patterned atomic dangling bonds on an otherwise Hydrogen-terminated silicon surface are robust and unchanging to over 200 C and offer useful electronic properties. This area was pioneered largely by Joseph Lyding more than 2 decades ago.

Many challenges stood in the way of tests and applications in this area. Over the last 20 years we have doggedly pursued and overcome innumerable fabrication and measurement issues related to dangling bonds and as well have come to greatly advance understanding of dangling bonds assemblies and their environment. Crucially, we recognize and utilize the gap-state character of dangling bond structures to make 2D surface circuits that are isolated from the bulk. We also use the controllable electron occupation of DBs. Operation of binary atomic silicon logic gates and a binary wire have been demonstrated. These are derived from earlier, non-atomic, field-controlled computing ideas developed by Lent, Snider, Porod and others at Notre Dame. Our atomic building blocks attain fast, low power qualities while removing a cryogenic operation requirement. Because our devices are truly identical we can introduce a new era of variance-free devices. We see that our atom-defined components can embody not only classical circuitry but some quantum phenomena become routinely accessible also.

In this talk I will show new results including fabrication and multi-spm-probe characterization of nm-scale silicon wires that are intimately bonded to, yet electrically isolated from bulk Si. Also, atom-defined wires and their quantized states will be shown. A surprising result involving atomic wires of switchable covalent and ionic bonding character will be shown. A new(?) boron cluster in silicon will be mentioned as will atomic wire coupling to the boron species. Discussion of first atom-defined commercial products such as a truly portable quantum random number generator, a fast comparator, and a quantum magnetometer might be chatted about in our ad hoc sessions.